

**Niet-lineair gedrag in nanofotonische golfgeleiders  
en resonatoren voor ultrasnelle signaalverwerking**

**Nonlinear behaviour in nanophotonic waveguides  
and resonators for ultrafast signal processing**

---

**Gino Priem**

Promotoren: prof. dr. ir. G. Morthier, prof. dr. ir. R. Baets  
Proefschrift ingediend tot het behalen van de graad van  
Doctor in de Ingenieurswetenschappen: Natuurkunde

Universiteit Gent  
Faculteit Ingenieurswetenschappen  
Vakgroep Informatietechnologie  
Voorzitter: prof. dr. ir. P. Lagasse  
Academiejaar: 2005-2006



**Promotoren:**

prof. dr. ir. G. Morthier  
prof. dr. ir. R. Baets

Universiteit Gent, INTEC  
Universiteit Gent, INTEC

**Examencommissie:**

prof. dr. P. Kiekens (voorzitter)  
prof. dr. ir. P. Bienstman (secretaris)  
dr. R. Raj  
prof. dr. ir. M. Haelterman  
prof. dr. ir. P. De Visschere  
prof. dr. ir. F. Olyslager

Universiteit Gent, Textielkunde  
Universiteit Gent, INTEC  
LPN-PHOTONIQ, France  
Universite Libre de Bruxelles  
Universiteit Gent, ELIS  
Universiteit Gent, INTEC

Universiteit Gent  
Faculteit Ingenieurswetenschappen

Vakgroep Informatietechnologie (INTEC)  
Sint-Pietersnieuwstraat 41  
B-9000 Gent  
België

Tel.: +32-9-264 34 48  
Fax: +32-9-264 35 93  
<http://www.intec.ugent.be>

Dit werk kwam tot stand in het kader van een mandaat van Aspirant bij het Fonds voor Wetenschappelijk Onderzoek (FWO) - Vlaanderen (België).

This work was carried out in the context of a doctoral fellowship from the Fund for Scientific Research (FWO) - Flanders (Belgium).



# Voorwoord - Preface

Doctoreren kun je - zoals de meeste mensen wel denken - helemaal niet omschrijven als 'werken'. In het begin lijkt het eerder op zoeken naar een pinguïn op de noordpool: van het ene dwaalspoor kom je op het andere, een leerproces... Met de frisse ideeën van mijn promotoren Geert en Roel en de onmisbare hulp van mijn twee bureaugenoten Jos en Pieter had ik na ongeveer een half jaar tijd eindelijk enig idee van wat mijn onderwerp precies allemaal inhield. Alle problemen van de baan!! Nu kon ik beginnen wachten op simulaties, Peter lastig vallen over CAMFR, met Jos en Pieter meer nieuwe problemen veroorzaken dan oude oplossen, weer wachten op simulaties, ...

Na een paar honderd koffiepauzes en tientallen brésilienekes begonnen mijn resultaten wat samenhang te vertonen en ging de wereld van de conferenties voor mij open: toch wel een van de leukste aspecten aan doctoreren. Je krijgt de kans om op korte tijd heel wat bij te leren over allerhande onderwerpen en komt bovendien op plaatsen die je niet voor mogelijk had gehouden. Zo belandde ik met Jos en Wim in Kyoto, totally lost in translation, maar met een fantastische kamerjas: arigatô gozaimasu. Met D'Oos kwam ik terecht in San Diego om daarna met Pieter - inderdaad onze huurauto heeft ABS - het Californische binnenland onveilig te maken. Dank je, Diederik, voor de logies en de langlaufinstructies! Het woord jet-lag kreeg echter pas echt betekenis toen ik ook naar Sydney op conferentie mocht, samen met Roel en Günther. Three wise (?) monkeys in the land of the kangaroo...

Ondertussen hadden Ilse en Pieter mij leren meten en kon ik mij niet-lineair gaan uitleven op echte structuren. Tot wanhoop van Sam, D'Oos, Hendrik en Dries waarschijnlijk, want bijna alle meetapparatuur was wel ergens op mijn meettafel te vinden. Uiteindelijk kwam alles wel op zijn pootjes terecht en ben ik erin geslaagd dit kleine boekje bijeen te schrijven.

Laat mij voor alle duidelijk vermelden dat ik ook deze mensen in deze drieënhalve jaar heel wat heb lastiggevallen en hen daarvoor wil bedanken: Wim, Dirk, Bert, Kris, Reinhard, Bart, Olivier, Peter, Lieven, Freddy, Wouter, Stijn, nog eens Peter, Bjorn, ook nog eens Freddy, Jon, Joost, Joris, Katrien, Benoit, Shankar, Iwan, Zeger, Ilse, Ilse, Karien, Bernadette, het hele TDC-team ... en alle anderen die ik nu tot mijn schaamte vergeten ben. I would also like to thank Tak-Keung and Romeu for their help in performing nonlinear experiments and the opportunity to do some of the measurements myself at the NICT.

Ik wil zeker en vast ook mijn ouders en mijn tante bedanken voor alle aanmoedigingen en financiële steun tijdens mijn studies en mijn doctoraatsjaren. Natuurlijk ben ik mijn tiggertje niet vergeten: dank je wel voor alles wat je met mij al hebt meegemaakt :) En tot slot een woordje van dank aan haar ouders en haar broer en zus voor alles wat jullie voor mij hebben gedaan de voorbije vijf jaar. Doe!

Gino Priem

Zingem, 26 april 2006

# Contents

<b>Voorwoord - Preface</b>	<b>i</b>
<b>Contents</b>	<b>iii</b>
<b>Nederlandstalige samenvatting</b>	<b>ix</b>
<b>English summary</b>	<b>xiii</b>
<b>1 Introduction</b>	<b>1</b>
1.1 Photonics . . . . .	1
1.2 Ultrafast, nonlinear, all-optical signal processing . . . . .	2
1.3 Focus of this work . . . . .	3
1.4 Publications . . . . .	3
<b>2 Nonlinear effects in standard semiconductor systems</b>	<b>7</b>
2.1 Mathematical formulation . . . . .	7
2.2 Bound-electronic Kerr effect . . . . .	11
2.3 Two-photon absorption . . . . .	16
2.4 Figure of merit . . . . .	17
2.5 Carrier effects . . . . .	20
2.6 Thermal effects . . . . .	25
2.7 Complete nonlinear picture . . . . .	26
2.8 Material anisotropy . . . . .	29
2.9 Material engineering . . . . .	31
2.10 Conclusions . . . . .	31
<b>3 Transverse nonlinear confinement: waveguides</b>	<b>33</b>
3.1 Waveguide confinement . . . . .	33
3.1.1 Silicon-on-Insulator (SOI) system . . . . .	34
3.1.2 GaAs-AlGaAs system . . . . .	37
3.1.3 AlGaAs-AlO <sub>x</sub> system . . . . .	38

3.2	Applications . . . . .	40
3.2.1	Bound-electronic Kerr effect . . . . .	41
3.2.2	Two-photon absorption effect . . . . .	43
3.3	Figure of merit . . . . .	46
3.4	Conclusions . . . . .	47
<b>4</b>	<b>Longitudinal nonlinear confinement: resonators</b>	<b>49</b>
4.1	One-dimensional optical resonator . . . . .	50
4.2	Applications . . . . .	52
4.2.1	Bound-electronic Kerr effect . . . . .	53
4.2.2	Two-photon absorption effect . . . . .	83
4.3	Figure of merit . . . . .	88
4.4	Conclusions . . . . .	89
<b>5</b>	<b>Experimental verification</b>	<b>91</b>
5.1	SOI waveguides . . . . .	92
5.1.1	Fabricated structures . . . . .	92
5.1.2	Single-signal operation . . . . .	92
5.1.3	Pump-probe operation . . . . .	96
5.2	Resonators . . . . .	103
5.2.1	Fabricated structures . . . . .	103
5.2.2	Single-signal operation . . . . .	105
5.2.3	Pump-probe operation . . . . .	112
5.3	Conclusions . . . . .	115
<b>6</b>	<b>Conclusions and perspectives</b>	<b>117</b>
6.1	Conclusions . . . . .	117
6.2	Future work . . . . .	118
<b>A</b>	<b>Material anisotropy</b>	<b>121</b>
<b>B</b>	<b>Effective nonlinear coefficients</b>	<b>125</b>
B.1	Nonlinear effects in a slab waveguide . . . . .	125
B.1.1	Transverse electric case . . . . .	127
B.1.2	Transverse magnetic case . . . . .	131
B.2	Effective nonlinear coefficients . . . . .	136
B.2.1	Definition . . . . .	136
B.2.2	Plane wave and parallel plate verification . . . . .	138

---

<b>C</b>	<b>Linear properties of one-dimensional optical resonators</b>	<b>141</b>
C.1	Linear properties for 1 period . . . . .	141
C.2	Properties for $\infty$ periods . . . . .	143
C.3	Comparison between 1 and $\infty$ periods . . . . .	146
C.4	Properties for $N$ periods . . . . .	147
C.5	Free spectral range . . . . .	148
C.6	Field profile . . . . .	151
<b>D</b>	<b>Kerr-nonlinear properties of one-dimensional resonators</b>	<b>153</b>
D.1	Shift of resonance frequency . . . . .	153
D.2	Nonlinear transmission relation $ t_{tot,NL} ^2$ . . . . .	156
D.2.1	Transmission of 1 resonator period . . . . .	156
D.2.2	Transmission of $\infty$ resonator periods . . . . .	159
D.2.3	Transmission of $N$ resonator periods . . . . .	159
D.3	Nonlinear phase relation $\phi_{NL}$ . . . . .	160
D.3.1	Phase shift for 1 period . . . . .	160
D.3.2	Phase shift for $\infty$ periods . . . . .	161
D.3.3	Comparison and generalization . . . . .	161
D.4	Modal theory approach . . . . .	162
D.4.1	Shift of phase relation $\phi$ . . . . .	163
<b>E</b>	<b>Two-photon absorption properties of resonators</b>	<b>167</b>
<b>F</b>	<b>Bit-error rate calculation</b>	<b>173</b>
	<b>Bibliography</b>	<b>175</b>



## **Samenvatting - Summary**



# Nederlandstalige samenvatting

Vandaag de dag vormen optische vezels de basis voor de telecommunicatie over lange afstand. Ze maken het transport mogelijk van enorme hoeveelheden informatie door het feit dat ze verschillende golflengtekanalen tegelijkertijd kunnen vervoeren zonder dat deze elkaar beïnvloeden. De volledige capaciteit van deze vezels kan echter nog niet worden gebruikt doordat de schakel- en de signaalverwerkingsmogelijkheden in de optische laag nog te beperkt zijn: wanneer een optisch signaal door een knoop in een netwerk passeert, moet de data eerst omgezet worden naar het elektrisch domein voor ze kan verwerkt worden. Daarna wordt ze terug omgezet naar het optisch domein en kan ze verder worden getransporteerd. Voor hoge informatiestromen is dit een kostelijk en moeilijk proces.

Hoewel goedkope integratie met het behoud van deze elektrisch-optische conversies een eerste stap vormt, wordt verwacht dat de werkelijke doorbraak naar ultrahog datatransport gevormd wordt door signaalverwerking in het optische domein zelf. Om dit op een geïntegreerde manier te doen, bestaan er op dit moment twee belangrijke routes:

- met behulp van vrijeladingsdragereffecten. Alhoewel het bewerken van datastromen met deze aanpak beperkt is door de recombinatietijd van deze ladingsdragers tot ongeveer 10 Gb/s, laat het gebruik van interferometrische technieken toe om hogere datastromen te verwerken.
- met behulp van ultrasnelle niet-lineaire effecten veroorzaakt door het licht zelf: sterke optische signalen induceren in bepaalde materialen niet-lineair gedrag met een praktisch ogenblikkelijke responstijd, wat ultrasnelle optisch signaalverwerking mogelijk

maakt. Deze effecten zijn echter typisch heel zwak en vergen daarom heel wat vermogen.

In dit werk onderzoeken we deze laatste route omdat ze intrinsiek het grootste potentieel voor ultrasnelle signaalverwerking bezit, met de nadruk op de volgende twee niet-lineaire effecten: het Kerr effect en twee-foton absorptie. Om de zware vermogenvereisten te beperken, maken we gebruik van nanofotonische componenten die de interactie tussen het licht en het materiaal in een belangrijke mate versterken.

Het gebonden-elektronisch of optisch Kerr effect en het twee-foton-absorptieproces stemmen respectievelijk overeen met de lineaire afhankelijkheid van de brekingsindex en de absorptiecoëfficiënt van de lichtintensiteit. Deze effecten zijn ultrasnel omdat ze geen werkelijke elektronische overgangen vereisen, maar enkel de mogelijkheid ervan. Hun respons- en hersteltijd is van de orde van ps. Welk effect nu precies in een bepaald materiaal domineert, is afhankelijk van de verhouding van de lichtfrequentie tot de grootte van verboden zone van dat materiaal. AlGaAs is bijvoorbeeld een van de meest geschikte halfgeleidermaterialen voor Kerr gedrag bij de telecom golflengte van 1.55  $\mu\text{m}$ . Voor deze golflengte zijn GaAs en InP dan weer uitstekende materialen voor twee-fotonabsorptie. In Silicium zijn beide effecten belangrijk bij 1.55  $\mu\text{m}$ , wat dit materiaal een geschikt materiaal maakt voor wetenschappelijk onderzoek. Zoals hierboven vermeld zijn ultrasnelle niet-lineaire effecten typisch heel klein. In halfgeleidermaterialen zijn dan ook lichtintensiteiten van de orde 1 – 10  $\text{GW}/\text{cm}^2$  nodig om deze fenomenen waar te nemen.

Om dergelijke hoge intensiteiten te verkrijgen met een aanvaardbaar vermogenbudget zijn optische componenten vereist met extreem kleine dimensies die bovendien gemaakt zijn in een materiaalsysteem met een hoog brekingsindexcontrast in beide transversale richtingen. Op die manier wordt het licht opgesloten in een heel kleine ruimte en is de interactie tussen het licht en het materiaalsysteem veel sterker. Een voorbeeld van een dergelijk halfgeleidersysteem is o.a. Silicium-op-Isolator (SOI): nanofotonische SOI golfgeleiders met doorsneden tot 0.1  $\mu\text{m}^2$  kunnen worden gefabriceerd. In deze ultrakleine golfgeleiders - ook fotonische draden genoemd - kan het Kerr effect gebruikt worden voor optische faseverschuivingen, terwijl twee-fotonabsorptie aanleiding geeft tot saturatie en golflengteconversie. Hiervoor zijn vermogens van de orde 1-10 W nodig voor golfgeleiders met een lengte van enkele mm. Datastromen hoger dan 1 Tb/s zijn bovendien mogelijk.

Om die vermogenvereisten (of componentlengtes) nog verder te beperken kunnen we het licht ook nog in de longitudinale richting opsluiting. Dit gebeurt in optische resonatoren waarin het licht wordt opgesloten in een soort caviteit en het maar geleidelijk kan ontsnappen. Hoe beter het licht in zo een structuur wordt opgesloten, hoe lager de bruikbare bandbreedte wordt. Naast een beter vermogengebruik geven optische resonatoren ook aanleiding tot nieuwe functionaliteiten, zoals optische bistabiliteit en geheugenwerking, die niet mogelijk zijn met fotonische draden. Om de wisselwerking tussen vermogen en bandbreedte te onderzoeken en de resonatorstructuur te kunnen optimaliseren voor elke toepassing hebben we een theoretisch model opgesteld dat de invloed van elke designparameter weergeeft. Op die manier hebben we berekend dat voor 40 Gb/s en 100 Gb/s werking typisch pulsenergieën van de orde 5-20 pJ en 25-100 pJ nodig zijn voor resonatorcomponenten met een lengte van slechts 100  $\mu\text{m}$ .

Deze theoretische resultaten hebben we geverifieerd met behulp van experimentele metingen van zowel fotonische draden (in samenwerking met het Nationaal Instituut van Informatie- en Communicatietechnologie, Japan) als ringresonatoren<sup>1</sup> gemaakt uit SOI. Tijdens deze experimenten hebben we een belangrijke bijdrage van secundaire effecten in onze structuren vastgesteld: twee-fotonabsorptie geeft aanleiding tot de creatie van vrije ladingsdragers die op hun beurt een invloed hebben op de brekingsindex en de materiaalabsorptie. Bovendien geven deze ladingsdragers na recombinatie aanleiding tot warmte en opnieuw een verandering van de brekingsindex. Om deze effecten te vermijden moet men de datastroom beperken. Op die manier hebben we in fotonische draden optische limitering en golflengteconversie gebaseerd op twee-fotonabsorptie aangetoond tot pulsfrequenties van 40 GHz met een ingangsvermogen beneden 10 W.

Sterke secundaire effecten kunnen natuurlijk ook zelf gebruikt worden voor optische signaalverwerking, maar met een datasnelheid die beperkt is door hun relaxatietijd: voor thermische effecten is dit ongeveer 100 ns, terwijl de recombinatietijd van vrije ladingsdragers van de orde 1 – 10 ns is. In SOI ringresonatoren hebben we op die manier thermische bistabiliteit aangetoond met ingangsvermogen van slechts 0.3 mW. Bovendien werd zowel geïnverteerde als niet-geïnverteerde golflengteconversie gebaseerd op vrijeladingsdragerdispersie gedemonstreerd met een pulslengte 10 ns en een piekvermogen van 0.7 mW, zodat 0.1 Gb/s werking mogelijk is. Bij hogere vermogens stelden we

---

<sup>1</sup>In deze optische resonatoren heeft de caviteit de vorm van een ring.

onstabiel gedrag vast door een interactie tussen thermische en vrijeladingsdragerdispersie. Dit is een gevolg van het feit dat deze effecten een verschillende tijdsconstante en een tegengesteld teken hebben. Alle experimentele resultaten hebben we nagerekend met behulp van simulaties en een goede overeenkomst tussen theorie en experiment werd bekomen.

Hoewel we met dit werk het potentieel van optische signaalverwerking gebaseerd op ultrasnelle niet-lineaire effecten duidelijk hebben aangetoond, kunnen deze resultaten op verschillende manieren verder worden verbeterd:

- Terwijl wij voor dit werk ringresonatoren hebben gebruikt, verwachten we voor resonatoren gebaseerd op fotonisch kristallen nog lagere vermogenniveaus door hun grote mogelijkheden voor optimalizatie. Fabricatie van dergelijke structuren met lage verliezen is echter heel moeilijk.
- De impact van secundaire effecten kan worden beperkt met behulp van oppervlaktepassivatie en ladingsdragerextractie door het aanbrengen van een p-i-n junctie. Op die manier kan de levensduur van de ladingsdragers worden verkleind en warmteontwikkeling worden vermeden. Bovendien zou dit optische bistabiliteit gebaseerd op vrijeladingsdragerdispersie mogelijk maken.
- Zoals hierboven vermeld is Silicium niet het optimale materiaal voor optische signaalverwerking. Naast gebruik te maken van andere halfgeleidermaterialen (vb. AlGaAs) kan men ook meer geavanceerde materiaalsystemen zoals kwantumputten, nanokristallen, ... aanbrengen op een reeds bestaande technologie om zo de voordelen van beide te combineren. Op die manier kan een volledig optisch platform voor ultrasnelle signaalverwerking mogelijk worden.

# English summary

Today, optical fiber forms the basis for long-haul telecommunication. It is able to carry multiple independent wavelengths or data signals at the same time, allowing the transport of huge amounts of information. However, to explore the full capacity of the optical fiber, the switching and processing functionality inside the optical layer is too limited. Typically, the optical signals that are passing through a network node are first converted to the electrical domain before they are processed and then they are reconverted back to the optical domain for further transportation. For high bitrates, this is both a costly and difficult process.

Although low-cost integration while maintaining the conversion from the optical layer to the electrical and back is a first step, all-optical signal processing is expected to form the real breakthrough towards ultra-high bandwidth telecommunication. To achieve this in an integrated way, two heavily investigated routes exist today:

- using carrier effects. Although they are intrinsically limited by their recombination time to bitrates of about 10 Gb/s, the use of interferometric structures allows to achieve much higher bitrates.
- using ultrafast nonlinear effects induced by the light itself: strong optical signals can induce nonlinear behaviour with practically instantaneous response times, which would allow ultrafast all-optical signal processing. However, these effects are typically very small and require very high optical powers.

In this work, we investigate the second approach, as it intrinsically has the largest potential, with the emphasis on the following two nonlinear phenomena: the Kerr effect and two-photon absorption. To reduce the harsh power requirements, high-quality nanophotonic devices will be used, which enhance the interaction between the light and the material significantly.

The bound-electronic or optical Kerr effect and the two-photon absorption effect respectively correspond to the linear dependence of the refractive index and the absorption coefficients on the intensity of the light. These effects are ultrafast because they do not require real electronic transitions; simply the possibility of an electronic transition is enough. Their response and recovery time is of the order of fs. Which one of the two nonlinear effects in a specific material dominates, is largely determined by the relative position of the light frequency compared to the material bandgap. As a result, AlGaAs is one of the most appropriate materials for Kerr-nonlinear operation at the telecom wavelength 1.55  $\mu\text{m}$ . At this wavelength, GaAs and InP on the other hand are excellent candidates for two-photon absorption. In Silicon, both the Kerr effect and two-photon absorption are important at 1.55  $\mu\text{m}$ , making it an excellent material for research applications. As mentioned above, these ultrafast nonlinear phenomena are very small. In semiconductor materials, optical intensities of the order of 1 – 10  $\text{GW}/\text{cm}^2$  are therefore needed to obtain a significant response.

To obtain these high intensities with a reasonable power budget, optical components are required which have extremely small dimensions and are fabricated in a material system with a high refractive index contrast in all transverse directions. In this way, the light is confined in a very narrow space and the nonlinear interaction with the material is much stronger. An example of such a semiconductor platform on which this is possible is e.g. Silicon-on-Insulator (SOI): low-loss nanophotonic SOI waveguides can be fabricated with cross sections down to 0.1  $\mu\text{m}^2$ . In these ultrasmall waveguides which are called photonic wires, the optical Kerr effect gives rise to all-optical phaseshifting, while two-photon absorption allows all-optical limiting and wavelength conversion. Theoretically, power requirements are of the order of 1-10 W for waveguide lengths in the mm range and bit rates exceeding 1 Tb/s are possible.

To reduce the power needs (or device length) even further, the light can additionally be confined in the longitudinal direction. This is the case in optical resonators, in which the light is locked up in a sort of cavity and is only gradually able to leak out. In these structures, a better confinement gives rise to a slower cavity response (limited bandwidth). In addition to improved power conditions, optical resonators allow new functionalities such as optical bistability and memory operation, which cannot be achieved with photonic wires. To evaluate the trade-off between pulse power and signal bandwidth and to determine

the optimum design for each application, we constructed a theoretical model which incorporates the effect of all resonator parameters. For 40 Gb/s and 100 Gb/s operation, typical pulse energies of the order of respectively 5-20 pJ and 25-100 pJ were obtained with devices lengths below 100  $\mu\text{m}$ .

To confirm our theoretical results, nonlinear experiments were performed both on photonic wires (in cooperation with the National Institute of Information and Communications Technology, Japan) and ring resonators - in which the cavity has the form of a ring - fabricated in SOI. During these experiments, significant secondary effects were observed in our structures: the presence of two-photon absorption gives rise to the creation of free carriers, which can effect the refractive index and absorption coefficient. In addition, the recombination of these carriers leads to heating and another change of the refractive index. To avoid the impact of these phenomena, one can reduce the pulse repetition rate, however at the cost of a decrease in optical data rate. Using this approach, we demonstrated all-optical limiting and wavelength conversion based on two-photon absorption in photonic wires for pulse trains up to 40 GHz and powers below 10 W.

These secondary effects are much stronger and can also be used for all-optical signal processing, however within the limitation of their relaxation time and possible unstable behaviour: the thermal recovery time is approximately 100 ns, while the free carrier lifetime is of the order of 1 – 10 ns. Using SOI ring resonators, we demonstrated thermal bistability with input powers of only 0.3 mW. In addition, both inverted and non-inverted all-optical wavelength conversion based on free-carrier dispersion were observed for a pulse length of 10 ns and a power of 0.7 mW, indicating that 0.1 Gb/s operation is feasible. At higher powers, unstable behaviour due to interaction between thermal and free-carrier dispersion effects was obtained. This is possible because both effects have different time constants and opposite signs. All these experimental results were verified by simulations and an excellent agreement between theory and experiment was obtained.

Although proving the potential of all-optical signal processing based on ultrafast nonlinear effects, the results that we obtained during this work can still be further improved:

- While our best experimental results were obtained with ring resonators, photonic crystal structures form the most versatile and tunable system for constructing optical resonators. Fabricating low-loss photonic crystals is however very difficult.

- To reduce the impact of secondary effects, surface engineering and carrier extraction by integrating a p-i-n junction may prove to be a viable way to reduce detrimental carrier accumulation and avoid heating effects. Moreover, as free carrier effects can also be used for signal processing purposes, increasing the reverse voltage of the junction would allow bitrates above 10 Gb/s and free-carrier all-optical bistability should become possible as thermal dispersion effects are avoided.
- As mentioned above, Silicon is not the best material to be used for all-optical signal processing. In addition to evaluating other semiconductor platforms (e.g. AlGaAs), new material systems such as quantum dots, nanocrystals... can be integrated onto the existing Silicon technology, combining the potential of both worlds. In this way, we expect an ultrafast all-optical nonlinear platform to be implementable.

**English Text**



# Chapter 1

## Introduction

### 1.1 Photonics

Although some of its principles were already applied in ancient times (when the caveman threw his spear in front of the fish to catch it<sup>1</sup>), the field of photonics - being the science and technology of generating and controlling light for the purpose of information transport, data processing, energy generation, sensing, ... - only really began with the invention of the laser in 1960 and the optical fiber in 1970. This new method of transporting data showed many potential advantages [1] over existing electrical connections, the most important one probably being its ability to carry multiple wavelengths (data signals) at the same time - known as wavelength division multiplexing (WDM). Exactly this huge bandwidth capacity of the optical fiber allowed the evolution of telecommunication to where it is now: worldwide, fiber forms the backplane of the modern telecom infrastructure based on the SONET/SDH (synchronous optical network/synchronous digital hierarchy) standards.

Apart from the cost issues at the receiver end, which in many cases prohibit the implementation of fiber to the end-user, one of the main reasons that the capacity of the optical backbone is not yet fully exploited at this moment, is the fact that the switching and processing functionality inside the optical layer is limited. Typically, the optical data passing through a network node must first be converted to the electrical domain, after which they are processed and reconverted to the optical domain for further transportation. As bitrates increase,

---

<sup>1</sup>And so taking into account the refraction of light.

electronic signal processing however becomes very expensive (costly transceiver technologies and packaging) or extremely difficult (physical limitations of electronics).

Therefore, it is not surprising that a lot of research is done towards low-cost integration of photonic components (photonic integrated circuits or PICs) [2, 3, 4, 5] and all-optical signal processing, both at the hardware [6, 7] and at the network level [8]. As optical communication is gradually finding its way to local area networks and short-distance applications, the field is only gaining more interest [9, 10, 11].

## 1.2 Ultrafast, nonlinear, all-optical signal processing

One of the most promising routes to improve the optical functionality in the near future is probably low-cost integration of the individual photonic and electronic components necessary for optical signal processing. An excellent example of this strategy is the work of the companies Infinera Inc. [12] and Luxtera Inc. [11], which base their optical technology respectively on InP and Silicon while maintaining the signal processing in the electrical domain.

Another interesting approach is to switch and process the different data signals all-optically and in doing so, avoid costly and inelegant optical-electrical (O-E) conversions. Although this is possible in several ways, integration will also here be a key issue. Today, two heavily investigated routes exist:

- using carrier effects. In this context, we think of the nonlinear gain and phase effects in semiconductor optical amplifiers [13, 6, 7] and more recently the plasma effect in Silicon [14, 15, 10]. Unfortunately, carrier effects are limited in response time, making it intrinsically difficult to obtain data rates above 10 Gb/s. The use of special interferometric structures however makes it possible to go to much higher bitrates.
- using ultrafast nonlinear effects induced by the light itself. In the presence of strong optical signals, many materials exhibit nonlinear behaviour with practically instantaneous response times. Theoretically, this would allow ultrafast all-optical signal processing. These effects are however typically very small and therefore require very high optical powers. The recent breakthrough in fabricating ultrasmall, nanophotonic devices however has made it possible to reduce these requirements significantly.

Clearly, each solution has its pros and cons and it is hard to tell which one will prove to be the most interesting and cost effective in a few decades from now. At this point, ultrafast nonlinear optics - at least intrinsically - seems to have the largest potential and will be investigated in this work.

### 1.3 Focus of this work

As mentioned above, one of the largest bottlenecks for ultrafast nonlinear effects is the fact that they require very high optical powers. With the recent realization of high-quality nanophotonic structures [3], this barrier is significantly lowered due to an increased interaction between the light and the material. However, power is not the only problem and also new issues arise as a result of the use of these tiny structures. In this work, we will try to answer the question how far one can go.

As the field of nonlinear optics is so vast, we will concentrate on two specific nonlinear phenomena: the Kerr effect and two-photon absorption. A detailed investigation of these two effects can be found in chapter 2. In chapters 3 and 4, we thoroughly examine the potential of nanophotonic structures for ultrafast signal processing from a theoretical point of view. To do this, we develop a theoretical model which takes into account the different ultrafast nonlinear effects. This model is then used to investigate different applications. Special attention is paid to one of the most interesting material systems at the moment: Silicon-on-Insulator (SOI). The obtained results are then verified experimentally in chapter 5. The SOI structures used for the experiments have been fabricated at the Interuniversity Micro-Electronics Center (IMEC, Leuven). The nonlinear measurements have been performed in partial cooperation with the National Institute of Information and Communications Technology (NICT, Japan). Finally, conclusions are drawn and future work is discussed in chapter 6.

### 1.4 Publications

The results obtained within this work have been published in various papers and presented at various conferences. This paragraph gives an overview of the publications. They can also be found in the [publications](http://photonics.intec.ugent.be) section of the photonics research group website : <http://photonics.intec.ugent.be>. These publications may be down-

loaded for personal use only. For any other use, the permission of the copyright owner (usually the publisher of the journal) must be obtained.

The following papers have been published in international peer reviewed journals or are accepted for publication:

1. G. Priem, P. Bienstman, G. Morthier, R. Baets, "Impact of absorption mechanisms on Kerr-nonlinear resonator behaviour," *J. Appl. Phys.*, vol. 99, 063103, March 2006.
2. G. Priem, P. Dumon, W. Bogaerts, D. Van Thourhout, G. Morthier, R. Baets, "Optical bistability and pulsating behaviour in Silicon-on-Insulator ring resonator structures," *Opt. Express*, vol. 13, pp. 9623-9628, November 2005.
3. G. Priem, I. Notebaert, P. Bienstman, G. Morthier, R. Baets, "Resonator-based all-optical Kerr-nonlinear phase shifting: Design and limitations," *J. Appl. Phys.*, vol. 97, 023104, January 2005.
4. G. Priem, I. Notebaert, B. Maes, P. Bienstman, G. Morthier, R. Baets, "Design of all-optical non-linear functionalities based on resonators," *IEEE J. Select. Topics Quantum Electron.*, vol. 10, pp. 1070-1078, September-October 2004.
5. P. Dumon, G. Priem, L. Nunes, W. Bogaerts, D. Taillaert, D. Van Thourhout, P. Bienstman, T. Liang, M. Tsuchiya, P. Jaenen, S. Beckx, J. Wouters, R. Baets, "Ultra-compact linear and nonlinear nanophotonic wire based devices and circuits in Silicon-on-Insulator," *Jap. J. Appl. Phys.*, accepted for publication.
6. T. Liang, L. Nunes, T. Sakamoto, K. Sasagawa, T. Kawanishi, M. Tsuchiya, G. Priem, D. Van Thourhout, P. Dumon, R. Baets, H. Tsang, "Ultrafast all-optical switching by cross-absorption modulation in Silicon wire waveguides," *Opt. Express*, vol. 13, pp. 7298-7303, August 2005.

The following papers have been presented at international conferences and are published in the conference proceedings:

7. G. Priem, P. Dumon, W. Bogaerts, D. Van Thourhout, G. Morthier, R. Baets, "Nonlinear effects in ultrasmall Silicon-on-Insulator ring resonators," in *Proceedings of 2006 Photonics Europe Conference*, 6183-47, Strasbourg, France, April 3-7, 2006.

8. G. Priem, P. Vandersteegen, P. Bienstman, G. Morthier, R. Baets, "Ultrafast, all-optical regeneration functionalities inside a Kerr-nonlinear platform," in *Proceedings of 2005 IEEE/LEOS Annual Meeting*, WF4, Sydney, Australia, October 23-27, 2005.
9. G. Priem, I. Moreels, P. Dumon, Z. Hens, W. Bogaerts, D. Van Thourhout, G. Morthier, R. Baets, "InP-nanocrystal monolayer deposition onto Silicon-on-Insulator structures," in *Proceedings of 2005 IEEE/LEOS Annual Meeting*, TuB1, Sydney, Australia, October 23-27, 2005.
10. G. Priem, P. Dumon, W. Bogaerts, D. Van Thourhout, G. Morthier, R. Baets, "Optical bistability analysis inside a two-bus ring resonator," in *Proceedings of 2005 IEEE/LEOS Annual Meeting*, MN4, Sydney, Australia, October 23-27, 2005.
11. G. Priem, P. Dumon, P. Bienstman, G. Morthier, R. Baets, "Effect of loss mechanisms on Kerr-nonlinear resonator behaviour," in *Proceedings of 2005 Integrated Photonics Research and Applications Conference (IPRA)*, ITu-C4, San Diego, United States, April 11-13, 2005.
12. G. Priem, P. Bienstman, G. Morthier, R. Baets, "Resonator-based all-optical phase shifting in pump-probe configuration," in *Proceedings of 2004 IEEE/LEOS Benelux Annual Symposium*, pp. 259-262, Ghent, Belgium, December 2-3, 2004.
13. G. Priem, P. Bienstman, G. Morthier, R. Baets, "Effect of two-photon absorption on Kerr-nonlinear resonator behaviour," in *Proceedings of 2004 IEEE/LEOS Benelux Annual Symposium*, pp. 231-234, Ghent, Belgium, December 2-3, 2004.
14. G. Priem, G. Morthier, R. Baets, "Bandwidth limitations and optimal design of all-optical nonlinear functionalities by means of resonators," in *Technical Digest: International Symposium on Photonic and Electromagnetic Crystal Structures (PECS-V)*, Th-P35, Kyoto, Japan, March 7-11, 2004.
15. G. Priem, G. Morthier, R. Baets, "Optical phase shifting with 1D Kerr-nonlinear resonators," in *Proceedings of 2003 IEEE/LEOS Benelux Annual Symposium*, pp. 241-244, Twente, Netherlands, December 9, 2003.

16. G. Priem, G. Morthier, R. Baets, "Potential of 1D Kerr-nonlinear resonators for all-optical phase shifting," in *Proceedings of International School of Quantum Electronics, 39th course: Microresonators as building blocks for VLSI photonics*, pp. 433-434, Erice, Italy, October 18-25, 2003.
17. F. Morichetti, A. Melloni, P. Bienstman, G. Priem, J. Petráček, "Self-phase modulation in slow-wave structures: a comparative numerical analysis," in *Proceedings of 2006 Optical Waveguide Theory and Numerical Modelling (OWTNM) Workshop*, accepted for publication.
18. D. Van Thourhout, P. Dumon, W. Bogaerts, G. Roelkens, G. Priem, R. Baets, "Recent progress in SOI nanophotonic waveguides (invited)," in *Proceedings of 2005 European Conference on Optical Communication (ECOC)*, Tu3.6.2, Glasgow, United Kingdom, September 25-29, 2005.
19. R. Baets, P. Dumon, W. Bogaerts, G. Roelkens, D. Taillaert, B. Luyssaert, G. Priem, G. Morthier, P. Bienstman, D. Van Thourhout, "Silicon-on-Insulator based Nano-photonics: Why, How, What for? (invited)", in *Proceedings of 2nd International Group IV Photonics Conference*, pp. 168-170, Antwerp, Belgium, September 21-23, 2005.

The following paper has been presented at a local symposium:

20. G. Priem, P. Bienstman, D. Van Thourhout, "Nonlinear behaviour in nanophotonic structures for ultrafast signal processing", in *6th UGent-FirW PhD symposium*, Gent, Belgium, pp. 39, November 30, 2005.

## Chapter 2

# Nonlinear effects in standard semiconductor systems

In this chapter, we will discuss the origin of two nonlinear phenomena with ultrafast response times - i.e. the bound-electronic Kerr effect and the two-photon absorption effect - and evaluate their potential in different semiconductor material systems. Furthermore, we pay attention to secondary effects that may occur as a result of these ultrafast effects and that may interfere with their operation. Finally, a few words are spent on material anisotropy and the possibility of material engineering for increasing the nonlinear interaction.

### 2.1 Mathematical formulation

Mathematically, the nonlinear refractive index effect, known as the Kerr effect, can be represented by a refractive index which linearly depends on the intensity of the light at a certain position:

$$n = n_0 + n_{2,I}I \quad (2.1)$$

with  $n$  the total refractive index,  $n_0$  the linear refractive index,  $n_{2,I}$  the Kerr coefficient and  $I$  the optical intensity. Equivalently, one can write

$$n = n_0 + n_2 |E|^2 \quad (2.2)$$

since the light intensity is related to the electric field by

$$I = \frac{1}{2} \epsilon_0 c n_0 |E|^2 \quad (2.3)$$

with  $\epsilon_0 = 8.854 \times 10^{-12}$  F/m the free-space permittivity and  $c = 2.998 \times 10^8$  m/s the speed of light. So one has

$$n_{2,I} = \frac{2}{\epsilon_0 c n_0} n_2 \quad (2.4)$$

$$n_2 = \frac{\epsilon_0 c n_0}{2} n_{2,I} \quad (2.5)$$

Many other representations exist [16], however these two are the most common ones.

In a similar way, the linear dependence of the absorption coefficient on the intensity, which is called the two-photon absorption effect (2PA), can be expressed as

$$\alpha_{tot} = \alpha_0 + \alpha_{2,I} I \quad (2.6)$$

or, using equation (2.3),

$$\alpha_{tot} = \alpha_0 + \alpha_2 |E|^2 \quad (2.7)$$

with  $\alpha_{tot}$  the total absorption coefficient,  $\alpha_0$  the linear or single-photon absorption coefficient and  $\alpha_{2(I)}$  the two-photon absorption coefficient. Often the notation  $\beta$  is used instead of  $\alpha_2$  to represent this nonlinear absorption effect, in which case the notation  $\alpha$  is used to indicate the linear part.

The occurrence of these two nonlinear effects can be understood as a third-order field dependence of the total macroscopic polarization of a material in the frequency space [16]. In general, the total polarization can be expanded as a function of the electric field in the time domain as

$$\mathbf{P}(t) = \mathbf{P}^{(0)}(t) + \mathbf{P}^{(1)}(t) + \mathbf{P}^{(2)}(t) + \dots \quad (2.8)$$

with  $\mathbf{P}^{(0)}(t)$  independent of the electric field,  $\mathbf{P}^{(1)}(t)$  linear in the electric field, and so on. Equivalently, one has in the frequency domain<sup>1</sup>,

$$\mathbf{P}(\omega) = \mathbf{P}^{(0)}(\omega) + \mathbf{P}^{(1)}(\omega) + \mathbf{P}^{(2)}(\omega) + \dots \quad (2.9)$$

with

$$\mathbf{P}^{(n)}(t) = \frac{1}{2\pi} \int_{-\infty}^{\infty} d\omega \mathbf{P}^{(n)}(\omega) \exp(j\omega t) \quad (2.10)$$

$$\mathbf{P}^{(n)}(\omega) = \int_{-\infty}^{\infty} dt \mathbf{P}^{(n)}(t) \exp(-j\omega t) \quad (2.11)$$

<sup>1</sup>In this work, the phase convention  $\exp(j\omega t)$  will be used.

Under the conditions of time invariance, causality and the absence of spatial dispersion, the most general form for the  $n$ th order polarization is given by [16, 17]

$$\mathbf{P}^{(n)}(\omega) = \epsilon_0 \left( \frac{1}{2\pi} \right)^n \int_{-\infty}^{\infty} d\omega_1 \dots \int_{-\infty}^{\infty} d\omega_n \chi^{(n)}(-\omega_\sigma; \omega_1, \dots, \omega_n) | \mathbf{E}(\omega_1) \dots \mathbf{E}(\omega_n) \delta(\omega - \omega_\sigma) \quad (2.12)$$

with  $\epsilon_0$  the free-space permittivity and  $\mathbf{E}(\omega)$  the electric field component with frequency  $\omega$ .  $\chi^{(n)}$  is called the  $n$ th order susceptibility tensor and determines the process that is represented. The frequency  $\omega_\sigma$  is defined by  $\omega_\sigma = \sum_{i=1}^n \omega_i$  and its minus sign in the susceptibility tensor notation is only conventional.

Consider now only the first and third order term

$$\mathbf{P}(\omega) \approx \mathbf{P}^{(1)}(\omega) + \mathbf{P}^{(3)}(\omega) \quad (2.13)$$

and suppose that only a field with one frequency component - i.e. a monochromatic wave - is present, so that

$$\mathbf{E}(t) = \text{Re} [\mathbf{E}_{\omega'} \exp(j\omega't)] = \frac{\mathbf{E}_{\omega'}}{2} \exp(j\omega't) + \frac{\mathbf{E}_{\omega'}^*}{2} \exp(-j\omega't) \quad (2.14)$$

$$\mathbf{E}(\omega) = \pi \mathbf{E}_{\omega'} \delta(\omega - \omega') + \pi \mathbf{E}_{\omega'}^* \delta(\omega + \omega') \quad (2.15)$$

Possible polarization frequencies  $\omega_\sigma$  are  $\omega'$  and  $-\omega'$  for  $\mathbf{P}_{\omega'}^{(1)}$  and  $3\omega', \omega', -\omega'$  and  $-3\omega'$  for  $\mathbf{P}_{\omega'}^{(3)}$ . The polarization with the original frequency  $\omega'$  (and  $-\omega'$ ) is defined by

$$\mathbf{P}(t) = \text{Re} [\mathbf{P}_{\omega'} \exp(j\omega't)] = \frac{\mathbf{P}_{\omega'}}{2} \exp(j\omega't) + \frac{\mathbf{P}_{\omega'}^*}{2} \exp(-j\omega't) \quad (2.16)$$

$$\mathbf{P}(\omega) = \pi \mathbf{P}_{\omega'} \delta(\omega - \omega') + \pi \mathbf{P}_{\omega'}^* \delta(\omega + \omega') \quad (2.17)$$

then consists of following parts:

$$\begin{aligned} \mathbf{P}_{\omega'} &= \epsilon_0 \chi^{(1)}(-\omega'; \omega') \cdot \mathbf{E}_{\omega'} + \epsilon_0 \chi^{(3)}(-\omega'; \omega', -\omega', \omega') : \frac{\mathbf{E}_{\omega'}}{2} \frac{\mathbf{E}_{\omega'}^*}{2} \mathbf{E}_{\omega'} \\ &\quad + \epsilon_0 \chi^{(3)}(-\omega'; -\omega', \omega', \omega') : \frac{\mathbf{E}_{\omega'}^*}{2} \frac{\mathbf{E}_{\omega'}}{2} \mathbf{E}_{\omega'} \\ &\quad + \epsilon_0 \chi^{(3)}(-\omega'; \omega', \omega', -\omega') : \frac{\mathbf{E}_{\omega'}}{2} \frac{\mathbf{E}_{\omega'}}{2} \mathbf{E}_{\omega'}^* \end{aligned} \quad (2.18)$$

Due to permutation symmetry [16], this simplifies to

$$\mathbf{P}_{\omega'} = \epsilon_0 \chi^{(1)}(-\omega'; \omega') \cdot \mathbf{E}_{\omega'} + \frac{3}{4} \epsilon_0 \chi^{(3)}(-\omega'; \omega', -\omega', \omega') : \mathbf{E}_{\omega'} \mathbf{E}_{\omega'}^* \mathbf{E}_{\omega'} \quad (2.19)$$

or in the case of a scalar susceptibility tensor

$$\mathbf{P}_{\omega'} = \epsilon_0 \left( \chi^{(1)}(-\omega'; \omega') + \frac{3}{4} \chi^{(3)}(-\omega'; \omega', -\omega', \omega') |E_{\omega'}|^2 \right) \mathbf{E}_{\omega'} \quad (2.20)$$

The complex refractive index  $n_c = n - jK$  with  $n$  the refractive index and  $K$  the extinction coefficient, is defined by

$$\mathbf{P}_{\omega} = \epsilon_0 (n_c^2(\omega) - 1) \mathbf{E}_{\omega} \quad (2.21)$$

and for semiconductors, one typically has  $n \gg K$ , so that  $(n - jK)^2 \approx n(n - j2K)$  and the refractive index is given by

$$n \approx \sqrt{1 + \text{Re}\chi^{(1)}(-\omega; \omega) + \frac{3}{4} \text{Re}\chi^{(3)}(-\omega; \omega, -\omega, \omega) |E_{\omega}|^2} \quad (2.22)$$

$$\approx \sqrt{1 + \text{Re}\chi^{(1)}(-\omega; \omega) + \frac{3\text{Re}\chi^{(3)}(-\omega; \omega, -\omega, \omega)}{8\sqrt{1 + \text{Re}\chi^{(1)}(-\omega; \omega)}} |E_{\omega}|^2} \quad (2.23)$$

$$\equiv n_0 + n_2 |E_{\omega}|^2 \quad (2.24)$$

with

$$n_0 \equiv \sqrt{1 + \text{Re}\chi^{(1)}(-\omega; \omega)} \quad (2.25)$$

$$n_2 \equiv \frac{3\text{Re}\chi^{(3)}(-\omega; \omega, -\omega, \omega)}{8n_0} \quad (2.26)$$

for small nonlinear effects ( $n_0 \gg n_2 |E_{\omega}|^2$ ). In this way, the Kerr coefficient  $n_2$  can be related to the real part of the third-order susceptibility:  $n_2 \propto \text{Re}\chi^{(3)}(-\omega; \omega, -\omega, \omega)$ .

Equivalently, one has

$$K \approx -\frac{\text{Im}\chi^{(1)}(-\omega; \omega)}{2n_0} - \frac{3\text{Im}\chi^{(3)}(-\omega; \omega, -\omega, \omega)}{8n_0} |E_{\omega}|^2 \quad (2.27)$$

$$\equiv K_0 + K_2 |E_{\omega}|^2 \quad (2.28)$$

with

$$K_0 \equiv -\frac{\text{Im}\chi^{(1)}(-\omega; \omega)}{2n_0} \quad (2.29)$$

$$K_2 \equiv -\frac{3\text{Im}\chi^{(3)}(-\omega; \omega, -\omega, \omega)}{8n_0} \quad (2.30)$$

The single- and two-photon absorption coefficients are associated with the extinction coefficients  $K_0$  and  $K_2$  as follows:

$$\alpha = 2\frac{\omega}{c}K_0 \quad (2.31)$$

$$\beta = 2\frac{\omega}{c}K_2 \quad (2.32)$$

relating the two-photon absorption coefficient directly to the imaginary part of the third-order susceptibility:  $K_2 \propto \text{Im}\chi^{(3)}(-\omega; \omega, -\omega, \omega)$ .

From this, we can conclude that the presence of the Kerr effect and the two-photon absorption effect is inevitably related, as they are both part of the same nonlinear susceptibility. This relation is much like that of the linear refractive index  $n_0$  and the absorption coefficient  $\alpha_0$ , which is known as the Kramers-Kronig relation. This will be further discussed in the next section.

So far, nothing has however been said about the particular physical origin of intensity dependent refractive index and absorption effects. Describing them as a third-order nonlinear polarization still covers many grounds and does not provide any information about its magnitude and response time.

## 2.2 Bound-electronic Kerr effect

The ultrafast Kerr-nonlinear effect, that is investigated in this work, is called the bound-electronic or two-photon resonant optical Kerr effect. The origin of its ultrafast nature can be understood in the same way as that of the linear refractive index: it does not require real electronic transitions, simply the possibility of an electronic transition is enough. Therefore, its speed is estimated as that of electronic vibrations (order fs). This in contrast to e.g. the corrections to the refractive index due to the presence of a significant amount of free carriers, which is of course related to the real transition of electrons and holes in the system and therefore limited by their relaxation times. This will be further discussed in section 2.5.

Theoretical calculations of the bound-electronic Kerr effect are very difficult because of the high order perturbation theory that is required and the need for accurate wavefunctions and energies of many excited states. One of the first attempts to calculate it was done by Boyle et al. [18, 19] for the element Helium in 1966. The first estimates for  $n_2$  in semiconductor materials were obtained in 1968 by considering the

molecular bonding orbitals at each atomic position [20, 21] and by considering the zero-frequency limit of the Franz-Keldish effect [22]. Further work has among others been done by Boling, Glass and Owyong [18, 23], who deduced a semi-empirical expression valid for several low refractive index materials and glasses in 1978. All these formulae however only predicted values in the limit of low frequencies. The first limited dispersion calculations considered the region close to the bandgap [24].

A real breakthrough concerning the nonlinear dispersion was realized in the early 90s by Sheik-Bahae et al. [25, 26]. In 1984, Wherrett discovered that  $n_2$  roughly scales with  $\frac{\sqrt{E_p}}{n_0 E_g^4}$  [27] with  $E_g$  the bandgap energy and  $E_p$  the momentum parameter. Sheik-Bahae et al. plotted  $n_2 n_0 E_g^4 / \sqrt{E_p}$  ( $n_0 E_g^4 / \sqrt{E_p}$  to remove material dependence) as a function of  $\frac{\hbar\omega}{E_g}$  for various materials and saw that this curve around half the bandgap qualitatively resembles the linear index profile  $n_0$  around the bandgap [25, 26]. This verified that there exists a similar causality relation between  $\text{Re}\chi^{(3)}$  and  $\text{Im}\chi^{(3)}$  as there is between the linear refractive index (related to  $\text{Re}\chi^{(1)}$ ) and single-photon absorption (related to  $\text{Im}\chi^{(1)}$ ), as mentioned in the previous section. Linearly, this Kramers-Kronig relation is given by [17]

$$n_0(\omega) - 1 = \frac{c}{\pi} \int_0^\infty \frac{\alpha(\omega')}{\omega'^2 - \omega^2} d\omega' \quad (2.33)$$

If a perturbation  $\xi$  is now introduced into the system, then the Kramers-Kronig transformation states that the change in refractive index  $\Delta n$  at frequency  $\omega$  is associated with a change in absorption  $\Delta\alpha$  throughout the spectrum  $\omega'$ , given by,

$$\Delta n(\omega, \xi) = \frac{c}{\pi} \int_0^\infty \frac{\Delta\alpha(\omega', \xi)}{\omega'^2 - \omega^2} d\omega' \quad (2.34)$$

The cause of  $\xi$  is not necessarily of optical origin. To make the left-hand side correspond to the Kerr-nonlinear refractive index change  $\Delta n = n_2 |E|^2$ , one must set  $\xi = \omega$ . So to perform this Kramers-Kronig calculation, one must determine the non-degenerate absorption  $\Delta\alpha(\omega', \omega)$  - related to  $\text{Im}\chi^{(3)}(-\omega'; \omega', \omega, -\omega)$  - which is the absorption/emission of light with frequency  $\omega'$  due to the presence of light with frequency  $\omega$ . Mechanisms contributing to this are non-degenerate two-photon absorption effects, stimulated Raman scattering and ac Stark effects:

- Non-degenerate two-photon absorption is the absorption of two photons which have frequencies  $\omega'$  and  $\omega$ . Due to this process, an electron-hole pair is created or an electron is excited from the valence band into the conduction band (and vice versa for the corresponding hole). Therefore, this is only possible if  $\hbar\omega' + \hbar\omega \geq E_g$ .
- Stimulated Raman scattering (figure 2.1) corresponds to the absorption of a photon with frequency  $\omega$  ( $\omega'$ ) under the influence of a photon with frequency  $\omega'$  ( $\omega$ ) together with the emission of a new photon with frequency  $\omega'$  ( $\omega$ ). So one either has  $-\hbar\omega' + \hbar\omega \geq E_g$  or  $\hbar\omega' - \hbar\omega \geq E_g$ . Note that in this case, only the bound-electronic contribution is important and not the (typically) resonant contribution which has a limited response time [28].

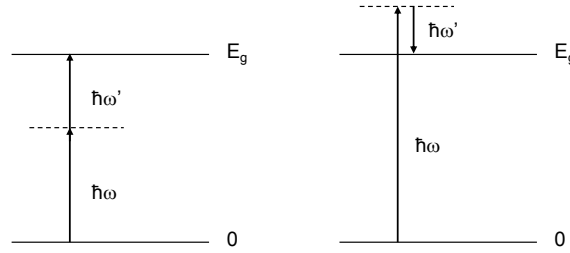


**Figure 2.1:** Representation of non-degenerate 2PA (left) and stimulated Raman scattering (right).

- In addition to these multi-photon absorption processes, the linear absorption of  $\omega'$  can also change due to a shift of the bandgap as a result of ac Stark effects. Two effects are contributing to  $\text{Im}\chi^{(3)}(-\omega'; \omega', \omega, -\omega)$ : the so-called linear Stark effect corresponding to a coupling between the conduction or valence band with itself and the quadratic Stark effect corresponding to a coupling between the conduction and valence band. Both are triggered by the presence of light with frequency  $\omega$ .

It is important to note that in fact more than the knowledge of the degenerate two-photon absorption effect ( $\omega' = \omega$ ) - which was discussed in section 2.1 - is required.

All these effects were determined theoretically in [26] using a two-parabolic band model and using relation (2.34), the total bound-electronic Kerr effect can be calculated. This is shown in figure 2.2.

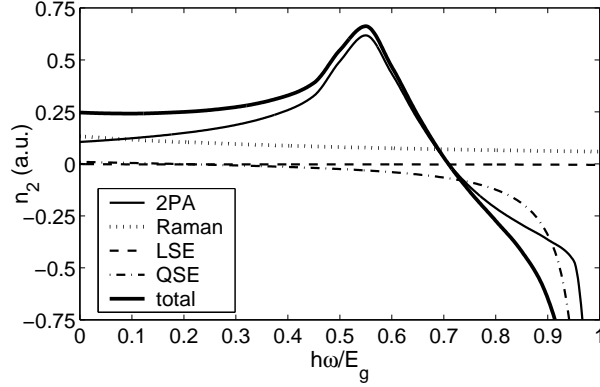


**Figure 2.2:** Different contributions to the bound-electronic Kerr effect as a function of the photon energy-bandgap fraction.

Clearly, the contribution of two-photon absorption is most significant except for the region close to the bandgap where the quadratic Stark effect dominates. An obvious enhancement of  $n_2$  can be seen for  $\hbar\omega > \frac{E_g}{2}$ . In addition, a change in the sign of  $n_2$  is expected around  $\frac{\hbar\omega}{E_g} \approx 0.7$ . Phenomena which are not yet taken into account in this model are higher band effects and excitonic enhancements. Even without these contributions, a good overall agreement with experimental results was obtained.

A theory that does include higher band effects was developed by Hutchings et al. [29]. This time, not a Kramers-Kronig approach was used, but an explicit calculation of  $\text{Re}\chi^{(3)}(-\omega'; \omega', \omega, -\omega)$  was performed using the Kane band model. Such a quantum-mechanical approach immediately allows to take into account all contributions to the Kerr effect, in contrast with the former approach in which several effects were calculated one by one and then added in the end. Using this approach, a similar dispersion shape was obtained as in [25, 26], only with a slightly higher midgap enhancement.

Despite all theoretical work, experimental results are still necessary for realistic modeling. This is in particular the case for indirect bandgap structures such as Si, for which the theoretical work of Sheik-Bahae does not apply immediately. The bound-electronic Kerr-nonlinear co-

efficient obtained in literature for different semiconductor systems<sup>2</sup> are summarized in table 2.1.

material	$\lambda(\mu\text{m})$	$\hbar\omega/E_g$	$n_0$	$n_{2,I}(\text{cm}^2/\text{W})$	$n_2(\text{cm}^2/\text{V}^2)$
SiO <sub>2</sub>	1.06	0.13	1.45	$0.32 \times 10^{-15}$	$0.06 \times 10^{-17}$
Si	1.54	0.72	3.48	$0.60 \times 10^{-13}$	$0.28 \times 10^{-15}$
Si	1.54	0.72	3.48	$0.45 \times 10^{-13}$	$0.21 \times 10^{-15}$
Si	1.5	0.74	3.48	$0.70 \times 10^{-13}$	$0.33 \times 10^{-15}$
Si	1.27	0.87	3.51	$0.26 \times 10^{-13}$	$0.12 \times 10^{-15}$
AlAs	1.55	0.37	2.89	$0.58 \times 10^{-13}$	$0.22 \times 10^{-15}$
AlGaAs	1.60	0.49	3.33	$1.30 \times 10^{-13}$	$0.58 \times 10^{-15}$
AlGaAs	1.55	0.51	3.33	$1.50 \times 10^{-13}$	$0.66 \times 10^{-15}$
AlGaAs	1.50	0.53	3.33	$1.90 \times 10^{-13}$	$0.84 \times 10^{-15}$
AlGaAs	0.85	0.93	3.46	$-4.86 \times 10^{-13}$	$-2.23 \times 10^{-15}$
GaAs	1.54	0.57	3.37	$1.59 \times 10^{-13}$	$0.71 \times 10^{-15}$
GaAs	1.27	0.69	3.42	$-0.79 \times 10^{-13}$	$-0.36 \times 10^{-15}$
GaAs	1.06	0.82	3.48	$-3.20 \times 10^{-13}$	$-1.48 \times 10^{-15}$
InP	1.55	0.60	3.17	(unknown)	(unknown)

**Table 2.1:**  $n_2$  values for several semiconductors, obtained from literature [26, 29, 30, 31, 32, 33, 34, 35, 36]

Measurements from different groups show some variation in the extracted values of  $n_2$ , which are typically of the order of  $\approx 10 - 15\%$ . It must be noted that many values from literature (especially from older papers) must be interpreted with caution, if they were measured for  $\hbar\omega/E_g > 0.5$  (see also section 2.5). The reported values are not necessarily bound-electronic.

While it is clear that the bound-electronic nonlinear Kerr effect is a very small effect, its main advantage is however its ultrafast response and relaxation time. Due to device limitations, it has not been possible yet to measure them, but both are believed to be at least in the fs-regime. This means that for all practical signal pulse lengths, the bound-electronic Kerr effect may be considered to be instantaneous.

<sup>2</sup>In this work, AlGaAs stands for Al<sub>0.18</sub>Ga<sub>0.82</sub>As. This composition is of particular interest for nonlinear research because its bandgap energy  $E_g$  is about twice the photon energy at  $\lambda = 1.55 \mu\text{m}$ .

### 2.3 Two-photon absorption

As derived in the beginning of this chapter, the intrinsic counterpart of the bound-electronic Kerr effect is (degenerate) two-photon absorption<sup>3</sup>. In this process, two photons with the same energy  $\hbar\omega$  are absorbed with the creation of a free electron and hole or an electron-hole pair as a result. Of course, this is only possible if  $\hbar\omega \geq \frac{E_g}{2}$ .

A model for two-photon absorption dispersion was also calculated by Sheik-Bahae et al. [25], using again a two-parabolic band model and the result is plotted in figure 2.3.

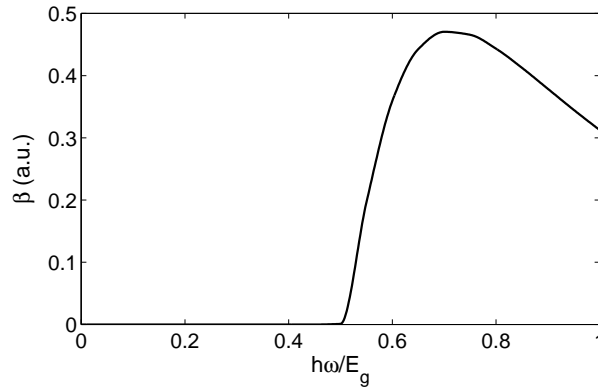


**Figure 2.3:** Two-photon absorption as a function of the photon energy-bandgap fraction.

Hutchings et al. [37] used a four-band Kane model to calculate  $\beta(\omega)$ , in accordance with their approach for determining the bound-electronic  $n_2$ . This calculation is substantially more difficult than when using a two-band model, and excellent agreement with experimental results was obtained.

The two-photon absorption coefficients obtained in literature for semiconductor systems are summarized in table 2.2.

Like the bound-electronic Kerr effect, two-photon absorption may also be considered to be ultrafast, but also very weak.

<sup>3</sup>and not the non-degenerate two-photon absorption effect, Raman scattering and ac Stark effects, since only a single frequency is to be considered. This is in contrast with the calculation of  $n_2$  using the KK transformation.

material	$\lambda(\mu\text{m})$	$\hbar\omega/E_g$	$n_0$	$\beta_I(\text{cm/W})$	$\beta(\text{cm/V}^2)$
SiO <sub>2</sub>	1.06	0.13	1.45	$\approx 0$	$\approx 0$
Si	1.54	0.72	3.48	$0.45 \times 10^{-9}$	$2.08 \times 10^{-12}$
Si	1.54	0.72	3.48	$0.79 \times 10^{-9}$	$3.65 \times 10^{-12}$
Si	1.5	0.74	3.48	$0.90 \times 10^{-9}$	$4.16 \times 10^{-12}$
Si	1.27	0.87	3.51	$0.74 \times 10^{-9}$	$3.45 \times 10^{-12}$
AlAs	1.55	0.37	2.89	(unknown)	(unknown)
AlGaAs	1.60	0.49	3.33	$0.15 \times 10^{-9}$	$0.66 \times 10^{-12}$
AlGaAs	1.55	0.51	3.33	$0.18 \times 10^{-9}$	$0.80 \times 10^{-12}$
AlGaAs	1.50	0.53	3.33	$1.00 \times 10^{-9}$	$4.42 \times 10^{-12}$
AlGaAs	0.85	0.93	3.46	(unknown)	(unknown)
GaAs	1.54	0.57	3.37	$10.20 \times 10^{-9}$	$45.62 \times 10^{-12}$
GaAs	1.27	0.69	3.42	$15.10 \times 10^{-9}$	$68.54 \times 10^{-12}$
GaAs	1.06	0.82	3.48	$18.00 \times 10^{-9}$	$83.14 \times 10^{-12}$
InP	1.55	0.60	3.17	$24 - 33 \times 10^{-9}$	$101 - 139 \times 10^{-12}$

**Table 2.2:**  $\beta$  values, obtained from literature [29, 32, 33, 35, 36, 38, 39], for the same material systems

## 2.4 Figure of merit

Since the bound-electronic Kerr effect and degenerate two-photon absorption are part of the same third-order susceptibility and therefore unavoidably related, they will simultaneously influence the behaviour of possible nonlinear components. From figures 2.2 and 2.3, it can be seen that both the magnitude of  $n_2$  and the proportion between  $n_2$  and  $\beta$  change for different  $\hbar\omega/E_g$ . Therefore, an optimum can be expected, for which  $n_2$  is relatively high and  $\beta$  is tolerable. To determine the amount of two-photon absorption which can be tolerated, one has to solve the wave equation. For the monochromatic wave in the case of an isotropic material, this equation is given by [40]

$$\nabla^2 \mathbf{E}_\omega + \frac{\omega^2}{c^2} \mathbf{E}_\omega = -\mu_0 \omega^2 \mathbf{P}_\omega \quad (2.35)$$

Considering again only the first and third order polarization, this becomes

$$\nabla^2 \mathbf{E}_\omega + \frac{\omega^2}{c^2} \left( 1 + \chi^{(1)}(-\omega, \omega) + \frac{3}{4} \chi^{(3)}(-\omega, \omega, -\omega, \omega) |E_\omega|^2 \right) \mathbf{E}_\omega = 0 \quad (2.36)$$

A possible method to solve this nonlinear equation is using a multi-scale approach [41]. In one dimension with  $z$  the axis of propagation, in the absence of linear loss and considering only a wave propagating in the forward direction, this results (in first order) in [42]:

$$E_\omega = \frac{E_{0,\omega}}{\sqrt{1 + \beta |E_{0,\omega}|^2 z}} \exp\left(-j\frac{\omega}{c}n_0z - j\frac{\omega n_2}{c\beta} \ln(1 + \beta |E_{0,\omega}|^2 z)\right) \quad (2.37)$$

with  $E_{0,\omega}$  the electric field at  $z = 0$ . Higher order corrections can be obtained by further calculation, however such calculations are increasingly difficult and do not give significant changes.

The influence of two-photon absorption not only results in a decreasing amplitude of the field along the direction of propagation, but also in a smaller phase change: the induced change is now only,

$$\Delta\phi(z) = -\frac{\omega n_2}{c\beta} \ln(1 + \beta |E_{0,\omega}|^2 z) \quad (2.38)$$

instead of

$$\Delta\phi(z) = -\frac{\omega n_2}{c} |E_{0,\omega}|^2 z \quad (2.39)$$

in the absence of two-photon absorption.

In figure 2.4, the relation between total intensity transmission  $T = \frac{1}{1 + \beta |E_{0,\omega}|^2 z}$  and the obtained phase shift  $|\Delta\phi|$  is plotted for different values of  $\frac{n_2}{\beta\lambda}$ .

Starting from equation (2.37), a figure of merit for Kerr-nonlinear materials is defined [43, 44, 45] by stating that a certain phase shift  $\Delta\phi$  should be obtainable with a remaining transmission of at least  $1/e$ . From equation (2.37), it can be derived that this is possible if

$$|\Delta\phi| < \frac{\omega n_2}{c\beta} \quad (2.40)$$

In case a phase shift of  $\pi$  is required (e.g. for Kerr-nonlinear phase shifting [45]), the figure of merit condition becomes

$$FOM \equiv \left| \frac{n_2}{\lambda\beta} \right| > \frac{1}{2} \quad (2.41)$$

while a phase shift of  $4\pi$  (e.g. for a Kerr-nonlinear directional coupler [44]) would require that,

$$FOM \equiv \left| \frac{n_2}{\lambda\beta} \right| > 2 \quad (2.42)$$

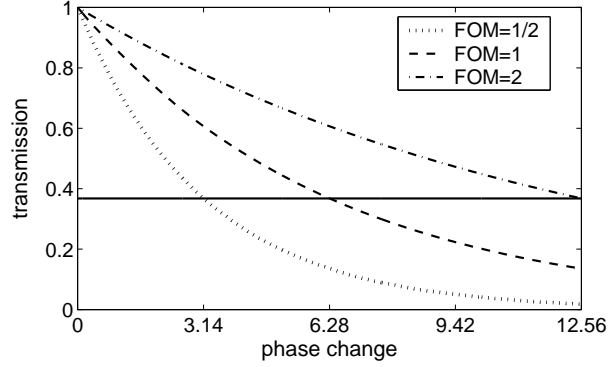


**Figure 2.4:** Intensity transmission as a function of phase shift for different values of  $\frac{n_2}{\beta\lambda} \equiv FOM$ . The line  $T = 1/e$  is also drawn (see further).

with the figure of merit  $FOM$  defined as  $\left| \frac{n_2}{\lambda\beta} \right|$ .

Using the results from [25] and [26], the figure of merit can be estimated theoretically as a function of the optical energy relative to the bandgap. This is plotted in figure 2.5. The lines  $FOM = 2$  and  $FOM = \frac{1}{2}$  are also indicated.

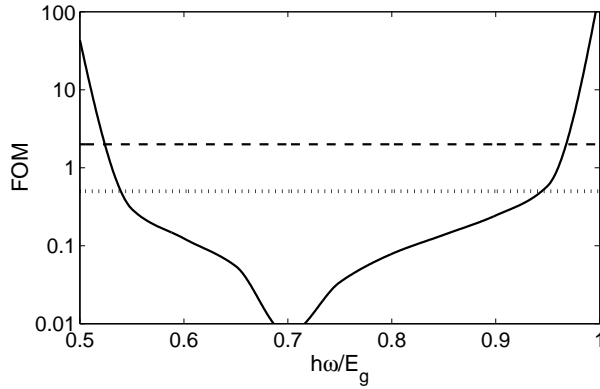


**Figure 2.5:** Figure of merit as a function of the relative frequency  $\frac{\hbar\omega}{E_g}$ . The lines  $FOM = 0.5$  and  $FOM = 2$  are also shown.

As can be seen, two frequency regions show possibly useful  $FOM$ -values for Kerr-nonlinear operation, i.e.  $0 \leq \hbar\omega \leq 0.55E_g$  and  $0.95E_g \leq \hbar\omega \leq E_g$ . In the other parts, two-photon absorption will be the dominant effect. However, because of large carrier related effects (see section 2.5) close to the bandgap, the midgap region is generally preferred.

On the other hand, the lower end of the midgap region is limited by three-photon absorption [36, 46] and has relatively small  $n_2$ -values (see figure 2.2), leading to an optimum frequency region of approximately  $0.45 \leq \hbar\omega \leq 0.55E_g$ .

The figures of merit for the materials and wavelengths of tables 2.1 and 2.2 are shown in table 2.3.

material	$\lambda(\mu\text{m})$	$\hbar\omega/E_g$	$n_0$	$FOM$
SiO <sub>2</sub>	1.06	0.13	1.45	$\gg 1$
Si	1.54	0.72	3.48	0.866
Si	1.54	0.72	3.48	0.370
Si	1.5	0.74	3.48	0.519
Si	1.27	0.87	3.51	0.277
AlAs	1.55	0.37	2.89	(unknown)
AlGaAs	1.60	0.49	3.33	5.417
AlGaAs	1.55	0.51	3.33	5.376
AlGaAs	1.50	0.53	3.33	1.264
AlGaAs	0.85	0.93	3.46	(unknown)
GaAs	1.54	0.57	3.37	0.101
GaAs	1.27	0.69	3.42	0.041
GaAs	1.06	0.82	3.48	0.167
InP	1.55	0.60	3.17	(unknown)

**Table 2.3:**  $FOM$  values, based on tables 2.1 and 2.2

Based on the discussion above, this means that AlGaAs is by far the best Kerr-nonlinear material for operation around the wavelength of 1.55  $\mu\text{m}$ . Although SiO<sub>2</sub> also has a good  $FOM$ , its Kerr coefficient is much smaller than that of Al<sub>0.18</sub>Ga<sub>0.82</sub>As (see table 2.1). For two-photon absorption on the other hand, GaAs is clearly an excellent candidate. The potential of Si at 1.55  $\mu\text{m}$  at this point is unclear, due to the incompatibility of the measurement results in literature.

## 2.5 Carrier effects

The result of two-photon or even single-photon absorption - if  $\hbar\omega \geq E_g$  - is the creation of free carriers (and electron-hole pairs), which will in turn change the electrical and optical properties of the structure. They give rise to additional nonlinear effects, which can also be used in their own right. As these contributions can be significant, it is interesting to look into some of the more important effects in more detail.

Bandfilling occurs when the probability that an electron state in the conduction band or a hole state in the valence band is filled, is not zero anymore. Free carriers partially fill the conduction and valence band and as a consequence, the shape and position of the absorption edge change (see figure 2.6). Bandfilling decreases the absorption coefficient for frequencies close to the bandgap ( $\Delta\alpha < 0$ ). This effect is also called the Burstein-Moss effect [47, 48, 49, 50, 51].

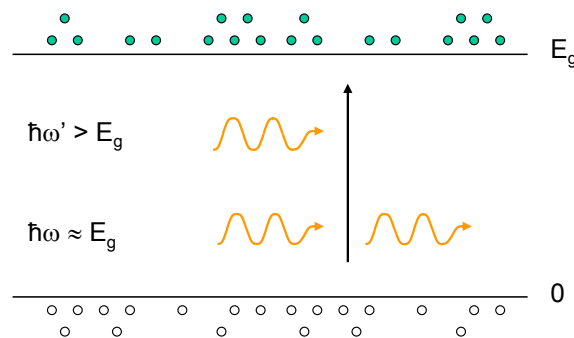


**Figure 2.6:** Representation of the bandfilling effect. Due to the filling of the valence and conduction band, the absorption changes and moves to higher frequencies.

In addition, the wave functions of the occupied states in the valence and conduction band will start to overlap, giving rise to a interacting gas of particles. On top of that, particles with the same spin will try to avoid each other due to the Pauli exclusion principle. The net effect is a screening of the electrons and holes, resulting in a decrease in their energy and a shrinkage of the bandgap [47, 48, 49]. In contrast to the case of bandfilling, now  $\Delta\alpha > 0$ , so it partially compensates the bandfilling effect, depending on the carrier density. Again the change is most significant close to the bandgap<sup>4</sup>.

If the total absorption change due to bandfilling and plasma screening is given by  $\Delta\alpha(N)$ , then the corresponding refractive index change

<sup>4</sup>In a MQW, effects other than bandfilling and plasma screening dominate the carrier generated nonlinearities around the bandgap. Especially exciton bleaching due to phase-space filling [52, 53, 54, 55] - which resembles bandfilling but then for excitons - becomes important.

can again be calculated using the Kramers-Kronig relation (2.34)<sup>5</sup>,

$$\Delta n(\omega, N) = \frac{c}{\pi} \int_0^\infty \frac{\Delta \alpha(\omega', N)}{\omega'^2 - \omega^2} d\omega' \quad (2.43)$$

Until now, only interband absorption effects were discussed. However also intraband effects have to be taken into account. A free carrier can absorb a photon and move to a higher energy state within the band. In this way, a hot(ter) carrier is created (figure 2.7). Note that this free-carrier absorption (FCA) - also known as the plasma effect - is only existing due to the presence of free electrons and holes, which in turn were created by single- and two-photon absorption processes.

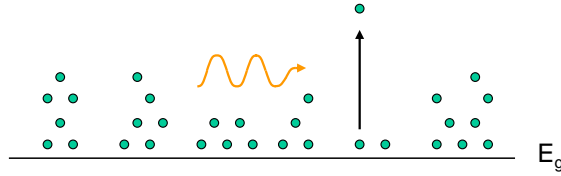


**Figure 2.7:** Representation of free-carrier absorption. Absorption of the incoming light due to the presence of free carriers, in this figure free electrons.

This change in absorption and the associated change in refractive index (also indicated as free-carrier dispersion (FCD)) can be written as as [47, 56, 57, 58]

$$\Delta \alpha^{FCA}(N) = \sigma_a N \quad (2.44)$$

$$\Delta n^{FCD}(N) = \sigma_r N \quad (2.45)$$

with  $\sigma_a$  the free-carrier absorption cross section and  $\sigma_r$  the free-carrier refractive volume.

The full carrier impact can now be summarized as follows. As a first step, the light loss along the propagation axis  $z$  is given by,

$$\begin{aligned} \frac{dI}{dz}(z, t) = & -\alpha I(z, t) - \alpha_{add} I(z, t) - \beta I^2(z, t) \\ & - (\Delta \alpha(N) + \sigma_a N(z, t)) I(z, t) \end{aligned} \quad (2.46)$$

<sup>5</sup>Intrinsic materials are assumed so that the free electron concentration  $N$  is equal to the free hole concentration  $P$ .

Possible absorption processes consist of single- and two-photon absorption (depending on the frequency region of the optical pulse) and extra carrier absorption processes. In addition, also not absorptive loss mechanisms can be present such as radiative and scattering loss (modeled by the additional parameter  $\alpha_{add}$ ). Carriers are only generated by absorption and can be calculated by solving,

$$\frac{dN}{dt}(z, t) = \frac{\alpha I(z, t)}{\hbar\omega} + \frac{\beta I^2(z, t)}{2\hbar\omega} + \frac{\Delta\alpha(N)I(z, t)}{\hbar\omega} - f(N, I) \quad (2.47)$$

In this equation, the term  $f(N, I) \equiv \frac{N(z, t)}{\tau(N, I)}$  represents the possible carrier recombination processes (both radiative and non-radiative) which may depend on both the carrier density and optical intensity, with  $\tau$  the time constant. To be correct, an extra thermalization term would be required in equation (2.47): created high-energetic carriers will heat the rest of the distribution through carrier-carrier scattering and then cool down by means of phonon emission on a timescale of  $\approx 1$  ps (depending on the amount of carriers). Since this is much faster than the typical carrier recombination time constant, the carrier distribution may be considered to be at equilibrium temperature and there is no need for the extra term in equation (2.47) [56]. Note that equations (2.46) and (2.47) are coupled and need to be solved simultaneously.

Once this is done and  $N(z, t)$  is determined, the total carrier related refractive index change is given by,

$$\Delta n(z, t) = \Delta n(N) + \sigma_r N(z, t) \quad (2.48)$$

In this way, index changes can be achieved which are several times higher than the ones obtainable using the bound-electronic Kerr effect with the same input power. Note that depending on the relation between  $N$  and  $I$ , this index change may have the mathematical form of a Kerr effect as often is the case for e.g. bandfilling effects, in which case the effect is not two-photon resonant, but instead single-photon resonant [40]. In contrast to the bound-electronic Kerr effect, carrier related refractive index effects involve real transitions of electrons and holes - i.e. free carriers must effectively be created - and are therefore limited in speed by the carrier lifetime.

This recovery or recombination of the electron and hole densities is possible through a large range of processes, which can be radiative and non-radiative. The recombination time constant is then determined by the dominant mechanism, which among other things can depend

on the carrier density, the optical intensity, the material and its processing...

To obtain fast nonlinear operation, the following recombination mechanisms can be used [59, 51, 56],

- Stimulated emission. In this case, an electron and hole recombine in the presence of another photon(s) with generation of a photon with identical properties. This mechanism is also used in optical amplifiers and lasers. In nonlinear structures, it can be used in a pump-probe configuration, in which the pump beam not only induces nonlinear behaviour onto the probe, but also amplifies it. In InP, time constants down to 7 ps were obtained in this way [60].
- Carrier recombination induced by deep recombination centers. By means of proton bombardment, deep recombination centers can be produced, where the carriers can recombine efficiently. In this way, recovery times of 150-270 ps were achieved in GaAs MQWs [61, 62]. Further reduction is possible by further bombardment, however accompanied by a decreasing nonlinear response.
- Surface recombination. In small waveguides, the carriers can diffuse to the structure surface where they quickly recombine. Very fast recovery can be obtained by using very small waveguides. Recovery time constants of 30-50 ps have been obtained in GaAs [57, 58, 61, 63] and 100-120 ps in InP [58] for waveguides of  $\approx 0.5 \mu\text{m}$  wide. In Si, values of the order of 0.1-10 ns were achieved [64, 65, 66, 67] and values down to 8 ps in AlGaAs [68].
- Carrier sweeping by applying an external dc electric field. Recovery time reductions from 1 ns to 80-90 ps in GaAs are reported using this technique [51, 69]. However, a p-i-n material layer structure must be used instead of standard waveguide structures to reduce the perturbation due to the extra applied field. Furthermore, extra loss can be introduced in this structure due to the Franz-Keldish effect [51]. Recently, this technique was used to create fast Si modulators with recovery time of down to 50-100 ps [14, 15, 70].

From this, it can be concluded that surface recombination is the most efficient recovery mechanism in terms of reducing the time constant without the requirement of additional structural complexity. Solutions like stimulated emission and carrier sweeping can in some cases

even be more effective, however they require more advanced fabrication techniques. Up till now, carrier related effects are therefore recovery-limited to data operations of about 10 Gb/s.

Note also that the lower the carrier lifetime, the higher the required input power becomes to obtain the same carrier density and thus carrier related nonlinearity. In the ultimate case of  $\tau_{\text{carr}} = 0$ , no regime carrier density can exist and therefore no related nonlinearity is possible, which is a fundamental difference with the bound-electronic nonlinear effects.

It is however possible to go to even higher bitrates without the need for reducing the carrier lifetime by using interferometric techniques. An example of this approach is described in [71, 72].

## 2.6 Thermal effects

Absorption of the incoming light does not only give rise to carrier related effects, but it also causes thermal heating. This effect has already indirectly been introduced in the previous section: high-energetic carriers relax by means of phonon emission, which results in a temperature change.

In reality, this carrier-phonon interaction is very complex and largely depends on the dominant carrier decay mechanism and material. Apart from the heat produced due to carrier thermalization, the phonon production in the recombination mechanisms mentioned in section 2.5 is the following,

- Stimulated emission. In principle, phonon creation is possible, if the band structure of the active material is indirect. However, most of the energy which is released in the recombination process is carried away by the created photon [59].
- Carrier recombination induced by deep recombination centers. In this case, much depends on the band diagram of the defects. If e.g. the defect is a donor with an H-atom like conduction band, then a free electron can lower its energy by consecutively emitting a phonon for each level it descends (the outer levels typically have an energy separation of the order of 0.1 eV. However, as the lowest energy states of such a donor are separated by larger energies, these final states can only be reached by photon emission (with a wavelength much longer than the band gap).

- Surface recombination. Surface states typically form a quasi-continuum of states between the conduction and valence band. As a result, recombination is possible without photon emission, i.e. all energy is converted into heat.
- Carrier sweeping by applying a reverse biased, external dc electric field. In this case, the energy of the carriers is largely converted into heat in an external resistor.

From this, it is clear that it is possible that a large amount of the absorbed optical power is ultimately converted into heat inside the device. To obtain the exact percentage, a detailed balance calculation has to be performed. The temperature change can in general be calculated as [73],

$$\frac{dT}{dt} = \frac{x\xi}{\rho C_p} - \frac{T - T_0}{\tau_{th}} \quad (2.49)$$

with  $T$  the temperature,  $T_0$  the ambient temperature,  $\xi$  the absorbed energy density,  $x$  the fraction of  $\xi$  which is converted in heat,  $\rho$  the density,  $C_p$  the specific heat at constant pressure and  $\tau_{th}$  the thermal relaxation time constant.

Like the presence of carriers, temperature also has an influence on the electrical and optical properties of the material. The most important effect is the temperature-dependence of the refractive index,

$$\Delta n(T) = \left. \frac{dn}{dT} \right|_{T=T_0} (T - T_0) \quad (2.50)$$

with  $\frac{dn_0}{dT}$  incorporating both the direct temporal dependence (i.e.  $\frac{\partial n_0}{\partial T}$ ) and thermal expansion effects [74]. Other parameters that change with temperature are a.o. the band gap...

## 2.7 Complete nonlinear picture

From the previous sections, it is clear that the complete nonlinear picture is very complex: multiple nonlinear effects are competing with each other, all depending on each other. In figure 2.8, the situation is qualitatively represented for light inside a material systems which has a frequency around half the bandgap.

Quantitatively, the overall effect of both carriers and heat can be estimated using sections 2.5 and 2.6. Let us do this for AlGaAs ( $\lambda =$

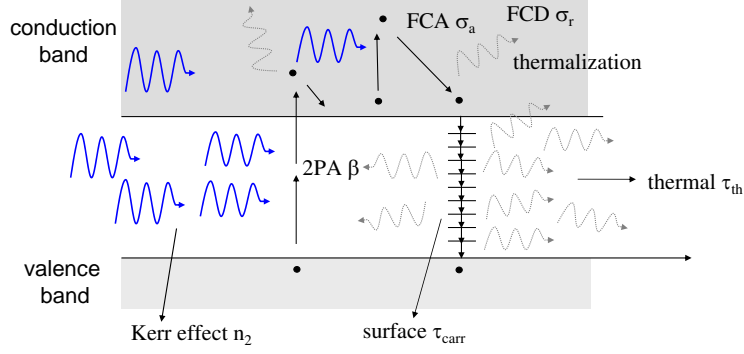


**Figure 2.8:** When light enters in this material, it can be absorbed through two-photon absorption and give rise to a change in the refractive index effect proportional to the light intensity: the Kerr effect. Free carriers that are excited through the 2PA process, can give rise to free-carrier absorption and associated a refractive index change: free carrier dispersion. After a while, these carriers will recombine and in the case of submicron structures (such as photonic wires), this is mainly due to surface recombination. This interband relaxation together with the intraband relaxation effects from carriers created due to 2PA and FCA will mainly lead to phonon creation, which results in heating of the structure and gives rise to thermal expansion and a thermal refractive index change. Due to conduction and convection, the structure finally cools down to a steady-state temperature.

1.55  $\mu\text{m}$ ), one of the most interesting semiconductor materials for Kerr-nonlinear effects.

Using equations (2.46), (2.47) and (2.49), the complete picture can be summarized in these three equations:

$$\frac{dI}{dz}(z, t) = -\alpha_{add}I(z, t) - \beta_I I^2(z, t) - \sigma_a N(z, t)I(z, t) \quad (2.51)$$

$$\frac{dN}{dt}(z, t) = \frac{\beta_I I^2(z, t)}{2\hbar\omega} - \frac{N(z, t)}{\tau_{carr}} \quad (2.52)$$

$$\frac{dT}{dt}(z, t) = \frac{\beta_I I^2(z, t) + \sigma_a N(z, t)I(z, t)}{\rho C_p} - \frac{T(z, t) - T_0}{\tau_{th}} \quad (2.53)$$

with  $\tau_{carr}$  the carrier and  $\tau_{th}$  the thermal life time. At the wavelength of 1.55  $\mu\text{m}$ , linear absorption is negligible and the main free carrier contribution is the plasma effect.

For high-bitrate operation, an average carrier and heat distribution will be generated since  $\tau_{carr}$  and  $\tau_{th}$  are relatively high:  $\frac{dN}{dt} \approx \frac{dT}{dt} \approx 0$ ,

parameter	(dim)	AlGaAs	Ref
$n_{2,I}$	(cm <sup>2</sup> /W)	$1.50 \times 10^{-13}$	[35]
$\beta_I$	(cm/W)	$0.18 \times 10^{-9}$	[35]
$\gamma_I$	(cm <sup>3</sup> /W <sup>2</sup> )	$0.06 \times 10^{-18}$	[36]
$\sigma_r$	(cm <sup>3</sup> )	$-1.0 \times 10^{-20}$	[57, 58]
$\sigma_a$	(cm <sup>2</sup> )	$1.5 \times 10^{-16}$	[57, 58]
$\tau_{carr}$	(ps)	30	[57]
$\left. \frac{dn}{dT} \right _{T=300K}$	(1/K)	$1.3 \times 10^{-4}$	[75]
$\tau_{th}$	(ns)	25	[75, 76]
$\rho C_p$	(J/K cm <sup>3</sup> )	1.75	[75]

**Table 2.4:** Material parameters of AlGaAs at 1.55  $\mu\text{m}$ .

leading to

$$\frac{dI}{dz}(z,t) = -\alpha_{add}I(z,t) - \beta_I I^2(z,t) - \frac{\sigma_a \beta_I I_0^2(z) \tau_{carr}}{4\hbar\omega} I(z,t) \quad (2.54)$$

$$N(z) = \frac{\beta_I I_0^2(z) \tau_{carr}}{4\hbar\omega} \quad (2.55)$$

$$T(z) - T_0 \approx \beta_I I_0^2(z) \frac{(4\hbar\omega + \sigma_a I_0(z) \tau_{carr}) \tau_{th}}{8\hbar\omega \rho C_p} \quad (2.56)$$

in the assumption of a NRZ signal with peak power  $I_0(z)$ . The average power is then  $\frac{I_0(z)}{2}$ .

In this way, the refractive index effects are given by:

$$\Delta n_{Kerr}(z,t) = n_{2,I} I(z,t) \quad (2.57)$$

$$\Delta n_{carr,\beta}(z) \approx \frac{\sigma_r \beta_I I_0^2(z) \tau_{carr}}{4\hbar\omega} \quad (2.58)$$

$$\Delta n_{th,\beta}(z) \approx \left. \frac{dn}{dT} \right|_{T=T_0} \beta_I I_0^2(z) \frac{(4\hbar\omega + \sigma_a I_0(z) \tau_{carr}) \tau_{th}}{8\hbar\omega \rho C_p} \quad (2.59)$$

For materials like AlGaAs with a small two-photon absorption coefficient, three-photon absorption can become dominant (represented by  $\Delta\alpha = \gamma_I I^2$ ), leading to the following additional secondary refractive index effects:

$$\Delta n_{carr,\gamma}(z) \approx \frac{\sigma_r \gamma_I I_0^3(z) \tau_{carr}}{6\hbar\omega} \quad (2.60)$$

$$\Delta n_{th,\gamma}(z) \approx \left. \frac{dn}{dT} \right|_{T=T_0} \gamma_I I_0^3(z) \frac{(6\hbar\omega + \sigma_a I_0(z) \tau_{carr}) \tau_{th}}{12\hbar\omega \rho C_p} \quad (2.61)$$

These different contributions are plotted in figure 2.9, using the material parameters<sup>6</sup> for AlGaAs at 1.55  $\mu\text{m}$  given in table 2.4.

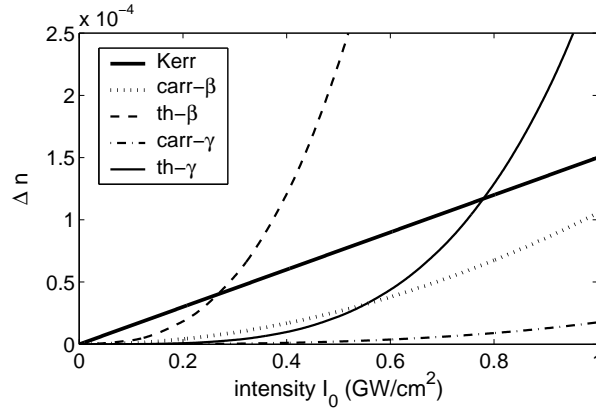


**Figure 2.9:** Different contributions to the nonlinear refractive index change in AlGaAs as function of the peak power.

From this figure, it can be seen that the bound-electronic Kerr effect is dominant at lower intensities. At higher intensity, the thermal contribution - which is dominated by two-photon absorption - surpasses the Kerr effect due to its  $I_0(z)^2$  and  $I_0(z)^3$  dependence. This means that possible fluctuations of the thermal effects (e.g. long 000... or 111... signals) can really be expected to interfere with possible ultrafast operation.

## 2.8 Material anisotropy

In section 2.1, the nonlinear effects were assumed to be isotropic, however in reality, the semiconductor materials mentioned above have a cubic symmetry. As a result, these nonlinear materials cannot be described by a simple third-order susceptibility  $\chi^{(3)}(-\omega; \omega, -\omega, \omega)$ , but instead, they have three independent elements in their susceptibility tensor [16].

<sup>6</sup>For the carrier constants ( $\sigma_r, \sigma_a, \tau_{carr}$ ), values of GaAs are used as Drude calculations do not always provide accurate results [77]. To estimate  $\tau_{th}$ , a one-dimensional material system model was used for the AlGaAs-AlOx system of section 3.1.

If one now calculates the third-order polarization  $\mathbf{P}_\omega^{(3)}$ , true Kerr-nonlinear and two-photon absorptive behaviour, as described by

$$\mathbf{P}_\omega^{(3)} = \frac{3}{4} \epsilon_0 \chi_{eff}^{(3)}(-\omega, \omega, -\omega, \omega) |E_\omega|^2 \mathbf{E}_\omega \quad (2.62)$$

is only found for specific field polarizations:

- the linear polarizations  $(\pm 1, 0, 0)$ ,  $(0, \pm 1, 0)$ ,  $(0, 0, \pm 1)$ ;  $(\pm \frac{1}{\sqrt{2}}, \pm \frac{1}{\sqrt{2}}, 0)$ ,  $(\pm \frac{1}{\sqrt{2}}, 0, \pm \frac{1}{\sqrt{2}})$ ,  $(0, \pm \frac{1}{\sqrt{2}}, \pm \frac{1}{\sqrt{2}})$ ;  $(\pm \frac{1}{\sqrt{3}}, \pm \frac{1}{\sqrt{3}}, \pm \frac{1}{\sqrt{3}})$
- the circular polarizations  $(\pm \frac{1}{\sqrt{2}}, \pm j \frac{1}{\sqrt{2}}, 0)$ ,  $(\pm \frac{1}{\sqrt{2}}, 0, \pm j \frac{1}{\sqrt{2}})$ ,  $(0, \pm j \frac{1}{\sqrt{2}}, \pm \frac{1}{\sqrt{2}})$ ;  $(\pm \frac{1}{\sqrt{3}}, \pm \frac{1}{\sqrt{3}} \exp(\pm j \frac{2\pi}{3}), \pm \frac{1}{\sqrt{3}} \exp(\mp j \frac{2\pi}{3}))$

with  $(u, v, w)$  the vector representation in the crystallographic basis. Furthermore, the nonlinear coefficients  $n_2$  and  $\beta$  are different along each of these six subsets. This was calculated in appendix A.

This anisotropic and polarization dependent behaviour of the third-order polarization has theoretically been modeled by Hutchings et al., both for the Kerr coefficient  $n_2$  [78] and two-photon absorption coefficient  $\beta$  [37]. Experimental verification of these results has been carried out for the Kerr coefficients of AlGaAs and Si (table 2.5, the polarization type is always linear). The obtained values are in good agreement with the theoretical anisotropy predicted by Hutchings.

material<dir>	$\lambda(\mu\text{m})$	$\hbar\omega/E_g$	$n_0$	$n_{2,I}(\text{cm}^2/\text{W})$	$n_2(\text{cm}^2/\text{V}^2)$
Si<110>	1.54	0.72	3.48	$0.45 \times 10^{-13}$	$0.21 \times 10^{-15}$
Si<111>	1.54	0.72	3.48	$0.43 \times 10^{-13}$	$0.20 \times 10^{-15}$
AlGaAs<100>	1.55	0.51	3.33	$1.50 \times 10^{-13}$	$0.66 \times 10^{-15}$
AlGaAs<110>	1.55	0.51	3.33	$1.40 \times 10^{-13}$	$0.62 \times 10^{-15}$

**Table 2.5:** Anisotropic  $n_2$  values for several semiconductors, obtained from literature [32, 35, 36]

As can be seen, these differences for  $n_2$  between the different (linear) polarization directions are relatively small. For the case of  $\beta$  however, the differences are more important, which may lead to the situation that the direction with optimal  $n_2$  has a much poorer *FOM* than other polarization directions. This is e.g. the case for AlGaAs (table 2.6, the polarization type is again linear), leading to even better *FOM* values than reported in table 2.3. In some cases, the main limitation will be formed by three-photon rather than two-photon absorption.

material<dir>	$\lambda(\mu\text{m})$	$\hbar\omega/E_g$	$n_0$	$\beta_I(\text{cm/W})$	$\beta(\text{cm/V}^2)$
Si<110>	1.54	0.72	3.48	$0.79 \times 10^{-9}$	$3.65 \times 10^{-12}$
Si<111>	1.54	0.72	3.48	$0.88 \times 10^{-9}$	$4.07 \times 10^{-12}$
AlGaAs<100>	1.55	0.51	3.33	$0.18 \times 10^{-9}$	$0.80 \times 10^{-12}$
AlGaAs<110>	1.55	0.51	3.33	$\approx 0$	$\approx 0$

**Table 2.6:** Anisotropic  $\beta$  values, obtained from literature [32, 36]

## 2.9 Material engineering

As mentioned in section 2.2, it has been derived by Wherrett that the plots  $n_2 n_0 E_g^4 / \sqrt{E_p}$  and  $\beta n_0 E_g^3 / \sqrt{E_p}$  as a function of  $\frac{\hbar\omega}{E_g}$  are almost independent of the specific semiconductor material. Since the optimum  $E_g$  is now determined by the wavelength of the light  $\lambda$  (e.g. for optimum Kerr-nonlinear behaviour  $0.45 \frac{1}{\lambda_g} \leq \frac{1}{\lambda} \leq 0.55 \frac{1}{\lambda_g}$  with  $\lambda_g$  the bandgap wavelength) and for semiconductors,  $n_0 \approx 3$  and  $E_p \approx 22$  eV, there are in fact no parameters left to optimize the value of  $n_2$  in the case of bulk semiconductor materials. Although the model of Wherrett has its limitations, large improvements of the obtainable  $n_2$  and  $\beta$  values at  $\lambda = 1.55 \mu\text{m}$  should not be expected, at least not with bulk materials. Only tuning for the anisotropic effects remains.

To further improve the Kerr and two-photon absorption coefficients, more complex material systems are being investigated, such as polymers [79, 80], quantum wells/wires/dots [81, 82, 83, 84, 85, 86], nanocrystals [87, 88, 89]... However, at the moment, most research has been done at wavelengths which are not directly suited for telecom purposes (typically  $1 \mu\text{m}$ ) or at effects which are carrier related. Very promising preliminary results in this field have also been obtained by co-researchers at the Department of Inorganic and Physical Chemistry of Ghent University in the context of colloidal nanocrystals [90].

## 2.10 Conclusions

In this chapter, we discussed the mathematical and physical origin of two ultrafast nonlinear effects: the bound-electronic Kerr effect and the two-photon absorption process. Both are parts of the same nonlinear susceptibility and therefore interdependent. Which one of these two weak effects dominates, is largely determined by the relative position of the light frequency compared to the material bandgap. As a result,

AlGaAs is one of the most appropriate materials for Kerr-nonlinear operation at the telecom wavelength 1.55  $\mu\text{m}$ . At this wavelength, GaAs and InP on the other hand are excellent candidates for two-photon absorption. Whether Si at 1.55  $\mu\text{m}$  is more suited for either Kerr-nonlinear or two-photon absorption behaviour is difficult to say due to incompatibility of the measurement results in literature.

In addition, it was shown that secondary effects - such as the influence of generated carriers and heating - may have a significant impact on the ultrafast nonlinear operation and must be taken into account. These secondary effects are typically much slower, but also much stronger. Even in the case of a good Kerr-nonlinear material such as AlGaAs, thermal effects can be dominant. A possible way to prevent heating is e.g. carrier sweeping. Carrier effects themselves on the other hand can provide a viable alternative for data processing up to about 10 Gb/s (higher bitrates are possible with differential techniques).

## Chapter 3

# Transverse nonlinear confinement: waveguides

In the previous chapter, we have seen that ultrafast nonlinear effects are typically also very small (figure 2.9): for a refractive index change of  $\Delta n = 10^{-4}$ , intensities of the order  $1 - 10 \text{ GW/cm}^2$  are required for semiconductor materials. To obtain these high intensities with reasonable power budgets, waveguides with very small effective modal areas - such as photonic wires [91] and photonic crystal (PhC) waveguides [92] - must be used.

In this chapter, we calculate this enhancement for two very different waveguide configurations and apply the results to determine what the optimum configuration would be. We also discuss the possible applications of the bound-electronic Kerr and two-photon absorption effect in such waveguides and determine typical power levels in absence of secondary effects.

### 3.1 Waveguide confinement

In this section, we will use the theory discussed in appendix B to calculate the effective nonlinear coefficients of waveguides in three different nonlinear semiconductor material systems:

- the first system is the high contrast<sup>1</sup> Silicon-on-Insulator (SOI) system which is evaluated both for Kerr and two-photon absorp-

---

<sup>1</sup>both laterally and vertically.

tion purposes:<sup>2</sup>  $n_{2,Si} = 0.45 \times 10^{-13} \text{ cm}^2/\text{V}^2$ ,  $n_{2,SiO_2} = 0$  and  $\beta_{Si} = 3.65 \times 10^{-12} \text{ cm}/\text{V}^2$ ,  $\beta_{SiO_2} = 0$ . The Si thickness is taken to be 220 nm and the width of the waveguide is varied.

- the second system is the GaAs-AlGaAs system with low vertical and high lateral contrast, used in [58]. This system is considered for two-photon absorption effects with  $\beta_{GaAs} = 45.62 \times 10^{-12} \text{ cm}/\text{V}^2$  and  $\beta_{AlGaAs} \approx 0$ . The GaAs thickness is equal to 500 nm and the thickness of the upper AlGaAs cladding layer is 300 nm. The width of the waveguide is again varied.
- the third system is the high contrast<sup>3</sup> AlGaAs- $\text{AlO}_x$  system with Kerr coefficients  $n_{2,AlGaAs} = 1.50 \times 10^{-13} \text{ cm}^2/\text{V}^2$  and  $n_{2,AlO_x} = 0$ . Now, both the height and the width of the waveguide is varied.

### 3.1.1 Silicon-on-Insulator (SOI) system

This material system is shown in figure 3.1. The width  $w$  of the waveguide is still to be optimized.

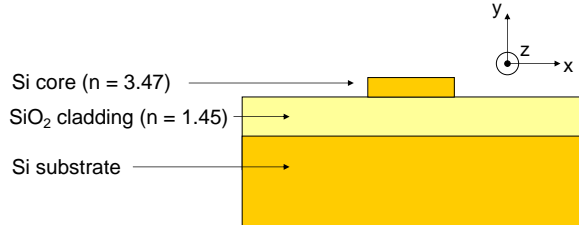


**Figure 3.1:** Silicon-on-Insulator waveguide system

Using the eigenmode expansion tool of CAMFR [93, 94] and equation (B.53), the linear and nonlinear effective indices, which express the effective index change as a function of the optical power (appendix B), were determined - for up to 8 guided modes - as a function of waveguide width for a wavelength of  $\lambda = 1.55 \mu\text{m}$  and the results are given in figure 3.2. The effective two-photon absorption coefficient  $\beta_{eff}$  curve is identical to the  $n_{2,eff}$  curve, except for a constant factor given by

<sup>2</sup>Despite the incompatibility, most papers in literature cite the nonlinear Si coefficients measured by Dinu et al. [32]. Therefore, these values will also be used in this work.

<sup>3</sup>also both laterally and vertically.

$\beta_I/n_{2I}$ . Linear interpolation was used to replace divergent simulation solutions.

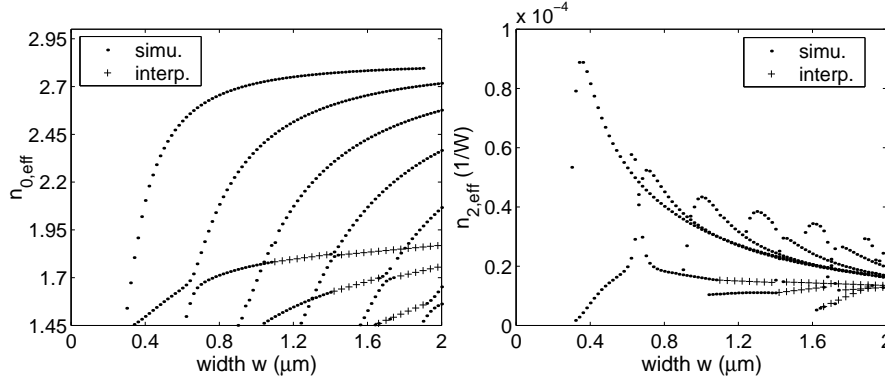


**Figure 3.2:** Linear and nonlinear effective index as function of wire width at the telecom wavelength  $\lambda = 1.55 \mu\text{m}$ .

In figure 3.2, the modes with the highest linear effective index are TE-like<sup>4</sup>, while the modes with the lower indices (bottom figure 3.2) are TM-like. Interactions between odd TE-like and even TM-like (and vice versa) resulting in anti-crossings are visible (see also [3]). At the telecom wavelength  $\lambda = 1.55 \mu\text{m}$ , the SOI structure has only a ground TE-like mode for widths of approximately  $0.3 - 0.6 \mu\text{m}$ .

For  $n_{2,eff}$ , this results in a curve with a single maximum for each mode: this maximum corresponds to an optimum confinement of the light inside the waveguide. Clearly, this optimum is higher for lower orders due to the better confinement. For the ground TE-like mode, the highest nonlinear interaction is obtained for a width of  $0.35 \mu\text{m}$ . However, because of imperfect fabrication and the resulting loss [91, 65] due to sidewall roughness and surface absorption, it can be better to use wider waveguides in practice<sup>5</sup>.

To determine the Kerr effect and two-photon absorption as a function of power  $P$  instead of intensity  $I$ , we can define an effective third-

<sup>4</sup>In three-dimensional structures, the designation TE and TM is not completely correct - in particular for very small waveguides, however conventionally the same indication as used as in the two-dimensional slab waveguide case: TE with transverse electric field  $E_x$  and TM with transverse electric field  $E_y$ .

<sup>5</sup>For safety reasons, it is not advisable to tolerate modes with the same parity as the mode one plans to use. In this case, this means  $w < 0.9 \mu\text{m}$  (beginning of the third TE-like mode).

order nonlinear area by  $\Delta n = n_{2,I} \frac{P}{A_{eff}^{(3)}}$  and equivalently  $\Delta\alpha = \beta_I \frac{P}{A_{eff}^{(3)}}$ . This is also discussed in section B.2. Using the equation (B.53), the effective third-order nonlinear area<sup>6</sup>  $A_{eff}^{(3)}$  is then given by:

$$A_{eff}^{(3)} = \frac{1}{\epsilon_0^2 c^2} \frac{[\text{Re} \int (\mathbf{E} \times \mathbf{H}^*) \cdot \mathbf{e}_z dx dy]^2}{\int_{NL} n_0^2(x, y) |E(x, y)|^4 dx dy} \quad (3.3)$$

In general, this value is not equal to the effective modal area  $A_{eff}^m$ , defined as [95]

$$A_{eff}^m = \frac{\int n_0^2(x, y) |E(x, y)|^2 dx dy}{\max(n_0^2(x, y) |E(x, y)|^2)} \quad (3.4)$$

which is used to indicate confinement of the light in a structure. Here,  $A_{eff}^m$  has a minimum for  $w = 0.45 \mu\text{m}$  ( $A_{eff}^m = 0.063 \mu\text{m}^2$ ). Both are nevertheless of the same magnitude.

In this work, a wire width of  $w = 0.5 \mu\text{m}$  will generally be assumed. Its properties are compared to that of  $w = 0.35 \mu\text{m}$  in table 3.1:

$w$ ( $\mu\text{m}$ )	$n_{0,eff}$	$n_{2,eff}$ ( $\text{W}^{-1}$ )	$\beta_{eff}$ ( $\text{W}^{-1}\text{cm}^{-1}$ )
0.35	1.85	$8.81 \times 10^{-5}$	1.55
0.5	2.37	$6.40 \times 10^{-5}$	1.12
$w$ ( $\mu\text{m}$ )	$A_{eff}^{(3)}$ ( $\mu\text{m}^2$ )		$A_{eff}^m$ ( $\mu\text{m}^2$ )
0.35	0.051		0.071
0.5	0.071		0.064

**Table 3.1:** Linear and nonlinear properties of different SOI wires.

The  $n_{2,eff}$  value for  $w = 0.5 \mu\text{m}$  is already 40% smaller than the optimum value for the width of  $w = 0.35 \mu\text{m}$ . Nevertheless, even in the case of  $w = 0.5 \mu\text{m}$ , the obtained nonlinear coefficient is still much higher than that for  $w > 2 \mu\text{m}$ .

<sup>6</sup>Other definitions of  $A_{eff}^{(3)}$  are used in literature, such as [36, 65]:

$$A_{eff}^{(3)} = \frac{[\int dx n_0^2(x, y) |E(x, y)|^2 dx dy]^2}{\int_{NL} n_0^4(x, y) |E(x, y)|^4 dx dy} \quad (3.1)$$

$$A_{eff}^{(3)} = \frac{[\int dx |E(x, y)|^2 dx dy]^2}{\int_{NL} |E(x, y)|^4 dx dy} \quad (3.2)$$

all leading to similar values (variations up to 20%). Equation (3.3) however was found to coincide with direct numerical simulations of the effective index and absorption change as a function of power (within numerical accuracy).

### 3.1.2 GaAs-AlGaAs system

This layer structure, shown in figure 3.3, was used for two-photon absorption experiments by Ibrahim et al. [58] with a width of  $0.8 \mu\text{m}$ . Here, the width  $w$  of the waveguide is still considered to be undefined.

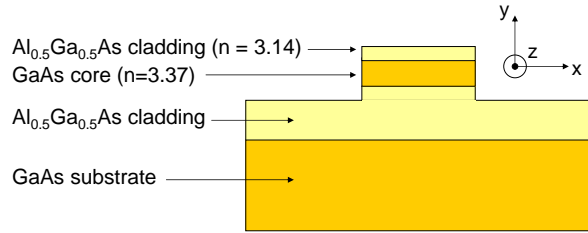


**Figure 3.3:** GaAs-AlGaAs waveguide system

The effective linear and nonlinear indices as a function of waveguide width are plotted in figure 3.4 for a wavelength of  $\lambda = 1.55 \mu\text{m}$ .

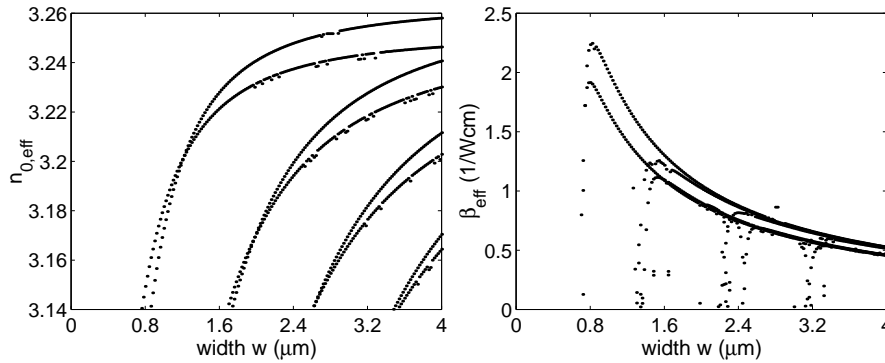


**Figure 3.4:** Effective linear index and two-photon absorption coefficient as function of wire width at the telecom wavelength  $\lambda = 1.55 \mu\text{m}$ .

In this low vertical contrast system, TM-like modes have the highest effective index at lower waveguide widths, while TE-like modes dominate wider waveguides: for the ground modes, one has e.g. that  $n_{0,eff}^{TM,0} > n_{0,eff}^{TE,0}$  for  $w < 1.2 \mu\text{m}$  while for  $w > 1.2 \mu\text{m}$   $n_{0,eff}^{TM,0} < n_{0,eff}^{TE,0}$ . The effective two-photon absorption coefficient - and lowest  $A_{eff}^{(3)}$  value - is

obtained for the ground TE-like mode at a width of  $0.8\ \mu\text{m}$  and not for the ground TM mode. This can be explained by the fact that the linear refractive index profile with  $n_{0,\text{GaAs}} \approx n_{0,\text{AlGaAs}}$  is very different from the spatial profile of the two-photon absorption coefficient, for which  $\beta_{\text{GaAs}} \gg \beta_{\text{AlGaAs}}$ . As a result, the nonlinear material is much more excited in case of a TE-like mode than in the TM-like case.

The results for the two ground modes at a width of  $0.8\ \mu\text{m}$  are summarized in table 3.2.

mode	$n_{0,eff}$	$\beta_{eff}$ ( $\text{W}^{-1}\text{cm}^{-1}$ )	$A_{eff}^{(3)}$ ( $\mu\text{m}^2$ )	$A_{eff}^m$ ( $\mu\text{m}^2$ )
TE	3.12	2.235	0.456	0.242
TM	3.15	1.916	0.532	0.263

**Table 3.2:** Linear and nonlinear properties of  $0.8\ \mu\text{m}$  GaAs waveguide polarizations.

Taking into account the fact that the two-photon absorption coefficient  $\beta$  of GaAs is approximately  $12\times$  higher than that of Si, this advantage is almost completely lost by using GaAs in a (partially) low contrast system compared to the high contrast SOI system: the highest  $\beta_{eff}$  value of the discussed GaAs system is only about  $1.5\times$  higher than that of the best SOI structure - or otherwise - its nonlinear effective area  $A_{eff}^{(3)}$  is about  $8\times$  higher.

### 3.1.3 AlGaAs- $\text{AlO}_x$ system

From the two cases above, it is clear that for efficient nonlinear operation, the nonlinear material AlGaAs should be used in a high contrast configuration. An example of this is shown in figure 3.5. To determine an optimum structure, both the height  $h$  and width  $w$  of the waveguide are still left undefined.

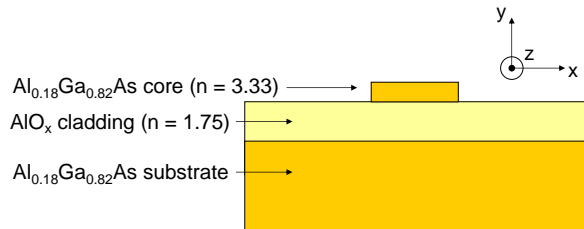


**Figure 3.5:** AlGaAs- $\text{AlO}_x$  material system

The effective nonlinear coefficient  $n_{2,eff}$  ( $W^{-1}$ ) at a wavelength of  $\lambda = 1.55 \mu\text{m}$  is shown in figure 3.6 for the ground TE-like and TM-like mode respectively. The TE-like mode is the mode with both the

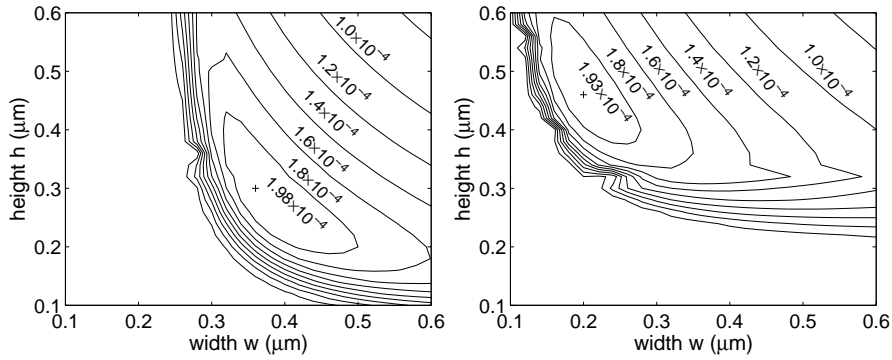


**Figure 3.6:** Effective nonlinear index  $n_{2,eff}$  ( $W^{-1}$ ) as function of waveguide width and height for the ground TE-like (left) and TM-like (right) mode at the telecom wavelength  $1.55 \mu\text{m}$ .

highest linear and nonlinear effective index for  $w > h$  (and vice versa for  $w < h$ ), which is in agreement with waveguide symmetry. Note that the optimum results do not lie on the symmetry axis  $w = h$  due to the air cladding. The best results for both ground modes are summarized in table 3.1.3.

$w$ ( $\mu\text{m}$ )	$h$ ( $\mu\text{m}$ )	mode	$n_{0,eff}$	$n_{2,eff}$ ( $W^{-1}$ )	$A_{eff}^{(3)}$ ( $\mu\text{m}^2$ )	$A_{eff}^m$ ( $\mu\text{m}^2$ )
0.36	0.30	TE	2.06	$1.98 \times 10^{-4}$	0.076	0.084
		TM	2.01	$1.26 \times 10^{-4}$	0.122	0.100
0.20	0.46	TE	1.63	$0.25 \times 10^{-7}$	598	222
		TM	2.08	$1.93 \times 10^{-4}$	0.078	0.065

**Table 3.3:** Linear and nonlinear properties of AlGaAs

Note that the highest effective nonlinear index is only approximately a factor 2 better than the optimum SOI values, instead of the expected factor 3. This is due to the fact that the refractive index ratio  $\frac{n_{Si}}{n_{SiO_2}} > \frac{n_{AlGaAs}}{n_{AlO_x}}$ , resulting in a better nonlinear optical confinement. This further underlines the importance of material systems with very high contrast.

Similar calculations can also be done for other types of guiding structures, such as photonic crystal waveguides, allowing potentially even higher nonlinear effective interaction - in particular in the case of air-clad membrane structures. As the main focus of this work was on photonic wires, this was not further investigated in detail.

### 3.2 Applications

In this section, the potential of nonlinear waveguides for ultrafast signal processing will be discussed. We will discriminate between so-called single-signal and pump-probe operation:

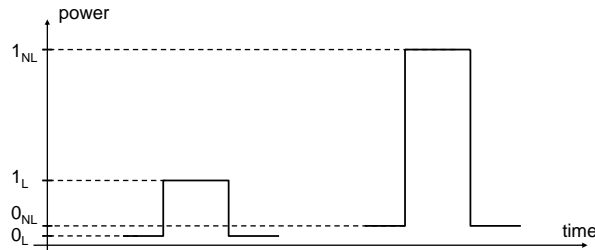


**Figure 3.7:** Example of a linear and nonlinear light pulse. The 0 and 1 levels are indicated. In single-signal operation, the left and right image correspond to the linear and nonlinear regime of the same data signal. In a pump-probe setup, they respectively represent the probe and pump signal.

- A first possibility to apply nonlinear effects for signal processing is using the data signal itself as trigger for the nonlinear actions, i.e. by varying the power of the data signal between low (linear regime) and high (desired nonlinear regime). This approach is called single-signal operation and can e.g. be used for self-routing data signals: simply by means of its power, the signal can find its path through the network. An example is shown in figure 3.7.
- In a second approach, data signals (one or more) can be influenced by means of an additional control signal: the pump-probe configuration. In contrast to the first, the data signals always remain in the linear power regime, while the additional signal induces the nonlinearity.

To evaluate typical power levels, the effective nonlinear coefficients of the Silicon-on-Insulator platform will be used (width  $0.5 \mu\text{m}$ , table 3.1).

As calculated in section 3.1, its values are not the best one can obtain by optimizing the material system and waveguide width. However, because of its compatibility with CMOS technology [91], SOI is one of the most investigated material systems today and its nonlinear values are of the same order of magnitude as the best results that can be achieved. First, the Kerr and the two-photon absorption effect will be discussed separately, which would be the case for e.g. AlGaAs or GaAs. In a separate section, the mutual impact of both effects is considered, which is important for e.g. Si.

### 3.2.1 Bound-electronic Kerr effect

The basic application of the bound-electronic Kerr effect - and any other refractive index effect - in waveguides is all-optical phase shifting as discussed in section 2.4. As mentioned before, two-photon absorption is not considered in this section.

#### 3.2.1.1 Single-signal operation

With the results of table 3.1, the nonlinear phase shift can be calculated as a function of the optical power  $P$  and wire length  $L$  as

$$\Delta\phi(P, L) = -\frac{\omega}{c}n_{2,eff}PL \quad (3.5)$$

This is shown in figure 3.8. To obtain a phase shift of  $\pi$ , large pulse

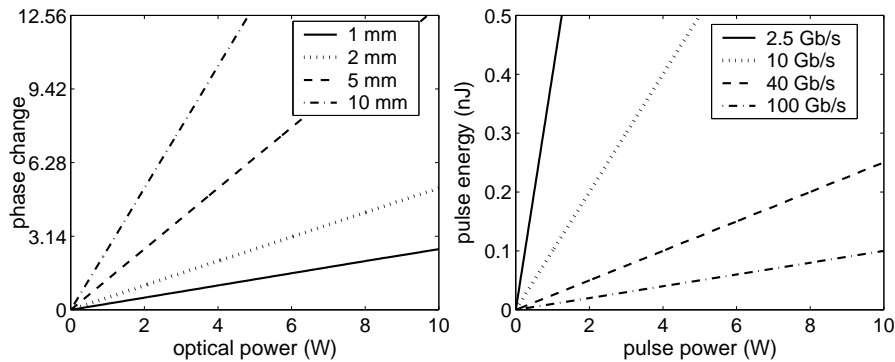


**Figure 3.8:** Phase shift  $\Delta\phi$  as function of optical power for different waveguide lengths at  $\lambda = 1.55 \mu\text{m}$  (left). Pulse energy as function of optical power for different data rates assuming a Non-Return-to-Zero (NRZ) format (right).

powers or device lengths are typically necessary: a peak power of about 1.2 W is required for a waveguide length of 10 mm. However, the main advantage<sup>7</sup> of photonic waveguides is their large optical bandwidth<sup>8</sup> so that data rates higher than 100 Gb/s can easily be sustained. As a result, the pulse energy can still be kept modest: for instance, the peak power of 1.2 W corresponds to a pulse energy of 12 pJ for a Non-Return-to-Zero (NRZ) bitrate of 100 Gb/s (figure 3.8).

### 3.2.1.2 Pump-probe operation

As the pump and data signal (normally) have different frequencies, the non-degenerate Kerr effect in this section is not exactly the same effect as discussed in chapter 2 (i.e.  $n_2 = \frac{3\text{Re}\chi^{(3)}(-\omega;\omega,-\omega,\omega)}{8n_0}$ ). Instead, the refractive index of the probe signal with frequency  $\omega_s$  is now changed by means of the intensity of the pump signal with frequency  $\omega_p$ . As a result, the relevant polarization is now described by

$$\mathbf{P}_{\omega_s} = \epsilon_0 \left( \chi^{(1)}(-\omega_s; \omega_s) + \frac{3}{4} \chi^{(3)}(-\omega_s; \omega_s, -\omega_p, \omega_p) |E_{\omega_p}|^2 \right) \mathbf{E}_{\omega_s} \quad (3.6)$$

instead of by equation (2.20),

$$\mathbf{P}_{\omega} = \epsilon_0 \left( \chi^{(1)}(-\omega; \omega) + \frac{3}{2} \chi^{(3)}(-\omega; \omega, -\omega, \omega) |E_{\omega}|^2 \right) \mathbf{E}_{\omega} \quad (3.7)$$

leading to the following Kerr coefficient:

$$n_{2,probe} = \frac{3\text{Re}\chi^{(3)}(-\omega_s; \omega_s, -\omega_p, \omega_p)}{4n_0} \quad (3.8)$$

The additional factor 2 compared to the single-signal case is due to the fact that the index change is caused by a physically distinguishable signal [40]. This can also be seen in equation (D.7).

For frequencies  $\omega_s \approx \omega_p$ , the nonlinear pump-probe susceptibility  $\chi^{(3)}(-\omega_s; \omega_s, -\omega_p, \omega_p)$  is approximately equal to  $\chi^{(3)}(-\omega_s; \omega_s, -\omega_s, \omega_s)$  [96], so that in a pump-probe configuration, the probe feels an index change which is about twice as large as the index change experienced by the pump itself. As a result, the probe phase change is given by

$$\Delta\phi_{probe}(P_{pump}, L) = -2\frac{\omega}{c} n_{2,eff} P_{pump} L \quad (3.9)$$

<sup>7</sup>In the case of photonic crystal waveguides, this statement is however not always valid.

<sup>8</sup>A 500 nm wide SOI photonic wire has a bandwidth of more than 50 THz!

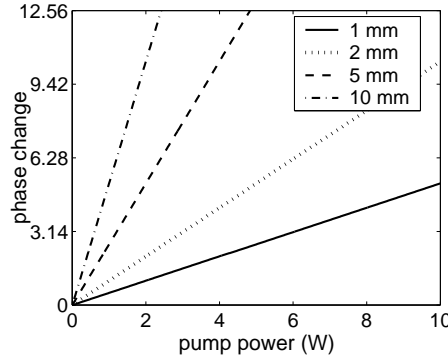


**Figure 3.9:** Pump-probe phase shift  $\Delta\phi_{probe}$  as function of optical pump power for different waveguide lengths at  $\lambda = 1.55 \mu\text{m}$ .

This phase change is plotted in figure 3.9.

Compared to the single-signal case, the required power-length product  $P_{pump}L$  for fixed bitrate drops by a factor 2. The conclusions of relatively high pulse power and/or device length however hold.

Phase shifting is a commonly used and very versatile method for data processing. Implemented in an interferometric structure such as a Mach-Zehnder interferometer, it allows all-optical switching, wavelength conversion, ...

### 3.2.2 Two-photon absorption effect

Compared to the bound-electronic Kerr effect, two-photon absorption has much less potential. As it essentially decreases the transmission as function of the applied power, it can be used for applications based on all-optical limiting. As mentioned before, the Kerr effect is not considered in this section.

#### 3.2.2.1 Single-signal operation

Using the results of table 3.1 and chapter 2, the nonlinear transmission can be calculated as a function of the optical power at the input of the waveguide  $P_{in}$  and wire length  $L$  as

$$T(P_{in}, L) = \frac{1}{1 + \beta_{eff}P_{in}L} \quad (3.10)$$

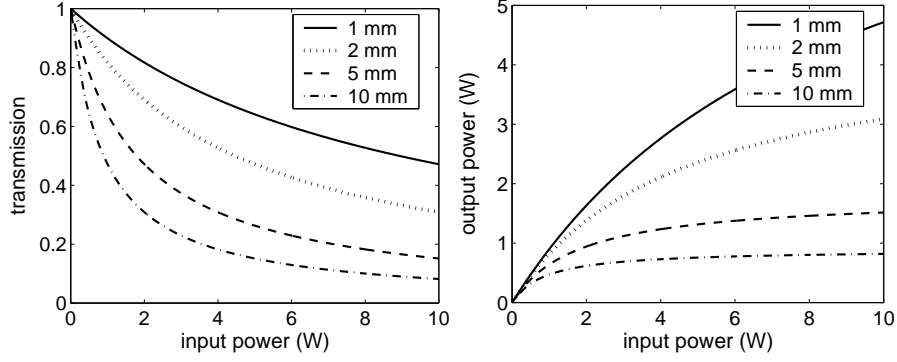


**Figure 3.10:** Intensity transmission  $T$  (left) and output power  $P_{out}$  (right) as function of the input power  $P_{in}$  for different waveguide lengths at  $\lambda = 1.55 \mu\text{m}$ .

This is shown in figure 3.10. The limiting behaviour can be seen by looking at the corresponding output power  $P_{out} = TP_{in}$ . Powers of the same order of magnitude as in the Kerr case are required to obtain significant all-optical limiting.

### 3.2.2.2 Pump-probe operation

Similar to the case of the non-degenerate Kerr effect, the non-degenerate two-photon absorption coefficient is  $2\times$  stronger than the degenerate two-photon absorption coefficient  $\beta_{eff}$ . With  $z$  the propagation axis, the nonlinear transmission of pump and probe can be calculated by solving

$$\frac{dP_{pump}(z)}{dz} = -\beta_{eff}P_{pump}^2(z) - 2\beta_{eff}P_{probe}(z)P_{pump}(z) \quad (3.11)$$

$$\frac{dP_{probe}(z)}{dz} = -2\beta_{eff}P_{pump}(z)P_{probe}(z) - \beta_{eff}P_{probe}^2(z) \quad (3.12)$$

with  $P_{pump}(z)$  and  $P_{probe}(z)$  respectively the pump and probe power at position  $z$ . If we neglect the non-degenerate two-photon absorption effect onto the pump signal and the degenerate two-photon absorption effect onto the probe - which is possible due to the fact that  $P_{pump} \gg P_{probe}$ , the pump and probe transmission after a waveguide with length

$L$  with input pump power  $P_{in,pump}$  become

$$T_{pump}(P_{in,pump}, L) \approx \frac{1}{1 + \beta_{eff} P_{in,pump} L} \quad (3.13)$$

$$T_{probe}(P_{in,pump}, L) \approx \left( \frac{1}{1 + \beta_{eff} P_{in,pump} L} \right)^2 \quad (3.14)$$

The pump transmission was represented as function of the pump power for different waveguide lengths in figure 3.10. The same is now done for the probe transmission in figure 3.11.

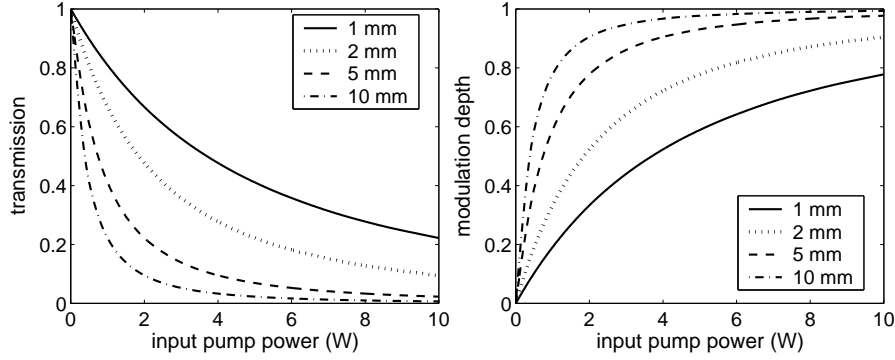


**Figure 3.11:** Probe transmission  $T_{probe}$  (left) and modulation depth (right) as function of input pump power  $P_{in,pump}$  for different waveguide lengths at  $\lambda = 1.55 \mu\text{m}$ .

The most important application for the two-photon absorption pump-probe operation is inverted wavelength conversion: the modulation of the pump signal induces inverted modulation (logic NOT function) onto a probe signal with a different wavelength. This is schematically represented in figure 3.12.

The obtainable modulation depth  $1 - \frac{T_{probe}(P_{pump}, L)}{T_{probe}(0, L)}$ <sup>9</sup> is shown in figure 3.11. A modulation depth of 95% can be obtained with an input pump power of 3 W using a waveguide length of 10 mm. Again, the required optical power is very high, even for relatively long nonlinear waveguides; however, due to the typically large waveguide bandwidth, this corresponds to modest pulse energies (in this case, 30 pJ for a NRZ bitrate of 100 Gb/s).

<sup>9</sup>In absence of linear loss, this is simply equal to  $1 - T_{probe}(P_{pump}, L)$ .

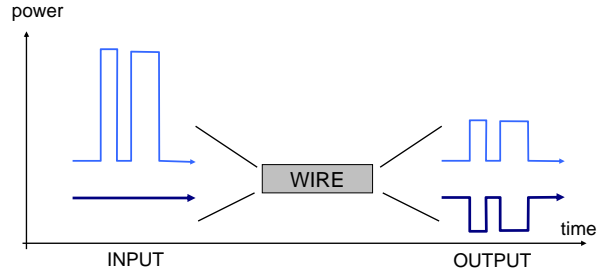


**Figure 3.12:** Principle of inverted modulation inside a nonlinear waveguide by means of non-degenerate two-photon absorption.

This NOT function can immediately be extended to a NOR function by noting that the increase of modulation depth saturates for high pump powers:  $P_{pump}$  and  $2P_{pump}$  then results in approximately the same modulation depth.

### 3.3 Figure of merit

Until now, the reciprocal impact of the bound-electronic Kerr and two-photon absorption effect have not been taken into account. This was already discussed in section 2.4. For two-photon absorption applications, this is not a problem as long as they are not used in interferometric structures: in that case, phase changes do not effect the transmission. Of course, this is not the case of applications based on the Kerr effect, in which both the transmission and the obtained phase change reduces. For the Si values of tables 2.1 and 2.2, the impact in the single-signal case is plotted in figure 3.13.

As can be seen, the impact of two-photon absorption can be quite important depending on the exact literature values. In this chapter, the coefficients measured by Dinu et al. [32] were used, corresponding to the worst case scenario. As a result, the real phase change is typically smaller than obtained in section 3.2.1, especially for  $\Delta\phi \gg \pi$ . Note that it is possible that the real phase shift surpasses the results of section 3.2.1, as the Kerr coefficients measured by Tsang et al. and Rieger et al. are somewhat larger [31, 33].

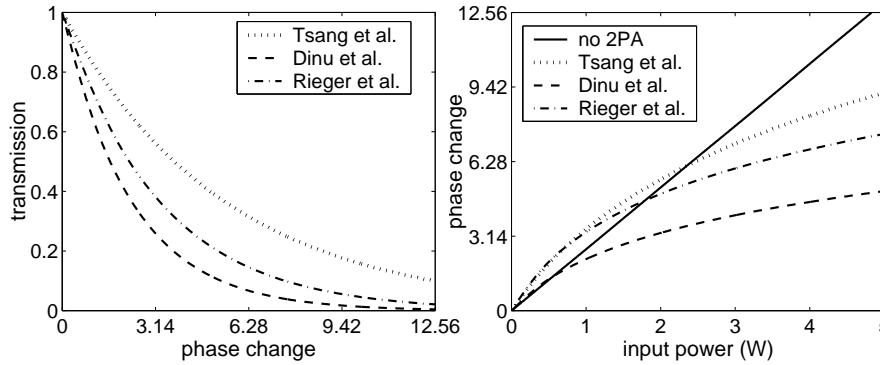


**Figure 3.13:** Intensity transmission  $T$  as a function of the real phase change using [31, 32, 33] (left). Obtained real phase shift using [31, 32, 33] compared to the results obtained in section 3.2.1 without taking into account two-photon absorption (waveguide length of 10 mm, right).

### 3.4 Conclusions

In this chapter, an effective nonlinear area was defined, which enables us to convert the optical intensities of chapter 2 into optical power levels and pulse energies. It was in particular shown that structures with high contrast in both transverse directions are essential to reduce the necessary power. As a result, a system like SOI - which has only moderate nonlinear coefficients - can compete with systems such as GaAs-AlGaAs and AlGaAs-AlO<sub>x</sub> with much higher  $n_2$  and  $\beta$  values. Especially, in the latter case, it is clear that even a slight decrease in contrast can have a severe power penalty.

Using these results, the power and energy requirements were determined for different nonlinear applications implemented in a standard SOI wire system. Typical power needs are of the order of 1-10 W for waveguide lengths in the mm range, leading to pulse energies of the order of 25-250 pJ for 40 Gb/s and 10-100 pJ for 100 Gb/s operation in NRZ modulation - although in principle bitrates exceeding 1 THz are possible. These considerations do not yet take into account linear loss mechanisms (mainly determined by fabrication) and secondary effects (see chapter 5).



## Chapter 4

# Longitudinal nonlinear confinement: resonators

From the previous chapter, it is clear that using high transverse confinement alone is not sufficient to obtain very small devices which operate at low power and allow large-scale integration of ultrafast nonlinear functionalities.

A possible solution to this problem is also confining the light in the longitudinal direction by using resonant structures. In optical resonators, the light is slowed down and enhanced leading to a larger interaction with the nonlinear material. This enhancement however takes place at the expense of a reduction of the optical bandwidth. As we have seen in chapter 3, the typical waveguide bandwidth is extremely large, so that this is essentially not a problem, but it puts a limit on the maximum improvement of the nonlinear behaviour that can be obtained.

In this chapter, we will investigate the additional enhancement that can be achieved with resonant structures by means of a one-dimensional analytical model including both the Kerr effect and two-photon absorption. To improve the readability, the mathematical description of this model will however not be given here, but can be found in the appendix. As in the previous chapter, we will also discuss possible nonlinear applications, which in the case of optical resonators are more extensive than in the waveguide case. For each of these applications, we will calculate typical power levels and pulse energies in the absence of secondary effects and determine the effect of the different resonator parameters. In addition, we will optimize the resonator structure by means of our one-dimensional model for a particular configuration

and discuss the value and the impact of properties - such as the quality factor and the effective modal volume - which are common terms in experimental work.

## 4.1 One-dimensional optical resonator

Essentially, an optical resonator is a structure in which light circles around - or resonates - and is only gradually able to leak out (and enter). This resonant behaviour can be induced by locking the light between two optical mirrors in a sort of cavity. Schematically, this is represented in figure 4.1.

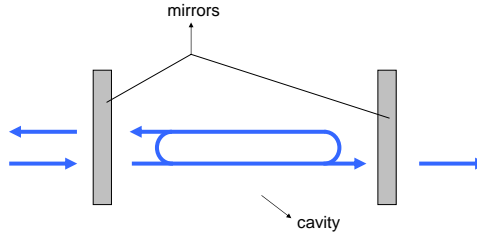


**Figure 4.1:** Schematic representation of resonant action

These mirror sections can be constructed by means of periodic structures which obey the Bragg condition [97], called distributed Bragg reflectors (DBR). In the one-dimensional case, the most efficient mirror structure with two different effective index layers  $n_a$  and  $n_b$  is composed of quarter-wavelength plates<sup>1</sup>:

$$l_a = \frac{\lambda}{4n_a} \quad (4.1)$$

$$l_b = \frac{\lambda}{4n_b} \quad (4.2)$$

In this work, we will consider a slightly more general situation, in which the lengths are given by,

$$l_a = m' \frac{\lambda}{4n_a} \quad (4.3)$$

$$l_b = m'' \frac{\lambda}{4n_b} \quad (4.4)$$

<sup>1</sup>In this case, the Bragg condition  $n_a l_a + n_b l_b = m \frac{\lambda}{2}$  with  $l_a$  and  $l_b$  the length of the two layers is fulfilled and additionally the reflection at each interface is constructive.

with  $m'$  and  $m''$  odd<sup>2</sup>.

To obtain a resonance around a certain center wavelength  $\lambda_c$ , a cavity must be constructed with a round-trip phase length equal to a multiple of  $2\pi$  [97]. One-dimensionally, this corresponds to a cavity composed of an integer number of half-wavelength plates<sup>3</sup>:

$$l_{cav} = N_{cav} \frac{\lambda_c}{2n_a} \quad (4.5)$$

with  $N_{cav}$  integer.

As a result, a single resonator<sup>4</sup> around the center wavelength  $\lambda_c$  can be depicted as

$$a_{in} \underbrace{b_{m'' \frac{\lambda_c}{4}} a_{m' \frac{\lambda_c}{4}} \dots b_{m'' \frac{\lambda_c}{4}}}_{\text{mirror}} a_{N_{cav} \frac{\lambda_c}{2}} \underbrace{b_{m'' \frac{\lambda_c}{4}} a_{m' \frac{\lambda_c}{4}} \dots b_{m'' \frac{\lambda_c}{4}}}_{\text{mirror}} a_{out}$$

The input and output sections with respectively a length of  $l_{in}$  and  $l_{out}$  are necessary for concatenation of more than one resonator period ( $N$  will be used to indicate the number of resonator periods). To avoid destructive interference in the case of more than one resonator, one requires that  $l_{in} + l_{out} = \frac{\lambda}{4n_a} + p \frac{\lambda}{2n_a}$  with  $p = 0, 1, 2, \dots$  which e.g. leads to  $l_{in} = l_{out} = \frac{m' \lambda_c}{8n_a}$ . So finally, one obtains schematically

$$\underbrace{a_{m' \frac{\lambda_c}{8}}}_{\text{input}} \underbrace{b_{m'' \frac{\lambda_c}{4}} \left( a_{m' \frac{\lambda_c}{4}} b_{m'' \frac{\lambda_c}{4}} \right)^{\frac{N_{dbr} - 1}{2}}}_{\text{mirror}} \underbrace{a_{N_{cav} \frac{\lambda_c}{2}}}_{\text{cavity}} \underbrace{b_{m'' \frac{\lambda_c}{4}} \left( a_{m' \frac{\lambda_c}{4}} b_{m'' \frac{\lambda_c}{4}} \right)^{\frac{N_{dbr} - 1}{2}}}_{\text{mirror}} \underbrace{a_{m' \frac{\lambda_c}{8}}}_{\text{output}}$$

with  $N_{dbr}$  is the total number of  $b$ -layers in a single resonator period. This is visually represented in figure 4.2.

<sup>2</sup>Now, the Bragg condition is still fulfilled and again the reflection at each interface is constructive, but the structure is less efficient in terms of length. Such a restriction can e.g. be imposed for technological purposes.

<sup>3</sup>One of two effective indices of the mirror sections is reused, e.g.  $n_a$ .

<sup>4</sup>Two cases can be distinguished:  $n_a > n_b$  and  $n_a < n_b$  with  $n_a$  the cavity index. The first case is the most common one. In the three-dimensional case, it can be achieved by etching a grating into a waveguide using a second etch step. Waveguides with a diffraction grating etched into the sidewalls and photonic crystal-based resonator structures are other examples (see also figure 5.10). The case of a waveguide with an 'external' sidewall grating is an example of the second case. In this work, it will implicitly be assumed that  $n_a > n_b$ , in the case distinction would be necessary.

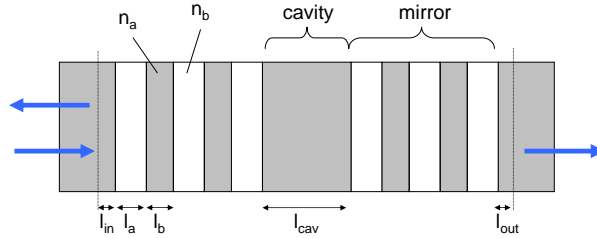


**Figure 4.2:** Visual representation of a single resonator period as used in this work.

The linear properties of resonator structures with one and more periods are described in detail in appendix C. The Kerr and two-photon absorption nonlinear properties are discussed in appendices D and E. This theoretical model is published in the journal paper [98]. Nonlinear simulations were done by means of an extension [99] to CAMFR [94]: the nonlinear solution is obtained by means of a spatial grid on which the nonlinear index changes are calculated in an iterative way, until convergence is obtained.

## 4.2 Applications

Now, the potential of nonlinear resonators for ultrafast signal processing will be discussed. Again, we will distinguish single-signal and pump-probe operation.

In contrast to chapter 3, the transmission spectra of optical resonators are not equal to unity, so that the signal data rates will not only be determined by the speed of the nonlinear effects but also by the properties of the resonators. Although data signals are explicitly time-domain related, we will discuss possible resonator applications from a frequency-domain point of view, as this leads to the best understanding. To estimate the time response of a data stream with pulse length  $t_{pulse}$ , we will consider a frequency region  $\Delta\nu_s = \frac{1}{t_{pulse}}$ , which is a reasonably good approximation.

To evaluate typical power levels, the effective nonlinear coefficients of the Silicon-on-Insulator platform will again be used (width  $0.5\ \mu\text{m}$ , table 3.1) although in fact one-dimensional structures are discussed. We will again discuss the Kerr and the two-photon absorption effect first separately, which would be the case for e.g. AlGaAs or GaAs, while the mutual impact of both effects, which is important for e.g. Si, will

be considered in a separate section. As an example, a mirror contrast of  $1 - \frac{n_b}{n_a} = 10\%$  will be assumed. Using the theoretical model in appendices D and E, we will optimize the mirror and cavity length for each specific application. To conclude, the results that we obtain will be discussed and verified by means of nonlinear simulations.

This work is published in the journal paper [98] and presented at several conferences.

### 4.2.1 Bound-electronic Kerr effect

As discussed in appendix D, the refractive index change due to the Kerr effect in the mirrors and the cavity of a resonator structure causes a shift of the resonance frequency  $\Delta\nu_c$  and the output phase  $\Delta\phi$  which is proportional to the input power. These two phenomena in an optical resonator give rise to much more applications than in the case of a simple waveguide. As mentioned before, two-photon absorption will not be taken into account in this section.

#### 4.2.1.1 Single-signal operation

Possible functionalities that can be implemented in this way in a single-signal approach are all-optical phase shifting, limiting, bistability, switching and regeneration.

- All-optical phase shifting has already been explained in section 3.2.1.
- All-optical limiting is the phenomenon in which the output intensity monotonically increases for increasing input power up to a limiting value and then remains more or less constant. Although the overall effect is the same as in section 3.2.1, its origin is now related to the shift of the resonance frequency instead of the decrease in the resonance transmissivity. This effect will be discussed in the context of all-optical switching (see below).
- All-optical bistability is the existence of two stable nonlinear solutions for a single input power. This effect will also be discussed in the context of all-optical switching (see below).
- All-optical switching in the strict sense used here is switching between zero and unity transmission by means of nonlinear interaction (and is to be distinguished from all-optical switching by

means of nonlinear phase shifting in an interferometric structure). Two situations are possible:

- Total transmission in the linear case, which is related to all-optical limiting
  - Total transmission in the nonlinear case, which is linked to all-optical bistability.
- All-optical regeneration is a bit of an outsider in this list: by combining the pulse shaping possibilities of a Kerr-nonlinear resonator with an optical amplifier, a data signal can be Re-amplified and Re-shaped (2R-regeneration).

**All-optical phase shifting** In this application, the transmission should remain unity in both the linear and nonlinear regime and only the phase is to be shifted, so the resonance frequency shift  $\Delta\nu_c$  should be smaller than the resonator bandwidth  $\Delta\nu_{BW}$ . The resonance peaks in the linear and the nonlinear case do not coincide and therefore the maximum signal bandwidth  $\Delta\nu_s$  is not equal to  $\Delta\nu_{BW}$ . In the case of an infinite number of periods,  $\Delta\nu_s$  will be equal to the bandwidth overlap between both cases. Unfortunately, for a finite structure, the resonance window will not be completely transmissive. At the edges, the transmission function will show a number of peaks (increasing with the number of periods), in between which the transmission can drop even more than 50%, depending on the index contrast of the mirrors (see e.g. the trend of figures C.1, C.2 and C.3). Therefore, only a fraction  $f_{corr}\Delta\nu_{BW}$  with  $f_{corr} < 1$  can be used, leading to a useful signal bandwidth of

$$\Delta\nu_s = f_{corr}\Delta\nu_{BW} - \Delta\nu_c \quad (4.6)$$

Based on simulations,  $f_{corr} = \frac{1}{2}$  is a good estimate.

From the results of appendix D and equation (4.6), it can be seen that a trade-off between input power, device length and signal bandwidth is to be made: to minimize the device length  $L_{tot}$ , the phase shift per unit of length  $\Delta\phi/L_{per}$  must be maximized. This implies that the resonance shift  $\Delta\nu_c$  should be as high and the resonance bandwidth  $\Delta\nu_{BW}$  as low as possible (section D.3.3). However, these last two conditions also result in a lower signal bandwidth  $\Delta\nu_s$ . Furthermore, a restriction to the resonance shift  $\Delta\nu_c$  will be imposed by the achievable input power.

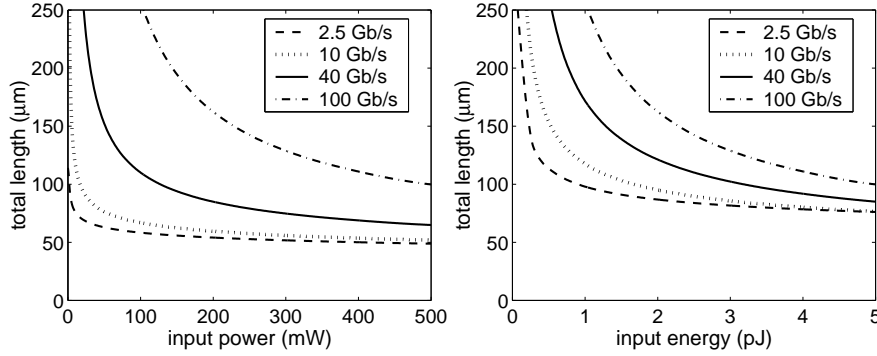


**Figure 4.3:** Trade-off between  $L_{tot}$  and  $P_{in}$  (left) and  $\mathbb{E}_{in}$  (right) for different signal bandwidths.

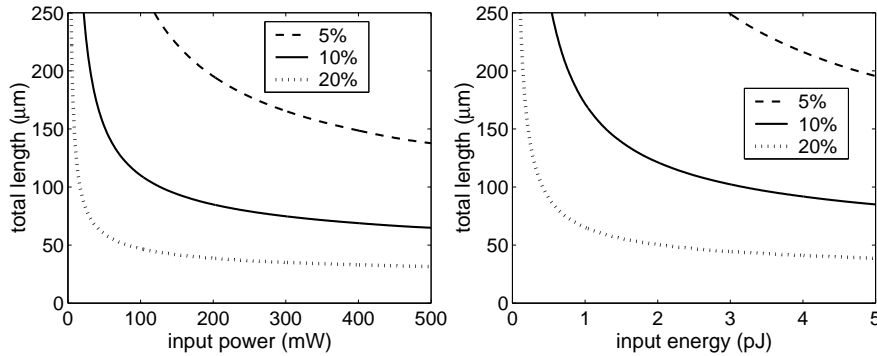


**Figure 4.4:** Influence of index contrast on the trade-off  $L_{tot}$  versus  $P_{in}$  (left) and  $\mathbb{E}_{in}$  (right) for 40 Gb/s.

For the example proposed above, the five optimum results are shown in figure 4.3: the required input power  $P_{in}$  and energy<sup>5</sup>  $\mathbb{E}_{in}$  to obtain a phase shift of  $\pi$  is given as function of device length for several signal bandwidths.

Comparing figures 4.3 and 3.8, it can be seen that - depending on the signal bandwidth - improvements in the order of 10000 for the device length are possible. The signal bandwidth is however an important limiting factor, especially for very high bitrates. Note also that from

<sup>5</sup>We again assume data rates in the NRZ format. Bitrates of 2.5, 10, 40 and 100 Gb/s correspond to signal bandwidths  $\Delta\nu_s$  of 2.5, 10, 40 and 100 GHz.

a certain input power on, the incremental improvement of  $L_{tot}$  drops very steeply.

In figure 4.4, the example above is recalculated with other index contrasts for a signal rate of 40 Gb/s. From this, it is clear that high index contrasts allow a major improvement in the device length. This is due to two factors: first of all, the length of mirrors with the same reflectivity substantially reduces for higher contrast. In addition, the resonance shift for a certain input power will also be larger for shorter mirrors, because a smaller part of the nonlinear phase change in the cavity will be used to compensate the phase shift in the mirrors, as discussed in section D.1.

An important remark is that for all situations depicted above, the optimum results were obtained for  $N_{cav} \approx 1$ : this means that enlarging  $|r_{dbr}|_{\nu_c}$  is more efficient in terms of device length than enlarging the cavity length.

Consider now the following case: we would like to minimize the device length for a signal rate of 40 Gb/s and input powers up to 250 mW (pulse energies up to 6.25 pJ). Using the theory of appendices C and D, the five optimum parameters configurations that were obtained, are shown in table 4.1, together with the required input power  $P_{in}$  and the total device length  $L_{tot}$ .

	$N_{cav}$	$N_{dbr}$	$N$	$P_{in}$ (mW)	$L_{tot}$ ( $\mu\text{m}$ )
1	2	44	6	228	94.07
2	5	42	6	241	95.81
3	3	44	6	199	96.03
4	1	46	6	175	96.24
5	6	42	6	219	97.77

**Table 4.1:** Five optimum parameter values for the example considered in the text.

Note also that the required input power already drops 30 mW for an increase in device length of 2  $\mu\text{m}$ . Due to trade-off requirements, several solutions are found which lie very close together.

Additional properties of the best result of table 4.1 are<sup>6</sup>:

$$\begin{aligned} |r_{dbr}|_{\nu_c}^2 &= 0.962 \\ \Delta\nu_{BW} &= 217 \text{ GHz} \end{aligned}$$

<sup>6</sup>The effective modal volume is estimated as  $A_{eff}^m L_{eff}^m$  with  $A_{eff}^m = 0.064 \mu\text{m}^2$  the value of a 500 nm SOI wire.

$$\begin{aligned}
 FSR &= 17.9 THz \\
 Q &= 891 \\
 V_{eff}^m &= 0.113 \mu m^3
 \end{aligned}$$

This result is now verified numerically in figure 4.5. However, because of simulation limitations, the number of periods was reduced to half. The obtained phase shift for  $\lambda = \frac{1}{2}(\lambda_{c,L} + \lambda_{c,NL})$  is  $\Delta\phi_{tot} \approx 1.59$ , which is close to  $\frac{\pi}{2}$ . As can be seen, the phase shift is fairly constant over a large area, however the usable wavelength range ( $|t_{tot}|^2 > 0.9$ ) is only  $\Delta\lambda_s = 0.44$  nm, which is close to the expected value of 0.32 nm.

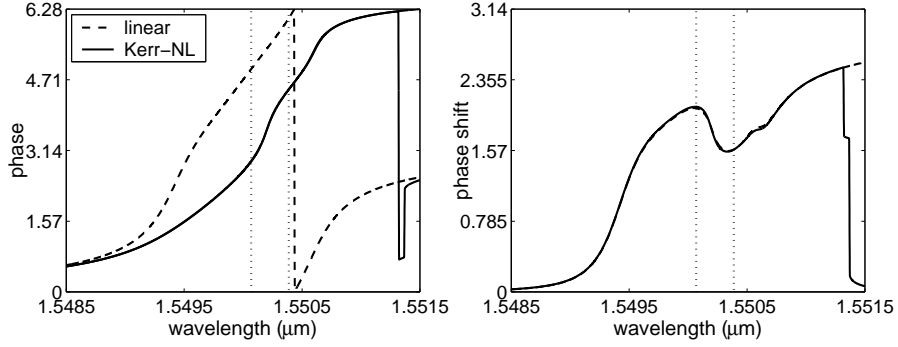


**Figure 4.5:** Numerical calculation of the linear and nonlinear phase relation (left). The region of interest is also shown. The obtained phase shift (right).

From equation (D.33), it follows that the total phase shift  $\Delta\phi_{tot}$  is proportional to both  $\left|\frac{d\phi}{d\nu}\right|_{\nu_c}$  and  $\Delta\nu_c$ . The resonance shift is approximately  $\Delta\lambda_c = 0.46$  nm, which is only about one fourth of the bandwidth. On the other hand,  $\left|\frac{d\phi}{d\nu}\right|_{\nu_c}$  is much steeper than in the absence of resonators. So both parameters contribute in this example. For higher  $P_{in}$  or  $n_2$ , the driving factor of the phase shift will typically be  $\Delta\nu_c$  ( $\Delta\nu_c \approx f_{corr}\Delta\nu_{BW}$ ), while in the case of lower  $n_2$  or  $P_{in}$ ,  $\left|\frac{d\phi}{d\nu}\right|_{\nu_c}$  will be more significant ( $\Delta\nu_c \ll f_{corr}\Delta\nu_{BW}$ ).

The corresponding intensity transmission relation of figure 4.5 is drawn in figure 4.6. As can be seen, the transmission relation deforms heavily in the presence of Kerr-nonlinear behaviour due to the coupling between the different resonator cavities, as discussed in appendix D.2.3. For higher wavelengths, bistable behaviour (see below) starts to occur,

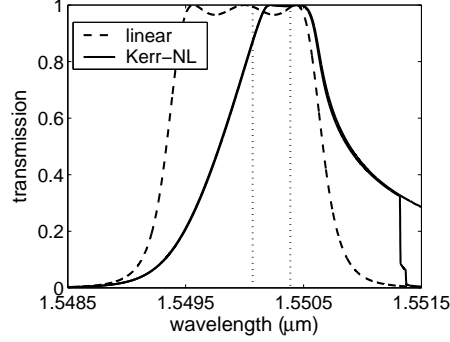


**Figure 4.6:** Numerical calculation of the linear and nonlinear intensity transmission relation. The region of interest is also shown.

which can pose an additional limit on the usable signal bandwidth, in particular for large resonance shifts [100]. In addition, the combination of anomalous group velocity dispersion (GVD) - which occur at the high-wavelength edge of the resonance bandwidth - with a large number of resonator cavities may lead to modulation instability, so that all-optical signal processing is not possible anymore [30, 101].

**'Linear-high and nonlinear-low' all-optical switching** In contrast to the previous application, a resonance frequency shift  $\Delta\nu_c$  which is much larger than the resonance bandwidth  $\Delta\nu_{BW}$  is desired for switching applications. To obtain a high transmission in the linear case, the signal bandwidth must again be centered around the linear resonance frequency  $\nu_c$ . In the nonlinear situation, the high-power data signal will shift the resonance frequency and the nonlinear transmission will become low. This transmission will be lower for higher input power. The minimal transmission contrast  $C$  is then given by

$$C = |t_{tot,L}|^2 - |t_{tot,NL}|^2 \quad (4.7)$$

with  $|t_{tot,L}|^2 = \min(|t_{tot,L}(\nu)|^2)$  and  $|t_{tot,NL}|^2 = \max(|t_{tot,NL}(\nu)|^2)$  for  $\nu \in [\nu_c - \frac{\Delta\nu_s}{2}, \nu_c + \frac{\Delta\nu_s}{2}]$ .

For the example proposed above, this contrast is optimized as function of the input power  $P_{in}$  and energy  $\mathbb{E}_{in}$  in figure 4.7 for a single resonator. From the discussion above, it is already clear that a trade-off between the achievable contrast and the input power of the nonlinear data signal is to be made. Figure 4.7 however shows that rather high powers are required to achieve reasonable transmission contrasts.

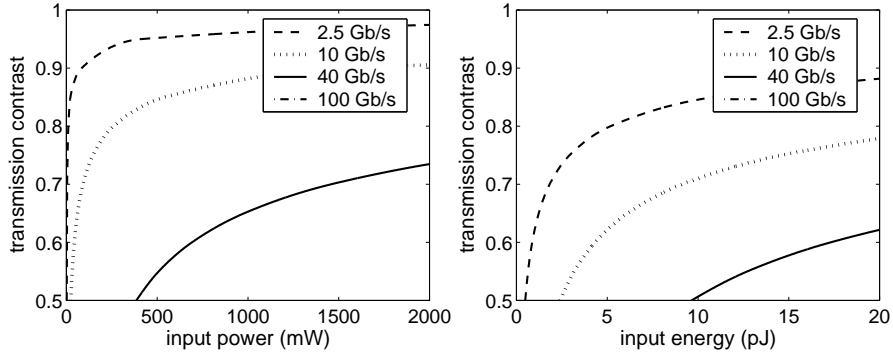


**Figure 4.7:** Minimal transmission contrast  $C$  as function of  $P_{in}$  (left) and  $\mathbb{E}_{in}$  (right) for different signal bandwidths. For these input powers/energies, the transmission contrast for the 100 Gb/s case is lower than 0.5.

A similar effect of the index contrast is observed as in the case of all-optical phase shifting.

Now, consider the case of maximizing the transmission contrast for a signal rate of 40 Gb/s and input powers up to 1000 mW (pulse energies up to 25 pJ). Note that  $P_{in} < 1000$  mW will always result in a lower transmission contrast for the optical resonator, because a lower  $P_{in}$  corresponds to lower resonance shift. The highest contrast is obtained for:

$$\left. \begin{array}{l} N_{cav} = 1 \\ N_{dbr} = 52 \end{array} \right\} C = 0.652$$

Next to the transmission contrast, some additional properties of this resonator structure are:

$$\begin{aligned} |r_{dbr}|_{\nu_c}^2 &= 0.983 \\ \Delta\nu_{BW} &= 103 \text{ GHz} \\ FSR &= 19.5 \text{ THz} \\ Q &= 1881 \\ V_{eff}^m &= 0.104 \mu\text{m}^3 \\ L_{tot} &= 18.1 \mu\text{m} \end{aligned}$$

The transmission contrast is checked numerically in figure 4.8. A transmission contrast of  $C = 0.655$  is obtained over the signal bandwidth, which is in very good agreement with the predicted  $C = 0.652$ .

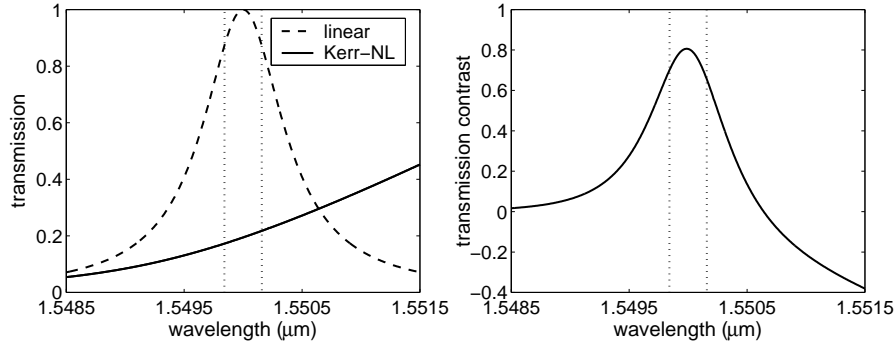


**Figure 4.8:** Numerical calculation of the linear and nonlinear transmission relation (left). The region of interest is also shown. The obtained transmission contrast (right).

Until now, only one period has been taken into account. It is intuitively clear that the contrast will increase for exactly the same parameters by using more resonator periods: the linear transmission  $|t_{tot,L}|^2$  will be higher and the nonlinear transmission  $|t_{tot,NL}|^2$  lower, because the resonance peak becomes more confined for higher  $N$ . This can be seen in figure 4.9: by using the same parameters and two periods instead of one, the transmission contrast is already improved to  $C = 0.826$ .

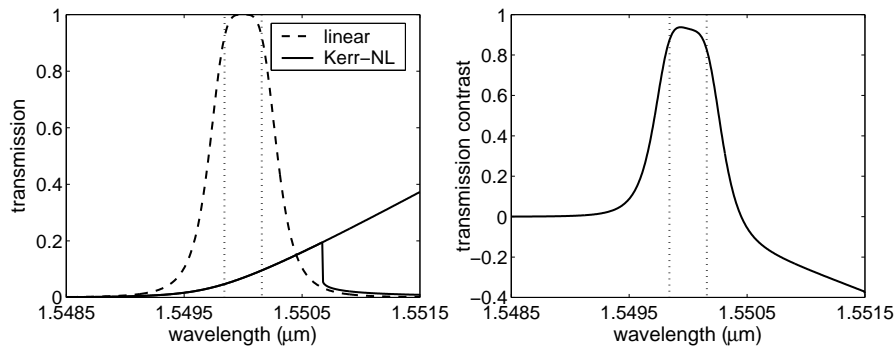


**Figure 4.9:** Numerical calculation of the linear and nonlinear transmission relation for two periods. The region of interest is also shown (left). The obtained transmission contrast (right).

In the extreme case of an infinite number of periods, a contrast of unity is achieved, if  $\Delta\nu_c = \Delta\nu_s + \frac{\Delta\nu_{BW} - \Delta\nu_s}{2} = \frac{\Delta\nu_{BW} + \Delta\nu_s}{2}$ . In the example discussed above, an input power of only  $P_{in} = 95$  mW would be needed for this.

However, in this discussion, one aspect has not yet been mentioned: the output power is not  $|t_{tot}|^2$ , but  $|t_{tot}|^2 P_{in}$ : while  $|t_{tot}|^2$  decreases with increasing input power,  $|t_{tot}|^2 P_{in}$  increases asymptotically (all-optical limiting functionality, figure 4.10).

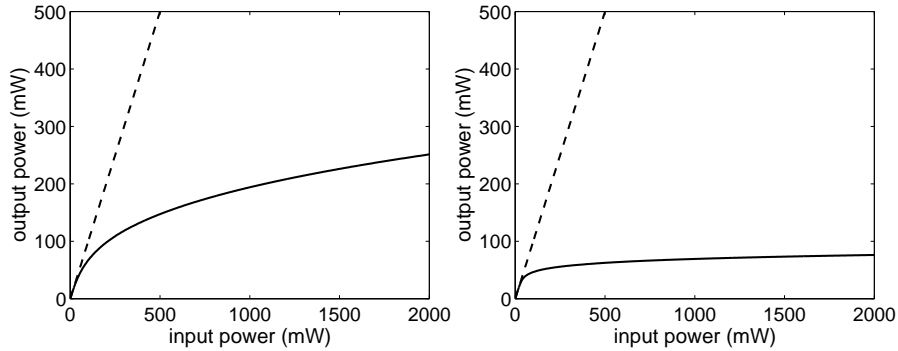


**Figure 4.10:** Output power  $P_{out}$  as function of input power  $P_{in}$  at the resonance frequency  $\nu_c$  for the case of one (left) and two (right) periods. The dotted line represents the case of unity transmission as a reference.

This means that the linear-high transmission state will have a lower output power than the nonlinear-low transmission state<sup>7</sup>.

All-optical linear-high/nonlinear-low switching can nevertheless still be used by adjusting the data processing method [98].

**'Linear-low and 'nonlinear-high' all-optical switching** This type of switching is in many aspects the opposite of the previous type. Since the nonlinear transmission must in this case be as high as possible, the signal bandwidth will be centered around the nonlinear resonance frequency  $\nu'_c$ . The minimal transmission contrast  $C$  is now defined as

$$C = |t_{tot,NL}|^2 - |t_{tot,L}|^2 \quad (4.8)$$

with  $|t_{tot,NL}|^2 = \min(|t_{tot,NL}(\nu)|^2)$  and  $|t_{tot,L}|^2 = \max(|t_{tot,L}(\nu)|^2)$  for  $\nu \in [\nu'_c - \frac{\Delta\nu_s}{2}, \nu'_c + \frac{\Delta\nu_s}{2}]$ .

<sup>7</sup>at least, in the case of small  $N$ . For higher  $N$ , the limiting operation becomes much more complex.

Again, this contrast will be larger for higher input powers. The optimization of the trade-off between contrast and input power/energy is shown in figure 4.11. Like in the previous cases, the use of a higher mirror contrast will significantly reduce the required optical power and energy.

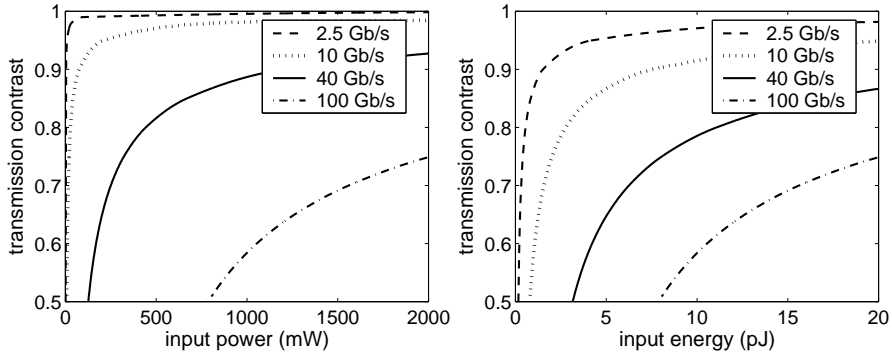


**Figure 4.11:** Minimal transmission contrast  $C$  as function of  $P_{in}$  (left) and  $\mathbb{E}_{in}$  (right) for different signal bandwidths. A resonator of one period is considered.

If we consider the same optimization example as above (maximizing the transmission contrast for a signal rate of 40 Gb/s and input powers up to 1000 mW), the following result is obtained:

$$\left. \begin{array}{l} N_{cav} = 2 \\ N_{dbr} = 48 \end{array} \right\} C = 0.883$$

Additional properties of this resonator structure are:

$$\begin{aligned} |r_{dbr}|_{\nu_c}^2 &= 0.975 \\ \Delta\nu_{BW} &= 143 \text{ GHz} \\ FSR &= 17.8 \text{ THz} \\ Q &= 1358 \\ V_{eff}^m &= 0.113 \mu\text{m}^3 \\ L_{tot} &= 17.1 \mu\text{m} \end{aligned}$$

Numerically, this result is verified in figure 4.12. Now, a transmission contrast of  $C = 0.889$  is obtained, in good agreement with the predicted value of  $C = 0.883$ . Therefore, this figure also shows that in

this particular case, one has actually two stable nonlinear solutions in the region of interest. In general, the solution that will be excited is the one with the lowest transmission ( $|t_{tot,NL}|^2 \approx |t_{tot,L}|^2$ ), because one is coming from  $\pm 0$  mW. Note that this solution is almost coincident with the linear one.

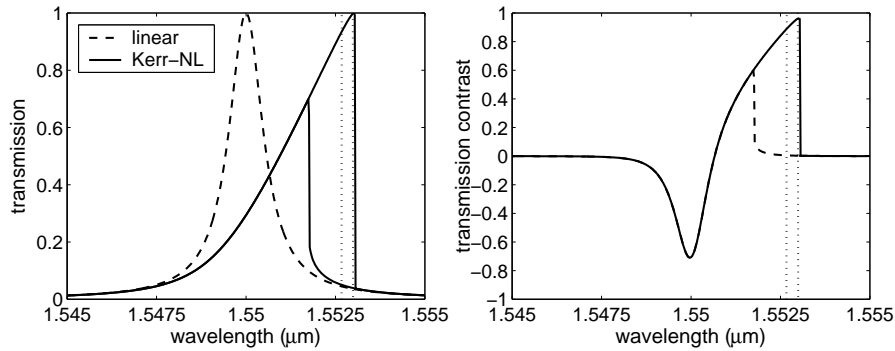


**Figure 4.12:** Numerical calculation of the linear and nonlinear transmission relation (left). The region of interest is also shown. The obtained transmission contrast (right).

A possible way however to overcome this obstacle is using pulses which have a very high power density at the beginning and then drop down to their regular value. In this way, the upper branch is excited and the total pulse energy is still acceptable<sup>8</sup> The main problem however is that this peak power  $P_{peak}$  is typically much larger ( $\gg 10\times$ ) than the regime pulse power  $P_{in}$ . Furthermore, the duration of the peak should be of the order of  $t_{peak} = \frac{1}{\Delta\nu_s}$  for the cavity to respond properly, so that  $t_{pulse} > t_{peak} = \frac{1}{\Delta\nu_s}$  to obtain the same pulse energy in the 'linear' and nonlinear case.

If more than one period is considered, the contrast  $C$  is further increased. This is shown in figure 4.13. However, increasing  $N$  will also increase the power density required at the start of the pulse in order to switch to the upper branch.

<sup>8</sup>Note that in this case, the 'linear' and nonlinear pulses can now have the same power for the off-state as well as for the on-state. The difference between linear and nonlinear regime is simply due to the power peak at the start of the pulse. In this case, there is no difference anymore between  $|t_{tot}|^2$  and  $|t_{tot}|^2 P_{in}$ . Combining this system with set and reset pulses leads to all-optical memory operation [102].

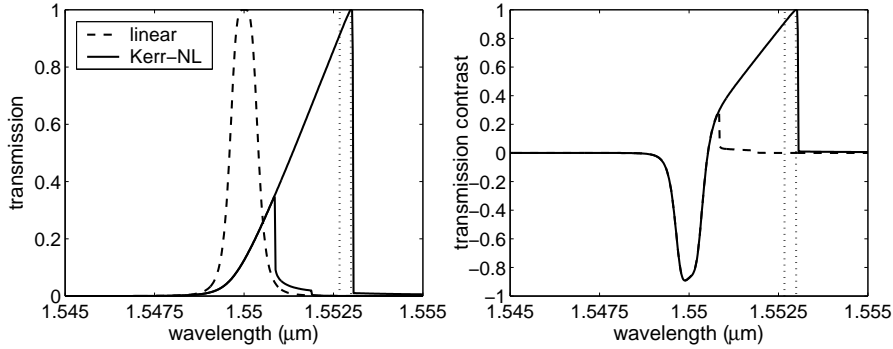


**Figure 4.13:** Numerical calculation of the linear and nonlinear transmission relation for the same resonator with two periods. The region of interest is also shown (left). The obtained transmission contrast (right).

**‘Linear-low and ‘nonlinear-high’ all-optical stable switching** One could wonder what the switching possibilities are without bistable regions. However, an additional constraint is taken into account to avoid bistable operation in the region of interest:  $[\nu_{c,NL} - \frac{\Delta\nu_s}{2}, \nu_{c,NL} + \frac{\Delta\nu_s}{2}] > \nu_{u,bistable}$  in the case of  $n_2 > 0$  and  $[\nu_{c,NL} - \frac{\Delta\nu_s}{2}, \nu_{c,NL} + \frac{\Delta\nu_s}{2}] < \nu_{l,bistable}$  in the case of  $n_2 < 0$  with  $[\nu_{l,bistable}, \nu_{u,bistable}]$  the bistable region.

Optimization of the transmission contrast as function of input power and input energy now leads to figure 4.14. By comparing figures 4.11

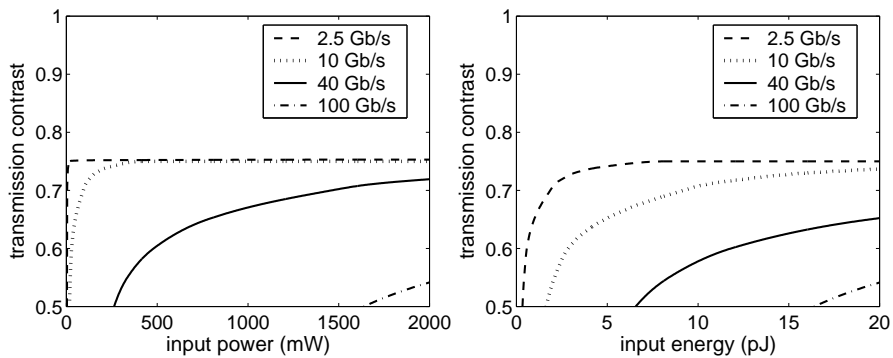


**Figure 4.14:** Minimal transmission contrast  $C$  as function of  $P_{in}$  (left) and  $E_{in}$  (right) for different signal bandwidths. A resonator of one period is considered.

and 4.14, it can be seen that now the obtainable contrast for the same situation is substantially lower. In addition, the maximum achievable contrast is limited and lower than unity.

For the example of maximizing the transmission contrast for a signal rate of 40 Gb/s and input powers up to 1000 mW, the optimum result is not necessarily obtained for  $P_{in} = 1000$  mW, although here it is the case. The other device parameters are:

$$\left. \begin{array}{l} N_{cav} = 1 \\ N_{dbr} = 44 \end{array} \right\} C = 0.683$$

and

$$\begin{aligned} |r_{dbr}|_{\nu_c}^2 &= 0.962 \\ \Delta\nu_{BW} &= 239 \text{ GHz} \\ FSR &= 19.7 \text{ THz} \\ Q &= 810 \\ V_{eff}^m &= 0.103 \mu\text{m}^3 \\ L_{tot} &= 15.4 \mu\text{m} \end{aligned}$$

This result is numerically represented in figure 4.15. A transmission contrast of  $C = 0.676$  is obtained which is in excellent agreement with the predicted value.

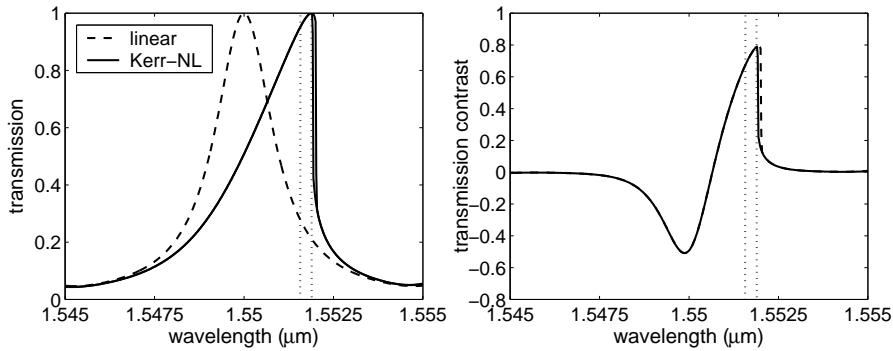


**Figure 4.15:** Numerical calculation of the linear and nonlinear transmission relation (left). The region of interest is also shown. The obtained transmission contrast (right).

If we now consider more than one period, the 'bistable' contrast  $C$  will increase with increasing  $N$ : this is shown in figure 4.16. However,

as indicated in this figure, the stable region will become smaller and therefore the region of interest will shift, resulting in a smaller obtainable 'stable' contrast. Therefore, the case of a single period will provide the best results.

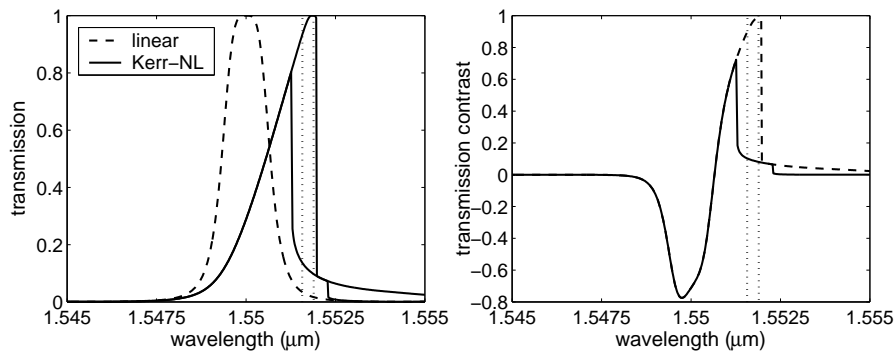


**Figure 4.16:** Numerical calculation of the linear and nonlinear transmission relation for the same resonator with two periods (left). The region of interest is again shown. The obtained transmission contrast (right).

**All-optical 2R regeneration** The quality of an optical data signal can be characterized by means of the Bit Error Rate (*BER*) detected for a certain average power at the receiver end. To obtain a good signal quality at the end, several regeneration stages can be introduced between the sender and the receiver, which clean the signal before the signal degradation becomes too large. The quality of a regeneration step can be investigated by the scheme depicted in figure 4.17 - by comparing the results in the presence and absence of regeneration. A method to approximate these results analytically is discussed in appendix F.

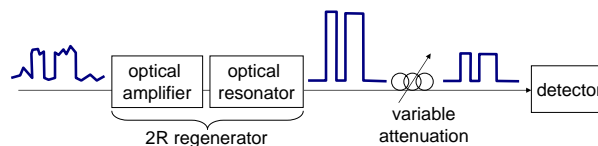


**Figure 4.17:** Set-up for measuring the BER as function of the average received power.

With a Kerr-nonlinear resonator, pulse reshaping is possible for frequencies on the bistable side of the spectrum<sup>9</sup>: this is shown for the cases  $|\nu - \nu_c| = n \frac{\sqrt{3}}{2} \Delta\nu_{BW}$  with  $n = \frac{1}{2}, \frac{3}{4}, 1, \frac{5}{4}$  in figure 4.18. The required decision powers are also shown.

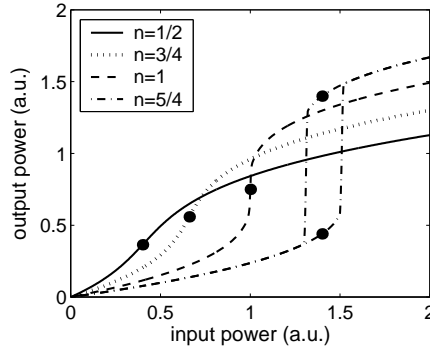


**Figure 4.18:** Input-output power relations at different carrier frequencies. For ease of comparison, rescaling to the decision power for  $|\nu - \nu_c| = \frac{\sqrt{3}}{2} \Delta\nu_{BW}$  has occurred.

For the frequencies  $|\nu - \nu_c| > \frac{\sqrt{3}}{2} \Delta\nu_{BW}$ , bistable solutions can occur, which may result in two problems:

- If the bistable region is very large, it may contain the average '0' and '1' data level so regeneration is not possible.
- If this is not the case, regeneration is possible but at the cost of an additional time offset or jitter<sup>10</sup> due to the presence of a hysteresis curve.

In this work, a small bistable region will be tolerated: the allowed frequency region was taken to be  $|\nu - \nu_c| \leq \frac{5}{4} \frac{\sqrt{3}}{2} \Delta\nu_{BW}$ .

<sup>9</sup>Remember that one only has a single solution for  $\nu > \nu_c - \frac{\sqrt{3}}{2} \Delta\nu_{BW}$  if  $n_2 > 0$  and  $\nu < \nu_c + \frac{\sqrt{3}}{2} \Delta\nu_{BW}$  if  $n_2 < 0$  (appendix D.2).

<sup>10</sup>e.g. in the case of asymmetrically shaped pulses.

To see the regenerative capabilities of a Kerr-nonlinear resonator, two situations of noisy data signals will be studied:

- in the first case, the data signal is specified by an average power of  $P_{av} = 0.1$  mW and extinction ratio  $\frac{P_{1,in}}{P_{0,in}} = 2$ . This corresponds to  $P_{0,in} = 0.067$  mW and  $P_{1,in} = 0.133$  mW. The signal variation  $\sigma$  is assumed to be zero. This data signal is only limited by its extinction ratio which is 3 dB. In this case, the main origin of noise will be the receiver.
- in the second case, the data signal is again assumed to have an average power of  $P_{av} = 0.1$  mW, but with an extinction ratio  $\frac{P_{1,in}}{P_{0,in}} = 8$ . This corresponds to  $P_{0,in} = 0.022$  mW and  $P_{1,in} = 0.178$  mW. The signal variation is now taken to be  $\sigma_{in} = 0.1$  mW. This data signal has a much better extinction ratio of 9 dB, but is subject to severe noise distortion.

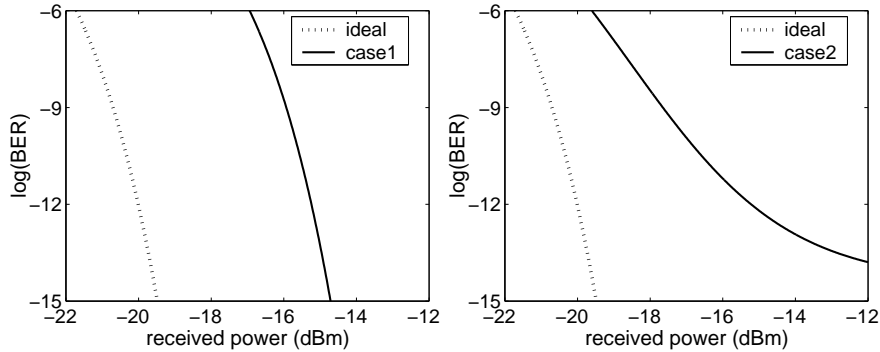


**Figure 4.19:** BER as a function of received power obtained with a perfect data signal and the two imperfect situations (case 1, left; case 2, right) discussed above in the absence of regeneration.

These data signals are now considered in a set-up of figure 4.17 with the following characteristics:

- the amplifier is assumed to have a noise figure  $NF = 3$ . The gain  $G$  can be tuned to the user's will (i.e. optimized later on).
- the receiver has a sensitivity of -20 dBm or 0.01 mW for a Bit Error Rate of  $10^{-12}$ , corresponding to a sigma value of  $\sigma_{rec} = 1.42$   $\mu$ W.

The  $BER$  that can be obtained with this receiver in the case of a perfect data signal, can be calculated from equation (F.2). It is plotted as function of the received power in figure 4.19.

In the two noisy cases presented above, the obtainable  $BER$  in absence of regeneration will be significantly smaller (figure 4.19). Instead of the -20 dBm received average power, both situations require a received power of approximately -15 dBm to obtain a Bit Error Rate of  $10^{-12}$ .

Consider now an optical system that requires a signal quality of  $BER = 10^{-12}$  for a maximum received power of -17 dBm (i.e. a 3 dB power penalty compared to the ideal case). For the first example, the Bit Error Rate for a received power of -17 dBm is only  $BER \approx 10^{-6}$  and in the second case only  $BER \approx 10^{-10}$ . This means that regeneration will be required to meet the objectives.

For a certain signal bandwidth  $\Delta\nu_s$ , we can define a maximum  $BER$  by:

$$\max \left( BER_{start} \Big|_{\nu_s + \frac{\Delta\nu_s}{2}}, BER_{new} \Big|_{\nu_s + \frac{\Delta\nu_s}{2}} \right) \leq BER \leq (BER_{start} + BER_{new}) \Big|_{\nu_s + \frac{\Delta\nu_s}{2}} \quad (4.9)$$

with  $BER_i(\nu)$  the bit error rate calculated at the frequency  $\nu$  (see also appendix F).

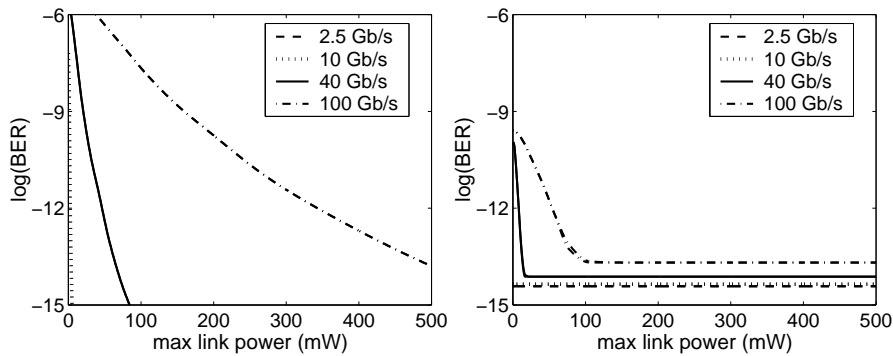


**Figure 4.20:** Obtainable  $BER$  as a function of maximum link power for case 1 (left) and case 2 (right).

If we optimize the bit error rate as a function of maximum link power (i.e. the power entering the optical resonator (figure 4.17), which is the maximum power of the optical link), figure 4.20 is obtained.

Only in the second case, a small difference between  $\max(BER_{start}, BER_{new})$  and  $BER_{start} + BER_{new}$  is visible: due to the assumed noise of the input signal,  $BER_{start}$  is approximately  $10^{-14} - 10^{-15}$ . As a result, this contribution becomes dominant for reshaping curves close to a step function (resulting in  $BER_{new} \ll BER_{start}$ ) and further regeneration is impossible. In the vicinity of  $BER = 10^{-12}$ , this is however not yet the case.

For the specific case of  $BER = 10^{-12}$  and a data rate of 40 Gb/s, the best optimum configuration in the first case is:

$$\begin{aligned} N_{cav} &= 2 \\ N_{dbr} &= 54 \\ P_{av,max} &= 44.45 \text{ mW} \\ \left| \frac{\nu_s - \nu_c}{\Delta\nu_{BW}} \right| &= 0.639 \end{aligned}$$

with

$$\begin{aligned} |r_{dbr}|_{\nu_c}^2 &= 0.987 \\ \Delta\nu_{BW} &= 75.8 \text{ GHz} \\ FSR &= 17.7 \text{ THz} \\ Q &= 2555 \\ V_{eff}^m &= 0.114 \mu\text{m}^3 \\ L_{tot} &= 19.1 \mu\text{m} \end{aligned}$$

and for the second example:

$$\begin{aligned} N_{cav} &= 2 \\ N_{dbr} &= 58 \\ P_{av,max} &= 8.23 \text{ mW} \\ \left| \frac{\nu_s - \nu_c}{\Delta\nu_{BW}} \right| &= 0.304 \end{aligned}$$

with

$$\begin{aligned} |r_{dbr}|_{\nu_c}^2 &= 0.996 \\ \Delta\nu_{BW} &= 49.7 \text{ GHz} \\ FSR &= 17.6 \text{ THz} \\ Q &= 3894 \\ V_{eff}^m &= 0.115 \mu\text{m}^3 \\ L_{tot} &= 20.5 \mu\text{m} \end{aligned}$$

The corresponding reshaping functions are plotted in figure 4.21. The lower and upper average 'regeneration' points  $P'_0 = GP_{0,in} + P_{ASE}$  and  $P'_1 = GP_{1,in} + P_{ASE}$  are also drawn<sup>11</sup> together with the decision power  $P'_d = \frac{P'_0 + P'_1}{2}$ .

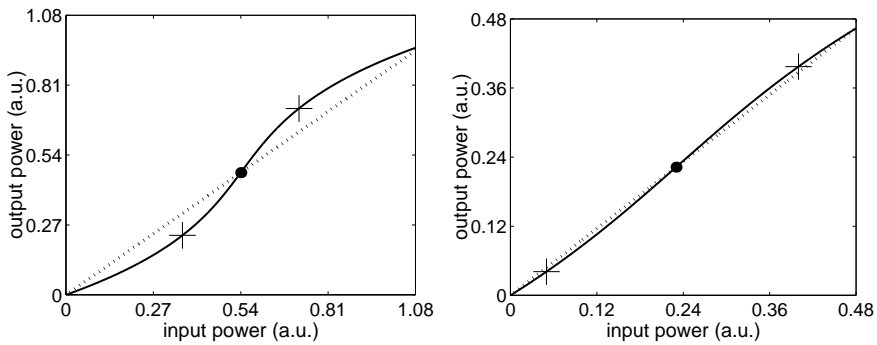


**Figure 4.21:** Required reshaping functions for case 1 (left) and case 2 (right). The decision points and the points where the regeneration takes place are also shown.

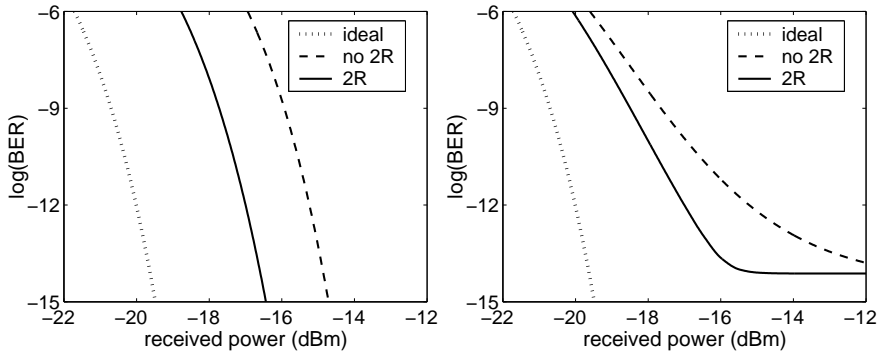


**Figure 4.22:** BER as a function of received power obtained with a perfect data signal and the two imperfect situations (case 1, left; case 2, right) discussed above in the absence and presence of regeneration.

In the first case, the regeneration is clearly a result of extinction ratio improvement. The obtained noise reduction on the other hand is

<sup>11</sup>The figure is again rescaled to the decision power for  $|\nu - \nu_c| = \frac{\sqrt{3}}{2} \Delta\nu_{BW}$

approximately zero  $\left( \left. \frac{dP_{reg,out}}{dP_{reg,in}} \right|_{P'_0} \approx \frac{dP_{reg,out}}{dP_{reg,in}} \right|_{P'_1} \approx 1 \right)$ . As the original signal was assumed to be noiseless, this would not have contributed.

In this second case, the regeneration is both the result of extinction ratio improvement and noise reduction:  $\left. \frac{dP_{reg,out}}{dP_{reg,in}} \right|_{P'_0} \approx \frac{dP_{reg,out}}{dP_{reg,in}} \right|_{P'_1} \approx 0.87$ . Both effects are small (indeed the reshaping curve is close to linear), but together they are sufficient to obtain the required Bit Error Rate of  $BER = 10^{-12}$ . The corresponding  $BER$  as function of the average received power is plotted in figure 4.22.

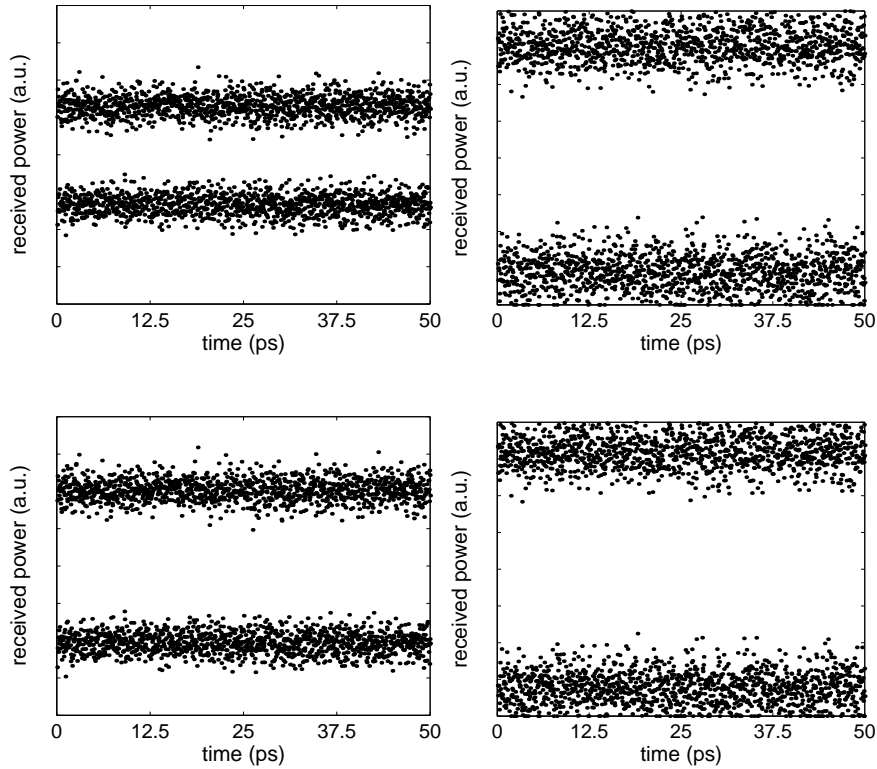


**Figure 4.23:** Visual representation by means of 'eye' diagrams of case 1 (left) and case 2 (right) without (top) and with (bottom) regeneration.

To visualize this regeneration effect on a time-like basis, an 'eye' diagram of the detected signal in the absence and presence of regeneration is shown in figure 4.23. Transient effects are not included as they

cannot be accurately predicted by a frequency approach. For the second example, the improvement is hard to see (which is in agreement with the almost linear reshaping curve in this case): the improvement can only be seen by looking closely to the most noisy data points on the inside of the 'eye'.

#### 4.2.1.2 Pump-probe operation

In contrast to section 3.2.1, the transmission spectrum of a resonator structure has several resonance peaks which are equally spaced as discussed in appendix C.5. As a result, one resonance can be used for the pump signal, while all other resonances can hold data signals. By splitting the data signal into different parallel signals, larger data flows can be processed compared to the single signal case. Additionally, the processing occurs at a lower bitrate which can be beneficial for possible surrounding electronics.

The total data bandwidth  $\Delta\nu_{s,total}$  that can be processed is determined by both the data bandwidth per signal  $\Delta\nu_s$  and the free spectral range  $FSR$ : in a frequency range of  $\Delta\nu_{range}$ , the total bandwidth is given by,

$$\Delta\nu_{s,total} = \frac{\Delta\nu_{range}}{FSR} \Delta\nu_s \quad (4.10)$$

This means that the information density [103] is equal to  $\frac{\Delta\nu_s}{FSR}$  or equivalently the frequency amount necessary for one bit information per second  $\Delta\nu_{bit/s}$  is given by

$$\Delta\nu_{bit/s} = \frac{FSR}{\Delta\nu_s} \quad (4.11)$$

As mentioned in section 3.2.1, the refractive index change felt by a probe signal is twice as large as the change felt by the pump. For the corresponding resonance shift for a probe signal  $\Delta\nu_{c,probe}$ , however, one has for a one-dimensional optical resonator:

$$\Delta\nu_{c,probe} \neq 2\Delta\nu_{c,pump} \quad (4.12)$$

with  $\Delta\nu_{c,pump}$  the frequency shift of the pump resonance. This can be understood as follows: at resonance, the pump beam produces an almost standing wave inside the resonator cavity (section C.6). This electric field profile  $E_{cav} \cos(\frac{\omega}{c}nz)$  with  $z$  the propagation axis and  $E_{cav}$

gives rise to a refractive index change given by  $n_2 |E_{cav}|^2 \cos^2(\frac{\omega}{c}nz)$  due to the bound-electronic Kerr effect. As a result of this standing wave pattern, the forward propagating field inside the cavity changes to

$$E_{cav,f}(z) = E_{cav,f,L}(z) \exp\left(-j \frac{2\pi\nu}{c} \frac{3}{4} n_2 |E_{cav}|^2 z\right) \quad (4.13)$$

and the backward propagating field is given by

$$E_{cav,b}(z) = E_{cav,b,L}(z) \exp\left(j \frac{2\pi\nu}{c} \frac{3}{4} n_2 |E_{cav}|^2 z\right) \quad (4.14)$$

with  $E_{cav,f,L}$  and  $E_{cav,b,L}$  the forward and backward propagating linear electric field components inside the cavity. If this effect would only be caused by the 'average' refractive index change  $n_2 |E_{cav}|^2 \langle \cos^2(\frac{\omega}{c}nz) \rangle = \frac{1}{2} n_2 |E_{cav}|^2$  due to the Kerr effect, the field components inside the cavity would be given by

$$E_{cav,f}(z) = E_{cav,f,L}(z) \exp\left(-j \frac{2\pi\nu}{c} \frac{1}{2} n_2 |E_{p,cav}|^2 z\right) \quad (4.15)$$

and the backward propagating field is given by

$$E_{cav,b}(z) = E_{cav,b,L}(z) \exp\left(j \frac{2\pi\nu}{c} \frac{1}{2} n_2 |E_{p,cav}|^2 z\right) \quad (4.16)$$

So the propagation effect and therefore the resonance shift is not only caused by an average change in the refractive index, but also enhanced by the cosine field profile.

For frequencies far from the pump frequency (which is the case if  $FSR \gg \Delta\nu_s$ ), this corrugation will not be in phase with the frequency of the incoming probe field and thus not work constructively. As a result, only the average effect remains, resulting in equations (4.15) and (4.16). As a result, the frequency shift of a probe resonance is a factor  $\frac{2}{3}$  smaller than predicted by equation (4.12) and given by,

$$\Delta\nu_{c,probe} = \frac{4}{3} \Delta\nu_{c,pump} \quad (4.17)$$

Despite this difference, possible functionalities in the pump-probe case will also be based on the shift of the resonance frequency, leading to similar applications in single-signal operation. For comparison, the discussion will be limited to:

- All-optical phase shifting
- All-optical switching with two possibilities:
  - Total transmission in the linear case, which is related to all-optical limiting
  - Total transmission in the nonlinear case, which is linked to all-optical bistability.

**All-optical phase shifting** To evaluate different set-ups in a pump-probe environment, we will compare configurations with the same information density  $\frac{1}{\Delta\nu_{bit/s}}$  or the same bandwidth per bit per second  $\Delta\nu_{bit/s}$ , i.e.

$$\frac{FSR}{\Delta\nu_s} = \text{constant} \quad (4.18)$$

This is in fact an extra degree of freedom compared to single-signal case, as it is now also possible to optimize the amount of data per channel  $\Delta\nu_s$  while the total bandwidth is constant.

In the light of equation (4.17), condition (4.6) must be changed to:

$$\Delta\nu_s = f_{corr}\Delta\nu_{BW} - \Delta\nu_{c,probe} \quad (4.19)$$

In this way, the data signals have total transmission in both the linear and nonlinear case, while the pump signal is able to interact fully with the cavity (i.e. by also having unity transmission).

Due to the additional constraint (4.18), a trade-off between input power, device length, signal bandwidth and also free spectral range will now have to be made.

For the example considered above with  $\Delta\nu_{bit/s}$  taken to be 20 Hz/(b/s), the optimum results are plotted in figure 4.24. Depending on the specific input power or energy, either a 40 Gb/s or 100 Gb/s signal provides the best results. The optimum results are now only about a factor 25-100 better than the simple wire case, which is much lower than in the single-signal case. Note that the pump-probe case behaves very differently from the single-signal set-up: in the latter, optimum results were obtained for very small signal bandwidth, which is due the larger resonator enhancements in these cases. However for a fixed  $\Delta\nu_{bit/s}$ , the restraints for  $FSR$  cause a new trade-off, which results in lower improvements compared to the single-signal case. Furthermore, the optimum results are now obtained for the larger signal bandwidth.

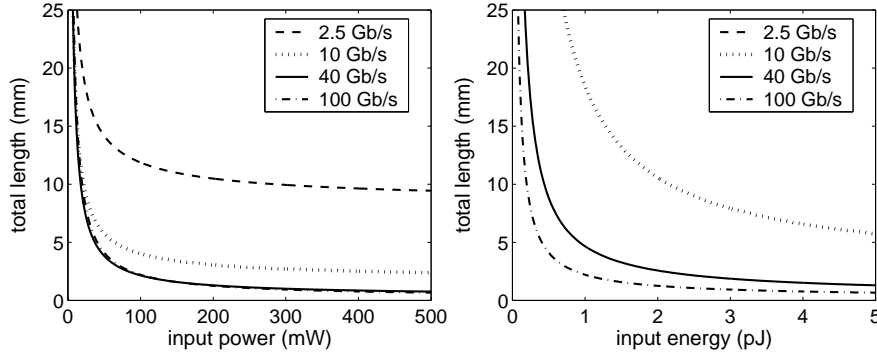


**Figure 4.24:** Trade-off between  $L_{tot}$  and  $P_{in}$  (left) and  $\mathbb{E}_{in}$  (right) for different signal bandwidths.

In figure 4.25, the example above is recalculated with other index contrasts for a signal rate of 40 Gb/s. In contrast to the single-signal case, the impact of index contrasts is close to negligible. As will be seen later, this is because the optimum configuration now consists of large cavities (to reduce the  $FSR$ ).

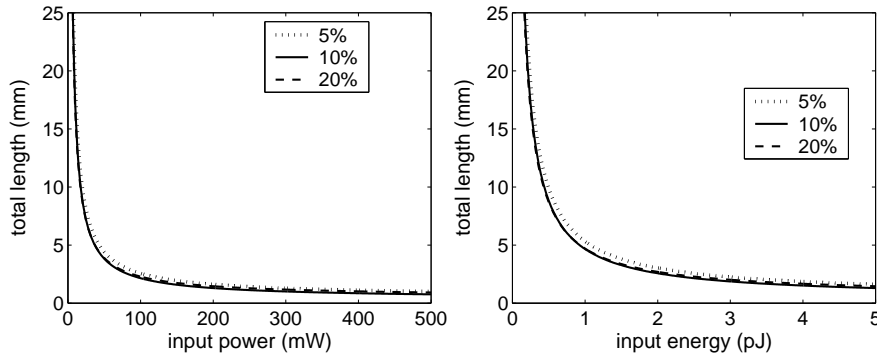


**Figure 4.25:** Influence of index contrast on the trade-off  $L_{tot}$  versus  $P_{in}$  (left) and  $\mathbb{E}_{in}$  (right) for 40 Gb/s.

The impact of  $\Delta\nu_{bit/s}$  is shown in figure 4.26: in contrast to the index contrast, the effect of information density is not negligible. The larger the frequency space available per bit per second  $\Delta\nu_{bit/s}$ , the larger the improvement. This is because for the same bandwidth, the free spectral range is larger (equation (4.18)) and thus obtainable improvement,

because the mirrors are stronger. For very large  $\Delta\nu_{bit/s}$ , this improvement will even be larger than the single-signal case, due to the fact that the probe resonance shift  $\Delta\nu_{c,probe}$  is factor  $\frac{4}{3}$  larger than the pump resonance shift  $\Delta\nu_{c,pump}$ .

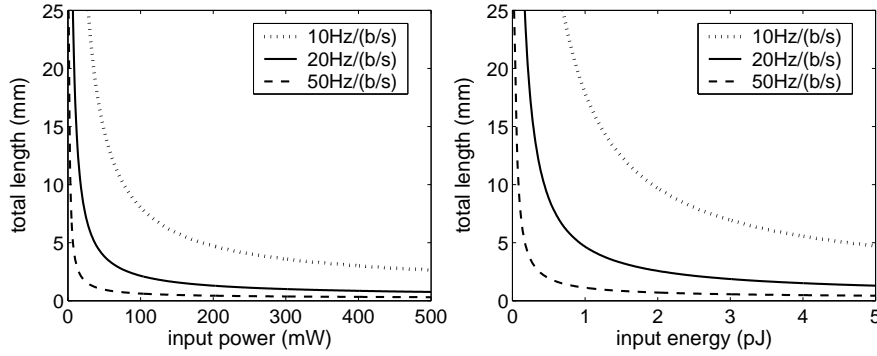


**Figure 4.26:** Influence of  $\Delta\nu_{bit/s}$  on the trade-off  $L_{tot}$  versus  $P_{in}$  (left) and  $\mathbb{E}_{in}$  (right) for 40 Gb/s.

We would now like to minimize the device length for a signal rate of 40 Gb/s and input powers up to 250 mW (pulse energies up to 6.25 pJ). Note that due to the discrete character of both  $N_{dbr}$  and  $N_{cav}$ , the condition  $\Delta\nu_{bit/s} = 20$  Hz/(b/s) can never exactly be met for a given index contrast. Therefore, this condition was relaxed to  $\Delta\nu_{bit/s} = 20$  Hz/(b/s)  $\pm 1\%$ . The results are shown in table 4.2.

	$N_{dbr}$	$N_{cav}$	$N$	$P_{in}$ (mW)	$L_{tot}$ ( $\mu\text{m}$ )
1	22	233	17	178.44	1415.60
2	22	234	17	177.69	1421.14
3	22	235	17	176.95	1426.67
4	22	236	17	176.21	1432.21
5	22	237	18	165.73	1522.32

**Table 4.2:** Best parameter values to minimize the device length for the considered example.

The values of  $N_{cav}$  are now indeed much larger than one, which is as already mentioned above, due to the extra  $FSR$  condition. Next to the total length, other interesting properties of the optimized structure

are:

$$\begin{aligned} |r_{dbr}|_{\nu_c}^2 &= 0.673 \\ \Delta\nu_{BW} &= 99 \text{ GHz} \\ FSR &= 805 \text{ GHz} \\ Q &= 3894 \\ V_{eff}^m &= 2.514 \mu\text{m}^3 \end{aligned}$$

The optimum result of table 4.2 is numerically checked in figure 4.27. In this figure, the probe phase relation is shown for a pump signal at wavelength  $\lambda_{pump} = 1.550028 \mu\text{m}$ . Note that the nonlinear phase rela-

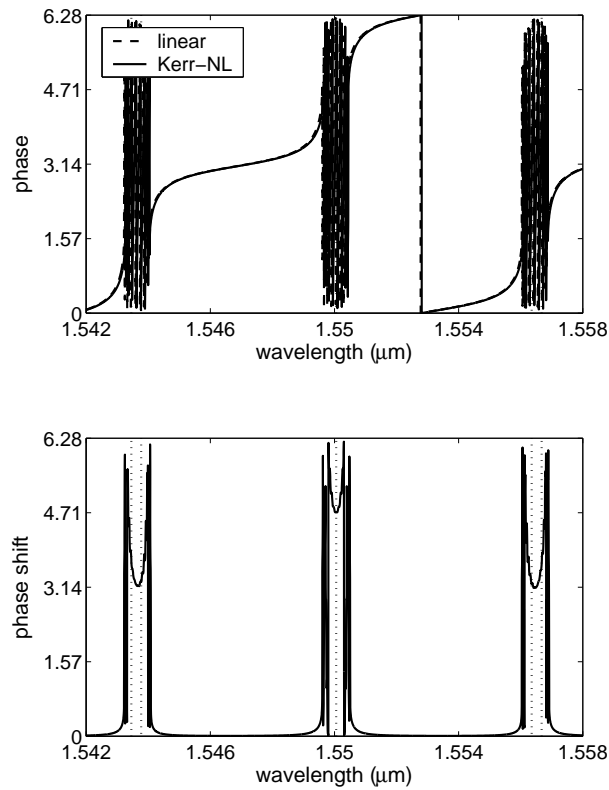


**Figure 4.27:** Numerical calculation of the linear and nonlinear phase relation (left). The obtained phase shift (right). The position of the pump signal at  $\lambda_{pump} = 1.550028 \mu\text{m}$  and the bandwidth region of the two nearest probe signals are also shown.

tion is not asymmetrical as it was in the case of a single signal. This

is because now a linear probe relation is plotted for a pump signal at a fixed frequency - in contrast to the single-signal figures in which the nonlinear calculation is not performed for fixed frequency.

A phase shift of approximately 3.19 is obtained, which is close to  $\pi$ . As can be seen, the phase shift is more or less constant over the probe bandwidth regions.

The pump resonance shift (felt by the pump itself) is equal to 0.053 nm, which is in good agreement with  $\Delta\lambda_{c,pump} \approx 0.055$  nm obtained from equation (D.46). Note that the resonance shift at the pump resonance (but felt by a probe) is indeed approximately a factor  $\frac{2}{3}$  larger than that of the nearby probe resonances and twice as large as the shift felt by the pump.

The corresponding intensity transmission relation of figure 4.27 is drawn in figure 4.28. Due to condition (4.19), both the pump and the probe signals are indeed located in frequency regions with high transmission. The obtained simulation results thus fully agree with the analytically optimized specifications.

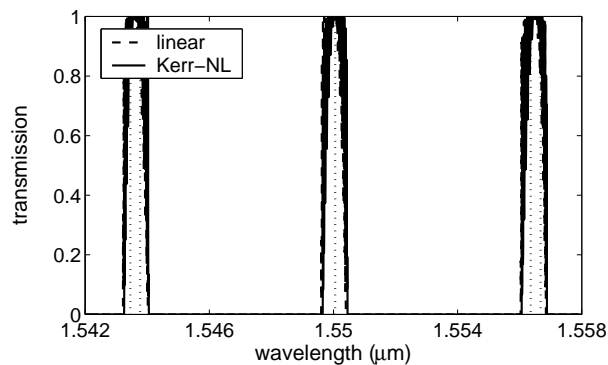


**Figure 4.28:** Numerical calculation of the linear and nonlinear intensity transmission relation.

**All-optical stable switching** While a separate treatment of the two switching types is necessary in the single-signal setup, both can be treated in one go in the pump-probe case. This is because we are now interested in the transmissivity of a linear data signal for a pump at a certain fixed position, instead of in a fully nonlinear transmission curve.

To obtain a large resonance shift, the nonlinear pump signal should always be placed on the nonlinear resonance frequency  $\nu_c + \Delta\nu_{c,pump}$ .

The position of the probe signals will then result in either a 'linear-high and nonlinear-low' transmission or 'linear-low and nonlinear-high' transmission. The minimal transmission contrast  $C$  observed by the probe signals is again given by,

$$C = |t_{tot,L}|^2 - |t_{tot,NL}|^2 \quad (4.20)$$

in the 'linear-high and nonlinear-low' transmission case with  $|t_{tot,L}|^2 = \min(|t_{tot,L}(\nu)|^2)$  and  $|t_{tot,NL}|^2 = \max(|t_{tot,NL}(\nu)|^2)$  for  $\nu \in [\nu_{c,L} - \frac{\Delta\nu_s}{2}, \nu_{c,L} + \frac{\Delta\nu_s}{2}]$  and

$$C = |t_{tot,NL}|^2 - |t_{tot,L}|^2 \quad (4.21)$$

in the 'linear-low and nonlinear-high' transmission case, with  $|t_{tot,L}|^2 = \max(|t_{tot,L}(\nu)|^2)$  and  $|t_{tot,NL}|^2 = \min(|t_{tot,NL}(\nu)|^2)$  for  $\nu \in [\nu_{c,NL} - \frac{\Delta\nu_s}{2}, \nu_{c,NL} + \frac{\Delta\nu_s}{2}]$ . However, as mentioned above, due to the symmetry of the probe transmission spectrum, both are in fact the same.

Optimization of the transmission contrast for the situation depicted above leads to figure 4.29 using a structure with a single period for stability reasons.

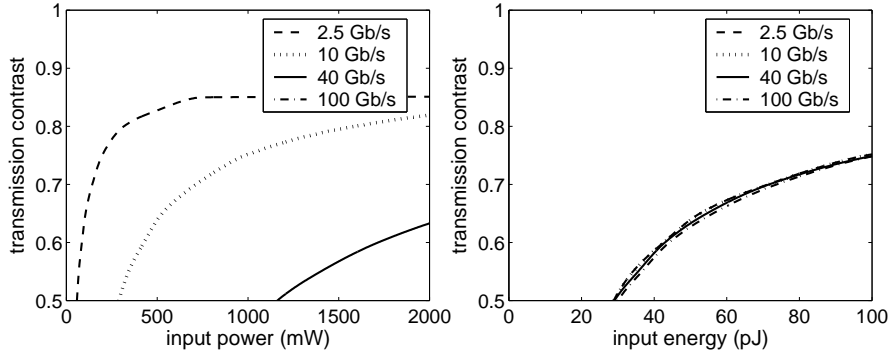


**Figure 4.29:** Minimal transmission contrast  $C$  as function of  $P_{in}$  (left) and  $E_{in}$  (right) for different signal bandwidths. A resonator of one period is considered. For these input powers, the transmission contrast for the 100 Gb/s case is lower than 0.5.

Due to stability considerations (like in figure 4.15), the minimum transmission contrast is limited to  $\approx 85\%$ . As can be seen, the largest contrasts for fixed power are obtained for the smallest data bandwidth,

while in terms of energy, approximately the same results are obtained for different  $\Delta\nu_s$ . The impact of the *FSR* condition is thus quite different in the case of all-optical switching compared to the all-optical phase shifting functionality.

Again, the impact of the index contrast of the mirror sections is close to negligible, while the effect of the frequency space per bit per second  $\Delta\nu_{bit/s}$  is very significant.

Using the relaxed condition  $\Delta\nu_{bit/s} = 20 \text{ Hz/(b/s)} \pm 1\%$ , the highest transmission contrast for  $P_{in} < 1000 \text{ mW}$  and a bitrate of  $40 \text{ Gb/s}$  is determined by:

$$\left. \begin{array}{l} N_{cav} = 232 \\ N_{dbr} = 28 \end{array} \right\} C = 0.453$$

with

$$\begin{aligned} |r_{dbr}|_{\nu_c}^2 &= 0.811 \\ \Delta\nu_{BW} &= 39.2 \text{ GHz} \\ FSR &= 806 \text{ THz} \\ Q &= 3626 \\ V_{eff}^m &= 2.512 \mu\text{m}^3 \\ L_{tot} &= 85.3 \mu\text{m} \end{aligned}$$

The values of  $N_{cav}$  are again much larger than unity due to the extra *FSR* condition. As a result, the obtainable transmission contrast  $C$  is much smaller than in the single-signal case for the same signal bandwidth and power level.

This result is now checked numerically in figure 4.30 for both the 'linear-high and nonlinear-low' and 'linear-low and nonlinear-high' transmission case. In this figure, the probe transmission relation is shown for a pump signal at wavelength  $\lambda_{pump} = 1.550339 \mu\text{m}$ . The transmissivity felt by the pump signal is only  $|t(\lambda_{pump})|^2 \approx 0.767$  because of stability issues (figure 4.15). A minimum transmission contrast of about 0.452 is obtained in both cases, which is close to the predicted 0.453. The resonance shift of the pump signal is equal to 0.582 nm, again in good agreement with equation (D.46):  $\Delta\lambda_{c,pump} = 0.585 \text{ nm}$ . Again, the resonance shift at the pump resonance felt by a probe is approximately a factor  $\frac{2}{3}$  larger than that of the nearby probe resonances and twice as large as the shift felt by the pump.

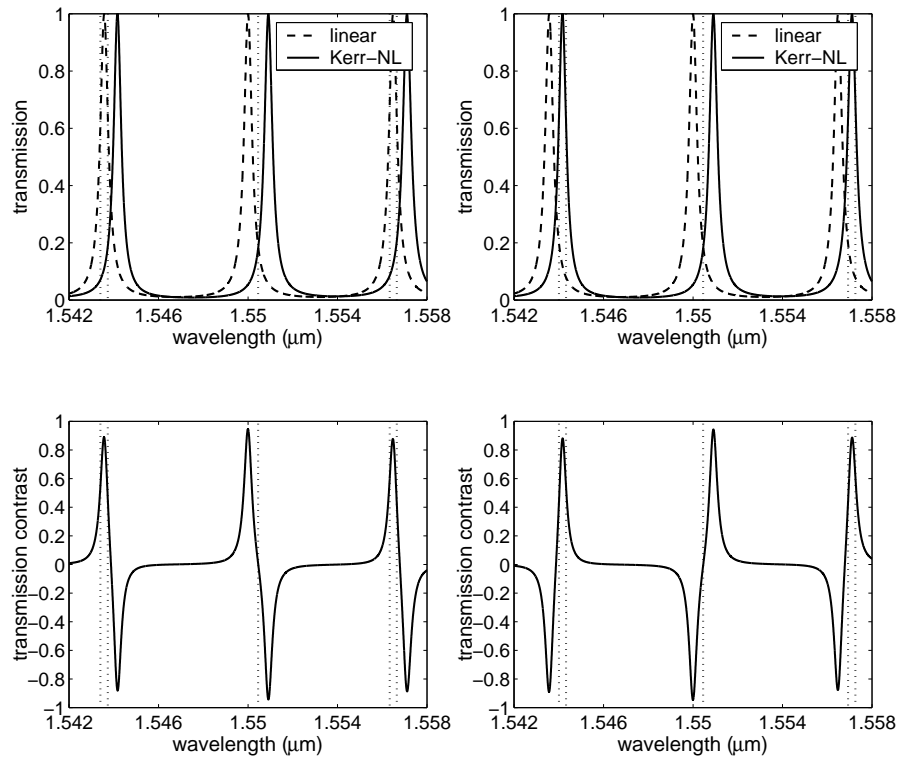


**Figure 4.30:** Numerical calculation (top) of the linear and nonlinear transmission relation for the 'linear-high and nonlinear-low' transmission case (left) and the 'linear-low and nonlinear-high' transmission case (right). The obtained transmission contrast (bottom). The position of the pump signal at  $\lambda_{pump} = 1.550339 \mu\text{m}$  and the bandwidth region of the two nearest probe signals are also shown.

### 4.2.2 Two-photon absorption effect

In contrast to the bound-electronic Kerr effect, the possible applications of two-photon absorption in optical resonators are the same as in the waveguide case.

#### 4.2.2.1 Single-signal operation

The application of two-photon absorption in single-signal operation is very similar to 'linear-high and nonlinear-low' all-optical switching in a Kerr-nonlinear resonator.

If the minimal transmission contrast  $C$  is defined as

$$C = |t_{tot,L}|^2 - |t_{tot,NL}|^2 \quad (4.22)$$

with  $|t_{tot,L}|^2 = \min(|t_{tot,L}(\nu)|^2)$  and  $|t_{tot,NL}|^2 = \max(|t_{tot,NL}(\nu)|^2)$  for  $\nu \in [\nu_c - \frac{\Delta\nu_s}{2}, \nu_c + \frac{\Delta\nu_s}{2}]$ , an optimum contrast as plotted in figure 4.31 is now obtained for a single resonator.

Compared to using waveguides (chapter 3), this corresponds to device length improvements of the order of 10000, like in the case of Kerr-nonlinear all-optical phase shifting. In addition, compared to figure 4.7, the results are slightly worse, although the results of Dinu et al. [32] were used which indicate two-photon absorption as dominant effect.

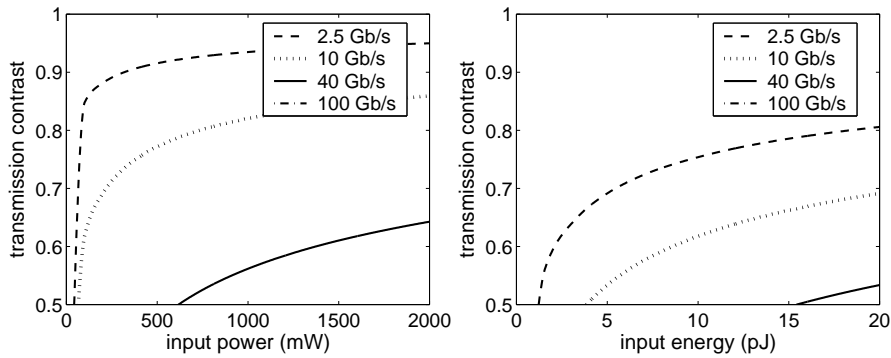


**Figure 4.31:** Minimal transmission contrast  $C$  as function of  $P_{in}$  (left) and  $\mathbb{E}_{in}$  (right) for different signal bandwidths. For these input powers/energies, the transmission contrast for the 100 Gb/s case is lower than 0.5.

The effect of the index contrast of the mirror sections is indicated in figure 4.32. Like for Kerr-nonlinear single-signal applications, the impact of this contrast is very important.

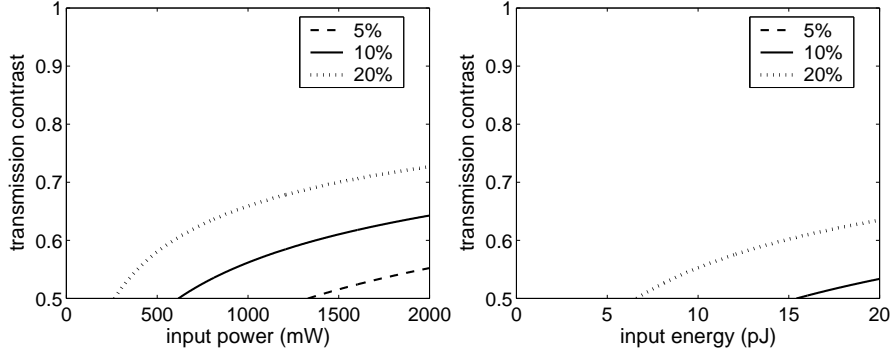


**Figure 4.32:** Influence of index contrast on the optimum transmission contrast for 40 Gb/s. For these input energies, the transmission contrast for the 5% case is lower than 0.5.

Maximizing the transmission contrast for a signal rate of 40 Gb/s and input powers up to 1000 mW (pulse energies up to 25 pJ) now leads to the following result:

$$\left. \begin{array}{l} N_{cav} = 1 \\ N_{dbr} = 54 \end{array} \right\} C = 0.560$$

Compared to section 4.2.1.1, the obtained contrast is about 15% worse. Additional properties of the optimum resonator structure are:

$$\begin{aligned} |r_{dbr}|_{\nu_c}^2 &= 0.986 \\ \Delta\nu_{BW} &= 83 \text{ GHz} \\ FSR &= 19.5 \text{ THz} \\ Q &= 2323 \\ V_{eff}^m &= 0.104 \mu\text{m}^3 \\ L_{tot} &= 18.8 \mu\text{m} \end{aligned}$$

The transmission contrast is checked numerically in figure 4.33. A transmission contrast of  $C = 0.553$  is obtained, which is in good agreement with the predicted  $C = 0.560$ .

This contrast will be further increased by using more periods: in the case of two periods, one already obtains  $C = 0.740$  (figure 4.34). In contrast to the Kerr effect, no issues with bistability arise now, so that higher contrasts than plotted in figure 4.31 are in fact possible, however at the cost of device length.

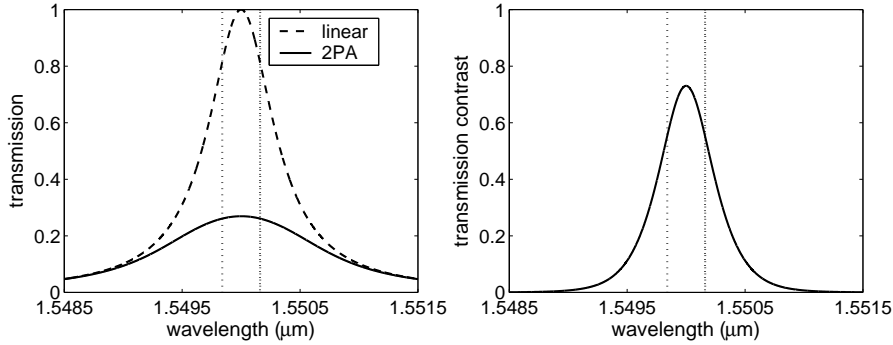


**Figure 4.33:** Numerical calculation of the linear and nonlinear transmission relation. The region of interest is also shown (left). The obtained transmission contrast (right).

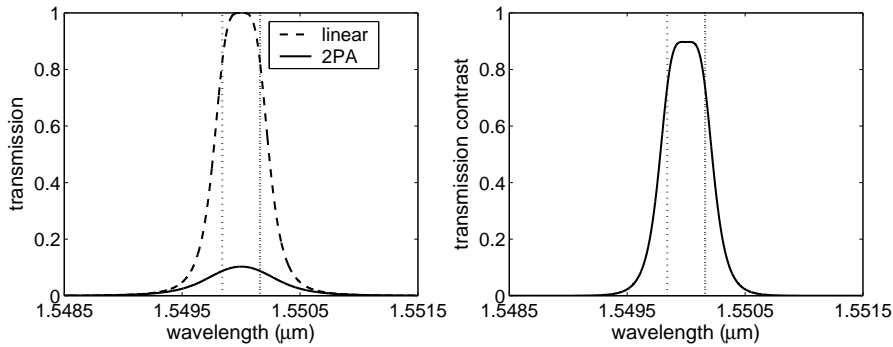


**Figure 4.34:** Numerical calculation of the linear and nonlinear transmission relation for two periods. The region of interest is also shown (left). The obtained transmission contrast (right).

#### 4.2.2.2 Pump-probe operation

Also in this configuration, the application of two-photon absorption is very similar to the 'linear-high and nonlinear-low' all-optical switching in a Kerr-nonlinear resonator.

Like in the Kerr-nonlinear pump-probe case, the theory of appendix E needs some adjustments. For frequencies far from the pump frequency (which is the case if  $FSR \gg \Delta\nu_s$ ), equation (E.12) has to be

replaced by

$$1 - B_{tot}^2(\nu'_c) \approx -\frac{4}{3} |t_{tot,NL,pump}(\nu'_c)|^2 |t_{tot,NL,probe}(\nu'_c)|^2 \frac{c}{\pi \nu'_c} \frac{\beta}{n_2} \frac{\Delta\nu_{c,lossless}}{\Delta\nu_{BW,lossless}} \quad (4.23)$$

Note the similarity with equation (3.12) and section 4.2.1.2. For frequencies around  $\nu_c$ , the factor  $\frac{4}{3}$  is to be replaced with 2 as can be expected.

If now a minimal transmission contrast  $C$  is defined as

$$C = |t_{tot,L}|^2 - |t_{tot,NL}|^2 \quad (4.24)$$

with  $|t_{tot,L}|^2 = \min(|t_{tot,L}(\nu)|^2)$  and  $|t_{tot,NL}|^2 = \max(|t_{tot,NL}(\nu)|^2)$  for  $\nu \in [\nu_c - \frac{\Delta\nu_s}{2}, \nu_c + \frac{\Delta\nu_s}{2}]$ , the optimum transmission contrasts of figure 4.35 are obtained for the single resonator case.  $\Delta\nu_{bit/s}$  was taken to be 20 Hz/(b/s). Similar to the Kerr effect, an improvement of a factor 25-100 in device length is obtained by using optical resonators instead of waveguides. Like for Kerr-based all-optical switching, the obtained transmission contrast is almost independent of the individual signal bandwidth in terms of pulse energy.

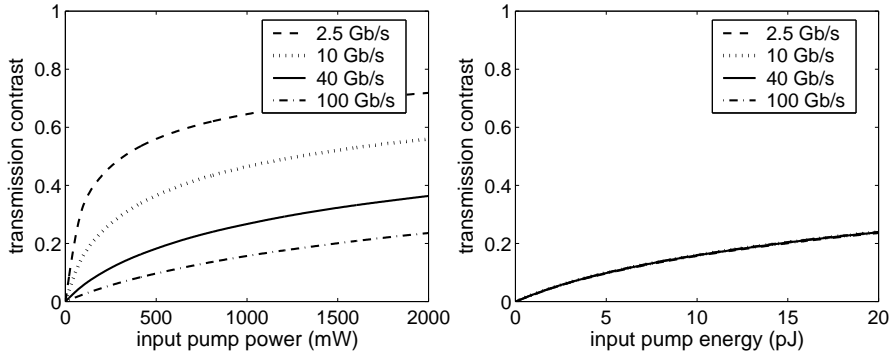


**Figure 4.35:** Minimal transmission contrast  $C$  as function of  $P_{in}$  (left) and  $\mathbb{E}_{in}$  (right) for different signal bandwidths.

The impact of  $\Delta\nu_{bit/s}$  is shown in figure 4.36. Like in the Kerr-nonlinear pump-probe configurations, the effect of information density is quite severe.

If the transmission contrast is optimized for a signal rate of 40 Gb/s and input powers up to 1000 mW (pulse energies up to 25 pJ), we obtain

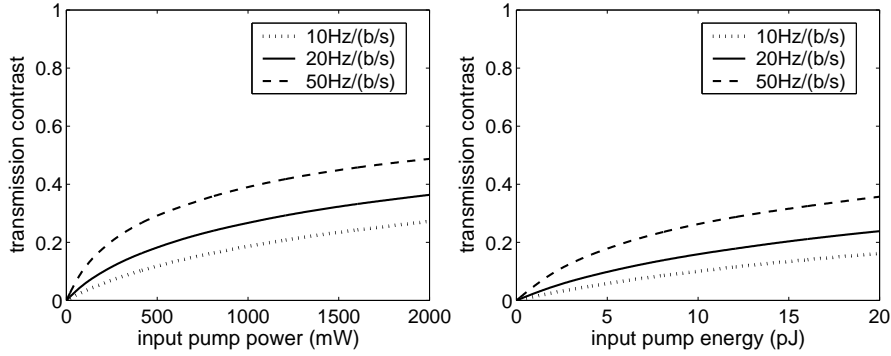


**Figure 4.36:** Influence of  $\Delta\nu_{bit/s}$  on the trade-off  $L_{tot}$  versus  $P_{in}$  (left) and  $\mathbb{E}_{in}$  (right) for 40 Gb/s.

the following configuration:

$$\left. \begin{array}{l} N_{cav} = 232 \\ N_{dbr} = 28 \end{array} \right\} C = 0.265$$

This contrast is about half the contrast obtained in section 4.2.1.1. Note also that exactly the same optimum structure is obtained. Additional properties of this resonator structure are:

$$\begin{aligned} |r_{dbr}|_{\nu_c}^2 &= 0.811 \\ \Delta\nu_{BW} &= 39.2 \text{ GHz} \\ FSR &= 806 \text{ THz} \\ Q &= 3626 \\ V_{eff}^m &= 2.512 \mu\text{m}^3 \\ L_{tot} &= 85.3 \mu\text{m} \end{aligned}$$

Numerically, the obtained contrast is verified in figure 4.37. In this figure, the probe transmission relation is shown for a pump signal at wavelength  $\lambda_{pump} = 1.55 \mu\text{m}$ .

A transmission contrast of  $C = 0.259$  is simulated, which is in agreement with the predicted  $C = 0.265$ . Note that the transmission at the pump resonance (but felt by a probe) is indeed smaller than that of the nearby probe resonances. This NOT functionality can be extended to a NOR function by noting that the increase of modulation depth saturates for high pump powers like in the waveguide set-up.

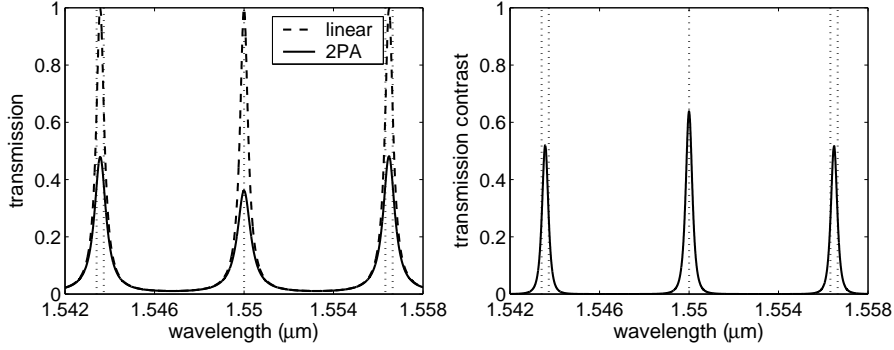


**Figure 4.37:** Numerical calculation of the linear and nonlinear transmission relation (left). The region of interest is also shown. The obtained transmission contrast (right).

Again, the use of more resonator periods will further increase the value of  $C$ .

### 4.3 Figure of merit

Until now, the mutual impact of the bound-electronic Kerr and two-photon absorption effect has not yet been considered. With the figure of merit defined as  $FOM = \frac{n_2}{\beta\lambda_c}$  and the resonance shift due to the Kerr effect in the presence of two-photon absorption given by<sup>12</sup>  $\Delta\nu_{c,lossy} = |t_{tot}(\nu'_c)|^2 \Delta\nu_{c,ll}$ , equation (E.12) together with equations (E.8) and (E.20) leads to [104]:

$$FOM \approx \frac{\sqrt{3 - |t_{tot}(\nu'_c)|^2}}{2\sqrt{2}\pi (1 - |t_{tot}(\nu'_c)|)} \frac{\Delta\nu_{c,lossy}}{\Delta\nu_{BW,lossy}} \quad (4.25)$$

With this expression, the nonlinear resonance transmission  $|t_{tot}(\nu'_c)|^2$  is related to the relative resonance shift  $\frac{\Delta\nu_{c,lossy}}{\Delta\nu_{BW,lossy}}$  by means of the figure of merit.

For two-photon absorption applications, the presence of the Kerr effect is not a problem and even beneficial: the resonance shift further

<sup>12</sup>This can be understood by the fact that the intensity inside the cavity roughly scales with the intensity transmission, except for frequencies far from resonance.

reduces the nonlinear transmission, leading to even higher transmission contrasts. This is shown in figure 4.38. In this figure, the transmission contrast due to the Kerr and two-photon absorption effect at the linear resonance frequency is plotted as function the transmission contrast only due to two-photon absorption for different *FOM* (using [31, 32, 33]). Significant improvements are possible, in particular

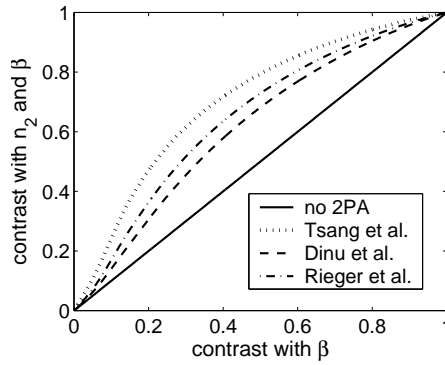


**Figure 4.38:** Transmission contrast due to  $n_2$  and  $\beta$  at the linear resonance frequency as function of the transmission contrast only due to  $\beta$ .

if a strong Kerr coefficient is present.

For Kerr-nonlinear functionalities, the presence of two-photon absorption is in most cases detrimental as firstly, it increases the required power and secondly, it decreases the obtained phase shift or transmission contrast (except for 'linear-high and nonlinear-low' all-optical switching). In figure 4.39, the resonance transmission is plotted as function of relative resonance shift  $\frac{\Delta\nu_{c,lossy}}{\Delta\nu_{BW,lossy}}$  using [31, 32, 33].

As can be seen, the decrease of the resonance transmission is significant in all cases. To obtain a relative shift of  $\frac{4\sqrt{3}}{9}$  (bistable limit) with a transmission  $|t_{tot}(\nu'_c)|^2 > 1/e$ , a figure of merit of  $FOM > 0.357$  is required, which is satisfied in all cases.

This work is published in the journal paper [104] and presented at different conferences.

## 4.4 Conclusions

In this chapter, the potential of optical resonators for reducing the power and length requirements for all-optical signal processing was investigated. To do this, we constructed a detailed theoretical model which

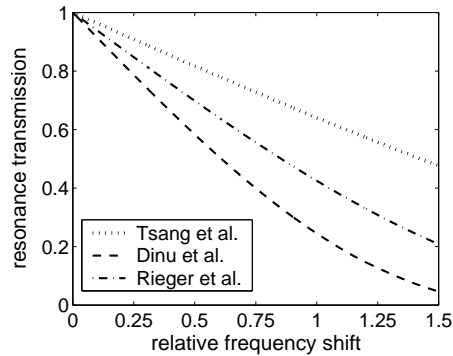


**Figure 4.39:** Reduction of the resonance transmission as function of the relative resonance shift.

takes into account both the Kerr effect and two-photon absorption. For all-optical phase shifting applications, it was found that - for the same power budget - length reductions up to 10000 are possible compared to the waveguide case. Important issues in this context are the minimization of the mirror and cavity lengths, the bandwidth trade-off and information density [98, 105].

In addition, new functionalities are possible with resonant structures which cannot immediately be obtained with simple waveguides, such as all-optical switching, bistability and reshaping. Typical power needs here are of the order of 1-4 W for bitrates of 40 Gb/s (i.e. pulse energies of 25-100 pJ) for device lengths below 100  $\mu\text{m}$ . Together with low power requirements for regeneration, this wide variety of nonlinear building blocks could allow an ultracompact, fully nonlinear platform with high bitrate capacities.

For Kerr-nonlinear applications, the presence of two-photon absorption and additional loss mechanisms may however require intermediate amplification steps. In addition, anomalous group velocity dispersion - which can occur at the resonator band-edge of resonators with a large number of cavities - may lead to modulation instability.

Next to optical resonators, also other structures display interesting features in the presence of nonlinear effects: a DBR mirror can e.g. exhibit resonances which are not present in the linear case, although typically with higher power budgets [106].

## Chapter 5

# Experimental verification

In the previous two chapters, the potential of waveguides and resonators for all-optical signal processing was investigated in detail. It was shown that by using powers of the order of 1-10 W, a whole range of nonlinear functionalities can be obtained, potentially allowing the creation of an ultradense high-bitrate all-optical platform. Until now however, many practical issues such as loss and fabrication limitations were not taken into account.

In this chapter, we will experimentally verify the Silicon-on-Insulator waveguide and resonator results discussed before and discuss the impact of different degradation mechanisms:

- Loss due to radiation, scattering, surface-state absorption...
- Linear and nonlinear dispersion
- Secondary effects such as carrier and thermal contributions
- Other nonlinear effects such as four-wave mixing...

The waveguide experiments were performed by means of a cooperation between the National Institute of Information and Communications Technology (NICT, Japan) and the Information Technology department of Ghent University-IMEC<sup>1</sup>. To complete the comparison between theory and experiment, additional experiments from literature will be used.

---

<sup>1</sup>Interuniversity Micro-Electronics Center

## 5.1 SOI waveguides

### 5.1.1 Fabricated structures

For our experimental work on nonlinear waveguide applications, SOI photonic wires were used, which have the benefit of a very small modal area. This was discussed thoroughly in chapter 3. These structures were created at IMEC (Leuven) on 200 mm SOI wafers with a thickness of the Silicon layer of 220 nm and a buried oxide of 1  $\mu\text{m}$ : a deep UV lithography stepper with a 248 nm illumination wavelength is used to define the structures in the resist. A dry etching process then transfers the patterns into the Silicon layer. A more detailed overview of the processing steps can be found in [3, 107]. The processes are in se CMOS processes, characterized and adapted for the fabrication of photonic circuits, which enforces quite different technological boundary conditions. An example of a fabricated photonic wire and a sketch of it is shown in figure 5.1.

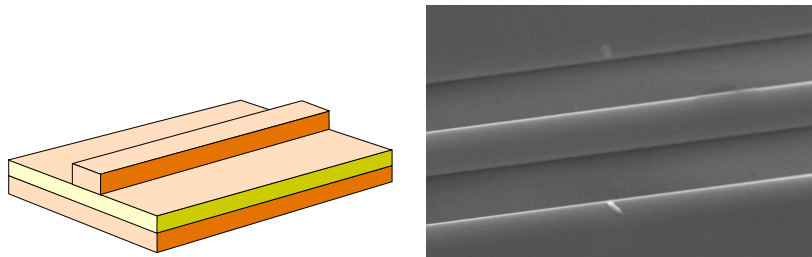


**Figure 5.1:** Sketch (left) and fabricated result (right) of a photonic wire.

Other types of waveguides like photonic crystal waveguides also have the advantage of small modal areas, but were not investigated.

### 5.1.2 Single-signal operation

#### 5.1.2.1 Experiments

Using 4 ps pulses at a repetition rate of 20 MHz and with a peak power of about 110 W, Boyraz et al. [108] obtained an all-optical phase shift<sup>2</sup> of  $2.5\pi$  in a 2 cm long SOI rib waveguide with an effective modal area

<sup>2</sup>Part of this phase shift however occurs in the EDFA preceding the waveguide, as reported in the text.

of  $5 \mu\text{m}^2$ . A significant power reduction due to two-photon absorption was also observed.

In a cooperation between NICT and UGent-IMEC, all-optical limiting experiments were performed based on two-photon absorption [109] using a 2 mm long SOI wire with an effective modal area of  $0.064 \mu\text{m}^2$ . Pulses of 49 ps at a repetition rate of 50 MHz were used with peak powers up to 12 W. The output power - input power relation is shown in figure 5.2, together with the theoretical result based on section 3.2.2.

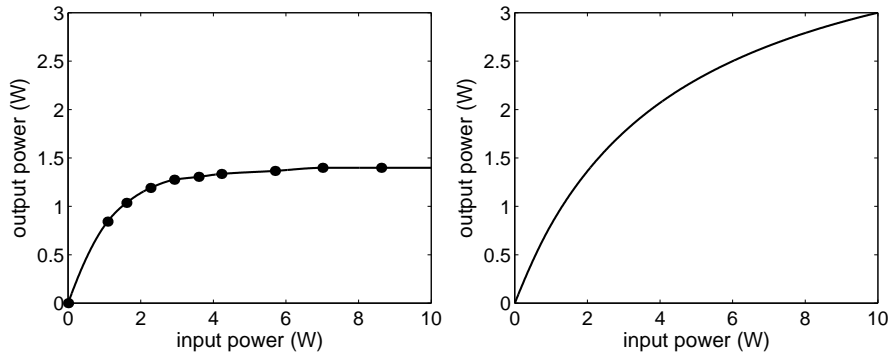


**Figure 5.2:** Experimental (left) and theoretical (right) output power  $P_{out}$  (right) as function of the input power  $P_{in}$ . Experimental results by courtesy of Liang et al. [109]

To study the difference between both results in more detail, the output pulse profile was measured for various input peak powers (figure 5.3).

Similar experiments in the context of all-optical limiting behaviour can also be found in [28, 110, 111, 112].

### 5.1.2.2 Discussion

The experiment of Boyraz et al. [108] is in agreement with the results of section 3.3: theoretically, a Kerr-nonlinear phase shift of  $1.0 - 1.4\pi$  is expected<sup>3</sup>, using the nonlinear coefficients in [31, 32, 33]. The high power required in the experiment is due to its large modal area. Using

<sup>3</sup>This value is lower than reported in [108]. As mentioned above, part of the  $2.5\pi$  phase shift occurs in the EDFA preceding the waveguide. To estimate the contribution due to the Kerr effect, the authors however did not take into account two-photon absorption, leading to an significant overestimation (section 3.3).

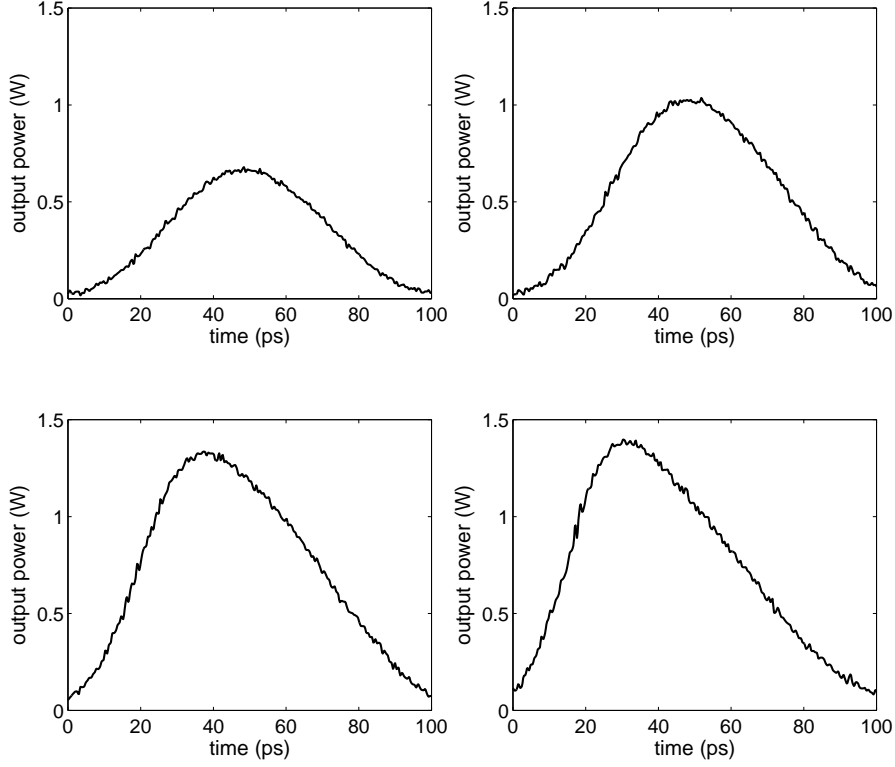


**Figure 5.3:** Output pulse profile respectively with input peak powers of 1 W (top-left), 1.6 W (top-right), 4.2 W (bottom-left) and 10 W (bottom-right). Results by courtesy of Liang et al. [109]

a 500 nm wide photonic wire, the same shift would be obtained with a power of only 1.5 W.

When the shape of the nonlinear pulse is not rectangular, the obtained phase shift will vary along the pulse: using equation (2.38) and taking into account the ultrafast, nonlinear response time, the time-dependent phase change is given by

$$\Delta\phi(L, t) = -\frac{\omega n_2}{c\beta} \ln(1 + \beta_{eff} P(0, t)L) \quad (5.1)$$

leading to nonlinear dispersion (frequency chirp) and spectral broadening. This effect has applications such as supercontinuum generation and soliton propagation, both however heavily limited by two-photon

absorption [16, 30, 108]. For signal processing functionalities based on a  $\pi$  phase shift, the chirp is however limited (spectral broadening of a factor 2 requires about a  $2.7\pi$  phase shift [30]).

The difference between the theoretical and experimental result in figure 5.2 can be explained by the presence of additional loss mechanisms such as linear and free-carrier absorption. This is described by equations (2.51) and (2.52). To analyze the effect of these loss factors, it would be interesting to convert the intensities in these expressions to optical powers. However, because the carrier density will spread throughout the structure, calculation of the exact carrier profile is extremely difficult. Therefore, all non-local effects will be neglected similar to [65], so that the carrier effects effectively behave like fifth-order nonlinearities with effective area  $A_{eff}^{(5)}$  defined as:

$$\left(A_{eff}^{(5)}\right)^2 = \frac{2}{\epsilon_0^3 c^3} \frac{[\text{Re} \int (\mathbf{E} \times \mathbf{H}^*) \cdot \mathbf{e}_z dx dy]^3}{\int_{NL} n_0^3(x, y) |E(x, y)|^6 dx dy} \quad (5.2)$$

Calculation of  $A_{eff}^{(5)}$  and higher-order effective areas for the considered waveguide structure showed that  $A_{eff}^{(3)} \approx A_{eff}^{(5)} \approx A_{eff}^{(7)} \approx \dots$  so that a single area  $A_{eff}$  will be used. In this way, equations (2.51) and (2.52) simplify to:

$$\frac{dP}{dz}(z, t) = -\alpha_{add}P(z, t) - \beta_I \frac{P^2(z, t)}{A_{eff}} - \sigma_a N(z, t)P(z, t) \quad (5.3)$$

$$\frac{dN}{dt}(z, t) = \frac{\beta_I P^2(z, t)}{2\hbar\omega A_{eff}^2} - \frac{N(z, t)}{\tau_{carr}} \quad (5.4)$$

The free-carrier refractive index and absorption change in Silicon due to the plasma effect are given by

$$\Delta n^{FCD}(N, P) = -\sigma_{r,N}N - (\sigma_{r,P}P)^{0.8} \quad (5.5)$$

$$\Delta \alpha^{FCA}(N, P) = \sigma_{a,N}N + \sigma_{a,P}P \quad (5.6)$$

with at  $1.55 \mu\text{m}$   $\sigma_{a,N} = 8.5 \times 10^{-18} \text{ cm}^2$ ,  $\sigma_{a,P} = 6.0 \times 10^{-18} \text{ cm}^2$ ,  $\sigma_{r,N} = 8.8 \times 10^{-22} \text{ cm}^3$  and  $\sigma_{r,P} = 4.6 \times 10^{-22} \text{ cm}^3$  at  $1.55 \mu\text{m}$ . The effect of linear loss and free-carrier absorption is plotted in figure 5.4 for different carrier lifetimes  $\tau_{carr}$ , assuming an NRZ data format and high-bit rate operation (section 2.7). As can be seen, the influence of typical linear loss is almost negligible. The contribution of free-carrier absorption on the other hand can easily dominate the limiting effect of two-photon

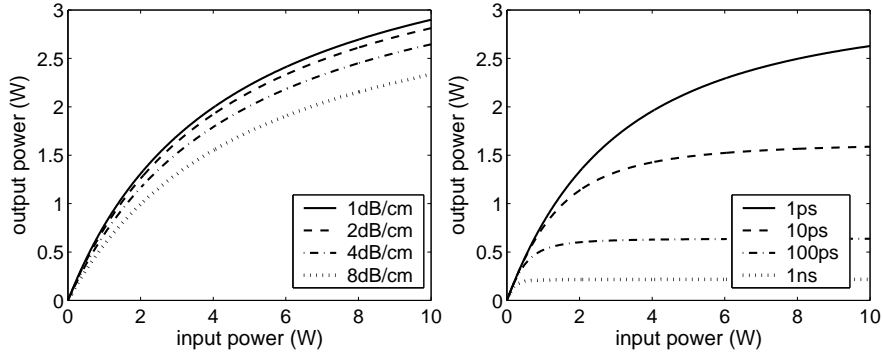


**Figure 5.4:** Impact of linear loss (left) and free-carrier absorption (right) on the output power for the example considered in section 5.1.2.1.

absorption, explaining the difference between the theoretical and experimental result in figure 5.2. To avoid this effect in NRZ operation, carrier lifetimes of 1 ps would be required, which are unrealistically small for Silicon. A solution to this problem is using other data formats with less efficient bandwidth usage (Return-to-Zero, RZ).

In the experiment of Liang et al. [109], very small repetition rates were used so that the carrier concentration is only built up during the propagation of a single pulse. As the pulse length is much smaller than the carrier lifetime (typically ns scale), there are little relaxation effects present leading an increasing carrier density along the pulse. This results in the highly asymmetric pulse shapes which are observed in figure 5.3.

### 5.1.3 Pump-probe operation

#### 5.1.3.1 Experiments

In [113], Boyraz et al. demonstrated all-optical switching based on all-optical phaseshifting in an (external) Mach-Zehnder configuration using a pump-probe setup. In this experiment, a 2.5 cm long SOI rib waveguide with an effective modal area of  $2 \mu\text{m}^2$  is used. The 1550 nm pump pulses with a pulse length of 1 ps and repetition rate of 20 MHz have a peak power of about 150 W [114]. The probe signal is operated in CW with a wavelength of 1537 nm. In this way, an on-off switching ratio of 13 dB is obtained. Free carrier accumulation was observed with a carrier lifetime of 7 ns.

Pump-probe experiments were also performed in the cooperation between NICT and UGent-IMEC, showing the waveguide potential of inverted wavelength conversion based on two-photon absorption [115, 116]. A 10 mm long SOI wire with an effective modal area of  $0.064 \mu\text{m}^2$  was used. The pump pulses have a length of only 1.5 ps at a repetition rate of 10 GHz and with a wavelength of 1552.7 nm. The peak powers are varied from 0 to 7.5 W. The probe signal is positioned at a wavelength of 1568 nm. Because of the response limitations of the photodiode and the fact that the DC component of the detected signal is filtered by the detection circuit, the modulation depth cannot be obtained with a CW probe. Instead, a pulsed probe signal (1.5 ps pulse length) is used which is delayed compared to the pump pulse: the modulation depth then reaches a maximum if the delay between pump and probe pulse is zero. The obtained result is plotted in figure 5.5, together with the theoretical fit. An example of the measured modulation depth as a function of probe pulse delay is also shown: for an input pump power of 6 W, a modulation depth of 92% is observed. Improving the repetition rate up to 40 GHz did not lead to significant degradation due to free-carrier effects.

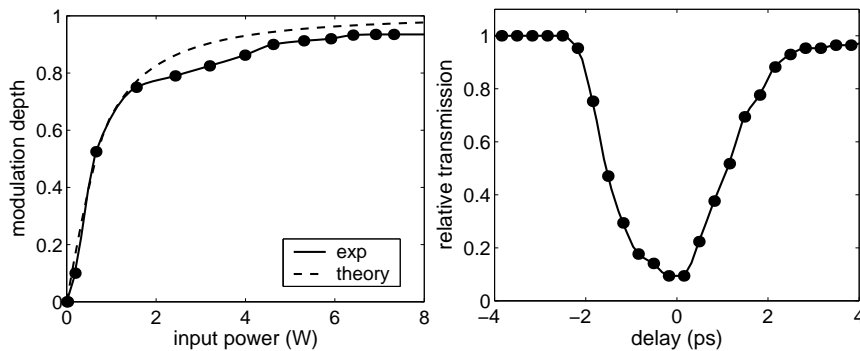


**Figure 5.5:** Theoretical and experimental modulation depth as a function of the input pump power (left). Modulation depth as a function of probe delay for an input pump power of 6 W (right). Experimental results by courtesy of Nunes et al. [116].

This work is published in the journal paper [115] and presented at different conferences.

### 5.1.3.2 Discussion

Converted to a 500 nm wire, the pump power in the pump-probe experiment of Boyraz et al. [113] corresponds to approximately 5.3 W; in the absence of free-carrier effects, the obtained pump-probe phase shift would theoretically be  $3.4\pi - 4.8\pi$ . Therefore, similar to [109], free carrier accumulation along the pulse will lead to an additional refractive index change, which we estimate at  $0.67\pi$  in agreement with the experimental results<sup>4</sup>. Due to FCA, the Kerr-nonlinear phase shift is reduced to  $3.3\pi - 4.6\pi$ . Also here, frequency chirp has to be taken into account.

The free-carrier effect itself can also be used for phase shifting (as can thermal dispersion), however typically limited by the carrier (or thermal) lifetime. This limitation can be avoided by means of an interferometric configuration [6, 117, 118]: using two different control pulses which are slightly detuned in time, a switching window is opened which is not limited by the carrier lifetime. In such a configuration, the index effect does not have to be ultrafast. This is schematically represented in figure 5.6.

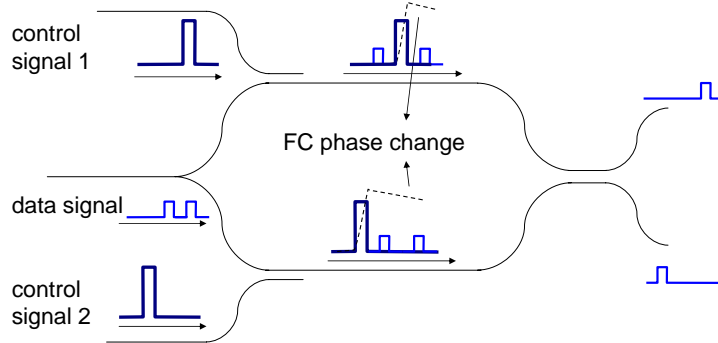


**Figure 5.6:** Differential operation principle using two control pulses in a Mach-Zehnder interferometer.

Using the theory of section 5.1.2.2, the required pump power to obtain a free-carrier phase shift of  $\pi$  based on two-photon absorption can be calculated as function of the pulse length for different wire lengths. This is done in figure 5.7.

Compared to the ultrafast Kerr effect, the improvement ranges from 1 to 10: only in the case of short waveguides and longer pulses (i.e low

<sup>4</sup>We expect that this is also the case in the single-signal experiment [108] - where the peak power is only 1.5 W, but the pulse length is  $4\times$  larger, leading to an additional  $0.71\pi$  phase shift.

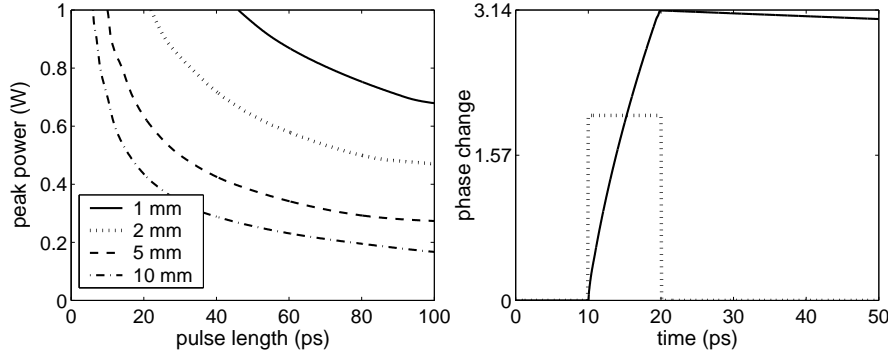


**Figure 5.7:** Pump power as function of pulse length to obtain a free-carrier phase shift of  $\pi$  (left). Example of created phase shift after a 10 mm wire with a pulse length of 10 ps. The peak power is 0.68 W and the carrier lifetime was assumed to be 1 ns (right).

peak power), a significant enhancement is found, because strong pulses exhibit a strong Kerr-nonlinear index change independent of the pulse length. For these power levels, transient thermal dispersion effects are negligible on a timescale below 1 ns. In high-bitrate operation, a significant thermal background will however be present.

To utilize the FCD effect more effectively, single-photon absorption should be deployed [119] - i.e. a pump signal with  $\lambda_p < 1.11 \mu\text{m}$ . Absorption coefficients range from  $\alpha = 1 - 10^6 \text{ cm}^{-1}$  [75]. In figure 5.8 (left), the required pump power to obtain a phase shift of  $\pi$  is recalculated for the single-signal absorption case as function of the pulse period  $T$  for a wire length of 1 mm. Note that the required power does not further improve for  $\alpha > 10^2 \text{ cm}^{-1}$ : this can be explained by noting that the plasma effect in Silicon is slightly less than linear in the carrier density (equation (5.5)). For  $\alpha > 10^2 \text{ cm}^{-1}$ , the pump power is reduced to about zero within a length of  $100 \mu\text{m}^5$ , so in all cases the same total carrier density is created. Therefore, the larger  $\alpha$ , the smaller the area where the carriers are created and the less efficient they are used.

In the pump-probe experiment performed by Nunes et al. [116], excellent agreement was obtained with our theoretical predictions neglecting free-carrier absorption (figure 5.5). To avoid detrimental free-carrier effects as discussed in section 5.1.2.2, deviation from the stan-

<sup>5</sup>This can be seen by comparing figures 5.8 (left) and (right): for  $\alpha > 10^2 \text{ cm}^{-1}$ , the pump power does not improve anymore when longer wires are used.

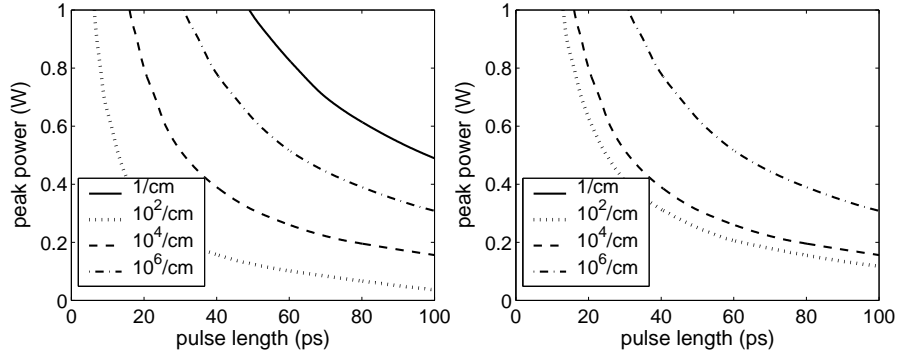


**Figure 5.8:** Pump power as function of pulse length to obtain a free-carrier phase shift of  $\pi$  for a 1 mm (left) and 0.1 mm (right) wire. For these pulse lengths, the required peak power for  $\alpha = 1 \text{ cm}^{-1}$  is larger than 1 W in the case of a 0.1 mm long wire.

standard NRZ scheme in the experiment was necessary. By reducing the data information - i.e. decreasing the repetition rate - accumulation of the created carriers can be minimized. Intrinsically, the pump pulse length of 1.9 ps would allow a repetition rate of about 500 GHz. Reducing this rate to 40 GHz would correspond to an information reduction with a factor 12.5. At this repetition rate, free-carrier absorption effects are only negligible for carrier lifetimes below 200 ps. Although this carrier lifetime may seem surprisingly low, surface recombination times down to 100 ps have already been reported [66, 67], although not in photonic wires. In addition, several papers [65, 120] indicate that the surface recombination time reduces with increasing carrier densities. Physically, this can be understood by the fact that in the presence of large carrier densities, internal fields may arise which enhance the recombination process. In the experiment here, carrier densities up to  $10^{18} \text{ cm}^{-3}$  are created at the beginning of the waveguide, making the low carrier lifetime value fully plausible.

The free-carrier absorption effect itself can of course also be used for inverted wavelength conversion. Unfortunately, no differential operation is possible - in contrast to the case of free carrier dispersion - making it limited by the carrier lifetime. Therefore bitrates of 10 Gb/s are very difficult to obtain.

In addition to secondary effects, other ultrafast nonlinear effects may appear in pump-probe configurations, apart from cross-phase and

cross-absorption modulation: due to presence of multiple signals, in particular four-wave mixing (FWM) effects become possible [16, 40]. Although not discussed in this work, FWM effects form another interesting branch of nonlinear optics with applications in the wavelength conversion domain [121, 122, 123]. A key difference with the nonlinear phenomena described in chapter 2 is however the condition of phase matching: efficient wavelength conversion is only possible if the different signals are phase matched<sup>6</sup>.

In the context of this work, four-wave mixing however gives rise to additional nonlinear loss and crosstalk: in the presence of a strong pump signal  $\mathbf{E}_{\omega_1}$  with frequency  $\omega_1$  and weaker probe signal  $\mathbf{E}_{\omega_2}$  with frequency  $\omega_2$ , an additional idler signal  $\mathbf{E}_{\omega_3}$  will be created<sup>7</sup> with frequency  $\omega_3 = 2\omega_1 - \omega_2$ , caused by the nonlinear polarization:

$$\mathbf{P}_{2\omega_1 - \omega_2} = \epsilon_0 \frac{3}{4} \chi^{(3)}(-2\omega_1 + \omega_2; \omega_1, \omega_1, -\omega_2) : \mathbf{E}_{\omega_1}^2 \mathbf{E}_{\omega_2}^* \exp(-jk_P z) \quad (5.7)$$

with  $k_P = 2k_{\omega_1} - k_{\omega_2}$ . For frequencies  $\omega_1 \approx \omega_2$ , one has in good approximation that  $\chi^{(3)}(-2\omega_1 + \omega_2; \omega_1, \omega_1, -\omega_2) = \chi^{(3)}(-\omega; \omega, -\omega, \omega)$ , so that the four-wave mixing process - in absence of linear and free-carrier loss and pump depletion - is described by

$$\frac{d\mathbf{E}_{\omega_1}}{dz}(z, t) = -j \frac{\omega_1}{c} n_2 |E_{\omega_1}(z, t)|^2 \mathbf{E}_{\omega_1}(z, t) - \frac{\beta}{2} |E_{\omega_1}(z, t)|^2 \mathbf{E}_{\omega_1}(z, t) \quad (5.8)$$

$$\begin{aligned} \frac{d\mathbf{E}_{\omega_2}}{dz}(z, t) &= -2j \frac{\omega_2}{c} n_2 |E_{\omega_1}(z, t)|^2 \mathbf{E}_{\omega_2}(z, t) - \beta |E_{\omega_1}(z, t)|^2 \mathbf{E}_{\omega_2}(z, t) \\ &\quad - j \frac{\omega_2}{c} n_2 \mathbf{E}_{\omega_1}^2(z, t) \mathbf{E}_{\omega_3}^*(z, t) \exp(j\Delta k z) \\ &\quad - \frac{\beta}{2} \mathbf{E}_{\omega_1}^2(z, t) \mathbf{E}_{\omega_3}^*(z, t) \exp(j\Delta k z) \end{aligned} \quad (5.9)$$

$$\begin{aligned} \frac{d\mathbf{E}_{\omega_3}}{dz}(z, t) &= -2j \frac{\omega_3}{c} n_2 |E_{\omega_1}(z, t)|^2 \mathbf{E}_{\omega_3}(z, t) - \beta |E_{\omega_1}(z, t)|^2 \mathbf{E}_{\omega_3}(z, t) \\ &\quad - j \frac{\omega_3}{c} n_2 \mathbf{E}_{\omega_1}^2(z, t) \mathbf{E}_{\omega_2}^*(z, t) \exp(j\Delta k z) \\ &\quad - \frac{\beta}{2} \mathbf{E}_{\omega_1}^2(z, t) \mathbf{E}_{\omega_2}^*(z, t) \exp(j\Delta k z) \end{aligned} \quad (5.10)$$

<sup>6</sup>In the case of two signals, this means that  $n_{eff,1} = n_{eff,2}$ . In practice, some phase mismatch will always remain if both signals have a different wavelength.

<sup>7</sup>Many other FWM effects may occur, although not in the vicinity of  $\omega_1$  and  $\omega_2$ . Nevertheless, for sufficiently long structures, also the frequency  $2\omega_2 - \omega_1$  will be created together with new crossover terms.

with a phase mismatch given by  $\Delta k = k_{2\omega_1 - \omega_2} + k_{\omega_2} - 2k_{\omega_1} = \frac{4\pi}{\lambda_1} \frac{d^2 n_{eff}}{d\lambda^2} (\lambda_2 - \lambda_1)^2$ . The signals are then fully mismatched<sup>8</sup> after a (linear) coherence length  $L_{coh} = \frac{\pi}{\Delta k}$ .

As an example, let us consider the experimental setups above [116]: an idler will be created at 1.538  $\mu\text{m}$  with a coherence length of 2.76 mm. The input pump powers are taken to be 0.5 W and 2 W. The evolution of the probe and the idler signal along the waveguide is plotted in figure 5.9. The probe situation without FWM effects is also shown.

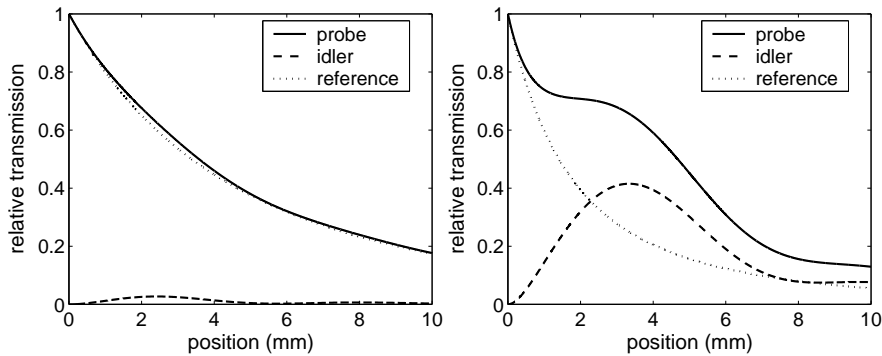


**Figure 5.9:** FWM effects along the waveguide for the experiments described by [116] with an input power of 0.5 W (left) and 2 W (right). The reference probe case without FWM is also considered. The different transmissions are scaled to the probe input power.

For pump power of 0.5 W, the FWM effect is relatively small. As can be seen, the exact coherence length approaches the linear value  $L_{coh}$  quite well. For the 2 W pump signal however, considerable FWM can be seen and the idler signal is comparable in power level with the probe signal. In this case, the phase mismatch is partially compensated by nonlinear phase effects. As a result, the coherence length is now much larger, which explains the strong idler signal. Note that also the probe signal is much higher than in the absence of FWM due to energy transfer from the pump through the idler<sup>9</sup>. In reality, the FWM contribution will be smaller due to pump depletion and free-carrier absorption ef-

<sup>8</sup>This formula is based on the linear case. However, in reality, the exact coherence length is slightly different due to nonlinear phase changes.

<sup>9</sup>This can explain the difference between theory and experiment is figure 5.5 for higher input powers.

fects [122]. Nevertheless, if multiple probe signals are present at the same time, considerable crosstalk can be obtained.

## 5.2 Resonators

### 5.2.1 Fabricated structures

Many three-dimensional implementations of the standing-wave optical resonator discussed in chapter 4 are possible (figure 5.10): starting from index guided waveguides, a straightforward approach is to introduce mirror sections by etching (entirely or partially) the waveguide or by adding holes. In a PhC waveguide, resonant behaviour can also be obtained with additional holes. These different approaches were also fabricated at IMEC (Leuven).

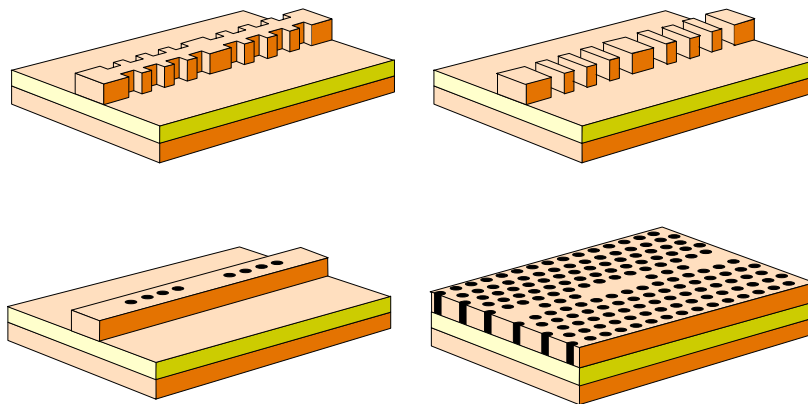


**Figure 5.10:** Sketch of different types of optical resonators: partially etched waveguide (top, left), fully etched waveguide (top, right), waveguide with holes (bottom, left), PhC resonator (bottom, right).

A slightly different type of resonator is the ring resonator (figure 5.11), in which the light literally travels in circles [2]. Depending on the shape, also racetracks, disks... exist. In contrast to the previous structures, these devices are traveling-wave optical resonators, which have slightly different linear and nonlinear properties compared to their standing-wave equivalent. The coupling between the ring and the in-

and output waveguides acts like a very short mirror section<sup>10</sup>, while the ring itself is to be considered as a large cavity. The latter is intrinsically limited by radiation loss depending on the index contrast. Furthermore, due to the absence<sup>11</sup> of a counterpropagating field, the third-order nonlinear interaction is reduced by a factor of 3 (see equation (D.7) and [125]). An important advantage of traveling-wave structures however is that the 'reflected' light is passed to an additional port and is not sent back into the system. This allows all-pass configurations [126], which are not possible with standing-wave resonators (not further discussed). A sketch of a ring resonator and an example of a fabricated result are shown in figure 5.11.

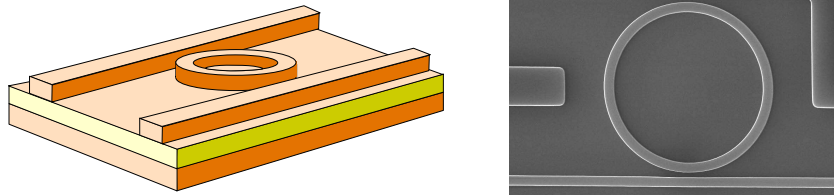


**Figure 5.11:** Sketch (left) and fabricated result (right) of an optical ring resonator.

Apart from these examples, many other types of optical resonators are still possible (e.g. PhC structures with shifted hole sections [92], ...) with similar properties.

The best results in terms of loss, Q-factor and modal volume that we obtained during this work, were with the ring structures in spite of their lower nonlinear interaction. From chapter 4, it is clear that the cavity length should be as small as possible<sup>12</sup>. Low-loss resonators were fabricated with a radius of  $R \geq 3 \mu\text{m}$ . Using other processing techniques, even better results in terms of nonlinear enhancement were obtained by other groups using PhC resonators. These will be cited in the text.

<sup>10</sup>The coupling coefficient between the ring and the waveguide corresponds to the mirror transmissivity  $|t|_{\nu_c}^2$  in our 1D model, while the intensity fraction that goes to the pass port is given by  $|r|_{\nu_c}^2$  [2].

<sup>11</sup>In practice, some counterpropagating light is possible due to backscattering as a result of surface roughness [124], although this is negligible for nonlinear purposes.

<sup>12</sup>Note that in the case of a ring resonator, the mirror length is already negligible and can therefore not be further optimized.

## 5.2.2 Single-signal operation

### 5.2.2.1 Experiments

Continuous-wave measurements were performed to investigate the influence of secondary effects on ring resonators. On plain waveguides, we have seen above that the impact of free carriers is quite severe. In this experiment, a ring resonator with a radius of  $4\ \mu\text{m}$  was used: the resonance at the wavelength  $1535.72\ \text{nm}$  has a bandwidth of  $6.03\ \text{GHz}$  ( $47.4\ \text{pm}$ ) corresponding to a Q-factor of  $32000$  and a reflection of  $|r|_{\nu_c}^2 = 0.997$ . The bandwidth of the resonance at the wavelength  $1556.97\ \text{nm}$  is approximately  $3.77\ \text{GHz}$  ( $30.5\ \text{pm}$ ), leading to a Q-factor of  $51000$  and a reflection of  $|r|_{\nu_c}^2 = 0.998$ . The measured free spectral

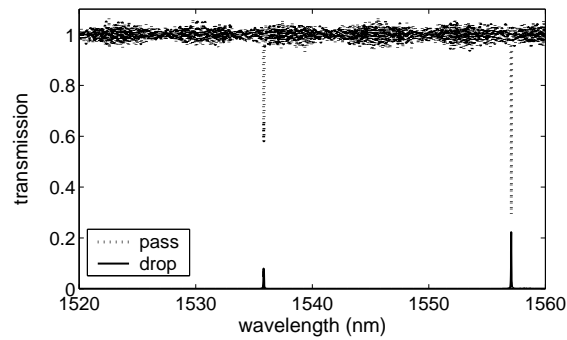


**Figure 5.12:** Normalized transmission of the pass and the drop port in the low-power regime.

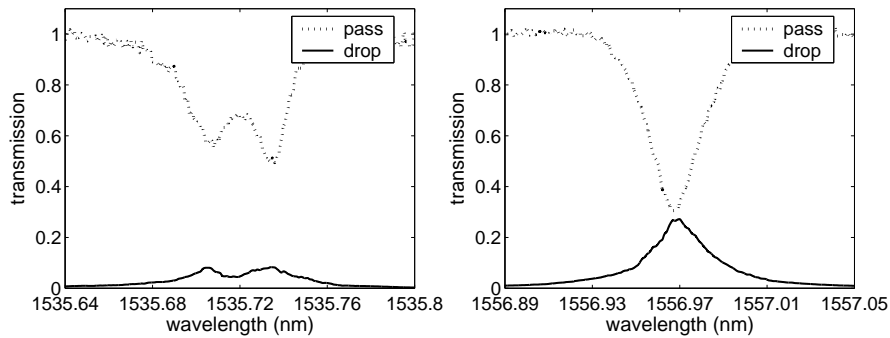


**Figure 5.13:** Detail around the resonance wavelength  $1535.72\ \text{nm}$  (left). Detail around the resonance wavelength  $1556.97\ \text{nm}$  (right).

range is 21.25 nm (figure 5.12). The peak transmission at the resonances is respectively 0.08 and 0.27 (figure 5.13). As can be seen, the resonance at the wavelength 1535.72 nm is slightly split due to surface roughness induced backscattering [124].

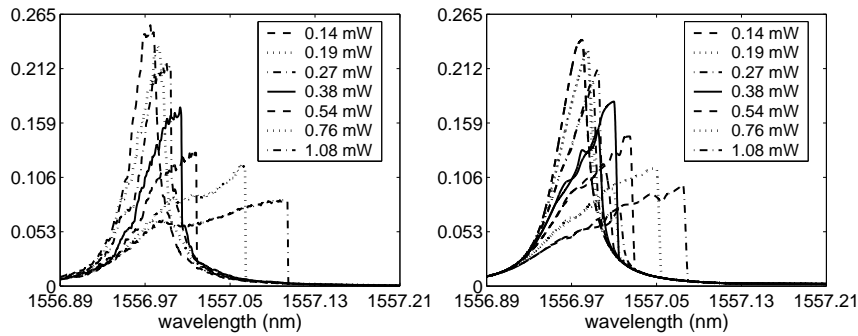


**Figure 5.14:** Experimental (left) and theoretical (right) nonlinear drop transmission spectra around the linear resonance wavelength 1557.51 nm.

As the second resonance has the highest Q-factor and mirror reflectivity, the area around 1556.97 nm was investigated on nonlinear behaviour: the signal power was varied from 0.14 mW to 1.09 mW in steps of 1.5 dB with an estimated error of  $\pm 0.5$  dB. The resulting drop transmission spectra are shown in figure 5.14. Due to the fact that the laser source could only be swept in the upward wavelength direction, only the upper (bistable) arm is plotted. From the steep declines in the transmission<sup>13</sup>, it can however be seen that all-optical bistability is obtained for powers of 0.27 mW and above.

By measuring the output signal using an optical oscilloscope, it was found that for sufficiently high input powers two separate power levels become visible. From our simulations (see below), we expect that periodic oscillations are in fact occurring. This periodicity could however not be seen in the measurements, which is probably due to noise in the input signal due to a pre-amplifier. As discussed in [127], this can lead to quasi-periodicity of the output signal. To show the impact of this behaviour, the standard deviation was calculated from the oscilloscope data and plotted together with the average transmission as a function of wavelength. This is done for an input power of 0.76 mW

<sup>13</sup>This behaviour is similar to section 4.2.1.1 (e.g. figure 4.12), although the origin here is not the Kerr effect, but thermal dispersion (see further).

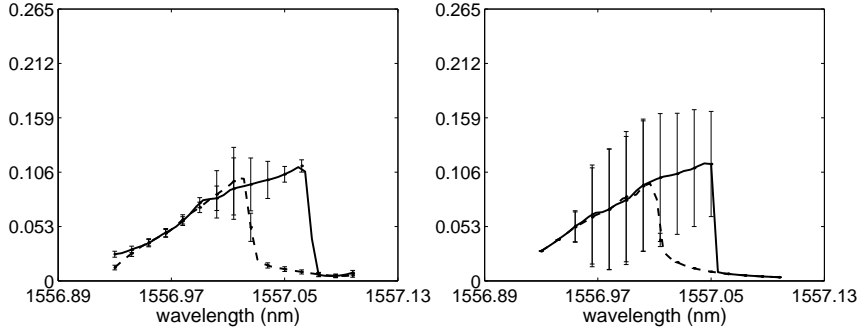


**Figure 5.15:** Experimental (left) and theoretical (right) nonlinear drop transmission spectra together with the measured standard deviation for an input power of 0.76 mW.

in figure 5.15. Both (bistable) arms are now present as the sweep was carried out manually.

The oscilloscope data is plotted explicitly for the wavelength 1557.02 nm and 1557.03 nm (lower arm) in figure 5.16. In the first plot, two different power levels can clearly be discriminated, demonstrating the instable behaviour.

This work is published in the journal paper [120] and presented at different conferences.

Similar continuous wave experiments on other types of optical resonators - in particular, PhC work - can be found in [65, 66, 128]. Recently, periodic pulsations and unstable behaviour was also directly observed by Johnson et al. [129].

### 5.2.2.2 Discussion

Like the carrier density, the temperature will also vary throughout the structure, making it very difficult to determine the carrier and temperature profile exactly. Therefore, the same approach of section 5.1.2.2 was used, leading to:

$$\begin{aligned} \frac{dP}{dz}(z, t) = & - \left[ \alpha^{(SSA)} + \alpha^{(SC+R)} \right] P(z, t) - \beta_I \frac{P^2(z, t)}{A_{eff}} \\ & - \sigma_a N(z, t) P(z, t) \end{aligned} \quad (5.11)$$

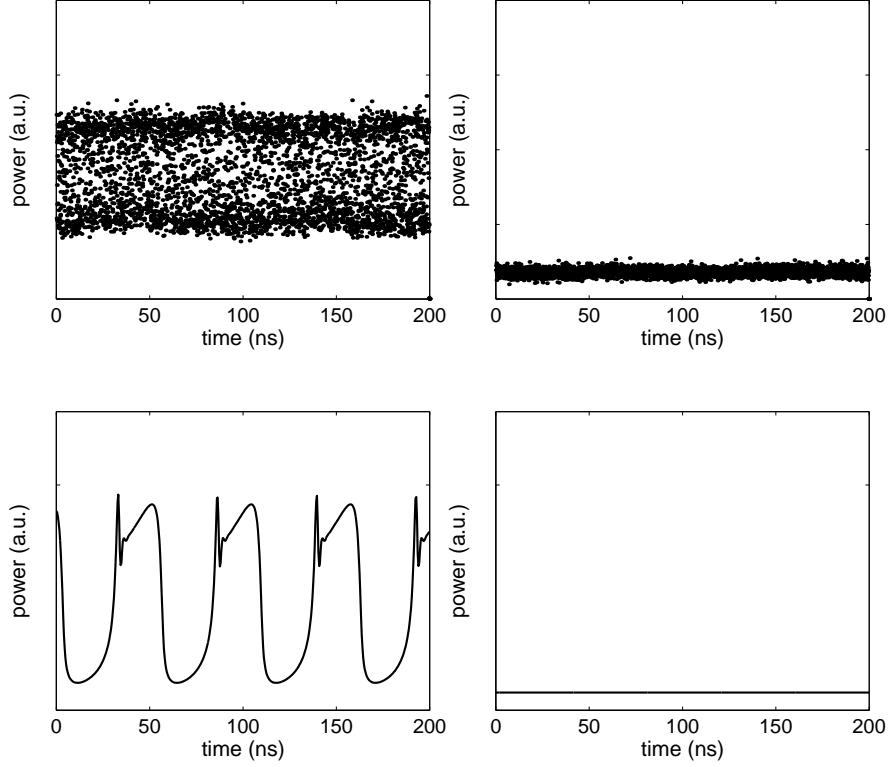


**Figure 5.16:** Oscilloscope data (top) and simulation results (bottom) at the wavelength 1557.02 nm (left) and 1557.03 nm (right) for an input power of 0.76 mW.

$$\frac{dN}{dt}(z, t) = \frac{\beta_I P^2(z, t)}{2\hbar\omega A_{eff}^2} - \frac{N(z, t)}{\tau_{carr}} \quad (5.12)$$

$$\frac{dT}{dt}(z, t) = \frac{\alpha^{(SSA)} P(z, t)}{\rho C_p A_{eff}} + \frac{\beta_I P^2(z, t)}{\rho C_p A_{eff}^2} + \frac{\sigma_a N(z, t) P(z, t)}{\rho C_p A_{eff}} - \frac{T(z, t) - T_0}{\tau_{th}} \quad (5.13)$$

In this equation, the linear loss mechanisms were split to distinguish effects which lead to additional heating (such as surface-state absorption, indicated by *SSA*) or not (such as scattering and radiation, indicated by *SC + R*). In addition, a temperature term was added to reflect this extra heating.

The free-carrier refractive index and absorption change in Silicon due to the plasma effect are given by equations (5.5) and (5.6), while the thermal dispersion effect is equal to:

$$\Delta n(T) = \left. \frac{dn}{dT} \right|_{T=T_0} (T - T_0) \quad (5.14)$$

with  $\left. \frac{dn}{dT} \right|_{T=300K} = 1.86 \times 10^{-4}$  at  $1.55 \mu\text{m}$ .

With this theoretical model, information concerning the carrier lifetime can be derived by fitting the reduction of the transmission as a function of the cavity power. This is done in figure 5.17.

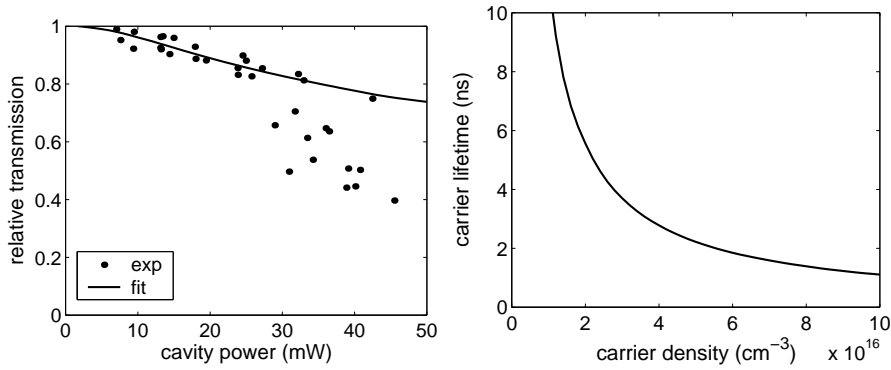


**Figure 5.17:** Measured and fitted nonlinear peak transmission (relative to the linear peak transmission 0.265) as a function of the estimated power inside the ring cavity (left). Fitted carrier lifetime as a function of carrier density (right).

Large deviations from the measurement data can be observed for cavity power above 25 mW. This can be explained by the observed quasi-periodic oscillating behaviour: as a result of these oscillations, the average output power is much lower than expected in a stable regime. The resulting carrier lifetime is plotted as function of the carrier density in figure 5.17: lifetimes in the range of 1 – 10 ns are found for carrier densities of the order of  $10^{16} - 10^{17} \text{ cm}^{-3}$ . This is in good agreement with the experimental results published in [64, 65, 66, 67, 128]. For higher carrier densities, even smaller recombination times are expected, which could explain the results in 5.1.3.2.

Once the carrier lifetime is obtained, we can determine the thermal lifetime and surface-state absorption coefficient  $\alpha^{(SSA)}$  by fitting the resonance wavelength shift. This is shown in figure 5.18. Due

to some exchange possibilities between the different contributions to the thermal dispersion at lower power levels, the thermal lifetime and surface-state absorption coefficient could only be determined to be in the range  $t_{th} = 60 - 110$  ns and  $\alpha^{(SSA)} = 0.1 - 0.3$  dB/mm. This is in agreement with the results of [65, 66]. Using a one-dimensional material system model, a thermal lifetime of 250 ns is obtained, which is of the same magnitude<sup>14</sup> For the parameter combination  $t_{th} = 65$  ns and  $\alpha^{(SSA)} = 0.22$  dB/mm, the different nonlinear refractive index contributions are shown in figure 5.18.

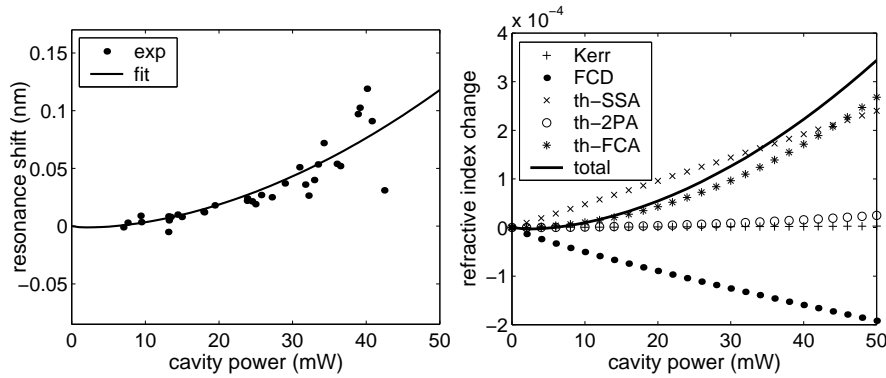


**Figure 5.18:** Measured and fitted nonlinear resonance wavelength shift  $\Delta\lambda_c$  as a function of the cavity power (left). Decomposition of the different nonlinear contributions to the refractive index change inside the ring resonator (right).

As can be seen, thermal contributions due to FCA and SSA are dominant, which could be concluded from the bistability on the upper wavelength side. However, the FCD refractive index change is also quite large. The fitted full transmission spectra are plotted in figure 5.15 and show good agreement with the experimental results.

The unstable behaviour observed in figures 5.15 and 5.16 can now be explained by the fact that two large nonlinear dispersion effects - thermal and free-carrier parts - are contributing to the index change with opposite signs and very different time constants, leading to a circling around the bistability loop, as explained in [130, 127]. This is confirmed by our simulations: despite the fact that a much wider unstable

<sup>14</sup>Note that this value is much larger than the one for the AlGaAs-AlO<sub>x</sub> structure of table 2.4, because of the very effective thermal conductivity of AlO<sub>x</sub> compared to SiO<sub>2</sub>.

area is predicted by simulations, the agreement is in principle correct and centered around the same wavelengths.

In configurations with less important free-carrier effects (e.g. by reduced carrier lifetime or due to the fact that the thermal effect due to FCA - which rises more quickly with the input power than FCD - is more dominant), this unstable behaviour disappears.

While in the waveguide case, the main loss mechanisms consist of free-carrier absorption, linear loss can now also be important: in the ring, the total linear loss was estimated  $\alpha = 0.72$  dB/mm. In addition, it should be noted that anomalous group velocity dispersion, which was estimated at  $-4$  ps<sup>2</sup>/m, counteracts the shift of the resonance frequency. Both of these considerations result in higher power requirements to obtain the certain frequency shift.

To conclude, we compare these results with the other experimental work [64, 65, 66, 128] in this field. Thermal bistability in optical ring resonators was also demonstrated by [64] with powers of 0.7 mW (5  $\mu$ m and Q of about 14000). As mentioned above, PhC structures promise a further reduction of the thermal bistability power compared to ring resonators:

- PhC resonators are standing-wave structures, leading to more efficient nonlinear interactions ( $3\times$ ,  $10\times$  and  $35\times$  higher for a third-, fifth- and seventh-order nonlinear effect).
- PhC resonators are not subject to radiation loss (limiting ring radius), although out of plane loss can be important.
- PhC resonators allow for very large tunability in terms of geometry.

As a result, thermal bistability was demonstrated with very small input powers: using a PhC resonator with a Q of 38000 and  $V_{eff}^m = 0.09$   $\mu$ m<sup>3</sup>, Barclay et al. [65] obtained optical bistability with powers of 0.1 mW. Notomi et al. [66] obtained bistability in PhC structure with a Q of 33000 and  $V_{eff}^m = 0.08$   $\mu$ m<sup>3</sup> using powers of only 40  $\mu$ W. Recently, thermal bistability was obtained by Uesugi et al. [128] with powers of only 28  $\mu$ W in a PhC cavity with a Q of 230000 and  $V_{eff}^m = 0.12$   $\mu$ m<sup>3</sup>.

Fitting these structures to a one-dimensional resonator structure as in chapter 4, mirror contrasts of the order 33% are obtained, showing that the results there typically can be improved by a factor of 5. Even higher improvements are expected in the future.

### 5.2.3 Pump-probe operation

#### 5.2.3.1 Experiments

Based on the previous analysis, secondary effects will clearly dominate the resonator behaviour for high repetition rate signal processing. Possible applications will be the same as discussed in section 4.2, but lifetime limited.

Using an all-pass ring resonator with a radius of  $5\ \mu\text{m}$  and  $Q$  of 14000, Almeida et al. [64] demonstrated thermal 'linear-high and nonlinear-low' switching with an average pump power of 0.55 mW (on resonance) and a CW probe signal positioned close to the next resonance with a 0.2 nm resonance wavelength offset. The  $Q$ -factor of the second resonance was estimated at 8000. The obtained modulation depth was 8 dB at a NRZ bitrate of only 0.2 Mb/s.

To demonstrate the lifetime limitation for carrier effects of our SOI ring resonator structures, a pump signal with a peak power of 0.66 mW and an extinction ratio of 5 dB was inserted on the second resonance of the resonator discussed in section 5.2.2. The pulses have a length of 10 ns and a repetition rate of 12.5 Mb/s (i.e. 10001000... bit pattern, figure 5.19). The CW probe signal was positioned near the first reso-

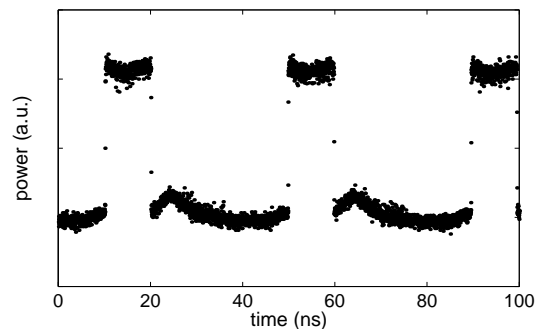


**Figure 5.19:** Pump signal inserted on the optical resonator.

nance with respectively a 0 nm and 0.08 nm resonance wavelength offset. The obtained output probe signals are plotted in figure 5.20. The measured extinction ratios were respectively 2.7 dB and 3.8 dB. Similar experiments were also performed by [67, 102].

Using higher pump powers, the extinction ratio can be improved, however deviations in the converted bit pattern (normally 10001000...

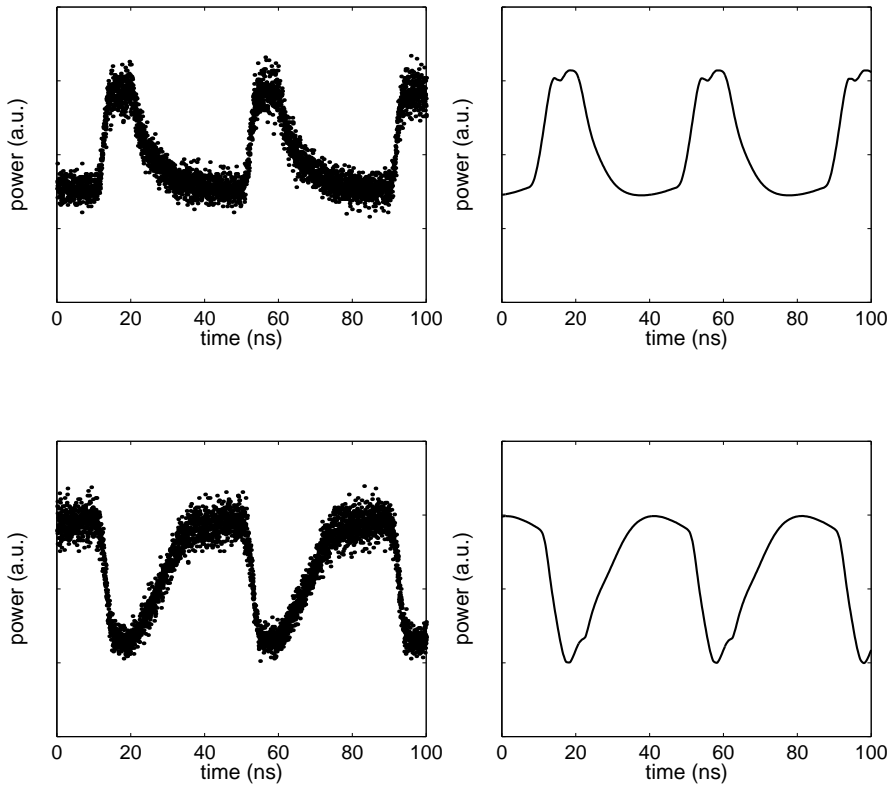


**Figure 5.20:** Measured (left) and simulated (right) output probe signals at the wavelengths 1535.72 nm (top) and 1535.80 nm (bottom) for a pump power of 0.66 mW.

respectively 01110111...) were observed. This is shown in figure 5.21 for the same setup with an input power of 1.32 mW.

### 5.2.3.2 Discussion

In the experiment performed by Almeida et al. [64], thermal 'linear-high and nonlinear-low' switching is obtained at the pass port, corresponding to 'linear-low and nonlinear-high' switching at the drop port of an add-drop configuration. This is in agreement with the mentioned wavelength offset of the probe.

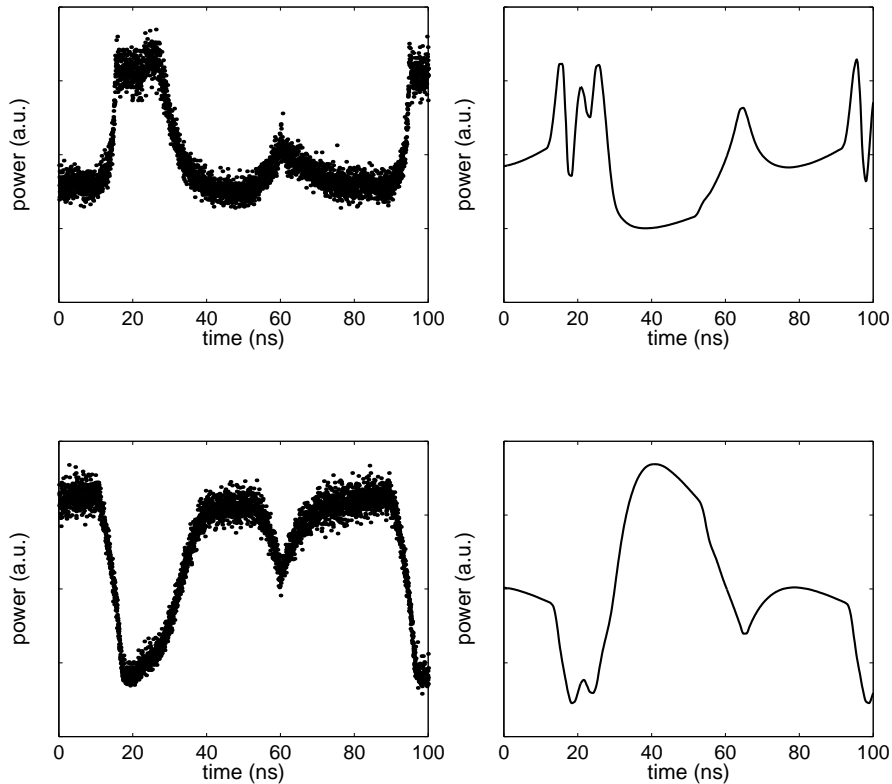


**Figure 5.21:** Measured (left) and simulated (right) output probe signals at the wavelengths 1535.72 nm (top) and 1535.80 nm (bottom) for a pump power of 1.32 mW.

In our free-carrier experiment, ‘linear-high and nonlinear-low’ or ‘linear-low and ‘nonlinear-high’ all-optical switching is obtained, depending on the position of the probe, similar to the behaviour discussed in section 4.2.1.2. As can be seen in figure 5.20, the obtained experimental data is in good agreement with the predicted results<sup>15</sup> The bi-trate is clearly limited by the carrier lifetime: carrier densities between

<sup>15</sup>In the timedomain, the nonlinear behaviour of a ring resonator can be simulated by using its linear rate equation model [2] in combination with equations (5.11), (5.12), (5.13) and equations (B.50), (B.56) (5.5), (5.6) and (5.14). For a standing-wave structure, timedomain simulations are much more difficult because of the presence of two counterpropagating waves and more complex tools such as FDTD are in general required.

$0.5 - 3.5 \times 10^{16} \text{ cm}^{-3}$  were simulated, theoretically allowing data rates up to 0.3 Gb/s. The slower recovering carrier tail however limits the data rate to about 0.1 Gb/s. The thermal background was estimated at  $\Delta T = 0.85 \text{ K}$ . Due to the low Q-factor of the probe resonance, the power to obtain pump-probe operation is larger than in the single-signal case. If the Q-factor of pump and probe resonance would be the same, the switching power could be reduced with a factor of  $\frac{51000^2}{32000^2} \approx 2.5$  (equation (D.51)).

For higher pump powers, the converted bit pattern shows errors due to unstable effects similar to the CW case. This is confirmed by our simulations (figure 5.21), although the agreement is not as good as for 0.66 mW. As a result of this unstable behaviour, the maximum obtainable extinction ratio - which typically improves for higher pump powers - is limited.

To avoid the dominance of secondary effects, the same approach can be used as for photonic wires: decreasing the repetition rate with the disadvantage of inefficient bandwidth usage. For optical resonators, this penalty is extra-hard because of the fact that bandwidth confinement is the key for nonlinear enhancement (appendices D and E). Differential operation could also be considered, however multiple optical resonators would be necessary just as in the case of all-optical Kerr-nonlinear phase shifting. Due to the presence of significant linear loss, this will be difficult in practice.

Like in the waveguide case, the presence of two or more optical signals inside the resonator structure can lead to additional four-wave mixing effects: (an) idler signal(s) with power levels comparable to the probe signal(s) can arise, in practice however limited by free-carrier effects [122].

### 5.3 Conclusions

In this chapter, we experimentally confirmed our previous theoretical results. Excellent agreement between simulation and experiment was obtained. In a cooperation between NICT and UGent-IMEC, all-optical limiting and wavelength conversion based on two-photon absorption were demonstrated in a photonic wire for pulse trains up to 40 GHz and powers below 10 W. We also demonstrated all-optical, thermal bistability in a SOI ring resonator with powers below 0.3 mW. In addition, two examples of all-optical switching were demonstrated with a pulse length of 10 ns and a power of 0.7 mW, indicating that 0.1 Gb/s opera-

tion is feasible. Unstable behaviour due to interaction between thermal and free-carrier effects was obtained at higher powers.

In addition, the impact of different degradation mechanisms was discussed: both in the waveguide and in the resonator experiments, significant secondary effects were observed in the SOI structures due to the creation of free carriers and heat. To avoid the impact of these phenomena, one can reduce the pulse repetition rate, however at the cost of a decrease in optical data rate. Even then, secondary effects may appear due to accumulation along the pulse itself. Such an approach has potential for all-optical header processing in packet-based networks (ns repetition rates, [8, 131])

Secondary effects and in particular free-carrier dispersion can be used for all-optical signal processing, however within the limitation of their relaxation time and possible unstable behaviour. Therefore, reducing the carrier lifetime by fabrication optimization or by means of carrier extraction [70] would be important. In the latter case, one would also avoid thermal effects leading to free-carrier bistable elements. Also here, applications can be found along the lines of all-optical packet routing. This relaxation limitation can however be overcome in photonic wires by using an interferometric approach.

Apart from secondary effects, further degrading in optical resonators occurs due to significant linear loss and the presence of linear dispersion. In pump-probe operation, particular attention should also be paid to four-wave mixing effects, which could lead to considerable crosstalk in multiple channel processing (e.g. broadcasting).

Finally, we would like to mention the particular potential of PhC resonators for ultrafast nonlinear signal processing due to their standing-wave properties and small modal volume.

## Chapter 6

# Conclusions and perspectives

### 6.1 Conclusions

Today, optical data transport forms the backbone for the modern long-haul telecom infrastructure and is already starting to penetrate the markets of high-end local area networks and short distance applications. To fully realize its potential, improved switching and processing functionalities are however necessary inside the optical layer. Although low-cost integration while maintaining optical-electrical conversions is a first step, all-optical signal processing is expected to form the real breakthrough towards ultra-high bandwidth telecommunication. In the context of the recent advances in fabricating high-quality nanophotonic devices, ultrafast nonlinear optics forms an excellent candidate to achieve this goal.

Of the many nonlinear effects that exist, two interdependent ultrafast phenomena were considered in this work: the bound-electronic Kerr effect and the two-photon absorption process. In common semiconductor materials, these effects are however very weak and therefore require high optical powers. In addition, secondary effects such as carrier generation and heating may arise which can dominate the nonlinear behaviour.

By using waveguides with high transverse confinement, the nonlinear interaction between the light and the material can be enhanced, leading to significant reductions in the power budget: with peak powers of the order 1-10 W and waveguides lengths in the mm range, all-

optical signal processing is theoretically possible with bitrates exceeding 1 THz.

Even further improvement is possible by introducing longitudinal confinement (i.e. resonator enhancement) at the expense of a reduction in signal bandwidth. To investigate and optimize this trade-off, a detailed theoretical model was constructed which takes into account the different nonlinear effects. For 40 Gb/s and 100 Gb/s operation, pulse energies of the order of respectively 5-20 pJ and 25-100 pJ are theoretically required for devices lengths below 100  $\mu\text{m}$ . In addition, new functionalities such as optical memory are possible with optical resonators, which cannot be achieved with simple waveguides.

Experimentally, these theoretical results were verified using SOI waveguides and ring resonators: in photonic wires, 40 GHz wavelength conversion was demonstrated in a cooperation between NICT and UGent-IMEC with powers in the range of 1-10 W. A severe degradation due to secondary effects was however observed, leading to the need for other data formats. In the ring resonator experiments, free-carrier and thermal effects are even more dominant and thermal bistability was obtained with input powers below 0.3 mW. For the first time, we also demonstrated unstable behaviour, which forms an important limitation for thermal all-optical switching, but also has potential for pulse generation. In addition, free-carrier based all-optical switching was demonstrated with a pump power of only 0.67 mW. At larger pump powers, we again observed instable behaviour, which limits the obtainable modulation depth. Despite these considerations, both the waveguide and resonator approach can be used for packet-based all-optical routing.

## 6.2 Future work

While proving the extremely large potential of nonlinear optics, the results that we obtained during this work can still be improved a lot: as technology and fabrication methods constantly get better, new routes become possible which will allow an increasingly better behaviour and performance.

In particular, we expect a lot from the following approaches:

- As already mentioned in chapter 5, photonic crystal structures form the most versatile and tunable system for fabricating optical resonators. In the light of using evolutionary algorithms to cre-

ate high-quality devices [5], we expect the modal volume and Q factor of these resonators to improve even more.

- In chapter 2, different approaches were already discussed to reduce the impact of secondary effects. In particular, carrier extraction by integration of a p-i-n junction may prove to be a viable way to avoid many detrimental carrier accumulation and heating effects [70, 132]. Moreover, as free carrier effects can also be used for signal processing purposes, increasing the reverse voltage of the junction would allow bitrates above 10 Gb/s and free-carrier all-optical bistability should become possible as thermal dispersion effects are avoided.
- In addition to the previous remark, we believe that much improvement is to be expected from surface engineering: interesting results are reported concerning the reduction of surface-state absorption and increasing the carrier diffusion (i.e. reducing the carrier response time) would be possible.
- From the results of this work, it is clear that Silicon may not be the best material to be used for all-optical signal processing. In addition to evaluating other semiconductor platforms (e.g. AlGaAs), new material systems such as quantum dots, nanocrystals... can be integrated onto the existing Silicon technology, combining the results of both worlds [90, 133]. In this way, an ultrafast all-optical nonlinear platform may become possible.



## Appendix A

# Material anisotropy

In a cubic symmetry, the three independent elements of the nonlinear susceptibility tensor  $\chi^{(3)}(-\omega; \omega, -\omega, \omega)$  with  $u, v, w$  the main axes of the cubic crystal structure are [16]:

$$\begin{aligned}
 \chi_{uuuu}^{(3)}(-\omega; \omega, -\omega, \omega) &= \chi_{vvvv}^{(3)}(-\omega; \omega, -\omega, \omega) = \chi_{wwww}^{(3)}(-\omega; \omega, -\omega, \omega) \\
 &\equiv \chi_1^{(3)}(-\omega; \omega, -\omega, \omega) \\
 \chi_{uuvv}^{(3)}(-\omega; \omega, -\omega, \omega) &= \chi_{vvuu}^{(3)}(-\omega; \omega, -\omega, \omega) = \chi_{uuww}^{(3)}(-\omega; \omega, -\omega, \omega) \\
 &= \chi_{wuuu}^{(3)}(-\omega; \omega, -\omega, \omega) = \chi_{vvww}^{(3)}(-\omega; \omega, -\omega, \omega) \\
 &= \chi_{wwvv}^{(3)}(-\omega; \omega, -\omega, \omega) = \chi_{uuvv}^{(3)}(-\omega; \omega, -\omega, \omega) \\
 &= \chi_{vuuu}^{(3)}(-\omega; \omega, -\omega, \omega) = \chi_{uwwu}^{(3)}(-\omega; \omega, -\omega, \omega) \\
 &= \chi_{uuuu}^{(3)}(-\omega; \omega, -\omega, \omega) = \chi_{vwww}^{(3)}(-\omega; \omega, -\omega, \omega) \\
 &= \chi_{wvvv}^{(3)}(-\omega; \omega, -\omega, \omega) \\
 &\equiv \chi_2^{(3)}(-\omega; \omega, -\omega, \omega) \\
 \chi_{uvuv}^{(3)}(-\omega; \omega, -\omega, \omega) &= \chi_{vuvu}^{(3)}(-\omega; \omega, -\omega, \omega) = \chi_{uuvw}^{(3)}(-\omega; \omega, -\omega, \omega) \\
 &= \chi_{wuuu}^{(3)}(-\omega; \omega, -\omega, \omega) = \chi_{vwww}^{(3)}(-\omega; \omega, -\omega, \omega) \\
 &= \chi_{wvvv}^{(3)}(-\omega; \omega, -\omega, \omega) \\
 &\equiv \chi_3^{(3)}(-\omega; \omega, -\omega, \omega)
 \end{aligned}$$

In this way, the third-order polarization in equation (2.19) becomes,

$$\begin{aligned}
 P_{u,\omega}^{(3)} &= \frac{3}{4}\epsilon_0 \left[ \chi_1^{(3)}(-\omega, \omega, -\omega, \omega) |E_{u,\omega}|^2 E_{u,\omega} \right. \\
 &\quad + 2\chi_2^{(3)}(-\omega, \omega, -\omega, \omega) (|E_{v,\omega}|^2 + |E_{w,\omega}|^2) E_{u,\omega} \\
 &\quad \left. + \chi_3^{(3)}(-\omega, \omega, -\omega, \omega) (E_{v,\omega}^2 + E_{w,\omega}^2) E_{u,\omega}^* \right] \quad (\text{A.1})
 \end{aligned}$$

$$\begin{aligned}
P_{v,\omega}^{(3)} &= \frac{3}{4}\epsilon_0 \left[ \chi_1^{(3)}(-\omega, \omega, -\omega, \omega) |E_{v,\omega}|^2 E_{v,\omega} \right. \\
&\quad + 2\chi_2^{(3)}(-\omega, \omega, -\omega, \omega) (|E_{w,\omega}|^2 + |E_{u,\omega}|^2) E_{v,\omega} \\
&\quad \left. + \chi_3^{(3)}(-\omega, \omega, -\omega, \omega) (E_{w,\omega}^2 + E_{u,\omega}^2) E_{v,\omega}^* \right] \quad (\text{A.2})
\end{aligned}$$

$$\begin{aligned}
P_{w,\omega}^{(3)} &= \frac{3}{4}\epsilon_0 \left[ \chi_1^{(3)}(-\omega, \omega, -\omega, \omega) |E_{w,\omega}|^2 E_{w,\omega} \right. \\
&\quad + 2\chi_2^{(3)}(-\omega, \omega, -\omega, \omega) (|E_{u,\omega}|^2 + |E_{v,\omega}|^2) E_{w,\omega} \\
&\quad \left. + \chi_3^{(3)}(-\omega, \omega, -\omega, \omega) (E_{u,\omega}^2 + E_{v,\omega}^2) E_{w,\omega}^* \right] \quad (\text{A.3})
\end{aligned}$$

This means that only the linear field polarizations  $(\pm 1, 0, 0)$ ,  $(0, \pm 1, 0)$ ,  $(0, 0, \pm 1)$ ;  $(\pm \frac{1}{\sqrt{2}}, \pm \frac{1}{\sqrt{2}}, 0)$ ,  $(\pm \frac{1}{\sqrt{2}}, 0, \pm \frac{1}{\sqrt{2}})$ ,  $(0, \pm \frac{1}{\sqrt{2}}, \pm \frac{1}{\sqrt{2}})$  and  $(\pm \frac{1}{\sqrt{3}}, \pm \frac{1}{\sqrt{3}}, \pm \frac{1}{\sqrt{3}})$  really have a Kerr-nonlinear behaviour<sup>1</sup>. These are the only linear cases that can be described by a single  $\chi^{(3)}(-\omega; \omega, -\omega, \omega)$ , which is respectively given by,

$$\chi^{(3)}(-\omega; \omega, -\omega, \omega) = \chi_1^{(3)}(-\omega, \omega, -\omega, \omega) \quad (\text{A.4})$$

$$\begin{aligned}
\chi^{(3)}(-\omega; \omega, -\omega, \omega) &= \frac{1}{2}\chi_1^{(3)}(-\omega, \omega, -\omega, \omega) + \chi_2^{(3)}(-\omega, \omega, -\omega, \omega) \\
&\quad + \frac{1}{2}\chi_3^{(3)}(-\omega, \omega, -\omega, \omega) \quad (\text{A.5})
\end{aligned}$$

$$\begin{aligned}
\chi^{(3)}(-\omega; \omega, -\omega, \omega) &= \frac{1}{3}\chi_1^{(3)}(-\omega, \omega, -\omega, \omega) + \frac{4}{3}\chi_2^{(3)}(-\omega, \omega, -\omega, \omega) \\
&\quad + \frac{2}{3}\chi_3^{(3)}(-\omega, \omega, -\omega, \omega) \quad (\text{A.6})
\end{aligned}$$

so that  $\mathbf{P}_\omega^{(3)}$  becomes,

$$\mathbf{P}_\omega^{(3)} = \frac{3}{4}\epsilon_0 \chi^{(3)}(-\omega, \omega, -\omega, \omega) |E_\omega|^2 \mathbf{E}_\omega \quad (\text{A.7})$$

with<sup>2</sup>  $|E_\omega|^2 = |E_{u,\omega}|^2 + |E_{v,\omega}|^2 + |E_{w,\omega}|^2$ .

In addition, the circular polarizations  $(\pm \frac{1}{\sqrt{2}}, \pm j \frac{1}{\sqrt{2}}, 0)$ ,  $(\pm \frac{1}{\sqrt{2}}, 0, \pm j \frac{1}{\sqrt{2}})$ ,  $(0, j \pm \frac{1}{\sqrt{2}}, \pm \frac{1}{\sqrt{2}})$  and  $(\pm \frac{1}{\sqrt{3}}, \pm \frac{1}{\sqrt{3}} \exp(\pm j \frac{2\pi}{3}), \pm \frac{1}{\sqrt{3}} \exp(\mp j \frac{2\pi}{3}))$  can also be described by a single third-order polar-

<sup>1</sup>In the other cases, the Kerr-nonlinear behaviour is accompanied with polarization rotation as described in [40].

<sup>2</sup>e.g. in the case  $(\pm \frac{1}{\sqrt{2}}, \pm \frac{1}{\sqrt{2}}, 0)$ , this means that  $|E_\omega|^2 = |E_{u,\omega}|^2 + |E_{v,\omega}|^2$  and  $|E_{u,\omega}|^2 = |E_{v,\omega}|^2 = \frac{|E_\omega|^2}{2}$ .

ization, namely,

$$\begin{aligned} \chi^{(3)}(-\omega; \omega, -\omega, \omega) &= \frac{1}{2}\chi_1^{(3)}(-\omega, \omega, -\omega, \omega) + \chi_2^{(3)}(-\omega, \omega, -\omega, \omega) \\ &\quad - \frac{1}{2}\chi_3^{(3)}(-\omega, \omega, -\omega, \omega) \end{aligned} \quad (\text{A.8})$$

$$\begin{aligned} \chi^{(3)}(-\omega; \omega, -\omega, \omega) &= \frac{1}{3}\chi_1^{(3)}(-\omega, \omega, -\omega, \omega) + \frac{4}{3}\chi_2^{(3)}(-\omega, \omega, -\omega, \omega) \\ &\quad - \frac{1}{3}\chi_3^{(3)}(-\omega, \omega, -\omega, \omega) \end{aligned} \quad (\text{A.9})$$

Note that the circular  $\chi^{(3)}(-\omega; \omega, -\omega, \omega)$  values are always smaller than the corresponding linear polarization susceptibilities.



## Appendix B

# Effective nonlinear coefficients

In chapter 2, the transverse dimensions of the propagating light were not yet taken into account. In reality however, light is confined transversally, so that the field can generally not be assumed to be independent of the directions perpendicular to the propagation. As a result, an effective nonlinear coefficient should be used. Furthermore, because of the fact that the electric field in realistic structures may have different components of which the importance changes along the cross section, the nonlinear anisotropic behaviour of the material system will come into play (appendix A).

In this appendix, we will study the effective nonlinear propagation both in the two- and three-dimensional space. In the two-dimensional case, we will investigate the effects of polarization, anisotropy and multimode behaviour explicitly for the bound-electronic Kerr effect. The same method can be used for the two-photon absorption effect, leading to similar results. In the three-dimensional case, we will discuss a method from literature to calculate an effective nonlinear coefficient and validate it with the results of the two-dimensional study.

### B.1 Nonlinear effects in a slab waveguide

Consider a two-dimensional symmetric slab waveguide as shown in figure B.1.

Due to spatial invariation in the  $x$  direction, such a waveguide has two types of solutions [17]:

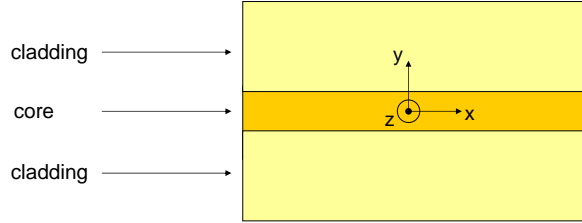


**Figure B.1:** Cross section of a two-dimensional symmetric slab waveguide.

- TE modes or transverse electric solutions, with only the field components  $E_x, H_y, H_z$ . The ground TE mode has electric field component  $E_x$  with positive parity, or  $\left. \frac{dE_x}{dy} \right|_{y=0} = 0$ .
- TM modes or transverse magnetic solutions, with only the field components  $H_x, E_y, E_z$ .  $E_y$  and  $E_z$  have a phase difference of  $\frac{\pi}{2}$ , which corresponds to an elliptic field polarization in the plane of propagation. Now, the ground TM mode has a  $E_y$  component with a positive parity, or  $\left. \frac{dE_y}{dy} \right|_{y=0} = 0$  (like  $E_x$  in the TE situation), while  $E_z$  has a negative parity, or  $E_z|_{y=0} = 0$ .

In the presence of nonlinear effects, this spatial symmetry will dictate the same types of solutions. However, because of the nonlinear field dependence, interaction between the different solutions is possible: interaction between different TE modes, interaction between different TM modes and interaction between both TE and TM modes. This complexity is even further increased by the material anisotropy discussed in appendix A.

Here, we will only examine two particular cases:

- the Kerr-nonlinearity in case of the ground TE mode with the  $x$ -axis along an axis which has exact Kerr-nonlinearity behaviour (so that a single  $\chi^{(3)}(-\omega; \omega, -\omega, \omega)$  value suffices to describe the complete effect. In this case, the field polarization is linear for each value of  $y$  (transverse direction).
- the Kerr-nonlinearity in case of the ground TM mode with the  $y$ - and  $z$ -axes both along a material axis (e.g. the  $y$ -axis along the material  $v$ -axis and the  $z$ -axis along the material  $w$ -axis). In this case, the field polarization changes from linear along the  $y$ -axis at  $y = 0$  to almost linear along the  $z$ -axis for  $|y| \gg 0$ . Such a

mode does not have exact Kerr-nonlinear behaviour and must be described by two  $\chi^{(3)}(-\omega; \omega, -\omega, \omega)$  values.

In addition, only the forward field propagation is considered.

### B.1.1 Transverse electric case

The case of the ground TE mode is discussed first. In this case, equation (2.36), given by

$$\nabla^2 \mathbf{E}_\omega + \frac{\omega^2}{c^2} \left( 1 + \chi^{(1)}(-\omega, \omega) + \frac{3}{4} \chi^{(3)}(-\omega, \omega, -\omega, \omega) |E_\omega|^2 \right) \mathbf{E}_\omega = 0 \quad (\text{B.1})$$

simplifies to

$$\begin{aligned} \frac{\partial^2}{\partial y^2} E_{x,\omega} + \frac{\partial^2}{\partial z^2} E_{x,\omega} + \frac{\omega^2}{c^2} \left( 1 + \chi^{(1)}(-\omega, \omega) \right. \\ \left. + \frac{3}{4} \chi^{(3)}(-\omega, \omega, -\omega, \omega) |E_{x,\omega}|^2 \right) E_{x,\omega} = 0 \end{aligned} \quad (\text{B.2})$$

To solve this equation, a multi-scale approach [41] can be used: we introduce additional variables  $y_i$  and  $z_i$ , which are function of a parameter of 'importance'  $\epsilon^1$  and which provide us with additional degrees of 'freedom':

$$y_i = \epsilon^i y \quad (\text{B.3})$$

$$z_i = \epsilon^i z \quad (\text{B.4})$$

In this way, one obtains for the derivatives  $\partial_y = \frac{d}{dy}$  and  $\partial_z = \frac{d}{dz}$ :

$$\partial_y = \partial_{y,0} + \epsilon \partial_{y,1} + \epsilon^2 \partial_{y,2} + \dots \quad (\text{B.5})$$

$$\partial_z = \partial_{z,0} + \epsilon \partial_{z,1} + \epsilon^2 \partial_{z,2} + \dots \quad (\text{B.6})$$

with  $\partial_{y,i} = \frac{d}{dy_i}$  and  $\partial_{z,i} = \frac{d}{dz_i}$ . In addition, we expand  $E_\omega$  as a function of  $\epsilon$ :

$$E_\omega = E_{0,\omega} + \epsilon E_{1,\omega} + \epsilon^2 E_{2,\omega} + \dots \quad (\text{B.7})$$

The Kerr-nonlinearity which is assumed to be weak is taken to be proportional to  $\epsilon$ . If the terms with the same dependence on  $\epsilon$  are now

<sup>1</sup>A larger dependence on  $\epsilon$  corresponds to a less important contribution or a higher order of perturbation.

taken together, one obtains in the first two orders in  $\epsilon$ :

$$\partial_{y,0}^2 E_{0,x,\omega} + \partial_{z,0}^2 E_{0,x,\omega} + \frac{\omega^2}{c^2} \left(1 + \chi^{(1)}(-\omega, \omega)\right) E_{0,x,\omega} = 0 \quad (\text{B.8})$$

$$\begin{aligned} \partial_{y,0}^2 E_{1,x,\omega} + \partial_{z,0}^2 E_{1,x,\omega} + \frac{\omega^2}{c^2} \left(1 + \chi^{(1)}(-\omega, \omega)\right) E_{1,x,\omega} = \\ -2\partial_{y,0}\partial_{y,1} E_{0,x,\omega} - 2\partial_{z,0}\partial_{z,1} E_{0,x,\omega} \\ - \frac{3\omega^2}{4c^2} \chi^{(3)}(-\omega, \omega, -\omega, \omega) |E_{0,y,\omega}|^2 E_{0,x,\omega} \quad (\text{B.9}) \end{aligned}$$

Considering only one mode, the solution of the zeroth order equation in  $\epsilon$  becomes,

$$\begin{aligned} E_{0,x,\omega} = \exp(-j\gamma z_0) \left( A(y_1, z_1, \dots) \exp(-j\sqrt{k^2 - \gamma^2} y_0) \right. \\ \left. + B(y_1, z_1, \dots) \exp(j\sqrt{k^2 - \gamma^2} y_0) \right) \quad (\text{B.10}) \end{aligned}$$

with<sup>2</sup>

$$k = \frac{\omega}{c} \sqrt{1 + \chi^{(1)}(-\omega, \omega)} = \frac{\omega n_0}{c} \quad (\text{B.11})$$

The first order equation is then given by,

$$\begin{aligned} \partial_{y,0}^2 E_{1,x,\omega} + \partial_{z,0}^2 E_{1,x,\omega} + \frac{\omega^2}{c^2} \left(1 + \chi^{(1)}(-\omega, \omega)\right) E_{1,x,\omega} = \\ \left[ 2j\sqrt{k^2 - \gamma^2} (\partial_{y,1} A) + 2j\gamma (\partial_{z,1} A) - \frac{3\omega^2}{4c^2} \chi^{(3)}(-\omega, \omega, -\omega, \omega) \right. \\ \left. \left( |A|^2 + 2|B|^2 \right) A \right] \exp(-j\sqrt{k^2 - \gamma^2} y_0) \exp(-j\gamma z_0) \\ + \left[ -2j\sqrt{k^2 - \gamma^2} (\partial_{y,1} B) + 2j\gamma (\partial_{z,1} B) - \frac{3\omega^2}{4c^2} \chi^{(3)}(-\omega, \omega, -\omega, \omega) \right. \\ \left. \left( 2|A|^2 + |B|^2 \right) B \right] \exp(j\sqrt{k^2 - \gamma^2} y_0) \exp(-j\gamma z_0) + \dots \quad (\text{B.12}) \end{aligned}$$

The ... stand for nonsecular terms<sup>3</sup>, which are only needed to calculate  $E_{1,x,\omega}$ <sup>4</sup>. If now the secular terms with the same spatial dependence are

<sup>2</sup>neglecting single-photon absorption

<sup>3</sup>Nonsecular terms are terms that do not lead to the same spatial dependence as that of the homogeneous solution. These terms do not cause problems at  $y = \infty$  or  $z = \infty$ .

<sup>4</sup>In the case that  $\gamma = k$ , some of the nonsecular terms become secular, so that the following derivation is only valid for  $\gamma < k$ . The case  $\gamma = k$  has however been calculated in chapter 2 with as result,

$$E_{x,\omega} \equiv E_0 \exp \left[ -j \frac{\omega}{c} (n_0 + n_2 |E_0|^2) z \right] \quad (\text{B.13})$$

with  $E_0$  the field amplitude.

put equal to zero<sup>5</sup>, 'infinity' problems are avoided and the  $y_1$  and  $z_1$  dependence of  $A$  and  $B$  can be determined:

$$A = a(y_2, z_2, \dots) \exp \left[ -j \frac{\omega n_2}{c} \left( |a|^2 + 2|b|^2 \right) \sqrt{1 - \frac{\gamma^2}{k^2}} y_1 \right] \cdot \exp \left[ -j \frac{\omega n_2}{c} \left( |a|^2 + 2|b|^2 \right) \frac{\gamma}{k} z_1 \right] \quad (\text{B.14})$$

$$B = b(y_2, z_2, \dots) \exp \left[ j \frac{\omega n_2}{c} \left( 2|a|^2 + |b|^2 \right) \sqrt{1 - \frac{\gamma^2}{k^2}} y_1 \right] \cdot \exp \left[ -j \frac{\omega n_2}{c} \left( 2|a|^2 + |b|^2 \right) \frac{\gamma}{k} z_1 \right] \quad (\text{B.15})$$

with<sup>6</sup>

$$n_2 = \frac{3\chi^{(3)}(-\omega, \omega, -\omega, \omega)}{8n_0} \quad (\text{B.16})$$

Neglecting higher order contributions, the electric field becomes,

$$E_{x,\omega} = a \exp \left[ -j \frac{\omega}{c} \sqrt{1 - \frac{\gamma^2}{k^2}} \left( n_0 + n_2(|a|^2 + 2|b|^2) \right) y \right] \cdot \exp \left[ -j \frac{\omega \gamma}{c k} \left( n_0 + n_2(|a|^2 + 2|b|^2) \right) z \right] + b \exp \left[ j \frac{\omega}{c} \sqrt{1 - \frac{\gamma^2}{k^2}} \left( n_0 + n_2(2|a|^2 + |b|^2) \right) y \right] \cdot \exp \left[ -j \frac{\omega \gamma}{c k} \left( n_0 + n_2(2|a|^2 + |b|^2) \right) z \right] \quad (\text{B.17})$$

The spatial symmetry of the ground TE solution now dictates that  $\frac{dE_x}{dy} \Big|_{y=0} = 0$ , so one finally obtains for  $\gamma < k$ ,

$$E_{x,\omega} = -2ja \cos \left[ \frac{\omega}{c} \sqrt{1 - \frac{\gamma^2}{k^2}} \left( n_0 + 3n_2|a|^2 \right) y \right] \cdot \exp \left[ -j \frac{\omega \gamma}{c k} \left( n_0 + 3n_2|a|^2 \right) z \right] \quad (\text{B.18})$$

<sup>5</sup>This is possible because of the additional degrees of freedom that we have introduced.

<sup>6</sup>neglecting two-photon absorption

or

$$E_{x,\omega} \equiv E_0 \cos \left[ \frac{\omega}{c} \sqrt{1 - \frac{\gamma^2}{k^2}} \left( n_0 + \frac{3}{4} n_2 |E_0|^2 \right) y \right] \cdot \exp \left[ -j \frac{\omega}{c} \frac{\gamma}{k} \left( n_0 + \frac{3}{4} n_2 |E_0|^2 \right) z \right] \quad (\text{B.19})$$

with  $E_0$  the maximum field of the mode. In this equation,  $\gamma$  is still to be determined. This can be done by imposing the boundary conditions at the material interfaces.

In most cases, the transverse influence of the Kerr-nonlinear effect can be neglected and  $\gamma$  can be approximated by the effective linear propagation constant:

$$\gamma = \frac{\omega}{c} n_{0,eff} \quad (\text{B.20})$$

Special cases are the following:

- $\gamma = k$  (or  $n_{0,eff} = n_0$ ), representing a homogeneous and thus one-dimensional material system. Remember that for this case, the former derivation does not hold.
- $\gamma = \sqrt{k^2 - \frac{\pi^2}{L^2}}$  with  $L$  the width of the waveguide, representing the ground TE mode of a parallel plate metallic system.

With equation (B.20), the intensity dependence of the propagation constant can be written as,

$$\exp \left[ -j \frac{\omega}{c} \left( n_{0,eff} + \frac{3}{4} n_2 \frac{n_{0,eff}}{n_0} |E_0|^2 \right) z \right] \quad (\text{B.21})$$

This means that the effective nonlinear effect reduces to the fraction  $\frac{3}{4} \frac{n_{0,eff}}{n_0}$  of that in the case of plane waves (equation (2.39)). In terms of the same maximum field, the nonlinear interaction will therefore be the highest if  $n_{0,eff} \approx n_0$ . This means that in the case of a single mode photonic wire, the width should be as close to the second mode cut-off as possible.

### B.1.2 Transverse magnetic case

Now, the situation of the ground TM mode is examined. Equation (2.36) becomes,

$$\begin{aligned} & \frac{\partial^2}{\partial y^2} \begin{bmatrix} 0 \\ E_{z,\omega} \end{bmatrix} + \frac{\partial^2}{\partial z^2} \begin{bmatrix} E_{y,\omega} \\ 0 \end{bmatrix} - \frac{\partial^2}{\partial y \partial z} \begin{bmatrix} E_{z,\omega} \\ E_{y,\omega} \end{bmatrix} \\ & + \frac{\omega^2}{c^2} \left( 1 + \chi^{(1)}(-\omega, \omega) \right) \cdot \begin{bmatrix} E_{y,\omega} \\ E_{z,\omega} \end{bmatrix} \\ & + \frac{3\omega^2}{4c^2} \begin{bmatrix} \chi_1^{(3)} |E_{y,\omega}|^2 E_{y,\omega} + 2\chi_2^{(3)} |E_{z,\omega}|^2 E_{y,\omega} + \chi_3^{(3)} E_{z,\omega}^2 E_{y,\omega}^* \\ \chi_1^{(3)} |E_{z,\omega}|^2 E_{z,\omega} + 2\chi_2^{(3)} |E_{y,\omega}|^2 E_{z,\omega} + \chi_3^{(3)} E_{y,\omega}^2 E_{z,\omega}^* \end{bmatrix} = 0 \end{aligned} \quad (\text{B.22})$$

Due to the fact that  $E_y$  and  $E_z$  have a phase shift of  $\frac{\pi}{2}$  (see above), this equation further simplifies to,

$$\begin{aligned} & \frac{\partial^2}{\partial y^2} \begin{bmatrix} 0 \\ E_{z,\omega} \end{bmatrix} + \frac{\partial^2}{\partial z^2} \begin{bmatrix} E_{y,\omega} \\ 0 \end{bmatrix} - \frac{\partial^2}{\partial y \partial z} \begin{bmatrix} E_{z,\omega} \\ E_{y,\omega} \end{bmatrix} \\ & + \frac{\omega^2}{c^2} \left( 1 + \chi^{(1)}(-\omega, \omega) \right) \begin{bmatrix} E_{y,\omega} \\ E_{z,\omega} \end{bmatrix} \\ & + \frac{3\omega^2}{4c^2} \begin{bmatrix} \chi_a^{(3)} |E_{y,\omega}|^2 E_{y,\omega} + \chi_b^{(3)} |E_{z,\omega}|^2 E_{y,\omega} \\ \chi_a^{(3)} |E_{z,\omega}|^2 E_{z,\omega} + \chi_b^{(3)} |E_{y,\omega}|^2 E_{z,\omega} \end{bmatrix} = 0 \end{aligned} \quad (\text{B.23})$$

with

$$\chi_a^{(3)} = \chi_1^{(3)} \quad (\text{B.24})$$

$$\chi_b^{(3)} = 2\chi_2^{(3)} - \chi_3^{(3)} \quad (\text{B.25})$$

Using the same multi-scale method as for the TE case, the zeroth and first order equations in  $\epsilon$  become,

$$\partial_{z,0}^2 E_{0,y,\omega} - \partial_{y,0} \partial_{z,0} E_{0,z,\omega} + \frac{\omega^2}{c^2} \left( 1 + \chi^{(1)}(-\omega, \omega) \right) E_{0,y,\omega} = 0 \quad (\text{B.26})$$

$$\partial_{y,0}^2 E_{0,z,\omega} - \partial_{y,0} \partial_{z,0} E_{0,y,\omega} + \frac{\omega^2}{c^2} \left( 1 + \chi^{(1)}(-\omega, \omega) \right) E_{0,z,\omega} = 0 \quad (\text{B.27})$$

$$\begin{aligned}
& \partial_{z,0}^2 E_{1,y,\omega} - \partial_{y,0} \partial_{z,0} E_{1,z,\omega} + \frac{\omega^2}{c^2} \left(1 + \chi^{(1)}(-\omega, \omega)\right) E_{1,y,\omega} = \\
& -2\partial_{z,0} \partial_{z,1} E_{0,y,\omega} + \partial_{y,0} \partial_{z,1} E_{0,z,\omega} + \partial_{z,0} \partial_{y,1} E_{0,z,\omega} \\
& - \frac{3\omega^2}{4c^2} \left(\chi_a^{(3)} |E_{0,y,\omega}|^2 + \chi_b^{(3)} |E_{0,z,\omega}|^2\right) E_{0,y,\omega} \quad (B.28)
\end{aligned}$$

$$\begin{aligned}
& \partial_{y,0}^2 E_{1,z,\omega} - \partial_{y,0} \partial_{z,0} E_{1,y,\omega} + \frac{\omega^2}{c^2} \left(1 + \chi^{(1)}(-\omega, \omega)\right) E_{1,z,\omega} = \\
& -2\partial_{y,0} \partial_{y,1} E_{0,z,\omega} + \partial_{y,0} \partial_{z,1} E_{0,y,\omega} + \partial_{z,0} \partial_{y,1} E_{0,y,\omega} \\
& - \frac{3\omega^2}{4c^2} \left(\chi_a^{(3)} |E_{0,z,\omega}|^2 + \chi_b^{(3)} |E_{0,y,\omega}|^2\right) E_{0,z,\omega} \quad (B.29)
\end{aligned}$$

Considering again only one mode, the zeroth order solution in  $\epsilon$  becomes,

$$\begin{aligned}
E_{0,y,\omega} &= \gamma \left( A(y_1, z_1, \dots) \exp(-j\sqrt{k^2 - \gamma^2}y_0) \right. \\
& \quad \left. + B(y_1, z_1, \dots) \exp(j\sqrt{k^2 - \gamma^2}y_0) \right) \exp(-j\gamma z_0) \quad (B.30)
\end{aligned}$$

$$\begin{aligned}
E_{0,z,\omega} &= \sqrt{k^2 - \gamma^2} \left( -A(y_1, z_1, \dots) \exp(-j\sqrt{k^2 - \gamma^2}y_0) \right. \\
& \quad \left. + B(y_1, z_1, \dots) \exp(j\sqrt{k^2 - \gamma^2}y_0) \right) \exp(-j\gamma z_0) \quad (B.31)
\end{aligned}$$

With this, the first order equations can be written as,

$$\begin{aligned}
& \partial_{z,0}^2 E_{1,y,\omega} - \partial_{y,0} \partial_{z,0} E_{1,z,\omega} + \frac{\omega^2}{c^2} \left(1 + \chi^{(1)}(-\omega, \omega)\right) E_{1,y,\omega} = \\
& \exp(-j\sqrt{k^2 - \gamma^2}y_0) \exp(-j\gamma z_0) \left[ j(k^2 + \gamma^2) \partial_{z,1} A \right. \\
& \quad \left. + j\gamma \sqrt{k^2 - \gamma^2} (\partial_{y,1} A) - \frac{3\omega^2}{4c^2} \left( \chi_a^{(3)} \gamma^2 |A|^2 \right. \right. \\
& \quad \left. \left. + \chi_b^{(3)} (k^2 - \gamma^2) |A|^2 + 2\chi_a^{(3)} \gamma^2 |B|^2 \right) \gamma A \right] \\
& + \exp(j\sqrt{k^2 - \gamma^2}y_0) \exp(-j\gamma z_0) \left[ j(k^2 + \gamma^2) \partial_{z,1} B \right. \\
& \quad \left. - j\gamma \sqrt{k^2 - \gamma^2} (\partial_{y,1} B) - \frac{3\omega^2}{4c^2} \left( \chi_a^{(3)} \gamma^2 |B|^2 \right. \right. \\
& \quad \left. \left. + \chi_b^{(3)} (k^2 - \gamma^2) |B|^2 + 2\chi_a^{(3)} \gamma^2 |A|^2 \right) \gamma B \right] + \dots \quad (B.32)
\end{aligned}$$

$$\begin{aligned}
\partial_{y,0}^2 E_{1,z,\omega} - \partial_{y,0} \partial_{z,0} E_{1,y,\omega} + \frac{\omega^2}{c^2} \left( 1 + \chi^{(1)}(-\omega, \omega) \right) E_{1,z,\omega} = \\
\exp(-j\sqrt{k^2 - \gamma^2} y_0) \exp(-j\gamma z_0) \left[ -j(2k^2 - \gamma^2) \partial_{y,1} A \right. \\
\left. - j\gamma \sqrt{k^2 - \gamma^2} \partial_{z,1} A - \frac{3\omega^2}{4c^2} \left( \chi_a^{(3)}(k^2 - \gamma^2) |A|^2 \right. \right. \\
\left. \left. + \chi_b^{(3)} \gamma^2 |A|^2 + 2\chi_a^{(3)}(k^2 - \gamma^2) |B|^2 \right) (-\sqrt{k^2 - \gamma^2} A) \right] \\
+ \exp(j\sqrt{k^2 - \gamma^2} y_0) \exp(-j\gamma z_0) \left[ -j(2k^2 - \gamma^2) \partial_{y,1} B \right. \\
\left. + j\gamma \sqrt{k^2 - \gamma^2} \partial_{z,1} B - \frac{3\omega^2}{4c^2} \left( \chi_a^{(3)}(k^2 - \gamma^2) |B|^2 \right. \right. \\
\left. \left. + \chi_b^{(3)} \gamma^2 |B|^2 + 2\chi_a^{(3)}(k^2 - \gamma^2) |A|^2 \right) \sqrt{k^2 - \gamma^2} B \right] + \dots \quad (\text{B.33})
\end{aligned}$$

where the ... again stand for nonsecular terms, which allow the calculation of  $E_{1,y,\omega}$  and  $E_{1,z,\omega}$ <sup>7</sup>. This gives four differential equations, which determine  $\partial_{y,1} A$ ,  $\partial_{z,1} A$ ,  $\partial_{y,1} B$  and  $\partial_{z,1} B$ . Simplified, one gets,

$$\begin{aligned}
2jk^4(\partial_{y,1} A) &= \frac{3\omega^2}{4c^2} \left( \chi_a^{(3)}(k^4 - 2\gamma^4) (|A|^2 + 2|B|^2) \right. \\
&\quad \left. + \chi_b^{(3)} 2\gamma^4 |A|^2 \right) \sqrt{k^2 - \gamma^2} A \quad (\text{B.36})
\end{aligned}$$

$$\begin{aligned}
2jk^4(\partial_{z,1} A) &= \frac{3\omega^2}{4c^2} \left( \chi_a^{(3)}(k^4 - 2(k^2 - \gamma^2)^2) (|A|^2 + 2|B|^2) \right. \\
&\quad \left. + \chi_b^{(3)} 2(k^2 - \gamma^2)^2 |A|^2 \right) \gamma A \quad (\text{B.37})
\end{aligned}$$

$$\begin{aligned}
2jk^4(\partial_{y,1} B) &= \frac{3\omega^2}{4c^2} \left( \chi_a^{(3)}(k^4 - 2\gamma^4) (|B|^2 + 2|A|^2) \right. \\
&\quad \left. + \chi_b^{(3)} 2\gamma^4 |B|^2 \right) (-\sqrt{k^2 - \beta^2} B) \quad (\text{B.38})
\end{aligned}$$

$$\begin{aligned}
2jk^4(\partial_{z,1} B) &= \frac{3\omega^2}{4c^2} \left( \chi_a^{(3)}(k^4 - 2(k^2 - \gamma^2)^2) (|B|^2 + 2|A|^2) \right. \\
&\quad \left. + \chi_b^{(3)} 2(k^2 - \gamma^2)^2 |B|^2 \right) \gamma B \quad (\text{B.39})
\end{aligned}$$

<sup>7</sup>again, the same remark holds for the case in which  $\gamma = k$ : some of the terms assigned by ... are then secular, so that the further derivation is only valid for  $\gamma < k$ . The case  $\gamma = k$  has the same result as in the TE case, namely,

$$E_{y,\omega} \equiv E_0 \exp \left[ -j \frac{\omega}{c} (n_0 + n_2 |E_0|^2) z \right] \quad (\text{B.34})$$

$$E_{z,\omega} \equiv 0 \quad (\text{B.35})$$

with  $E_0$  the field amplitude.

which leads to,

$$\begin{aligned}
A = a(y_2, z_2, \dots) \exp & \left[ -j \frac{\omega}{c} \left( n_{2,a} \left( 1 - 2 \frac{\gamma^4}{k^4} \right) k^2 \left( |a|^2 + 2 |b|^2 \right) \right. \right. \\
& \left. \left. + 2 n_{2,b} \frac{\gamma^4}{k^4} k^2 |a|^2 \right) \sqrt{1 - \frac{\gamma^2}{k^2} y_1} \right] \cdot \\
& \exp \left[ -j \frac{\omega}{c} \left( n_{2,a} \left( 1 - 2 \left( 1 - \frac{\gamma^2}{k^2} \right)^2 \right) k^2 \left( |a|^2 + 2 |b|^2 \right) \right. \right. \\
& \left. \left. + 2 n_{2,b} \left( 1 - \frac{\gamma^2}{k^2} \right)^2 k^2 |a|^2 \right) \frac{\gamma}{k} z_1 \right] \quad (\text{B.40})
\end{aligned}$$

$$\begin{aligned}
B = b(y_2, z_2, \dots) \exp & \left[ j \frac{\omega}{c} \left( n_{2,a} \left( 1 - 2 \frac{\gamma^4}{k^4} \right) k^2 \left( |b|^2 + 2 |a|^2 \right) \right. \right. \\
& \left. \left. + 2 n_{2,b} \frac{\gamma^4}{k^4} k^2 |b|^2 \right) \sqrt{1 - \frac{\gamma^2}{k^2} y_1} \right] \cdot \\
& \exp \left[ -j \frac{\omega}{c} \left( n_{2,a} \left( 1 - 2 \left( 1 - \frac{\gamma^2}{k^2} \right)^2 \right) k^2 \left( |b|^2 + 2 |a|^2 \right) \right. \right. \\
& \left. \left. + 2 n_{2,b} \left( 1 - \frac{\gamma^2}{k^2} \right)^2 k^2 |b|^2 \right) \frac{\gamma}{k} z_1 \right] \quad (\text{B.41})
\end{aligned}$$

with<sup>8</sup>

$$n_{2,a} = \frac{3\chi^{(3)a}(-\omega, \omega, -\omega, \omega)}{8n_0} \quad (\text{B.42})$$

$$n_{2,b} = \frac{3\chi^{(3)b}(-\omega, \omega, -\omega, \omega)}{8n_0} \quad (\text{B.43})$$

Neglecting higher order contributions and applying the spatial symmetry of the ground TM solution, one finally obtains

$$\begin{aligned}
E_{y,\omega} = 2\gamma a \cos & \left[ \frac{\omega}{c} \sqrt{1 - \frac{\gamma^2}{k^2}} \left( n_0 + 3n_{2,a} \left( 1 - 2 \frac{\gamma^4}{k^4} \right) k^2 |a|^2 \right. \right. \\
& \left. \left. + 2n_{2,b} \frac{\gamma^4}{k^4} k^2 |a|^2 \right) y \right] \cdot \\
& \exp \left[ -j \frac{\omega}{c} \frac{\gamma}{k} \left( n_0 + 3n_{2,a} \left( 1 - 2 \left( 1 - \frac{\gamma^2}{k^2} \right)^2 \right) k^2 |a|^2 \right. \right. \\
& \left. \left. + 2n_{2,b} \left( 1 - \frac{\gamma^2}{k^2} \right)^2 k^2 |a|^2 \right) z \right] \quad (\text{B.44})
\end{aligned}$$

<sup>8</sup>neglecting two-photon absorption

$$\begin{aligned}
E_{z,\omega} = 2j\sqrt{k^2 - \gamma^2}a \sin \left[ \frac{\omega}{c} \sqrt{1 - \frac{\gamma^2}{k^2}} \left( n_0 + 3n_{2,a} \left( 1 - 2\frac{\gamma^4}{k^4} \right) k^2 |a|^2 \right. \right. \\
\left. \left. + 2n_{2,b} \frac{\gamma^4}{k^4} k^2 |a|^2 \right) y \right] \cdot \\
\exp \left[ -j \frac{\omega}{c} \frac{\gamma}{k} \left( n_0 + 3n_{2,a} \left( 1 - 2\left( 1 - \frac{\gamma^2}{k^2} \right)^2 \right) k^2 |a|^2 \right. \right. \\
\left. \left. + 2n_{2,b} \left( 1 - \frac{\gamma^2}{k^2} \right)^2 k^2 |a|^2 \right) z \right] \quad (B.45)
\end{aligned}$$

or

$$\begin{aligned}
E_{y,\omega} \equiv \frac{\gamma}{k} E_0 \cos \left[ \frac{\omega}{c} \sqrt{1 - \frac{\gamma^2}{k^2}} \left( n_0 + \frac{3}{4}n_{2,a} \left( 1 - 2\frac{\gamma^4}{k^4} \right) |E_0|^2 \right. \right. \\
\left. \left. + \frac{1}{2}n_{2,b} \frac{\gamma^4}{k^4} |E_0|^2 \right) y \right] \cdot \\
\exp \left[ -j \frac{\omega}{c} \frac{\gamma}{k} \left( n_0 + \frac{3}{4}n_{2,a} \left( 1 - 2\left( 1 - \frac{\gamma^2}{k^2} \right)^2 \right) |E_0|^2 \right. \right. \\
\left. \left. + \frac{1}{2}n_{2,b} \left( 1 - \frac{\gamma^2}{k^2} \right)^2 |E_0|^2 \right) z \right] \quad (B.46)
\end{aligned}$$

$$\begin{aligned}
E_{z,\omega} \equiv j\sqrt{1 - \frac{\gamma^2}{k^2}} E_0 \sin \left[ \frac{\omega}{c} \sqrt{1 - \frac{\gamma^2}{k^2}} \left( n_0 + \frac{3}{4}n_{2,a} \left( 1 - 2\frac{\gamma^4}{k^4} \right) |E_0|^2 \right. \right. \\
\left. \left. + \frac{1}{2}n_{2,b} \frac{\gamma^4}{k^4} |E_0|^2 \right) y \right] \cdot \\
\exp \left[ -j \frac{\omega}{c} \frac{\gamma}{k} \left( n_0 + \frac{3}{4}n_{2,a} \left( 1 - 2\left( 1 - \frac{\gamma^2}{k^2} \right)^2 \right) |E_0|^2 \right. \right. \\
\left. \left. + \frac{1}{2}n_{2,b} \left( 1 - \frac{\gamma^2}{k^2} \right)^2 |E_0|^2 \right) z \right] \quad (B.47)
\end{aligned}$$

with  $E_0$  the characteristic electric field. In general,  $E_0$  is not the maximum field. In this equation,  $\gamma$  is again to be determined by imposing the boundary conditions at the material interfaces. The same particular cases for  $\gamma$  hold as for the TE situation.

Using equation (B.20), the field dependence of the propagation constant is now given by

$$\exp \left[ -j \frac{\omega}{c} \left( n_{0,eff} + \left\{ \frac{3}{4} n_{2,a} \left( 1 - 2 \left( 1 - \frac{n_{0,eff}^2}{n_0^2} \right)^2 \right) + \frac{1}{2} n_{2,b} \left( 1 - \frac{n_{0,eff}^2}{n_0^2} \right)^2 \right\} \frac{n_{0,eff}}{n_0} |E_0|^2 \right) z \right]$$

As discussed before, the Kerr-nonlinear effect in the TM case cannot be determined by a single value of  $\chi^{(3)}(-\omega; \omega, -\omega, \omega)$ . However, as seen in section 2.8, the anisotropy of  $n_2$  is rather small and it can be shown that  $n_{2,a} \approx n_{2,b}$ . In this case, field dependence of the propagation constant reduces to

$$\exp \left[ -j \frac{\omega}{c} \left( n_{0,eff} + n_2 \left( \frac{3}{4} - \left( 1 - \frac{n_{0,eff}^2}{n_0^2} \right)^2 \right) \frac{n_{0,eff}}{n_0} |E_0|^2 \right) z \right] \quad (\text{B.48})$$

For the ground TM mode, the effective nonlinear effect reduces to the fraction  $\left( \frac{3}{4} - \left( 1 - \frac{n_{0,eff}^2}{n_0^2} \right)^2 \right) \frac{n_{0,eff}}{n_0}$  of that in the case of plane waves (equation (2.39)). In terms of the same characteristic field, the nonlinear interaction will again be the highest if  $n_{0,eff} \approx n_0$ . Note also that in this case

$$\left( \frac{3}{4} - \left( 1 - \frac{n_{0,eff}^2}{n_0^2} \right)^2 \right) \frac{n_{0,eff}}{n_0} \longrightarrow \frac{3}{4} \frac{n_{0,eff}}{n_0} \quad (\text{B.49})$$

which is the same Kerr-nonlinear behaviour as in the TE case. This can be explained as follows: for high linear effective indices,  $E_y$  is the dominant field with the same spacial dependence as  $E_x$  in the TE case<sup>9</sup>.

For low values of  $n_{0,eff}$  however, the longitudinal component of the electric field becomes dominant and the nonlinear behaviour is smaller (equation (B.46)).

## B.2 Effective nonlinear coefficients

### B.2.1 Definition

Until now, we expressed the index changes either as a function of the maximum or characteristic electric field (or equivalently intensity). In

<sup>9</sup>this is expected, since in a one dimensional situation, the TE and TM case are identical (for perpendicular incidence on possible interfaces)

practice however, one will typically be interested in the change in effective index as a function of the input power.

For a Kerr-nonlinear waveguide, the total effective index can be defined as

$$n_{eff} = n_{0,eff} + n_{2,eff}P \quad (\text{B.50})$$

with  $n_{0,eff}$  the linear effective index,  $n_{2,eff}$  the Kerr-nonlinear effective index and  $P$  the optical power given by,

$$P = \frac{1}{2} \text{Re} \int dx \int dy (\mathbf{E} \times \mathbf{H}^*) \cdot \mathbf{e}_z \quad (\text{B.51})$$

$$= \frac{1}{2} \text{Re} \int dx \int dy E_x H_y^* - H_x^* E_y \quad (\text{B.52})$$

The propagation is again assumed to be along the  $z$ -axis, while  $x$  and  $y$  define the plane perpendicular to the axis of propagation (see figure B.1). By using coupled mode theory, it can be derived that this nonlinear effective index  $n_{2,eff}$  is given by [134, 135, 136],

$$n_{2,eff} = \frac{1}{2} c \epsilon_0 \frac{\int dx \int dy n_0(x, y) n_2(x, y) |E(x, y)|^4}{\left[ \frac{1}{2} \text{Re} \int dx \int dy (\mathbf{E} \times \mathbf{H}^*) \cdot \mathbf{e}_z \right]^2} \quad (\text{B.53})$$

$$\equiv \frac{\int dx \int dy n_{2,I}(x, y) I(x, y)^2}{\left[ \frac{1}{2} \text{Re} \int dx \int dy (\mathbf{E} \times \mathbf{H}^*) \cdot \mathbf{e}_z \right]^2} \quad (\text{B.54})$$

with

$$I(x, y) = \frac{1}{2} \epsilon_0 c n_0(x, y) |E(x, y)|^2 \quad (\text{B.55})$$

Note that material anisotropy has not been taken into account.

Similarly, the total effective absorption can be defined as

$$\alpha_{total,eff} = \alpha_{eff} + \beta_{eff}P \quad (\text{B.56})$$

with  $\alpha_{eff}$  the effective linear absorption (or loss) coefficient and  $\beta_{eff}$  the effective two-photon absorption coefficient. In the same way, it can be derived that  $\beta_{eff}$  is given by [134, 135, 136]

$$\beta_{eff} = \frac{1}{2} c \epsilon_0 \frac{\int dx \int dy n_0(x, y) \beta(x, y) |E(x, y)|^4}{\left[ \frac{1}{2} \text{Re} \int dx \int dy (\mathbf{E} \times \mathbf{H}^*) \cdot \mathbf{e}_z \right]^2} \quad (\text{B.57})$$

$$\equiv \frac{\int dx \int dy \beta_I(x, y) I(x, y)^2}{\left[ \frac{1}{2} \text{Re} \int dx \int dy (\mathbf{E} \times \mathbf{H}^*) \cdot \mathbf{e}_z \right]^2} \quad (\text{B.58})$$

### B.2.2 Plane wave and parallel plate verification

To show the agreement of equation (B.53) with the results obtained by using the multi-scale approach, we now reconsider the plane wave and parallel plate case.

In the case of plane waves (TE and TM case of section B.1 with  $\gamma = k$ ) and a certain cross section  $A_{cross}$  perpendicular to the beam propagation, the index change  $n_{2,eff}P$  corresponds to formula (2.1), as is required. Indeed, for the TE case, the optical power  $P$  becomes,

$$P = \frac{1}{2} \text{Re} \int dx \int dy E_x H_y^* \quad (\text{B.59})$$

$$= \frac{1}{2} \text{Re} \int dx \int dy n_{0,eff} c \epsilon_0 |E_x|^2 \quad (\text{B.60})$$

$$= \frac{1}{2} n_{0,eff} c \epsilon_0 |E_0|^2 A_{cross} \quad (\text{B.61})$$

while for the TM case, the optical power  $P$  is given by,

$$P = \frac{1}{2} \text{Re} \int dx \int dy (-1) H_x^* E_y \quad (\text{B.62})$$

$$= \frac{1}{2} \text{Re} \int dx \int dy \frac{n_0^2}{n_{0,eff}} c \epsilon_0 |E_y|^2 \quad (\text{B.63})$$

$$= \frac{1}{2} \frac{n_0^2}{n_{0,eff}} c \epsilon_0 |E_0|^2 A_{cross} \quad (\text{B.64})$$

and since for plane waves, the linear effective index  $n_{0,eff}$  is equal to the linear refractive index  $n_0$ , both situations reduce to,

$$P = \frac{1}{2} n_0 c \epsilon_0 |E_0|^2 A_{cross} \quad (\text{B.65})$$

With this, the index change  $n_{2,eff}P$  becomes,

$$n_{2,eff}P = c \epsilon_0 \frac{\int dx \int dy n_0(x, y) n_2(x, y) |E(x, y)|^4}{[\text{Re} \int dx \int dy (\mathbf{E} \times \mathbf{H}^*) \cdot \mathbf{e}_z]} \quad (\text{B.66})$$

$$= c \epsilon_0 \frac{n_0 n_2 |E_0|^4 A_{cross}}{n_0 c \epsilon_0 |E_0|^2 A_{cross}} \quad (\text{B.67})$$

$$= n_2 |E_0|^2 \quad (\text{B.68})$$

which is what was expected.

For the parallel plate structure of section B.1 in the case of TE polarization, the optical power  $P$  becomes,

$$P = \frac{1}{2} \text{Re} \int dx \int dy E_x H_y^* \quad (\text{B.69})$$

$$= \frac{1}{2} \text{Re} \int dx \int dy n_{0,eff} c \epsilon_0 |E_x|^2 \quad (\text{B.70})$$

$$= \frac{1}{4} \pi n_{0,eff} c \epsilon_0 |E_0|^2 \quad (\text{B.71})$$

so that

$$n_{2,eff} P = c \epsilon_0 \frac{\int dx \int dy n_0(x, y) n_2(x, y) |E(x, y)|^4}{[\text{Re} \int dx \int dy (\mathbf{E} \times \mathbf{H}^*) \cdot \mathbf{e}_z]} \quad (\text{B.72})$$

$$= c \epsilon_0 \frac{\frac{3}{8} \pi n_0 n_2 |E_0|^4}{\frac{1}{2} \pi n_{0,eff} c \epsilon_0 |E_0|^2} \quad (\text{B.73})$$

$$= \frac{3}{4} n_2 \frac{n_0}{n_{0,eff}} |E_0|^2 \quad (\text{B.74})$$

For the TM case (with  $n_{2,a} = n_{2,b} \equiv n_2$ ), the optical power is,

$$P = \frac{1}{2} \text{Re} \int dx \int dy (-1) H_x^* E_y \quad (\text{B.75})$$

$$= \frac{1}{2} \text{Re} \int dx \int dy \frac{n_0^2}{n_{0,eff}} c \epsilon_0 |E_y|^2 \quad (\text{B.76})$$

$$= \frac{1}{4} \pi n_{0,eff} c \epsilon_0 |E_0|^2 \quad (\text{B.77})$$

and the predicted index change becomes,

$$n_{2,eff} P = c \epsilon_0 \frac{\int dx \int dy n_0(x, y) n_2(x, y) |E(x, y)|^4}{[\text{Re} \int dx \int dy (\mathbf{E} \times \mathbf{H}^*) \cdot \mathbf{e}_z]} \quad (\text{B.78})$$

$$= c \epsilon_0 \frac{\frac{1}{4} \pi n_0 n_2 \left( 3 - 4 \frac{n_{0,eff}^2}{n_0^2} + 4 \frac{n_{0,eff}^4}{n_0^4} \right) |E_0|^4}{\frac{1}{4} \pi n_{0,eff} c \epsilon_0 |E_0|^2} \quad (\text{B.79})$$

$$= \left( \frac{3}{4} - \frac{n_{0,eff}^2}{n_0^2} + \frac{n_{0,eff}^4}{n_0^4} \right) n_2 \frac{n_0}{n_{0,eff}} |E_0|^2 \quad (\text{B.80})$$

Comparing all these results with section B.1, it can be seen that equation (B.53) is able to predict the effective Kerr-nonlinear behaviour correctly for the TE case, both not for the TM case [134, 135, 136]. As

discussed, the main problem for TM is the existence of an electric field component in the direction of propagation. However, for  $n_{0,eff} \approx n_0$ , the error is still reasonably small.

In real three-dimensional structures, the guided modes of the structures are not anymore completely TE or TM, which further complicates the study of the Kerr-nonlinear behaviour. However, for quasi TE-modes and quasi TM-modes with  $n_{0,eff} \approx n_0$ , equation (B.53) provides a good approximation. In literature, this formula is indeed used for both TE and TM modes [36].

## Appendix C

# Linear properties of one-dimensional optical resonators

In this appendix, the linear properties of the one-dimensional resonator structure, defined in section 4.1, will be calculated and discussed analytically.

### C.1 Linear properties for 1 period

A rigorous calculation using the transfer matrix method is in principle possible, but is not suitable to derive analytical formulae. Therefore, a few approximations will first be introduced. The wavelength dependence of the absolute mirror transmission and reflection coefficients  $|t_{dbr}|$  and  $|r_{dbr}|$  is neglected. It is indeed so that the most important  $\lambda$ -dependence of these coefficients is included in their phase - especially for long mirrors - while their amplitude is more or less constant for wavelength variation of the order of the resonance bandwidth:

$$t_{dbr} = |t_{dbr}| e^{j\varphi_t} \approx |t_{dbr}|_{\nu_c} e^{j\varphi_t} \quad (\text{C.1})$$

$$r_{dbr} = |r_{dbr}| e^{j\varphi_r} \approx |r_{dbr}|_{\nu_c} e^{j\varphi_r} \quad (\text{C.2})$$

with

$$|r_{dbr}|^2 + |t_{dbr}|^2 = 1 \quad (\text{C.3})$$

For the mirrors defined in section 4.1, calculations show that

$$|t_{dbr}|_{\nu_c} = \frac{2n_a^{\frac{N_{dbr}}{2}} n_b^{\frac{N_{dbr}}{2}}}{n_a^{N_{dbr}} + n_b^{N_{dbr}}} \quad (\text{C.4})$$

$$|r_{dbr}|_{\nu_c} = \frac{n_a^{N_{dbr}} - n_b^{N_{dbr}}}{n_a^{N_{dbr}} + n_b^{N_{dbr}}} \quad (\text{C.5})$$

Numerical calculations show that the phases  $\varphi_t$  and  $\varphi_r$  have approximately a linear dependence on the frequency

$$\varphi_t = \pm \frac{\pi}{2} + \left. \frac{d\varphi_t}{d\nu} \right|_{\nu_c} (\nu - \nu_c) \quad (\text{C.6})$$

$$\varphi_r = 0 + \left. \frac{d\varphi_r}{d\nu} \right|_{\nu_c} (\nu - \nu_c) \quad (\text{C.7})$$

where the sign of  $\varphi_t$  depends on  $N_{dbr}$ ,  $m'$  and  $m''$ . Due to the symmetry of the mirror section, one also has  $\left. \frac{d\varphi_t}{d\nu} \right|_{\nu_c} = \left. \frac{d\varphi_r}{d\nu} \right|_{\nu_c} \equiv \left. \frac{d\varphi}{d\nu} \right|_{\nu_c}$ . With this, one can calculate total field transmission, which is the relation between the input field  $E_{in}$  and output field  $E_{out}$ :

$$t_{tot}(\nu) \equiv \frac{E_{out}}{E_{in}} \quad (\text{C.8})$$

$$= \frac{e^{-j\varphi_{in} - j\varphi_{cav} - j\varphi_{out}} |t_{dbr}|_{\nu_c}^2 e^{2j\varphi_t}}{1 - e^{2j\varphi_r - 2j\varphi_{cav}} |r_{dbr}|_{\nu_c}^2} \quad (\text{C.9})$$

$$= \frac{-e^{-j\varphi_{in} + j\varphi_{cav} - j\varphi_{out}} |t_{dbr}|_{\nu_c}^2}{e^{2j\left(N_{cav} \frac{\pi}{\nu_c} - \left. \frac{d\varphi}{d\nu} \right|_{\nu_c}\right)(\nu - \nu_c)} - |r_{dbr}|_{\nu_c}^2} \quad (\text{C.10})$$

with  $\varphi_i = 2\pi \frac{z}{c} n_i l_i$ .

The total intensity transmission  $|t_{tot}(\nu)|^2$  over a single resonator period is then given by

$$|t_{tot}(\nu)|^2 = \frac{|t_{dbr}|_{\nu_c}^4}{1 + |r_{dbr}|_{\nu_c}^4 - 2|r_{dbr}|_{\nu_c}^2 \cos \left[ 2 \left( N_{cav} \frac{\pi}{\nu_c} - \left. \frac{d\varphi}{d\nu} \right|_{\nu_c} \right) (\nu - \nu_c) \right]} \quad (\text{C.11})$$

and the total phase change  $\phi(\nu)$ <sup>1</sup> by

$$\begin{aligned} \phi(\nu) = & \pm \frac{\pi}{2} + \frac{\pi}{2\nu_c} (2N_{cav} - m'')(\nu - \nu_c) \\ & - \arctan \left\{ \frac{\sin \left[ 2 \left( N_{cav} \frac{\pi}{\nu_c} - \frac{d\varphi}{d\nu} \Big|_{\nu_c} \right) (\nu - \nu_c) \right]}{\cos \left[ 2 \left( N_{cav} \frac{\pi}{\nu_c} - \frac{d\varphi}{d\nu} \Big|_{\nu_c} \right) (\nu - \nu_c) \right] - |r_{dbr}|_{\nu_c}^2} \right\} \end{aligned} \quad (C.12)$$

In this equation, the frequency dependence is mainly dominated by the third term and therefore the second term can be neglected. For frequencies close to the resonance frequency,  $|t_{tot}(\nu)|^2$  and  $\phi(\nu)$  are in good approximation equal to

$$|t_{tot}(\nu)|^2 \approx \frac{1}{1 + \frac{4|r_{dbr}|_{\nu_c}^2}{|t_{dbr}|_{\nu_c}^4} \left( N_{cav} \frac{\pi}{\nu_c} - \frac{d\varphi}{d\nu} \Big|_{\nu_c} \right)^2 (\nu - \nu_c)^2} \quad (C.13)$$

$$\phi(\nu) \approx \pm \frac{\pi}{2} - \arctan \left[ \frac{2}{|t_{dbr}|_{\nu_c}^2} \left( N_{cav} \frac{\pi}{\nu_c} - \frac{d\varphi}{d\nu} \Big|_{\nu_c} \right) (\nu - \nu_c) \right] \quad (C.14)$$

Equation (C.13) shows the typical lorentzian transmission characteristic of a single resonator, while equation (C.14) shows that its output phase relation has a arctan behaviour. This is shown in figure C.1.

The only parameter left to be determined is now  $\frac{d\varphi}{d\nu} \Big|_{\nu_c}$ .

## C.2 Properties for $\infty$ periods

Using the Floquet-Bloch theory [97], the general dispersion relation for a period consisting of  $N$  layers was derived by induction and is given by

$$\begin{aligned} 2^{N+1} n_a n_b \dots n_N \cos(kL_{per}) = & \quad (C.15) \\ & \sum_{a \dots N=0}^1 (-1)^{a+\dots+N} \cos \left( (-1)^a k_a l_a + (-1)^b k_b l_b + \dots + (-1)^N k_N l_N \right) \\ & \left( (-1)^a n_a + (-1)^b n_b \right) \left( (-1)^b n_b + (-1)^c n_c \right) \dots \left( (-1)^N n_N + (-1)^a n_a \right) \end{aligned}$$

<sup>1</sup>Note the difference between  $\phi$  and  $\varphi$ .  $\phi$  will be used for the phase change over 1 period, while  $\varphi$  (typically with subscript) indicates a phase shift in general.

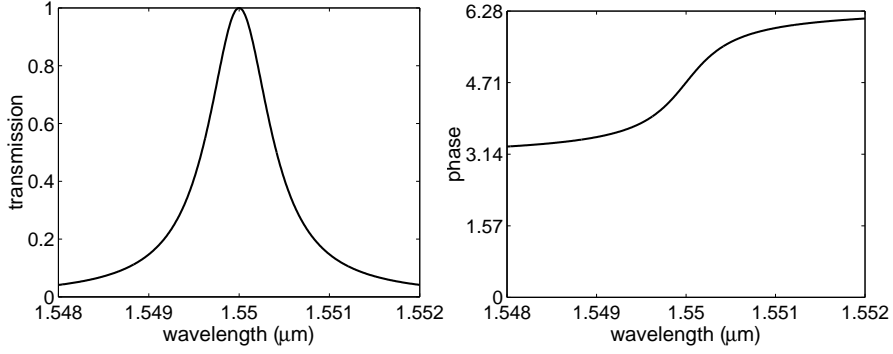


**Figure C.1:** Typical transmission  $|t_{tot}(\nu)|^2$  and phase relation  $\phi(\nu)$  of a single resonator. The following parameters were used:  $n_a = 2.37$ ,  $n_b = 0.9n_a$ ,  $N_{dbr} = 52$  and  $N_{cav} = 1$ .

with  $k_i = \frac{\omega}{c}n_i$ ,  $l_i$  the layer length and  $L_{per} = \sum l_i$  the period length<sup>2</sup>. In the case of the resonator period, this approach is not usable because there are too many layers. The dispersion relation around  $\nu = \nu_c$  is however approximately sinusoidal around the central frequency  $\nu_c$  [137], so it can be written as,

$$\nu - \nu_c = -\frac{\Delta\nu_{BW}}{2} \sin(kL_{per} \pm \frac{\pi}{2}) \quad (\text{C.17})$$

with  $\Delta\nu_{BW}$  the resonance bandwidth and the period length given by

$$L_{per} = \frac{\lambda_c}{4n_a} (m'(N_{dbr} - 1) + 2N_{cav}) + \frac{\lambda_c}{4n_b} (m''N_{dbr}) \quad (\text{C.18})$$

The exact sign depends on different structure parameters ( $m'$ ,  $m''$ ,  $N_{cav}$ ,  $N_{dbr}$ ), but is not very important for what follows.  $kL_{per}$  is the phase change between the input and output over a single period, denoted previously as  $\phi$ :

$$\phi(\nu) \pm \frac{\pi}{2} = -\arcsin\left(\frac{2}{\Delta\nu_{BW}}(\nu - \nu_c)\right) \quad (\text{C.19})$$

<sup>2</sup>For instance for  $N = 2$ , one has,

$$\begin{aligned} 8n_a n_b \cos(kL_{per}) = & \\ & \cos(k_a l_a + k_b l_b) (n_a + n_b)^2 - \cos(k_a l_a - k_b l_b) (n_a - n_b)^2 \\ & - \cos(-k_a l_a + k_b l_b) (-n_a + n_b)^2 + \cos(-k_a l_a - k_b l_b) (-n_a - n_b)^2 \end{aligned} \quad (\text{C.16})$$

which is nothing more than the dispersion relation for a DBR mirror.

Differentiation of equation (C.19) to the frequency gives

$$\left| \frac{d\phi}{d\nu} \right|_{\nu_c} = \frac{2}{\Delta\nu_{BW}} \quad (C.20)$$

so equation (C.19) can be written as

$$\phi(\nu) \pm \frac{\pi}{2} = -\arcsin \left( \left| \frac{d\phi}{d\nu} \right|_{\nu_c} (\nu - \nu_c) \right) \quad (C.21)$$

With the resonance bandwidth, another important parameter is associated, i.e. the Q-factor, which is a measure for the energy decay inside the cavity:

$$Q = \frac{\nu_c}{\Delta\nu_{BW}} \quad (C.22)$$

An analytical expression for  $\left| \frac{d\phi}{d\nu} \right|_{\nu_c}$  can now be obtained from equation (C.15). The calculation is straightforward, but very tedious, leading to

$$\begin{aligned} \left| \frac{d\phi}{d\nu} \right|_{\nu_c} = & \frac{\pi}{2\nu_c n_a^{N_{dbr}} n_b^{N_{dbr}}} \left[ m' n_a^2 n_b^2 \sum_{i=0}^{N_{dbr}-2} n_a^{2i} n_b^{2N_{dbr}-4-2i} \right. \\ & \left. + m'' n_a n_b \sum_{i=0}^{N_{dbr}-1} n_a^{2i} n_b^{2N_{dbr}-2-2i} + N_{cav} (n_a^{2N_{dbr}} + n_b^{2N_{dbr}}) \right] \end{aligned} \quad (C.23)$$

This can be rewritten as

$$\begin{aligned} \left| \frac{d\phi}{d\nu} \right|_{\nu_c} = & \frac{\pi}{2\nu_c} \left( \frac{n_b}{n_a} \right)^{N_{dbr}} \left[ m' \frac{n_a^2}{n_a^2 - n_b^2} \left( \left( \frac{n_a}{n_b} \right)^{2N_{dbr}-2} - 1 \right) \right. \\ & \left. + m'' \frac{n_a n_b}{n_a^2 - n_b^2} \left( \left( \frac{n_a}{n_b} \right)^{2N_{dbr}} - 1 \right) + N_{cav} \left( \left( \frac{n_a}{n_b} \right)^{2N_{dbr}} + 1 \right) \right] \end{aligned} \quad (C.24)$$

Using equation (C.5) or,

$$\left( \frac{n_a}{n_b} \right)^{N_{dbr}} = \frac{1 + |r_{dbr}|_{\nu_c}}{1 - |r_{dbr}|_{\nu_c}} \quad (C.25)$$

and equation (C.3), one finally obtains

$$\begin{aligned} \left| \frac{d\phi}{d\nu} \right|_{\nu_c} = & \frac{\pi}{2\nu_c |t_{dbr}|_{\nu_c}^2} \left[ (1 + |r_{dbr}|_{\nu_c}^2) (2N_{cav} - m') \right. \\ & \left. + 2|r_{dbr}|_{\nu_c} \frac{m'(n_a^2 + n_b^2) + 2m'' n_a n_b}{n_a^2 - n_b^2} \right] \end{aligned} \quad (C.26)$$

Equations (C.20), (C.21) and (C.26) fully describe the resonance bandwidth and the phase relation inside the bandwidth.

### C.3 Comparison between 1 and $\infty$ periods

The upper and lower limit for the number of resonator periods have now been calculated, namely 1 and  $\infty$ . We will now investigate how these two limits are related to each other. The two transmission and phase characteristics coincide exactly for one and only one frequency, that is for  $\nu = \nu_c$ . In that case,

$$|t_{tot}(\nu_c)|^2 = 1 \quad (\text{C.27})$$

$$\phi(\nu_c) = \pm \frac{\pi}{2} \quad (\text{C.28})$$

This could be expected as one has unity transmission for a single resonator period at the resonance frequency, making any number of periods decoupled. Also in the vicinity of  $\nu = \nu_c$ , both characteristics correspond very closely, while at the band edges the difference is quite large. This agreement was verified by simulations.

This observation allows to derive an analytical formula for  $\left. \frac{d\phi}{d\nu} \right|_{\nu_c}$ : starting from equations (C.14) and (C.21), one has around  $\nu = \nu_c$ ,

$$-\frac{\phi(\nu) \pm \frac{\pi}{2}}{\nu - \nu_c} \approx \frac{2}{|t_{dbr}|_{\nu_c}^2} \left( N_{cav} \frac{\pi}{\nu_c} - \left. \frac{d\phi}{d\nu} \right|_{\nu_c} \right) \quad (\text{C.29})$$

$$-\frac{\phi(\nu) \pm \frac{\pi}{2}}{\nu - \nu_c} \approx \left. \frac{d\phi}{d\nu} \right|_{\nu_c} \quad (\text{C.30})$$

so the phase derivative  $\left. \frac{d\phi}{d\nu} \right|_{\nu_c}$  is given by

$$\begin{aligned} \left. \frac{d\phi}{d\nu} \right|_{\nu_c} \approx & -\frac{\pi}{4\nu_c} \left( 2|r_{dbr}|_{\nu_c} \frac{m'(n_a^2 + n_b^2) + 2m''n_a n_b}{n_a^2 - n_b^2} - 4N_{cav} \right. \\ & \left. + (1 + |r_{dbr}|_{\nu_c}^2)(2N_{cav} - m') \right) \end{aligned} \quad (\text{C.31})$$

However, by definition,  $\left. \frac{d\phi}{d\nu} \right|_{\nu_c}$  cannot depend on  $N_{cav}$ , so

$$\left. \frac{d\phi}{d\nu} \right|_{\nu_c} \approx -\frac{\pi}{2\nu_c} \left( \frac{m'(n_a^2 + n_b^2) + 2m''n_a n_b}{n_a^2 - n_b^2} |r_{dbr}|_{\nu_c} - m' \right) \quad (\text{C.32})$$

This corresponds to taking the limit  $|r_{dbr}|_{\nu_c}^2 \rightarrow 1$ , but simulations show that this formula holds for every value of  $|r_{dbr}|_{\nu_c}^2$ .

As a result, the following transmission and phase relation can be used for the case of a single resonator structure:

$$|t_{tot}(\nu)|^2 \approx \frac{1}{1 + \left| \frac{d\phi}{d\nu} \right|_{\nu_c}^2 (\nu - \nu_c)^2} \quad (\text{C.33})$$

$$\phi(\nu) \approx \pm \frac{\pi}{2} - \arctan \left( \left| \frac{d\phi}{d\nu} \right|_{\nu_c} (\nu - \nu_c) \right) \quad (\text{C.34})$$

## C.4 Properties for $N$ periods

The transmission and phase characteristics for  $N$  periods will be somewhere between those for 1 and  $\infty$  periods. In the case of weak coupling between the resonators (i.e.  $|t_{dbr}|_{\nu_c}^2 \ll 1$ ), it is possible to calculate these characteristics using the results for a single period. The way to do this is explained in [138, 139].

For  $N = 2$ , this leads to<sup>3</sup>

$$|t_{tot}(\nu)|^2 = \frac{1}{1 + 4 \left| \frac{d\phi}{d\nu} \right|_{\nu_c}^4 (\nu - \nu_c)^4} \quad (\text{C.35})$$

$$\phi(\nu) = \pm \frac{\pi}{2} - \frac{1}{2} \arctan \left( \frac{2 \left| \frac{d\phi}{d\nu} \right|_{\nu_c}^2 (\nu - \nu_c)^2 - 1}{2 \left| \frac{d\phi}{d\nu} \right|_{\nu_c} (\nu - \nu_c)} \right) \quad (\text{C.36})$$

This transmission and phase relation are shown in figure C.2.

For  $N = 3$ , one obtains

$$|t_{tot}(\nu)|^2 = \frac{1}{1 + \left| \frac{d\phi}{d\nu} \right|_{\nu_c}^2 (\nu - \nu_c)^2 \left( 4 \left| \frac{d\phi}{d\nu} \right|_{\nu_c}^2 (\nu - \nu_c)^2 - 1 \right)^2} \quad (\text{C.37})$$

$$\phi(\nu) = \pm \frac{\pi}{2} - \frac{1}{3} \arctan \left( \frac{2 \left| \frac{d\phi}{d\nu} \right|_{\nu_c}^2 (\nu - \nu_c)^2 - 3}{4 \left| \frac{d\phi}{d\nu} \right|_{\nu_c} (\nu - \nu_c)} \right) \quad (\text{C.38})$$

and so on...

<sup>3</sup>Remember that  $\phi(\nu)$  is the phase change per period.

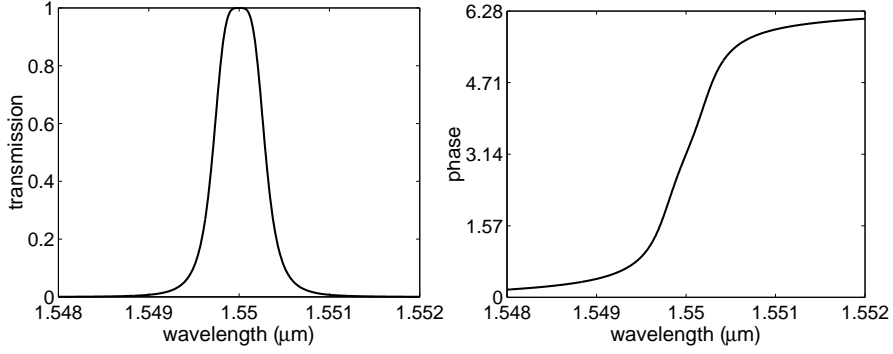


**Figure C.2:** Typical transmission  $|t_{tot}(\nu)|^2$  and phase relation  $2\phi(\nu)$  of a resonator with two periods. The following parameters were used:  $n_a = 2.37$ ,  $n_b = 0.9n_a$ ,  $N_{dbr} = 52$  and  $N_{cav} = 1$ .

Note that from equation (C.37), it can be seen that for three resonator periods, there are three frequencies for which the structure has unity transmission, i.e.

$$\nu_1 = \nu_c \quad (\text{C.39})$$

$$\nu_2 = \nu_c - \frac{1}{2 \left| \frac{d\phi}{d\nu} \right|_{\nu_c}} \quad (\text{C.40})$$

$$\nu_3 = \nu_c + \frac{1}{2 \left| \frac{d\phi}{d\nu} \right|_{\nu_c}} \quad (\text{C.41})$$

This is in contrast with the two resonator periods structure, for which only  $\nu = \nu_c$  has unity transmission (see equation (C.35)). The transmission and phase relation for a resonator with three periods are shown in figure C.3.

In general, a structure with  $p$  resonator periods has total transmission for  $p$  frequencies if  $p$  is odd, and for  $p - 1$  frequencies if  $p$  is even.

## C.5 Free spectral range

Until now, only the frequency region close to the resonance frequency  $\nu_c$  has been studied. However, from equations (C.10) and (C.11), it can be seen that the resonance around  $\nu_c$ , discussed above, is not the only

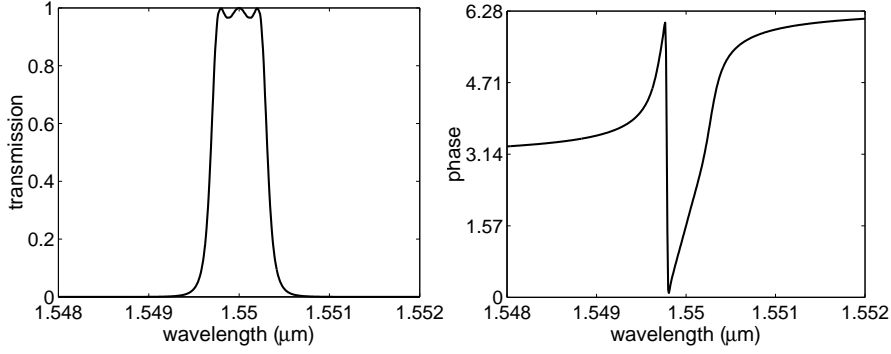


**Figure C.3:** Typical transmission  $|t_{tot}(\nu)|^2$  and phase relation  $3\phi(\nu)$  of a resonator with three periods. The following parameters were used:  $n_a = 2.37$ ,  $n_b = 0.9n_a$ ,  $N_{dbr} = 52$  and  $N_{cav} = 1$ .

resonance in the spectrum of a single resonator period. Other resonances occur at the frequencies,

$$\nu - \nu_c = q \frac{\pi}{N_{cav} \frac{\pi}{\nu_c} - \left. \frac{d\varphi}{d\nu} \right|_{\nu_c}} \quad (\text{C.42})$$

$$= q \frac{2\pi}{|t_{dbr}|_{\nu_c}^2 \left| \left. \frac{d\phi}{d\nu} \right|_{\nu_c} \right.} \quad (\text{C.43})$$

with  $q$  integer. This means that the different resonances are equally spaced with an intermediate distance of

$$FSR = \frac{2\pi}{|t_{dbr}|_{\nu_c}^2 \left| \left. \frac{d\phi}{d\nu} \right|_{\nu_c} \right.} \quad (\text{C.44})$$

which is called the free spectral range.

Based on equations (C.11) and (C.12), one would expect a complete spectrum consisting of equally spaced resonances. However, equations (C.1), (C.2), (C.4) and (C.5) are only valid for a limited frequency range, outside which the transmission relation does not consist of equally spaced resonances. This is shown in figure C.4. At the ends of this region, the resonances already show tremendous distortion. The width of this region is typically determined by the mirror index contrast. The resonator cavity itself (at least for small cavities) can typically be seen as a distortion of a continuous mirror consisting of  $a_{m'} \frac{\lambda_c}{4} b_{m''} \frac{\lambda_c}{4}$ -layers. Such

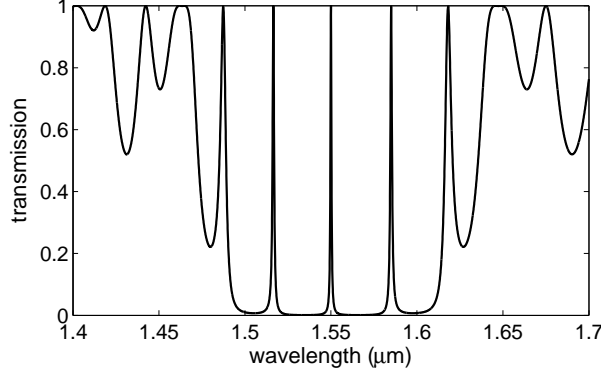


**Figure C.4:** Limited wavelength region consisting of equally spaced resonances. The case of  $n_a = 2.37$ ,  $n_b = 0.9n_a$ ,  $N_{dbr} = 36$  and  $N_{cav} = 40$  is considered. Outside this region, equations (C.1), (C.2), (C.4) and (C.5) are not anymore valid.

a structure has a bandgap centered around the resonance frequency  $\nu_c$  with a width  $\Delta\nu_{mirror}$  [97]:

$$\Delta\nu_{mirror} \approx \nu_c \frac{4}{\pi} \frac{n_a - n_b}{n_a + n_b} \quad (\text{C.45})$$

The cavity-like distortion now introduces a (series of) resonance(s) inside this bandgap centered around the specific frequency  $\nu_c$ : the center frequency  $\nu_c$  is therefore unique.

Other types of resonators such as ring resonators on the other hand do have a complete spectrum consisting of equally spaced resonances, in which case the frequency  $\nu_c$  is not anymore unique.

The effective modal length of the optical resonator can be associated with the free spectral range, which is defined as [95]:

$$L_{eff}^m = \frac{\int n_0^2(z) |E(z)|^2 dz}{\max(n_0^2(z) |E(z)|^2)} \quad (\text{C.46})$$

In good approximation, both parameters are related by

$$L_{eff}^m \approx N \frac{\lambda_c^2}{4n_0 FSR} \quad (\text{C.47})$$

which can be understood by considering equation (C.44) in the case that  $N_{cav} \rightarrow \infty$ , in which case  $L_{eff}^m = NL_{per}$ .

## C.6 Field profile

In the case of strong mirror sections ( $|t_{dbr}|_{\nu_c}^2 \ll 1$ ), the field profile inside this particular cavity will almost be a perfect standing wave. In the case of a single resonator, the maximum and minimum cavity field at the resonance frequency  $\nu = \nu_c$  are then given by

$$|E_{cav}|_{max} = \left(\frac{n_a}{n_b}\right)^{\frac{N_{dbr}}{2}} |E_{in}| \quad (C.48)$$

$$|E_{cav}|_{min} = \left(\frac{n_b}{n_a}\right)^{\frac{N_{dbr}}{2}} |E_{in}| \quad (C.49)$$

More generally, for any frequency  $\nu$ , maximum and minimum cavity field are

$$|E_{cav}|_{max} = \left(\frac{n_a}{n_b}\right)^{\frac{dbr}{2}} |t_{tot}(\nu)| |E_{in}| \quad (C.50)$$

$$|E_{cav}|_{min} = \left(\frac{n_b}{n_a}\right)^{\frac{dbr}{2}} |t_{tot}(\nu)| |E_{in}| \quad (C.51)$$

A typical field profile of a resonator with one period at resonance is shown in figure C.5. The field enhancement inside the cavity is approximately a factor 17.

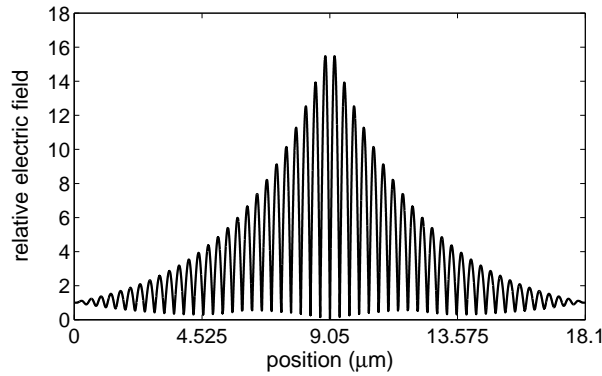


**Figure C.5:** Relative field profile  $\left|\frac{E(z)}{E_{in}}\right|$  at resonance for a resonator with one period (total resonator length  $L_{per}$  is 18.1  $\mu\text{m}$ ). The following parameters were used:  $n_a = 2.37$ ,  $n_b = 0.9n_a$ ,  $N_{dbr} = 52$  and  $N_{cav} = 1$ .

For more than one resonator period, the fields inside the different cavities are not equal, which means that equations (C.50)-(C.51) are

only valid for the last resonator. The only exception to this is for  $\nu = \nu_c$ , since for this frequency, every resonator period has total transmission and therefore they are independent.

## Appendix D

# Kerr-nonlinear properties of one-dimensional resonators

In this appendix, we will determine the Kerr-nonlinear properties of the one-dimensional resonator structure, defined in section 4.1.

The nonlinear effect on the transmission spectrum of a resonating structure can qualitatively be described as follows. The incoming light builds up inside the cavity and partially in the mirrors and therefore changes the refractive index of the complete structure. As a consequence, the round-trip phase will be different and thus the resonance peak and the output phase will shift. Due to these changes of the refractive index, the resonance bandwidth can also be different. In the most general case,  $n_{a,2} \neq n_{b,2}$ . It can roughly be said that the resonance shift is determined by the overall value of  $n_2$  (a shift to higher frequencies occurs for  $n_2 < 0$  and vice versa), while the change of bandwidth is due to the modulation of  $n_2$ .

In this work, we will assume that  $n_{a,2} \approx n_{b,2}$ , which is a good approximation for structures fabricated in a single material system. As a result, the change of resonance bandwidth will be neglected.

### D.1 Shift of resonance frequency

Since the electric field will be the strongest inside the cavity, it is interesting to consider first only the cavity as Kerr-nonlinear. To determine the nonlinear interaction inside the cavity, we solve the nonlinear wave equation (2.36) in one dimension with  $z$  the axis of propagation, in the

absence of single- and two-photon absorption by means of a multi-scale approach [41].

First the nonlinear enhancement in the cavity must be found. In section 2.4, the Kerr-nonlinear wave equation was derived for monochromatic plane waves, using a multi-scale approach. This method has already elaborately been discussed in appendix B.1. In the zeroth and first order, it leads to

$$\partial_0^2 E_{0,\omega} + \frac{\omega^2}{c^2} \left(1 + \chi^{(1)}(-\omega, \omega)\right) E_{0,\omega} = 0 \quad (\text{D.1})$$

$$\begin{aligned} \partial_0^2 E_{1,\omega} + \frac{\omega^2}{c^2} \left(1 + \chi^{(1)}(-\omega, \omega)\right) E_{1,\omega} = \\ -2\partial_0\partial_1 E_{0,\omega} - \frac{3\omega^2}{4c^2} \chi^{(3)}(-\omega, \omega, -\omega, \omega) |E_{0,\omega}|^2 E_{0,\omega} \end{aligned} \quad (\text{D.2})$$

In contrast to the results of section 2.4, both the forward and backward propagating waves now have to be taken into account as inside the cavity, the electric field approximates a standing wave. In zeroth order, the solution is then

$$E_{0,\omega} = E'_{f,\omega}(z_1, \dots) \exp(-jkz_0) + E'_{b,\omega}(z_1, \dots) \exp(jkz_0) \quad (\text{D.3})$$

with

$$k = \frac{\omega}{c} \sqrt{1 + \chi^{(1)}(-\omega, \omega)} \quad (\text{D.4})$$

$$= \frac{\omega n_0}{c} \quad (\text{D.5})$$

and equation (D.2) becomes

$$\begin{aligned} \partial_0^2 E_{1,\omega} + \frac{\omega^2}{c^2} \left(1 + \chi^{(1)}(-\omega, \omega)\right) E_{1,\omega} = \\ \left[2jk(\partial_1 E'_{f,\omega}) - \frac{3\omega^2}{4c^2} \chi^{(3)}(|E'_{f,\omega}|^2 + 2|E'_{b,\omega}|^2) E'_{f,\omega}\right] \exp(-jkz_0) \\ + \left[-2jk(\partial_1 E'_{b,\omega}) - \frac{3\omega^2}{4c^2} \chi^{(3)}(2|E'_{f,\omega}|^2 + |E'_{b,\omega}|^2) E'_{b,\omega}\right] \exp(jkz_0) \\ - \frac{3\omega^2}{4c^2} \chi^{(3)} [E'^2_{f,\omega} E'^*_{b,\omega} \exp(-3jkz_0) + E'^2_{b,\omega} E'^*_{f,\omega} \exp(3jkz_0)] \end{aligned} \quad (\text{D.6})$$

This leads to

$$E'_{f,\omega}(z_1, \dots) = E_{f,\omega}(z_2, \dots) \exp\left(-j\frac{\omega n_2}{c} (|E_{f,\omega}|^2 + 2|E_{b,\omega}|^2) z_1\right) \quad (\text{D.7})$$

$$E'_{b,\omega}(z_2, \dots) = E_{b,\omega}(z_2, \dots) \exp\left(j\frac{\omega n_2}{c} (2|E_{f,\omega}|^2 + |E_{b,\omega}|^2) z_1\right) \quad (\text{D.8})$$

with

$$n_2 = \frac{3\chi^{(3)}(-\omega, \omega, -\omega, \omega)}{8n_0} \quad (\text{D.9})$$

When the contribution of  $E_{1,\omega}$  to the electric field is neglected, the total field is given by

$$\begin{aligned} E_\omega = & E_{f,\omega} \exp\left(-j\frac{\omega}{c}\left(n_0 + n_2(|E_{f,\omega}|^2 + 2|E_{b,\omega}|^2)\right)z\right) \\ & + E_{b,\omega} \exp\left(j\frac{\omega}{c}\left(n_0 + n_2(2|E_{f,\omega}|^2 + |E_{b,\omega}|^2)\right)z\right) \end{aligned} \quad (\text{D.10})$$

To determine the nonlinear resonance frequency  $\nu'_c$ , the resonance condition (C.9) must be calculated:

$$2j\varphi_r - 2j\varphi_{cav} = q2\pi \quad (\text{D.11})$$

with  $q$  integer. Using the results above and from section C.6, the round-trip phase in the cavity  $2\varphi_{cav}$  is given by

$$2\varphi_{cav} = \varphi_{f,cav} + \varphi_{b,cav} \quad (\text{D.12})$$

$$= \pi \frac{\nu}{\nu_c} N_{cav} \frac{n_{a,0} + n_{a,2} \frac{1+2|r_{dbr}|_{\nu_c}^2}{|t_{dbr}|_{\nu_c}^2} |E_{out}|^2}{n_{a,0}} \quad (\text{D.13})$$

$$+ \pi \frac{\nu}{\nu_c} N_{cav} \frac{n_{a,0} + n_{a,2} \frac{2+|r_{dbr}|_{\nu_c}^2}{|t_{dbr}|_{\nu_c}^2} |E_{out}|^2}{n_{a,0}} \quad (\text{D.14})$$

$$= 2\pi \frac{\nu}{\nu_c} N_{cav} \left(1 + \frac{3}{2} \frac{n_{a,2}}{n_{a,0}} \frac{1 + |r_{dbr}|_{\nu_c}^2}{|t_{dbr}|_{\nu_c}^2} |E_{out}|^2\right) \quad (\text{D.15})$$

Together with equations (C.6)-(C.7), the resonance condition (C.9) is then:

$$2 \left. \frac{d\varphi}{d\nu} \right|_{\nu_c} (\nu - \nu_c) - 2\pi \frac{\nu}{\nu_c} N_{cav} \left(1 + \frac{3}{2} \frac{n_{a,2}}{n_{a,0}} \frac{1 + |r_{dbr}|_{\nu_c}^2}{|t_{dbr}|_{\nu_c}^2} |E_{out}|^2\right) \equiv q2\pi \quad (\text{D.16})$$

Solving this equation for  $\nu$  in both the linear and the nonlinear case finally leads to the following resonance shift:

$$\frac{\Delta\nu_c}{\nu_c} = - \frac{N_{cav}}{N_{cav} - \frac{\nu_c}{\pi} \left. \frac{d\varphi}{d\nu} \right|_{\nu_c}} \frac{3}{2} \frac{n_{a,2}}{n_{a,0}} \frac{1 + |r_{dbr}|_{\nu_c}^2}{|t_{dbr}|_{\nu_c}^2} |E_{in}|^2 \quad (\text{D.17})$$

$\left. \frac{d\varphi_t}{d\nu} \right|_{\nu_c} < 0$ , so the resonance shift asymptotically grows to  $-\frac{3}{2} \frac{n_{a,2}}{n_{a,0}} \frac{1+|r_{dbr}|_{\nu_c}^2}{|t_{dbr}|_{\nu_c}^2} |E_{in}|^2$  for large cavities or short mirrors. This can be explained as follows: due to the frequency dependence of the transmission phase  $\varphi_t(\nu)$  of the mirrors, a part of the nonlinear phase change of the cavity is used to compensated the phase shift  $\varphi_t(\nu_c + \Delta\nu_c) - \varphi_t(\nu_c)$ . As the frequency dependence of  $\varphi_t(\nu)$  is less pronounced for shorter mirrors, the asymptotical behaviour  $\Delta\nu_c \rightarrow -\frac{3}{2} \frac{n_{a,2}}{n_{a,0}} \frac{1+|r_{dbr}|_{\nu_c}^2}{|t_{dbr}|_{\nu_c}^2} |E_{in}|^2 \nu_c$  will be faster, as will it be for larger cavities since they provide a large phase change ( $\propto N_{cav}$ ). This has an important consequence: using  $N_{cav}$ -values larger than 1 can be very beneficial if large(r) resonance shifts are needed.

## D.2 Nonlinear transmission relation $|t_{tot,NL}|^2$

While in the case of  $\infty$  periods (band diagram) the Kerr-nonlinear effect just shifts the transmission window, this will not be the case for a finite number of periods. In that case, the resonance peak will shift with  $\Delta\nu_c$ , but frequencies with a lower linear transmission  $|t_{tot,L}|^2$  will not shift as much, because their (linear) average field will be less than the field at the linear resonance frequency  $\nu_c$ .

### D.2.1 Transmission of 1 resonator period

In section D.1, we have seen that the nonlinear effect inside the cavity scales with  $|E_{out}|^2$  and therefore with the transmission<sup>1</sup>. As a result, the frequency shift of any (linear) frequency  $\nu$  will be given by

$$\Delta\nu = |t_{tot,L}(\nu)|^2 \Delta\nu_c \quad (\text{D.18})$$

and the nonlinear transmission relation becomes<sup>2</sup>:

$$|t_{tot,NL}(\nu')|^2 = |t_{tot,L}(\nu)|^2 \quad (\text{D.19})$$

with  $\nu' = \nu + |t_{tot,L}(\nu)|^2 \Delta\nu_c = \nu + |t_{tot,NL}(\nu')|^2 \Delta\nu_c$ . This is also explained in figure D.1.

<sup>1</sup>In the case that only the cavity is Kerr-nonlinear, this is always correct. In the more general case of a fully nonlinear resonator, this is in good approximation correct, except for very low transmissions, in which case the field profile becomes strongly asymmetrical.

<sup>2</sup>This can easily be seen like this: if  $\nu = \nu_c$ , then  $\nu' = \nu'_c$  so indeed  $|t_{tot,NL}(\nu')|^2 = |t_{tot,L}(\nu)|^2$

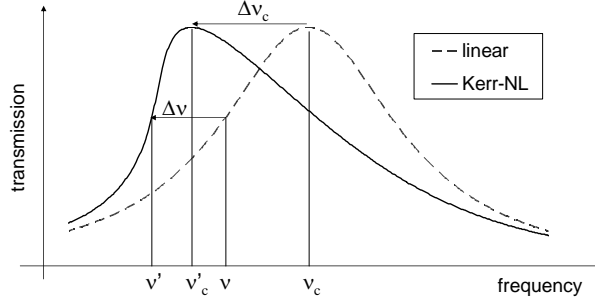


**Figure D.1:** Terminology in connection with the Kerr-nonlinear resonance shift.

Using equation (C.33), this leads to

$$|t_{tot,NL}(\nu')|^6 - 2\frac{\nu' - \nu_c}{\Delta\nu_c} |t_{tot,NL}(\nu')|^4 + \left( \frac{\Delta\nu_{BW}^2}{4\Delta\nu_c^2} + \left( \frac{\nu' - \nu_c}{\Delta\nu_c} \right)^2 \right) |t_{tot,NL}(\nu')|^2 - \frac{\Delta\nu_{BW}^2}{4\Delta\nu_c^2} = 0 \quad (\text{D.20})$$

This is in agreement with literature [140]. As the coefficients of this third order equation in  $|t_{tot,NL}(\nu')|^2$  are real for every frequency, one solution is always real and the other two solutions can be either complex conjugates or also real. In the latter case, one has three possible solutions for the same frequency, of which only two are stable - the solution is said to be bistable (see also section 4.2.1.1).

An example of this is shown in figure D.2. For low input intensities, the resonance shift is still relatively small. In this case, equation (D.20) has only one solution for each frequency. For higher input intensities, the resonance shift increases and finally becomes so high that a frequency region, in which three real solutions are possible, originates. In this region, the curve has a hysteresis-like form and only the upper and lower solution are stable. Note that in both figures, the frequency shifts are in good approximation proportional to  $|t_{tot,NL}(\nu')|^2$ .

A bistable region is present if for two frequencies  $\nu_1, \nu_2$  with  $\nu_1 > \nu_2$ , one has that  $\nu'_1 < \nu'_2$  with  $\nu' = \nu + |t_{tot,L}(\nu)|^2 \Delta\nu_c = \nu + |t_{tot,NL}(\nu')|^2 \Delta\nu_c$ .

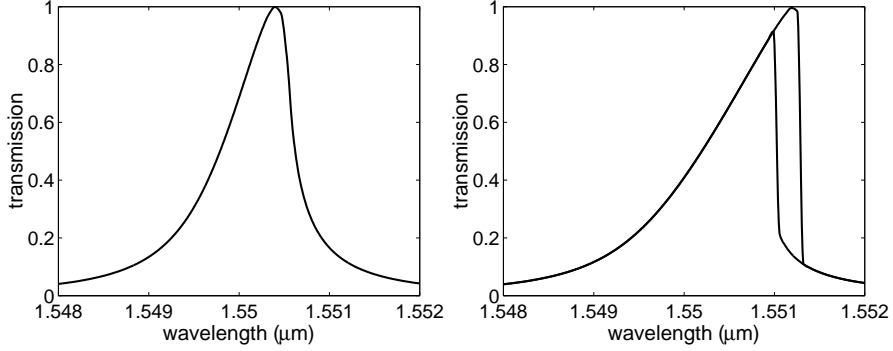


**Figure D.2:** Transmission of a resonator with one period without (left) and with (right) bistable region. The resonator parameters used are:  $n_a = 2.37$ ,  $n_b = 0.9n_a$ ,  $N_{dbr} = 52$  and  $N_{cav} = 1$ . An input power of  $n_2 |E_{in}|^2 = 0.6 \times 10^{-5}$  (left) and  $n_2 |E_{in}|^2 = 1.8 \times 10^{-5}$  (right) was inserted.

For the case  $n_2 > 0$ , this results in the following condition<sup>3</sup>

$$\exists \nu, \quad 0 < \left( \frac{d |t_{tot,L}(\nu)|^2}{d\nu} \right)^{-1} < -\Delta\nu_c \quad (\text{D.21})$$

while in the case of  $n_2 < 0$ , one has<sup>4</sup>

$$\exists \nu, \quad 0 < - \left( \frac{d |t_{tot,L}(\nu)|^2}{d\nu} \right)^{-1} < \Delta\nu_c \quad (\text{D.22})$$

The complete bistable region can then be obtained by solving

$$\left( \frac{d |t_{tot,L}(\nu)|^2}{d\nu} \right)^{-1} = -\Delta\nu_c \quad (\text{D.23})$$

and calculating  $\nu' = \nu + |t_{tot,L}(\nu)|^2 \Delta\nu_c$ . In this way, it can also be determined from which amount of resonance shift  $\Delta\nu_c$ , a bistable region appears. This is the case if equation (D.23) has a two-fold, real solution.

<sup>3</sup>This can be obtained by using  $|t_{tot,L}(\nu_1)|^2 > |t_{tot,L}(\nu_2)|^2$  (the bistability is on the lower frequency side) and taking the limit  $\nu_1 \rightarrow \nu_2$ .

<sup>4</sup>Now, one has  $|t_{tot,L}(\nu_1)|^2 < |t_{tot,L}(\nu_2)|^2$  (the bistability is on the higher frequency side) and one must again take the limit  $\nu_1 \rightarrow \nu_2$ .

Using equation (C.33), bistability arises if,

$$|\Delta\nu_c| > \frac{4\sqrt{3}}{9}\Delta\nu_{BW} \quad (\text{D.24})$$

and the two-fold solution is given by,

$$\nu_{sol} = \nu_c \pm \frac{\sqrt{3}}{2}\Delta\nu_{BW} \quad (\text{D.25})$$

depending on the sign of  $\Delta\nu_c$ . As a result, the frequency interval  $\left[\nu_c - \frac{\sqrt{3}}{2}\Delta\nu_{BW}, \nu_c + \frac{\sqrt{3}}{2}\Delta\nu_{BW}\right]$  can never be bistable.

### D.2.2 Transmission of $\infty$ resonator periods

The resonance frequency shift will still be given by  $\Delta\nu_c$ , since at resonance every period is independent and has the same field profile. Furthermore, as the resonance bandwidth is assumed to be constant, the transmission window is simply shifted compared to the linear situation.

It must again be noted that there exists a bistable region: this region is found at the upper frequency end if  $n_2 < 0$  en vice versa if  $n_2 > 0$ . The reason for this is that regions with  $|t_{tot,L}(\nu)|^2 = 0$  (almost<sup>5</sup>) do not feel any nonlinear interaction so that for these frequencies also  $|t_{tot,NL}(\nu)|^2 = 0$  is a true solution, independent from the fact that due to the shift of the transmission window, also  $|t_{tot,NL}(\nu)|^2 = 1$  is true.

### D.2.3 Transmission of $N$ resonator periods

For more than one resonator, the situation is much more complex. It must be taken into account that the field inside the different periods can have a different amplitude (see also section C.6) and therefore result in a different frequency shift. It is possible to obtain bistable and more generally multi-stable solutions [100]. At frequency  $\nu_c$ , the frequency shift can immediately be calculated and is again given by  $\Delta\nu_c$ .

<sup>5</sup>note that the field is not zero, only exponentially decaying.

### D.3 Nonlinear phase relation $\phi_{NL}$

#### D.3.1 Phase shift for 1 period

As it was assumed above that the resonance bandwidth change is negligible, one has

$$\left| \frac{d\phi_L}{d\nu} \right|_{\nu_c} \approx \left| \frac{d\phi_{NL}}{d\nu} \right|_{\nu'_c} \equiv \left| \frac{d\phi}{d\nu} \right|_{\nu_c} \quad (\text{D.26})$$

and the Kerr-nonlinear phase relation for one period will be given by

$$\phi_{NL}(\nu') \approx \pm \frac{\pi}{2} - \arctan \left( \left| \frac{d\phi}{d\nu} \right|_{\nu_c} (\nu - \nu_c) \right) \quad (\text{D.27})$$

$$= \pm \frac{\pi}{2} - \arctan \left( \left| \frac{d\phi}{d\nu} \right|_{\nu_c} (\nu' - \nu_c - |t_{tot,NL}(\nu')|^2 \Delta\nu_c) \right) \quad (\text{D.28})$$

with again  $\nu' = \nu + |t_{tot,L}(\nu)|^2 \Delta\nu_c = \nu + |t_{tot,NL}(\nu')|^2 \Delta\nu_c$ . This means that to determine  $\phi_{NL}(\nu')$ , one must first solve equation (D.20). Depending on the number of real solutions for  $|t_{tot,NL}(\nu')|^2$ , one can again have a bistable frequency region. The output phase relations corresponding to figure D.2 are respectively shown in figure D.3.

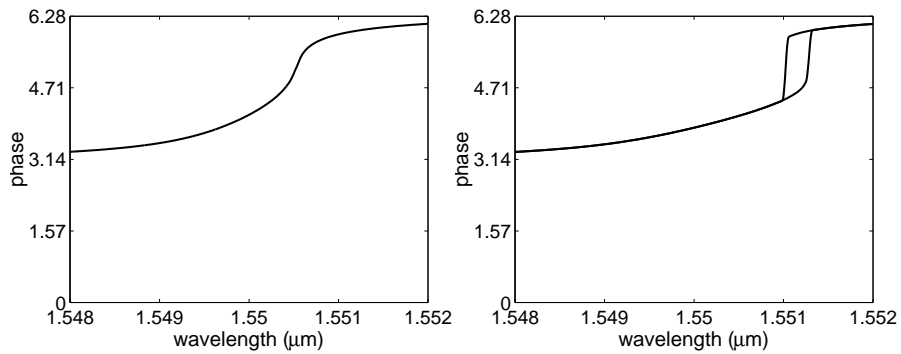


**Figure D.3:** Output phase relation of a resonator with one period without (left) and with (right) bistable region. The resonator parameters used are:  $n_a = 2.37$ ,  $n_b = 0.9n_a$ ,  $N_{dbr} = 52$  and  $N_{cav} = 1$ . An input power of  $n_2 |E_{in}|^2 = 0.6 \times 10^{-5}$  (left) and  $n_2 |E_{in}|^2 = 1.8 \times 10^{-5}$  (right) was inserted.

In general however, one will be interested in the phase shift in the neighborhood of the resonance peaks (e.g.  $\nu' = \frac{\nu_c + \nu'_c}{2}$ ). The equality

$$\nu + |t_{tot,L}(\nu)|^2 \Delta\nu_c = \frac{\nu_c + \nu'_c}{2} \quad (\text{D.29})$$

has a single real solution  $\nu = \nu_{sol}$ . For low frequency shifts for which  $|t_{tot,L}(\nu_{sol})|^2 \approx 1$ , the phase shift  $\Delta\phi$  will be given by

$$\Delta\phi \approx 2 \arctan \left( \left| \frac{d\phi}{d\nu} \right|_{\nu_c} \frac{\Delta\nu_c}{2} \right) \quad (\text{D.30})$$

### D.3.2 Phase shift for $\infty$ periods

For a structure with  $\infty$  resonator periods, the linear phase relation is given by equation (C.21) and the nonlinear phase relation is immediately<sup>6</sup>:

$$\phi_{NL}(\nu) = \pm \frac{\pi}{2} - \arcsin \left( \left| \frac{d\phi}{d\nu} \right|_{\nu_c} (\nu - \nu'_c) \right) \quad (\text{D.31})$$

So  $\Delta\phi$  is equal to

$$\Delta\phi = 2 \arcsin \left( \left| \frac{d\phi}{d\nu} \right|_{\nu_c} \frac{\Delta\nu_c}{2} \right) \quad (\text{D.32})$$

### D.3.3 Comparison and generalization

If small resonance shifts or large resonance bandwidths (which means a small value of  $\left| \frac{d\phi}{d\nu} \right|_{\nu_c}$ ) are assumed, equations (D.30) and (D.32) can be approximated as

$$\Delta\phi = \left| \frac{d\phi}{d\nu} \right|_{\nu_c} \Delta\nu_c \quad (\text{D.33})$$

which means that this  $\Delta\phi$  will also be valid for any finite number of periods  $N$ . This is shown in figure D.4.

The difference for equation (D.30) and simulations for the case  $N = 1$  has been discussed in section D.3.1. Note that formula (D.33) for  $\Delta\phi$  is completely in accordance with intuitive reasoning: a phase shift proportional to  $\Delta\nu_c$  and to  $\left| \frac{d\phi}{d\nu} \right|_{\nu_c}$  is indeed what one would expect.

<sup>6</sup>It must again be noted that in the bistable region of course two phase relation exist: the 'transmissive' one is given here, the other one is simply  $\phi_{NL}(\nu) = \pi$  if  $n_2 > 0$  and  $\phi_{NL}(\nu) = 0$  if  $n_2 < 0$

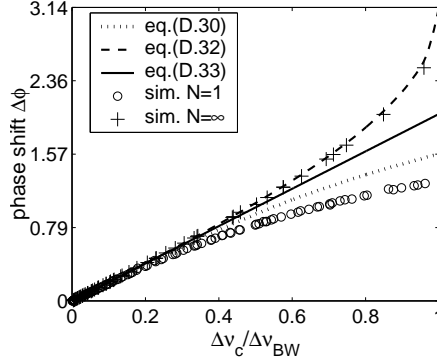


**Figure D.4:** Comparison between simulations and equations (D.30), (D.32) and (D.33).

## D.4 Modal theory approach

In section D.1, the resonance shift was determined in the case that only the cavity is Kerr-nonlinear. With the results of section D.3.3, we can extend this to a fully Kerr-nonlinear by means of modal theory [34, 141]. In this approach, the field profile along the propagation axis is assumed to be determined only by linear effects and in a 1D system, the nonlinear action then consists of changing the amplitude of the field along this axis. This approach is valid for weak nonlinearities (section 2.2).

The transmitted field  $E_t$  can generally be written as [141]

$$E_t(\omega) = t_{tot}(\omega)E_{in}(\omega) - \mu_0\omega^2 \int_0^{L_{tot}} G_t(\omega, z)P_{NL}(\omega, z) \quad (D.34)$$

with  $z$  the direction of propagation and

$$G_t(\omega, z) = t_{tot}(\omega)g_t(z) \quad (D.35)$$

where  $G_t(\omega, z)$  is the Green function of the structure with excitation located in the middle of the structure. The Kerr-nonlinear effect at a certain point  $z$  can now be written as (see also equation 2.20),

$$P_{NL}(\omega, z) = \epsilon_0 \frac{3}{4} \chi^{(3)}(-\omega, \omega, -\omega, \omega; z) |f(\omega, z)|^2 f(\omega, z) |E_t(\omega)|^2 E_t(\omega) \quad (D.36)$$

with  $f(\omega, z)$  the field profile along the  $z$ -axis for a certain frequency. Note that  $E_t(\omega)$  was used here and not  $E_{in}(\omega)$ , because, as said above,

the linear field profile along the z-axis is used, but its amplitude can change due to the nonlinear effects. Using (D.35) and (D.36), equation (D.34) now becomes:

$$E_t(\omega) = t_{tot}(\omega) \left( E_{in}(\omega) - \frac{3\omega^2}{4c^2} |E_t(\omega)|^2 E_t(\omega) \cdot \int_0^{L_{tot}} g_t(z) \chi^{(3)}(-\omega, \omega, -\omega, \omega; z) |f(\omega, z)|^2 f(\omega, z) \right) \quad (D.37)$$

#### D.4.1 Shift of phase relation $\phi$

Neglecting the nonlinear amplitude change for a moment and comparing equation (D.37) with

$$E_t(\omega) = E_{in}(\omega) t_{tot}(\omega) e^{j\varphi_{NL}} \quad (D.38)$$

$$\approx E_{in}(\omega) t_{tot}(\omega) (1 + j\varphi_{NL}) \quad (D.39)$$

the nonlinear phase shift  $\Delta\phi$  in the case of one resonator period is immediately given by

$$\Delta\phi \approx j \frac{3\omega^2}{4c^2} |t_{tot}(\omega)|^2 |E_{in}(\omega)|^2 \cdot \int_0^{L_{per}} g_t(z) \chi^{(3)}(-\omega, \omega, -\omega, \omega; z) |f(\omega, z)|^2 f(\omega, z) \quad (D.40)$$

$g_t(z)$  and  $f(z)$  are given by [141]

$$g_t(z) = -\frac{1}{2} \left( \mu_{12}(z) + j \frac{c}{\omega n_{a,0}} \mu_{22}(z) \right) \quad (D.41)$$

$$f(z) = \nu_{11}(z) - j \frac{\omega n_{a,0}}{c} \nu_{12}(z) \quad (D.42)$$

with  $\nu$  resp.  $\mu$  the transfer matrix of the electric field and its derivative from the input of the resonator period until  $z$  resp. from  $z$  until the output of the period. In other words, the total transfer matrix of the structure is in fact written as [142]

$$\begin{bmatrix} E_i \\ \frac{dE_i}{dz} \end{bmatrix} = \mu(z) \nu(z) \begin{bmatrix} E_{i+1} \\ \frac{dE_{i+1}}{dz} \end{bmatrix} \quad (D.43)$$

This is a different approach than in [97], however both transfer matrix representations are equivalent.

Now  $\Delta\phi$  can be calculated using equation (D.38). The calculations have been done for the case  $n_a > n_b$  around  $\nu = \nu_c$  in [34], leading to:

$$\Delta\phi \approx \frac{3\pi}{8} |E_{in}|^2 \left( \frac{n_{a,0}}{n_{b,0}} \right)^{2N_{dbr}} \frac{n_2}{n_{a,0}} \left( N_{cav} + \frac{m''n_{a,0}^4 + m'n_{b,0}^4}{n_{a,0}^4 - n_{b,0}^4} \right) \quad (D.44)$$

with  $n_2 \equiv n_{a,2} = n_{b,2}$ . From equation (D.44),  $\Delta\nu_c$  can be derived using equation (D.33) and one obtains,

$$\begin{aligned} \frac{\Delta\nu_c}{\nu_c} &= - \frac{N_{cav} + \frac{m''n_{a,0}^4 + m'n_{b,0}^4}{n_{a,0}^4 - n_{b,0}^4}}{N_{cav} - \frac{m'}{2} + \frac{1}{2} \frac{n_{a,0}^{2N_{dbr}} - n_{b,0}^{2N_{dbr}}}{n_{a,0}^{2N_{dbr}} + n_{b,0}^{2N_{dbr}}} \frac{m'(n_{a,0}^2 + n_{b,0}^2) + 2m'n_{a,0}n_{b,0}}{n_{a,0}^2 - n_{b,0}^2}} \\ &\quad \frac{3}{4} \left( \frac{n_{a,0}}{n_{b,0}} \right)^{N_{dbr}} \frac{n_{a,0}^{2N_{dbr}}}{n_{a,0}^{2N_{dbr}} + n_{b,0}^{2N_{dbr}}} \frac{n_2}{n_{a,0}} |E_{in}|^2 \quad (D.45) \end{aligned}$$

or

$$\begin{aligned} \frac{\Delta\nu_c}{\nu_c} &= - \frac{N_{cav} + \frac{m''n_{a,0}^4 + m'n_{b,0}^4}{n_{a,0}^4 - n_{b,0}^4}}{N_{cav} - \frac{m'}{2} + \frac{|r_{dbr}|}{2-|t_{dbr}|_{\nu_c}^2} \frac{m'(n_{a,0}^2 + n_{b,0}^2) + 2m'n_{a,0}n_{b,0}}{n_{a,0}^2 - n_{b,0}^2}} \\ &\quad \frac{3}{8} \frac{(1 + |r_{dbr}|_{\nu_c})^4}{|t_{dbr}|_{\nu_c}^2 (2 - |t_{dbr}|_{\nu_c}^2)} \frac{n_2}{n_{a,0}} |E_{in}|^2 \quad (D.46) \end{aligned}$$

Note the close agreement with equation (D.17) in absence of nonlinear mirrors. Comparing this formula with simulation data shows very good agreement. In the practical case that  $|r_{dbr}|_{\nu_c} \approx 1$ , the resonance shift is simply given by

$$\Delta\nu_c \approx - \frac{N_{cav} + \frac{m''n_{a,0}^4 + m'n_{b,0}^4}{n_{a,0}^4 - n_{b,0}^4}}{N_{cav} + n_{b,0} \frac{m''n_{a,0} + m'n_{b,0}}{n_{a,0}^2 - n_{b,0}^2}} \frac{3}{|t_{dbr}|_{\nu_c}^2} \frac{n_2}{n_{a,0}} |E_{in}|^2 \quad (D.47)$$

As  $\frac{N_{cav} + \frac{m''n_{a,0}^4 + m'n_{b,0}^4}{n_{a,0}^4 - n_{b,0}^4}}{N_{cav} + n_{b,0} \frac{m''n_{a,0} + m'n_{b,0}}{n_{a,0}^2 - n_{b,0}^2}} < 0$ , the resonance shift again asymptotically grows to  $-\frac{3}{|t_{dbr}|_{\nu_c}^2} \frac{n_2}{n_{a,0}} |E_{in}|^2$  for large cavities or short mirrors. This can be explained in the same way as in case of equation (D.17). Using equations (C.22) and (C.47), the limit of equation (D.47) for large cavities or

short mirrors for large cavities leads to:

$$\Delta\nu_c \propto \frac{Q}{L_{eff}^m} n_2 |E_{in}|^2 \quad (D.48)$$

In three dimensions, this corresponds to

$$\Delta\nu_c \propto \frac{Q}{V_{eff}^m} n_{2,eff} P_{in} \quad (D.49)$$

with  $V_{eff}^m$  the three-dimensional extension of the effective modal length  $L_{eff}^m$ , given by [95]:

$$V_{eff}^m = \frac{\int n_0^2(x, y, z) |E(x, y, z)|^2 dx dy dz}{\max(n_0^2(x, y, z) |E(x, y, z)|^2)} \quad (D.50)$$

which is in agreement with literature [140]. Using equation (C.22), one also obtains the relation:

$$\frac{\Delta\nu_c}{\Delta\nu_{BW}} \propto \frac{Q^2}{V_{eff}^m} n_{2,eff} P_{in} \quad (D.51)$$

Note however that equation (D.47) is also valid for small cavities and larger mirrors and is therefore to be preferred.



## Appendix E

# Two-photon absorption properties of one-dimensional resonators

In this appendix, we will examine the effect of two-photon absorption on one-dimensional resonator structures.

Qualitatively, two-photon absorption will cause a reduction of the transmission which depends on the optical power inside the cavity. The discussion will be limited to the case of a single resonator. Again, it is assumed that  $\beta_a = \beta_b$  in agreement with appendix D.

In the general case of counterpropagating waves, the multi-scale approach of appendix D cannot be used to study the effect of two-photon absorption. Therefore, simulation results from a large parameter variation of resonator structures will be applied to characterize the influence of two-photon absorption in a general way.

The total transmission, reflection and loss of any structure are for every frequency related by

$$|t_{tot}(\nu)|^2 + |r_{tot}(\nu)|^2 = B_{tot}^2(\nu) \quad (\text{E.1})$$

with  $t_{tot}(\nu)$  resp.  $r_{tot}(\nu)$  the total (nonlinear) field transmission resp. reflection and  $B_{tot}(\nu)$  the relative field amplitude after the complete resonator structure in the case of two-photon absorption. Two additional relations between  $|t_{tot}(\nu)|^2$ ,  $|r_{tot}(\nu)|^2$  and  $B_{tot}^2(\nu)$  now have to be found to determine these three quantities completely.

At nonlinear<sup>1</sup> resonance  $\nu'_c$  this is possible by fitting the simulation results presented in figure E.1. In this figure, the simulation results  $|r_{tot}(\nu'_c)|^2$  and  $1 - B_{tot}(\nu'_c)$  are plotted as a function of  $|t_{tot}(\nu'_c)|^2$  for a large variation of all resonator parameters: the refractive indices  $n_a$  and  $n_b$  of the two mirror materials were varied from 2.0 – 3.0 with  $n_a > n_b$ . Mirror and cavity lengths in the intervals  $N_{dbr} = 40 - 200$  and  $N_{cav} = 1 - 20$  were simulated with input fields leading to nonlinear effects of  $n_2|E_{in}|^2 = 10^{-6} - 10^{-4}$  and  $\beta\lambda_c|E_{in}|^2 = 10^{-6} - 10^{-4}$  for  $\lambda_c = 1.55\mu m$ .

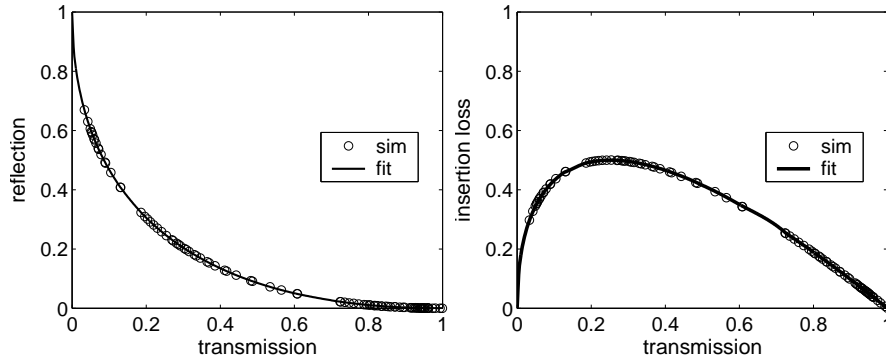


**Figure E.1:** Simulated results of total reflection  $|r_{tot}(\nu'_c)|^2$  and total insertion loss  $1 - B_{tot}(\nu'_c)$  as a function of total transmission  $|t_{tot}(\nu'_c)|^2$  for a large variation of all resonator parameters as indicated in the text.

The relation between  $|r_{tot}(\nu'_c)|^2$  and  $|t_{tot}(\nu'_c)|^2$  is symmetrical around  $|r_{tot}(\nu'_c)|^2 = |t_{tot}(\nu'_c)|^2$  and can therefore be expressed as

$$p + q(|t_{tot}(\nu'_c)|^2 + |r_{tot}(\nu'_c)|^2) + r|t_{tot}(\nu'_c)|^2|r_{tot}(\nu'_c)|^2 + s(|t_{tot}(\nu'_c)|^4 + |r_{tot}(\nu'_c)|^4) + \dots = 0 \quad (\text{E.2})$$

It was found that the choice

$$p = 1 \quad (\text{E.3})$$

$$q = -2 \quad (\text{E.4})$$

$$r = -2 \quad (\text{E.5})$$

$$s = 1 \quad (\text{E.6})$$

<sup>1</sup>In the case of negligible Kerr effect, this is also the linear resonance  $\nu_c$ .

holds a very good approximation for the obtained simulation results (see also figure E.1). In this way, one has

$$(|t_{tot}(\nu'_c)|^2 - |r_{tot}(\nu'_c)|^2)^2 - 2(|t_{tot}(\nu'_c)|^2 + |r_{tot}(\nu'_c)|^2) + 1 \approx 0 \quad (\text{E.7})$$

As all parameters used in the simulations were varied over a large range, this relation is considered to be generally valid. Now, both the (nonlinear) resonance transmission and reflection can be expressed in terms of  $B_{tot}^2(\nu'_c)$  as

$$|t_{tot}(\nu'_c)|^2 = \frac{1}{2} \left( B_{tot}^2(\nu'_c) + \sqrt{2B_{tot}^2(\nu'_c) - 1} \right) \quad (\text{E.8})$$

$$|r_{tot}(\nu'_c)|^2 = \frac{1}{2} \left( B_{tot}^2(\nu'_c) - \sqrt{2B_{tot}^2(\nu'_c) - 1} \right) \quad (\text{E.9})$$

To determine this nonlinear loss, the following method is used. For small intensities, the loss due to two-photon absorption is equivalent to the phase shift induced by the Kerr effect,

$$1 - B_{tot,small}^2(\nu'_c) \propto 2 \frac{\omega K_2}{c} |E_{in}|^2 \Leftrightarrow \Delta\phi \propto -\frac{\omega n_2}{c} |E_{in}|^2$$

The factor 2 in this expression is due to the fact that loss is related to the optical intensity, whereas the phase is related to the optical field. Using equations (D.33) and (C.20), one obtains for small intensities

$$1 - B_{tot,small}^2(\nu'_c) = -\frac{c}{\pi\nu'_c} \frac{\beta}{n_2} \frac{\Delta\nu_{c,ll}}{\Delta\nu_{BW,ll}} \quad (\text{E.10})$$

In contrast to the Kerr effect, two-photon absorption will change the resonance bandwidth<sup>2</sup>: this will explicitly be indicated by either *ll* (lossless) or *lossy* (also for other loss dependent properties). Note that this expression is independent of  $n_2$  as  $\Delta\nu_{c,ll} \propto n_2$ . For the general case, expansion of the results for single-photon absorption [104] leads to

$$1 - B_{tot}^2(\nu'_c) \approx |t_{tot}(\nu'_c)|^4 (1 - B_{tot,small}^2(\nu'_c)) \quad (\text{E.11})$$

$$= -|t_{tot}(\nu'_c)|^4 \frac{c}{\pi\nu'_c} \frac{\beta}{n_2} \frac{\Delta\nu_{c,ll}}{\Delta\nu_{BW,ll}} \quad (\text{E.12})$$

Using equation (E.8), one obtains the following implicit formula for the insertion loss:

$$1 - B_{tot}^2(\nu'_c) \approx -\frac{c}{4\pi\nu'_c} \frac{\beta}{n_2} \left( B_{tot}^2(\nu'_c) + \sqrt{2B_{tot}^2(\nu'_c) - 1} \right)^2 \frac{\Delta\nu_{c,ll}}{\Delta\nu_{BW,ll}} \quad (\text{E.13})$$

<sup>2</sup>In general, any absorption mechanism changes the bandwidth.

This equation together with equations (E.8) and (E.9) allows to determine the total transmission, reflection and insertion loss at nonlinear resonance.

For a general frequency  $\nu' \neq \nu'_c$ , equation (E.12) is to be expanded to,

$$1 - B_{tot}^2(\nu') \approx - |t_{tot}(\nu')|^4 \frac{c}{\pi \nu'_c} \frac{\beta}{n_2} \frac{\Delta \nu_{c,ll}}{\Delta \nu_{BW,ll}} \quad (\text{E.14})$$

In contrast to equation (E.12), equation (E.7) - and thus equations (E.8) and (E.9) - is not valid for general frequencies  $\nu' \neq \nu'_c$ . Instead, the following relation can be used: the nonlinear transmissivity  $|t_{tot,NL}(\nu')|^2$  is approximately related<sup>3</sup> to the linear transmissivity  $|t_{tot,L}(\nu)|^2$  by

$$\frac{|t_{tot,NL}(\nu')|^2 - |t_{tot,L}(\nu)|^2}{|t_{tot,L}(\nu)|^2} = U (1 - B_{tot}^2(\nu')) \quad (\text{E.15})$$

with  $U$  a constant. This means that the relative change in the transmission at a certain frequency is proportional to the total insertion loss at that frequency. This is in agreement with what could be expected. To calculate the constant  $U$ , this equation is evaluated at  $\nu' = \nu'_c$  or

$$U = \frac{|t_{tot,NL}(\nu'_c)|^2 - 1}{1 - B_{tot}^2(\nu'_c)} \quad (\text{E.16})$$

so that

$$\frac{|t_{tot,NL}(\nu')|^2 - |t_{tot,L}(\nu)|^2}{|t_{tot,L}(\nu)|^2} = \left( |t_{tot,NL}(\nu'_c)|^2 - 1 \right) \frac{1 - B_{tot}^2(\nu')}{1 - B_{tot}^2(\nu'_c)} \quad (\text{E.17})$$

Using equation (E.14), this becomes

$$\frac{|t_{tot,NL}(\nu')|^2}{|t_{tot,L}(\nu)|^2} - 1 = \left( |t_{tot,NL}(\nu'_c)|^2 - 1 \right) \frac{|t_{tot,NL}(\nu')|^4}{|t_{tot,NL}(\nu'_c)|^4} \quad (\text{E.18})$$

Finally, substituting equation (C.33), one obtains

$$\frac{1 - |t_{tot,NL}(\nu'_c)|^2}{|t_{tot,NL}(\nu'_c)|^4} |t_{tot,NL}(\nu')|^4 + \left( \frac{4(\nu' - \nu_c)^2}{\Delta \nu_{BW,ll}^2} + 1 \right) |t_{tot,NL}(\nu')|^2 = 1 \quad (\text{E.19})$$

An example of the effect of two-photon absorption is shown in figure E.2.

<sup>3</sup>Now, the impact of the Kerr effect (i.e. the shift of the resonance frequency) is explicitly neglected, so  $\nu' = \nu$  and  $\nu'_c = \nu_c$

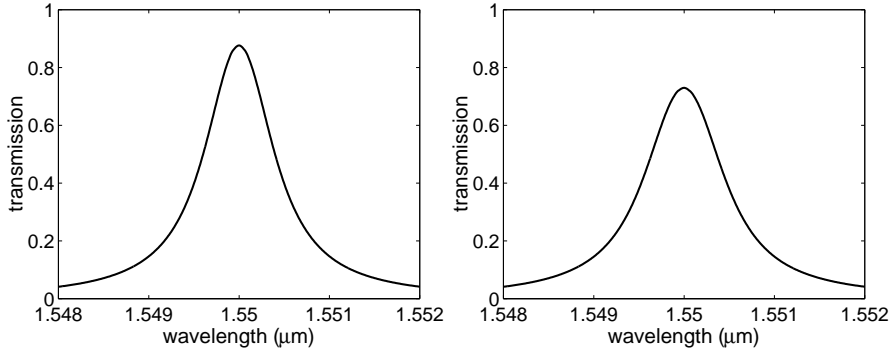


**Figure E.2:** Transmission of a resonator with one period in the presence of two-photon absorption. The following parameters are used:  $n_a = 2.37$ ,  $n_b = 0.9n_a$ ,  $N_{dbr} = 52$  and  $N_{cav} = 1$ . An input power of  $\beta\lambda_c |E_{in}|^2 = 0.6 \times 10^{-5}$  (left) and  $\beta\lambda_c |E_{in}|^2 = 1.8 \times 10^{-5}$  (right) were inserted.

From equation (E.19), a lossy resonance bandwidth can be determined, given by:

$$\Delta\nu_{BW,lossy} \approx \sqrt{\frac{3 - |t_{tot}(\nu'_c)|^2}{2 |t_{tot}(\nu'_c)|^2}} \Delta\nu_{BW,ll} \quad (\text{E.20})$$



## Appendix F

### Bit-error rate calculation

A theoretical prediction of the bit error rate as function of the detected average power is analytically possible if a gaussian distribution is assumed for all the dominant noise contributions [103]. In this case, the BER can be related to a quality factor  $Q$  which is defined as

$$Q = \frac{P_1 - P_0}{\sigma_0 + \sigma_1} \quad (\text{F.1})$$

with  $P_0$  and  $P_1$  respectively the mean '0' and '1' optical power level at the receiver end and  $\sigma_0$  and  $\sigma_1$  the (gaussian) variation of these levels. The corresponding BER is then given by,

$$BER = \frac{1}{2} \operatorname{erfc} \left( \frac{Q}{\sqrt{2}} \right) \quad (\text{F.2})$$

under the assumption that  $\sigma_0 \approx \sigma_1$  and the decision level for the detection of '0' and '1' is given by  $P_d = \frac{P_0 + P_1}{2}$

In the absence of regeneration, the different parameters  $P_0, P_1, \sigma_0 = \sigma_1 \equiv \sigma$  for the scheme of figure 4.17 are given by

$$P_0 = AP_{0,in} \quad (\text{F.3})$$

$$P_1 = AP_{1,in} \quad (\text{F.4})$$

$$\sigma^2 = A^2 \sigma_{in}^2 + \sigma_{rec}^2 \quad (\text{F.5})$$

with  $P_{0,in}, P_{1,in}, \sigma_{0,in} = \sigma_{1,in} \equiv \sigma_{in}$  the corresponding input parameters,  $A$  the variable attenuation in front of the receiver and  $\sigma_{rec}$  the noise introduced by the receiver. The parameter  $\sigma_{rec}$  can be related to the receiver sensitivity  $S$  for a specific  $BER_S$  by the following expression

$$BER_S = \frac{1}{2} \operatorname{erfc} \left( \frac{S}{\sqrt{2} \sigma_{rec}} \right) \quad (\text{F.6})$$

In the presence of regeneration, it is more difficult to calculate the  $BER$  analytically [143]. It is however possible to derive a lower and upper limit inbetween which the real  $BER$  is located. In general, a 2R-regenerator scheme can split into amplification and reshaping - characterized by a nonlinear function  $P_{reg,out}(P_{reg,in})$ , which in the ideal case is equal to a step function.  $P_0, P_1, \sigma_0 = \sigma_1 \equiv \sigma$  are then approximately given by

$$P_0 = AP_{reg,out}(GP_{0,in} + P_{ASE}) \quad (F.7)$$

$$P_1 = AP_{reg,out}(GP_{1,in} + P_{ASE}) \quad (F.8)$$

$$\sigma^2 = A^2 \left( \frac{dP_{reg,out}}{dP_{reg,in}} \right)^2 (G^2 \sigma_{in}^2 + \sigma_{ASE}^2) + \sigma_{rec}^2 \quad (F.9)$$

with  $G$  the gain of the optical amplifier,  $P_{ASE}$  the added mean signal-ASE power<sup>1</sup> and  $\sigma_{ASE}$  the added variation of the signal-ASE noise. To derive this, it was assumed that the nonlinear function can be assumed to be approximately linear around  $GP_{0,in} + P_{ASE}$  and  $GP_{1,in} + P_{ASE}$ , and  $\left. \frac{dP_{reg,out}}{dP_{reg,in}} \right|_{GP_{0,in}+P_{ASE}} = \left. \frac{dP_{reg,out}}{dP_{reg,in}} \right|_{GP_{1,in}+P_{ASE}} \equiv \left( \frac{dP_{reg,out}}{dP_{reg,in}} \right)$ , which is the case for a symmetrical reshaping function.

The BER is now underestimated by simply taking,

$$BER_{new} = \frac{1}{2} \operatorname{erfc} \left( \frac{P_1 - P_0}{2\sqrt{2}\sigma} \right) \quad (F.10)$$

because bit errors which are already present at the input of the reshaping element cannot be undone. These are however not yet taken into account in the above formula and given by

$$BER_{start} = \frac{1}{2} \operatorname{erfc} \left( G \frac{P_1 - P_0}{2\sqrt{2}\sqrt{G^2 \sigma_{in}^2 + \sigma_{ASE}^2}} \right) \quad (F.11)$$

The summation of both terms is on the other hand an overestimation of the  $BER$  as some of the errors 'after regeneration' may overlap with the latter bit errors  $BER_{new}$ . As a result, one has

$$\max(BER_{start}, BER_{new}) \leq BER \leq BER_{start} + BER_{new} \quad (F.12)$$

In most practical cases, one will have that  $BER_{start} \ll BER_{new}$  so that a very good evaluation of the Bit Error Rate is possible.

<sup>1</sup>This is assumed to be the dominant noise contribution

# Bibliography

- [1] D. Miller, "Physical reasons for optical interconnection," *Int. J. Optoelectronics*, vol. 11, no. 3, pp. 155–168, 1997.
- [2] I. Christiaens, *Vertically coupled microring resonators fabricated with wafer bonding*. Ghent University, Ph D thesis, 2004-2005.
- [3] W. Bogaerts, *Nanophotonic waveguides and photonic crystals in Silicon-on-Insulator*. Ghent University, Ph D thesis, 2003-2004.
- [4] D. Taillaert, *Grating couplers as interface between optical fibres and nanophotonic waveguides*. Ghent University, Ph D thesis, 2004-2005.
- [5] B. Luyssaert, *Compact planar waveguide spot-size converters in Silicon-on-Insulator*. Ghent University, Ph D thesis, 2004-2005.
- [6] J. De Merlier, *Optical signal regeneration based on integrated amplifying interferometers*. Ghent University, Ph D thesis, 2002-2003.
- [7] M. Zhao, *All-optical signal regeneration based on gain-clamped semiconductor optical amplifiers*. Ghent University, Ph D thesis, 2002-2003.
- [8] J. Cheyns, *Towards more packet switching in optical networks*. Ghent University, Ph D thesis, 2004-2005.
- [9] Lucent Technologies, <http://www.lucent.com>.
- [10] Intel Inc., <http://www.intel.com>.
- [11] Luxtera Inc., <http://www.luxtera.com>.
- [12] Infinera Inc., <http://www.infinera.com>.

- [13] J. Mørk, T. Berg, and S. Bischoff, "Fast processes in semiconductor optical amplifiers: theory and experiment," *IEEE/LEOS Newsletter*, pp. 21–24, October 2002.
- [14] A. Liu, R. Jones, L. Liao, D. Samara-Rubio, D. Rubin, O. Cohen, R. Nicolaescu, and M. Paniccia, "A high-speed Silicon optical modulator based on a metal-oxide-semiconductor capacitor," *Nature*, vol. 427, pp. 615–618, February 2004.
- [15] Q. Xu, B. Schmidt, S. Pradhan, and M. Lipson, "Micrometre-scale Silicon electro-optic modulator," *Nature*, vol. 435, pp. 325–327, May 2005.
- [16] P. Butcher and D. Cotter, *The elements of nonlinear optics*. Cambridge: University Press, 1st ed., 1990.
- [17] R. Baets, *Photonics*. Ghent University, course, 2003.
- [18] R. Adair, L. Chase, and S. Payne, "Nonlinear refractive index of optical crystals," *Phys. Rev. B*, vol. 39, pp. 3337–3350, February 1989.
- [19] L. Boyle, A. Buckingham, R. Disch, and D. Dunmur, "Higher polarizability of the Helium atom," *J. Chem. Phys.*, vol. 45, pp. 1318–1323, August 1966.
- [20] S. Jha and N. Bloembergen, "Nonlinear optical susceptibilities in group-IV and III-V semiconductors," *Phys. Rev.*, vol. 171, pp. 891–898, July 1968.
- [21] C. Flytzanis, "Third-order susceptibilities in IV-IV and III-V semiconductors," *Phys. Lett. A*, vol. 31, pp. 273–274, March 1970.
- [22] J. Van Vechten and D. Aspnes, "Franz-Keldysh contributions to third-order optical susceptibilities," *Phys. Lett. A*, vol. 30, pp. 346–347, 1969.
- [23] N. Boling, A. Glass, and A. Owyong, "Empirical relationships for predicting nonlinear refractive index changes in optical solids," *IEEE J. Quantum Electron.*, vol. 14, pp. 601–608, August 1978.
- [24] B. Wherrett, "A comparison of theories of resonant nonlinear refraction in semiconductors," *Proc. Roy. Soc. London A*, vol. 390, pp. 373–396, December 1983.

- [25] M. Sheik-Bahae, D. Hagan, and E. Van Stryland, "Dispersion and band-gap scaling of the electronic kerr effect in solids associated with two-photon absorption," *Phys. Rev. Lett.*, vol. 65, pp. 96–99, July 1990.
- [26] M. Sheik-Bahae, D. Hutchings, D. Hagan, and E. Van Stryland, "Dispersion of bound electronic nonlinear refraction in solids," *IEEE J. Quantum Electron.*, vol. 27, pp. 1296–1309, June 1991.
- [27] B. Wherrett, "Scaling rules for multiphoton interband absorption in semiconductors," *J. Opt. Soc. Am. B*, vol. 1, pp. 67–72, March 1984.
- [28] B. Jalali and R. Claps, "Light generation, amplification and wavelength conversion via stimulated raman scattering in silicon microstructures," *Topics Appl. Phys.*, vol. 94, pp. 199–239, 2004.
- [29] D. Hutchings and B. Wherrett, "Theory of the dispersion of ultrafast nonlinear refraction in zinc-blende semiconductors below the band edge," *Phys. Rev. B*, vol. 50, pp. 4622–4630, August 1994.
- [30] G. Agrawal, *Nonlinear fiber optics*. Boston: Academic press, 1th ed., 1989.
- [31] H. Tsang, C. Wong, T. Liang, I. Day, S. Roberts, A. Harpin, J. Drake, and M. Asghari, "Optical dispersion, two-photon absorption and self-phase modulation in silicon waveguides at 1.5  $\mu\text{m}$  wavelength," *Appl. Phys. Lett.*, vol. 80, pp. 416–418, January 2002.
- [32] M. Dinu, F. Quochi, and H. Garcia, "Third-order nonlinearities in Silicon at telecom wavelengths," *Appl. Phys. Lett.*, vol. 82, pp. 2954–2956, May 2003.
- [33] G. Rieger, K. Virk, and J. Young, "Nonlinear propagation of ultrafast 1.5  $\mu\text{m}$  pulses in high-index-contrast Silicon-on-Insulator waveguides," *Appl. Phys. Lett.*, vol. 84, pp. 900–902, February 2004.
- [34] U. Peschel, T. Peschel, and F. Lederer, "Optimization of bistable planar resonators operated near half the band gap," *IEEE J. Quantum Electron.*, vol. 30, pp. 1241–1249, May 1994.
- [35] A. Villeneuve, C. Yang, G. Stegeman, C.-H. Lin, and H.-H. Lin, "Nonlinear refractive-index and two photon-absorption near half

- the band gap in AlGaAs," *Appl. Phys. Lett.*, vol. 62, pp. 2465–2467, May 1993.
- [36] J. Aitchison, D. Hutchings, J. Kang, G. Stegeman, and A. Villeneuve, "The nonlinear optical properties of AlGaAs at the half band gap," *IEEE J. Quantum Electron.*, vol. 33, pp. 341–348, March 1997.
- [37] D. Hutchings and B. Wherrett, "Theory of anisotropy of two-photon absorption in zinc-blende semiconductors," *Phys. Rev. B*, vol. 49, pp. 2418–2426, January 1994.
- [38] T. Liang, H. Tsang, I. Day, J. Drake, A. Knights, and M. Asghari, "Silicon waveguide two-photon absorption detector at 1.5  $\mu\text{m}$  wavelength for autocorrelation measurements," *Appl. Phys. Lett.*, vol. 81, pp. 1323–1325, August 2002.
- [39] D. Vignaud, J. Lampin, and F. Mollot, "Two-photon absorption in InP substrates in the 1.55  $\mu\text{m}$  range," *Appl. Phys. Lett.*, vol. 85, pp. 239–241, July 2004.
- [40] R. Baets, I. Veretennicoff, and J. Danckaert, *Nonlinear and quantum optics*. Ghent University - VUB, course, 2004.
- [41] F. Verheest, *Nonlinear waves and solitons*. Ghent University, course, 2001.
- [42] S. Blair, J. Heebner, and R. Boyd, "Beyond the absorption-limited nonlinear phase shift with microring resonators," *Opt. Lett.*, vol. 27, pp. 357–359, March 2002.
- [43] K. DeLong, K. Rochford, and G. Stegeman, "Effect of two-photon absorption on all-optical guided-wave devices," *Appl. Phys. Lett.*, vol. 55, pp. 1823–1824, October 1989.
- [44] K. DeLong and G. Stegeman, "Two-photon absorption as a limitation to all-optical waveguide switching in semiconductors," *Appl. Phys. Lett.*, vol. 57, pp. 2063–2064, November 1990.
- [45] V. Mizrahi, K. DeLong, G. Stegeman, M. Saifi, and M. Andrejco, "Two-photon absorption as a limitation to all-optical switching," *Opt. Lett.*, vol. 14, pp. 1140–1142, October 1989.

- [46] A. Villeneuve, C. Yang, P. Wigley, G. Stegeman, J. Aitchison, and I. C.N., "Ultrafast all-optical switching in semiconductor nonlinear directional couplers at half the band gap," *Appl. Phys. Lett.*, vol. 61, pp. 147–149, July 1992.
- [47] B. Bennett, R. Soref, and J. Del Alamo, "Carrier-induced change in refractive index of InP, GaAs and InGaAsP," *IEEE J. Quantum Electron.*, vol. 26, pp. 113–122, January 1990.
- [48] Y. Lee, A. Chavez-Pirson, S. Koch, H. Gibbs, S. Park, J. Morhange, A. Jeffery, and N. Peyghambarian, "Room-temperature optical nonlinearities in GaAs," *Phys. Rev. Lett.*, vol. 57, pp. 2446–2449, November 1986.
- [49] A. Fox, A. Maciel, J. Ryan, and M. Scott, "Nonlinear optical absorption in bulk GaInAs/InP at room temperature," *Appl. Phys. Lett.*, vol. 50, pp. 398–400, February 1987.
- [50] L. Brzozowski, E. Sargent, A. Thorpe, and M. Extavour, "Direct measurements of large near-band edge nonlinear index change from 1.48 to 1.55  $\mu\text{m}$  InGaAs/InAlGaAs multiquantum wells," *Appl. Phys. Lett.*, vol. 82, pp. 4429–4431, June 2003.
- [51] S. Nakamura, K. Tajima, N. Hamao, and Y. Sugimoto, "High-speed all-optical switching experiment in Mach-Zehnder configuration using GaAs waveguide," *Appl. Phys. Lett.*, vol. 62, pp. 925–927, March 1993.
- [52] S. Park, J. Morhange, A. Jeffery, R. Morgan, A. Chavez-Pirson, H. Gibbs, S. Koch, N. Peyghambarian, M. Derstine, A. Gossard, J. English, and W. Weigmann, "Measurements of room-temperature band-gap-resonant optical nonlinearities of GaAs/AlGaAs multiple quantum wells and bulk GaAs," *Appl. Phys. Lett.*, vol. 52, pp. 1201–1203, April 1988.
- [53] S. Schmitt-Rink, D. Chemla, and D. Miller, "Theory of transient excitonic optical nonlinearities in semiconductor quantum-well structures," *Phys. Rev. B*, vol. 32, pp. 6601–6609, November 1985.
- [54] M. Kawase, E. Garmire, H. Lee, and P. Dapkus, "Single-pulse pump-probe measurement of optical nonlinear properties in GaAs/AlGaAs multiple quantum wells," *IEEE J. Quantum Electron.*, vol. 30, pp. 981–988, April 1994.

- [55] H.-C. Lee, A. Kost, M. Kawase, A. Hariz, P. Dapkus, and E. Garmire, "Nonlinear absorption properties of AlGaAs/GaAs multiple quantum wells grown by metalorganic chemical vapor deposition," *IEEE J. Quantum Electron.*, vol. 24, pp. 1581–1592, August 1988.
- [56] D. Van Thourhout, C. Doerr, C. Joyner, and J. Pleumeekers, "Observation of WDM crosstalk in passive semiconductor waveguides," *IEEE Photon. Technol. Lett.*, vol. 13, pp. 457–459, May 2001.
- [57] V. Van, T. Ibrahim, K. Ritter, P. Absil, F. Johnson, R. Grover, J. Goldhar, and P.-T. Ho, "All-optical nonlinear switching in GaAs/AlGaAs microring resonators," *IEEE Photon. Technol. Lett.*, vol. 14, pp. 74–76, January 2002.
- [58] T. Ibrahim, R. Grover, L.-C. Kuo, S. Kanakaraju, L. Calhoun, and P.-T. Ho, "All-optical AND/NAND logic gates using semiconductor microresonators," *IEEE Photon. Technol. Lett.*, vol. 15, pp. 1422–1424, October 2003.
- [59] P. Clauws, *Semiconductors*. Ghent University, course, 1999.
- [60] F. Raineri, C. Cojocaru, P. Monnier, A. Levenson, and R. Raj, "Ultrafast dynamics of the third-order nonlinear response in a two-dimensional InP-based photonic crystal," *Appl. Phys. Lett.*, vol. 85, pp. 1880–1882, September 2004.
- [61] Y. Lee, H. Gibbs, J. Jewell, J. Duffy, T. Venkatesan, A. Gossard, W. Wiegmann, and J. English, "Speed and effectiveness of windowless GaAs etalons as optical logic gates," *Appl. Phys. Lett.*, vol. 49, pp. 486–488, September 1986.
- [62] Y. Silberberg, P. Smith, D. Miller, B. Tell, A. Gossard, and W. Wiegmann, "Fast nonlinear optical response from proton-bombarded multiple quantum well structures," *Appl. Phys. Lett.*, vol. 46, pp. 701–703, April 1985.
- [63] J. Jewell, S. McCall, A. Scherer, H. Houh, N. Whitaker, A. Gossard, and J. English, "Transverse modes, waveguide dispersion and 30ps recovery in submicron GaAs/AlAs microresonators," *Appl. Phys. Lett.*, vol. 55, pp. 22–24, July 1989.

- [64] V. Almeida, C. Barrios, R. Panepucci, and M. Lipson, "All-optical control of light on a Silicon chip," *Nature*, vol. 431, pp. 1081–1084, October 2004.
- [65] P. Barclay, K. Srinivasan, and O. Painter, "Nonlinear response of Silicon photonic crystal microresonators excited via an integrated waveguide and fiber taper," *Opt. Express*, vol. 13, pp. 801–820, February 2005.
- [66] M. Notomi, A. Shinya, S. Mitsugi, G. Kira, E. Kuramochi, and T. Tanabe, "Optical bistable switching action of Si high-Q photonic-crystal nanocavities," *Opt. Express*, vol. 13, pp. 2678–2687, March 2005.
- [67] T. Tanabe, M. Notomi, S. Mitsugi, A. Shinya, and E. Kuramochi, "Fast bistable all-optical switch and memory on a Silicon photonic crystal on-chip," *Opt. Lett.*, vol. 30, pp. 2575–2577, October 2005.
- [68] A. Bristow, J.-P. Wells, W. Fan, A. Fox, M. Skolnick, D. Whittaker, A. Tahraoui, T. Krauss, and J. Roberts, "Ultrafast nonlinear response of AlGaAs two-dimensional photonic crystal waveguides," *Appl. Phys. Lett.*, vol. 83, pp. 851–853, August 2003.
- [69] P. LiKamWa, A. Miller, J. Roberts, and P. Robson, "130ps recovery of all-optical switching in a GaAs multiquantum well directional coupler," *Appl. Phys. Lett.*, vol. 58, pp. 2055–2057, May 1991.
- [70] S. Preble, Q. Xu, B. Schmidt, and M. Lipson, "Ultrafast all-optical modulation on a Silicon chip," *Opt. Lett.*, vol. 30, pp. 2891–2893, November 2005.
- [71] Y. Sugimoto, N. Ikeda, N. Carlsson, K. Asakawa, N. Kawai, and K. Inoue, "Fabrication and characterization of different types of two-dimensional AlGaAs photonic crystal slabs," *J. Appl. Phys.*, vol. 91, pp. 922–929, February 2002.
- [72] K. Asakawa, Y. Sugimoto, Y. Tanaka, N. Ikeda, H. Nakamura, K. Kanamoto, Y. Nakamura, S. Ohkouchi, and K. Inoue, "State-of-the-art and perspective of GaAs-based two-dimensional photonic crystal slab waveguides - towards ultra-small all-optical switches," in *Technical Digest: International Symposium on Photonic and Electromagnetic Crystal Structures (PECS-V)*, We-H1, Kyoto, Japan, March 7-11, 2004.

- [73] G. Stegeman and R. Stolen, "Waveguides and fibers for nonlinear optics," *J. Opt. Soc. Am. B*, vol. 6, pp. 652–662, April 1989.
- [74] A. Feldman, D. Horowitz, and R. Waxler, "Mechanisms for self-focusing in optical glasses," *IEEE J. Quantum Electron.*, vol. 9, pp. 1054–1061, November 1973.
- [75] NSM Archive - Physical Properties of Semiconductors, <http://www.ioffe.ru/SVA/NSM/Semicond/index.html>.
- [76] M. Teshima, "Dynamic wavelength tuning characteristics of the 1.5  $\mu\text{m}$  three-section DBR lasers: Analysis and experiment," *IEEE J. Quantum Electron.*, vol. 31, pp. 1389–1400, August 1995.
- [77] G. Coppola, A. Irace, G. Breglio, and A. Cutolo, "All-silicon mode-mixing router based on the plasma-dispersion effect," *J. Opt. A*, vol. 3, pp. 346–354, July 2001.
- [78] D. Hutchings and B. Wherrett, "Theory of the anisotropy of ultrafast refraction in zinc-blende semiconductors below the band edge," *Phys. Rev. B*, vol. 52, pp. 8150–8159, September 1995.
- [79] F. Filtrilawati, M. Tjia, S. Pfeiffer, H.-H. Hörnhold, A. Deutesfeld, E. H., and C. Bubeck, "Planar waveguides and PPV derivatives: attenuation loss, third-harmonic generation and photostability," *Opt. Mater.*, vol. 21, pp. 511–519, January 2003.
- [80] M. Bader, H.-M. Keller, and G. Marowsky, "Polymer-based waveguides and optical switching," *Opt. Mater.*, vol. 9, pp. 334–341, January 1998.
- [81] D. Chemla, D. Miller, P. Smith, A. Gossard, and W. Wiegmann, "Room temperature excitonic nonlinear absorption and refraction in GaAs/AlGaAs multiple quantum well structures," *IEEE J. Quantum Electron.*, vol. 20, pp. 265–275, March 1984.
- [82] J. Weiner, D. Pearson, D. Miller, D. Chemla, D. Sivco, and A. Cho, "Nonlinear spectroscopy of InGaAs/InAlAs multiple quantum well structures," *Appl. Phys. Lett.*, vol. 49, pp. 531–533, September 1986.
- [83] R. Jin, K. Okada, G. Khitrova, H. Gibbs, M. Pereira, S. Koch, and N. Peyghambarian, "Optical nonlinearities in strained-layer InGaAs/GaAs multiple quantum wells," *Appl. Phys. Lett.*, vol. 61, pp. 1745–1747, October 1992.

- [84] M. Islam, C. Soccolich, R. Slusher, A. Levi, W. Hobson, and M. Young, "Nonlinear spectroscopy near half-gap in bulk and quantum well GaAs/AlGaAs waveguides," *J. Appl. Phys.*, vol. 71, pp. 1927–1935, February 1992.
- [85] C. Hamilton, J. Marsh, D. Hutchings, J. Aitchison, G. Kennedy, and W. Sibbett, "Localized Kerr-type nonlinearities in GaAs/AlGaAs multiple quantum well structures at 1.55  $\mu\text{m}$ ," *Appl. Phys. Lett.*, vol. 68, pp. 3078–3080, May 1996.
- [86] J. Donnelly, H. Le, E. Swanson, S. Groves, A. Darwish, and E. Ippen, "Nondegenerate four-wave mixing wavelength conversion in low-loss passive InGaAsP-InP quantum-well waveguides," *IEEE Photon. Technol. Lett.*, vol. 8, pp. 623–625, May 1996.
- [87] M. Dvorak, B. Justus, and A. Berry, "Pump/probe Z-scan studies of GaAs nanocrystals grown in porous glass," *Opt. Commun.*, vol. 116, pp. 149–152, April 1995.
- [88] M. Zheng, L. Zhang, and J. Zhang, "Size dependence of nonlinear optical properties of SiO<sub>2</sub> thin films containing InP nanocrystals," *Appl. Phys. A - Materials Science and Processing*, vol. 73, pp. 183–187, August 2001.
- [89] P. Bettotti, M. Cazzanelli, L. Dal Negro, B. Danese, Z. Gaburro, C. Oton, G. Vijaya Prakash, and L. Pavesi, "Silicon nanostructures for photonics," *J. Phys.: Condens. Matter*, vol. 14, pp. 8253–8281, September 2002.
- [90] G. Priem, I. Moreels, P. Dumon, Z. Hens, W. Bogaerts, D. Van Thourhout, G. Morthier, and R. Baets, "InP-nanocrystal monolayer deposition onto Silicon-on-Insulator structures," in *Proceedings of 2005 IEEE/LEOS Annual Meeting*, TuB1, Sydney, Australia, October 23–27, 2005.
- [91] W. Bogaerts, R. Baets, P. Dumon, V. Wiaux, S. Beckx, D. Tailaert, B. Luyssaert, J. Van Campenhout, P. Bienstman, and V. T. D., "Nanophotonic waveguides in Silicon-on-Insulator fabricated with CMOS technology," *IEEE J. Lightwave Technol.*, vol. 23, pp. 401–412, January 2005.
- [92] M. Notomi, A. Shinya, S. Mitsugi, E. Kuramochi, and H.-Y. Ryu, "Waveguides, resonators and their coupled elements in photonic crystal slabs," *Opt. Express*, vol. 12, pp. 1551–1561, April 2004.

- [93] P. Bienstman, "Two-stage mode finder for waveguides with a 2d cross-section," *Opt. Quantum Electron.*, vol. 36, pp. 5–14, 2004.
- [94] CAvity Modelling FRamework, <http://camfr.sourceforge.net>.
- [95] O. Painter, R. Lee, A. Scherer, A. Yariv, J. O'Brien, P. Dapkus, and I. Kim, "Two-dimensional photonic band-gap defect mode laser," *Science*, vol. 284, pp. 1819–1821, June 1999.
- [96] M. Sheik-Bahae, J. Wang, and E. Van Stryland, "Nondegenerate optical Kerr effect in semiconductors," *IEEE J. Quantum Electron.*, vol. 30, pp. 249–255, February 1994.
- [97] R. Baets and H. Thienpont, *Microphotonics*. Ghent University - VUB, course, 2004.
- [98] G. Priem, I. Notebaert, B. Maes, P. Bienstman, G. Morthier, and R. Baets, "Design of all-optical nonlinear functionalities based on resonators," *IEEE J. Select. Topics Quantum Electron.*, vol. 10, pp. 1070–1078, September-October 2004.
- [99] B. Maes, P. Bienstman, and R. Baets, "Modeling of Kerr nonlinear photonic components with mode expansion," *Opt. Quantum Electron.*, vol. 36, pp. 15–24, 2004.
- [100] Y. Chen and S. Blair, "Nonlinearity enhancement in finite coupled-resonator slow-light waveguides," *Opt. Express*, vol. 12, pp. 3353–3366, July 2004.
- [101] A. Melloni, F. Morichetti, and M. Martinelli, "Optical slow-wave structures," in *Proceedings of 2005 European Conference on Optical Communication (ECOC)*, Mo 3.1.1, Glasgow, United Kingdom, September 25-29, 2005.
- [102] V. Almeida and M. Lipson, "Optical bistability on a Silicon chip," *Opt. Lett.*, vol. 29, pp. 2387–2389, October 2004.
- [103] G. Morthier and J. Danckaert, *Dynamics of Photonic Components*. Ghent University, course, 2004.
- [104] G. Priem, P. Bienstman, G. Morthier, and R. Baets, "Impact of absorption mechanisms on Kerr-nonlinear resonator behaviour," *J. Appl. Phys.*, vol. 99, p. 063103, March 2006.

- [105] V. Dragan and J. Sajeew, "Pulse reshaping in photonic crystal waveguides and microcavities with Kerr nonlinearity: Critical issues for all-optical switching," *Phys. Rev. A*, vol. 72, p. 013807, 2005.
- [106] H. Lee and G. Agrawal, "Nonlinear switching of optical pulses in fiber Bragg gratings," *IEEE J. Quantum Electron.*, vol. 39, pp. 508–515, March 2003.
- [107] W. Bogaerts, R. Baets, P. Dumon, V. Wiaux, S. Beckx, D. Tailaert, B. Luyssaert, J. Van Campenhout, P. Bienstman, and D. Van Thourhout, "Nanophotonic waveguides in silicon-on-insulator fabricated with cmos technology," *IEEE J. Lightwave Technol.*, vol. 23, pp. 401–412, January 2005.
- [108] O. Boyraz, T. Indukuri, and B. Jalali, "Self-phase-modulation induced spectral broadening in Silicon waveguides," *Opt. Express*, vol. 12, pp. 829–834, February 2004.
- [109] T. Liang, L. Nunes, M. Tsuchiya, K. Abedin, T. Miyazaki, D. Van Thourhout, P. Dumon, R. Baets, and H. Tsang, "Nonlinear self-distortion of picosecond optical pulses in Silicon wire waveguides," in *Proceedings of 2006 European Conference on Optical Communication (ECOC)*, (submitted), Long Beach, United States, May 21-26, 2006.
- [110] R. Claps, D. Dimitropoulos, V. Raghunathan, Y. Han, and B. Jalali, "Observation of stimulated raman amplification in Silicon waveguides," *Opt. Express*, vol. 11, pp. 1731–1739, July 2003.
- [111] A. Cowan, G. Rieger, and J. Young, "Nonlinear transmission of 1.5  $\mu\text{m}$  pulses through single-mode Silicon-on-Insulator waveguides structures," *Opt. Express*, vol. 12, pp. 1611–1621, March 2004.
- [112] T. Liang and H.-K. Tsang, "Nonlinear absorption and Raman scattering in Silicon-on-Insulator optical waveguides," *IEEE J. Select. Topics Quantum Electron.*, vol. 10, pp. 1149–1153, September-October 2004.
- [113] O. Boyraz, P. Koonath, V. Raghunathan, and B. Jalali, "All-optical switching and continuum generation in Silicon waveguides," *Opt. Express*, vol. 12, pp. 4094–4102, August 2004.

- [114] O. Boyraz, P. Koonath, V. Raghunathan, and B. Jalali, "All optical switching via XPM in Silicon waveguides," in *Proceedings of 2004 IEEE/LEOS Annual Meeting*, ThBB1, Puerto Rico, United States, November 7-11, 2004.
- [115] T. Liang, L. Nunes, T. Sakamoto, K. Sasagawa, T. Kawanishi, M. Tsuchiya, G. Priem, D. Van Thourhout, P. Dumon, R. Baets, and H. Tsang, "Ultrafast all-optical switching by cross-absorption modulation in Silicon wire waveguides," *Opt. Express*, vol. 13, pp. 7298–7303, August 2005.
- [116] L. Nunes, T. Liang, K. Abedin, T. Miyazaki, M. Tsuchiya, D. Van Thourhout, P. Dumon, R. Baets, and H. Tsang, "Low energy ultrafast switching in silicon wire waveguides," in *Proceedings of 2005 European Conference on Optical Communication (ECOC)*, Th4.2.3, Glasgow, United Kingdom, September 25-29, 2005.
- [117] C. Schubert, J. Berger, S. Diez, H. Ehrke, R. Ludwig, U. Feiste, C. Schmidt, H. Weber, G. Toptchiyski, S. Randel, and K. Petermann, "Comparison of interferometric all-optical switches for demultiplexing applications in high-speed OTDM systems," *IEEE J. Lightwave Technol.*, vol. 20, pp. 618–624, April 2002.
- [118] S. Nakamura, K. Tajima, and Y. Sugimoto, "Experimental investigation on high-speed switching characteristics of a novel symmetric Mach-Zehnder all-optical switch," *Appl. Phys. Lett.*, vol. 65, pp. 283–285, July 1994.
- [119] S. Stepanov and S. Ruschin, "Phase and amplitude modulation of light by light in Silicon-on-Insulator waveguides," *Electron. Lett.*, vol. 41, pp. 477–478, April 2005.
- [120] G. Priem, P. Dumon, W. Bogaerts, D. Van Thourhout, G. Morthier, and R. Baets, "Optical bistability and pulsating behaviour in Silicon-on-Insulator ring resonator structures," *Opt. Express*, vol. 13, pp. 9623–9628, November 2005.
- [121] T. Tsuchiwaza, K. Yamada, H. Fukuda, T. Watanabe, J.-I. Takahashi, M. Takahashi, T. Shoji, E. Tamechika, S.-I. Itabashi, and H. Morita, "Microphotronics devices based on Silicon microfabrication technology," *IEEE J. Select. Topics Quantum Electron.*, vol. 11, pp. 232–240, January-February 2005.

- [122] H. Fukuda, K. Yamada, T. Watanabe, T. Shoji, M. Takahashi, T. Tsuchiwaza, T. Watanabe, J.-I. Takahashi, and S.-I. Itabashi, "Four-wave mixing in Silicon wire waveguides," *Opt. Express*, vol. 13, pp. 4629–4637, June 2005.
- [123] R. Espinola, J. Dadap, R. Osgood Jr., S. McNab, and S. Vlasov, "C-band wavelength conversion in Silicon photonic wire waveguides," *Opt. Express*, vol. 13, pp. 4341–4349, May 2005.
- [124] B. Little, J.-P. Laine, and S. Chu, "Surface-roughness-induced contradirectional coupling in ring and disk resonators," *Opt. Lett.*, vol. 22, pp. 4–6, January 1997.
- [125] A. Melloni, F. Morichetti, and M. Martinelli, "Linear and nonlinear pulse propagation in coupled resonator slow-wave optical structures," *Opt. Quantum Electron.*, vol. 35, pp. 365–379, 2003.
- [126] J. Heebner, N. Lepeshkin, A. Schweinsberg, G. Wicks, R. Boyd, R. Grover, and P.-T. Ho, "Enhanced linear and nonlinear optical phase response of AlGaAs microring resonators," *Opt. Lett.*, vol. 29, pp. 769–771, April 2004.
- [127] H. Gibbs, *Optical bistability: controlling light with light*. Orlando: Academic Press, 1th ed., 1985.
- [128] T. Uesugi, B.-S. Song, T. Asano, and S. Noda, "Investigation of optical nonlinearities in an ultra-high-Q Si nanocavity in a two-dimensional photonic crystal slab," *Opt. Express*, vol. 14, pp. 377–386, January 2006.
- [129] T. Johnson, M. Borselli, and O. Painter, "Self-induced optical modulation of the transmission through a high-Q Silicon microdisk resonator," *Opt. Express*, vol. 14, pp. 817–831, January 2006.
- [130] S. McCall, "Instability and regenerative pulsation phenomena in fabry-perot nonlinear optic media devices," *Appl. Phys. Lett.*, vol. 32, pp. 284–286, March 1978.
- [131] D. Neilson, D. Stiliadis, and P. Bernasconi, "Ultra-high capacity optical ip routers for the networks of tomorrow: Iris project," in *Proceedings of 2005 European Conference on Optical Communication (ECOC)*, We 1.1.4, Glasgow, United Kingdom, September 25–29, 2005.

- [132] H. Rong, Y.-H. Kuo, A. Liu, M. Paniccia, and O. Cohen, "High efficiency wavelength conversion of 10 Gb/s data in Silicon waveguides," *Opt. Express*, vol. 14, pp. 1182–1188, January 2006.
- [133] M. Soljačić, "Novel devices based on photonic band gap cavities," in *Proceedings of 2005 European Conference on Optical Communication (ECOC)*, Tutorial Mo 3.6, Glasgow, United Kingdom, September 25-29, 2005.
- [134] G. Stegeman, "Guided wave approaches to optical bistability," *IEEE J. Quantum Electron.*, vol. 18, pp. 1610–1619, October 1982.
- [135] G. Stegeman and C. Seaton, "Nonlinear integrated optics," *J. Appl. Phys.*, vol. 58, pp. 57–78, December 1985.
- [136] G. Stegeman, E. Wright, N. Finlayson, Z. R., and C. Seaton, "Third order nonlinear integrated optics," *IEEE J. Lightwave Technol.*, vol. 6, pp. 953–970, June 1988.
- [137] A. Yariv, Y. Xu, R. Lee, and A. Scherer, "Coupled-resonator optical waveguide: a proposal and analysis," *Opt. Lett.*, vol. 24, pp. 711–713, June 1999.
- [138] H. Haus and Y. Lai, "Narrow-band distributed feedback reflector design," *IEEE J. Lightwave Technol.*, vol. 9, pp. 754–760, January 1991.
- [139] H. Haus and Y. Lai, "Theory of cascaded quarter wave shifted distributed feedback resonators," *IEEE J. Quantum Electron.*, vol. 28, pp. 205–213, January 1992.
- [140] M. Soljačić, M. Ibanescu, S. Johnson, Y. Fink, and J. Joannopoulos, "Optimal bistable switching in nonlinear photonic crystals," *Phys. Rev. E*, vol. 66, p. 055601, November 2002.
- [141] T. Peschel and F. Lederer, "Optical response of nonlinear planar resonators under pulsed-beam excitation," *Phys. Rev. B*, vol. 46, pp. 7632–7643, September 1992.
- [142] M. Born and E. Wolf, *Principles of optics*. Cambridge: University Press, 7th ed., 1999.
- [143] J. Mørk, F. Öhman, and S. Bischoff, "Analytical expression for the bit error rate of cascaded all-optical regenerators," *IEEE Photon. Technol. Lett.*, vol. 15, pp. 1479–1481, October 2003.